SPIN POLARIZATION TRANSFER IN EXCLUSIVE PHI ELECTROPRODUCTION

by

GREGORY LEIF RAKNESS

B. A., Saint Olaf College, 1993

A thesis submitted to the

Faculty of the Graduate School of the

University of Colorado in partial fulfillment

of the requirements for the degree of

Doctor of Philosophy

Department of Physics

2000

This thesis for the Doctor of Philosophy degree by

Gregory Leif Rakness

has been approved for the

Department of

Physics

by

____

Edward R. Kinney

____

John P. Cumalat

Date ____________________

The final copy of this thesis has been examined by the signators, and we find that both the content and the form meet acceptable presentation standards of scholarly work in the above mentioned discipline.

Rakness, Gregory Leif (Ph. D., Physics)

SPIN POLARIZATION TRANSFER IN EXCLUSIVE PHI ELECTROPRODUCTION

Thesis directed by Professor Edward R. Kinney

The helicity structure of the diffractive reaction $\gamma^* + A \rightarrow \phi + A$ was studied with ϕ mesons produced by longitudinally polarized positrons scattering from nuclear targets. By moment analysis of the distributions of data in the azimuthal production angle and two $\phi \rightarrow K^+K^-$ decay angles, values for the elements of the spin-density matrix of the ϕ meson were measured. As the helicity structure of the photon is known from the theory of Quantum Electrodynamics, the target contribution to the helicity of the ϕ meson can be inferred. The data indicate that the ϕ meson preserves the helicity of the photon in the kinematic range of this experiment, with the magnitude of the helicity preserving amplitude measured to be $|T_{11}| = 1.28 \pm 0.05$ and the magnitude of the largest helicity changing amplitude measured to be $|T_{1-1}| = 0.36 \pm 0.14$. The predictions of a $2g$ exchange model based on perturbative Quantum Chromodynamics are compared to the data, and found not to agree with the observed matrix elements.

With the observation that the helicity of the photon is preserved by the ϕ, the ratio of the longitudinal to transverse polarized photoproduction cross sections for the ϕ meson, $R_\phi = \sigma_L/\sigma_T$, can be computed from the measured longitudinal polarization of the ϕ. The data are combined with previous published data, and fit to the parameterization $R_\phi = (0.38 \pm 0.04)(Q^2/M_\phi^2)^{0.87 \pm 0.12}$, in approximate agreement with the Vector Meson Dominance model of the photon. The results are compared with the results for the ρ^0 vector meson.

DEDICATION

For my family.

ACKNOWLEDGMENTS

Although most of the work presented here was completed independently, by no means was it completed alone. As such, there are several people I would like to explicitly thank for helping me along the way. By the end, I'm sure I will have forgotten somebody that should have been on this list. I apologize for that in advance.

First and foremost, I would like to thank my advisor and friend, Ed Kinney, for lots of helpful discussions and many provocative questions. He's also a darn good snowboarder. Thank you for the encouragement and support. For addressing the many quandaries I have had about physics, analysis, and life in general, my friends Brendan Fox and Marc Welliver have been more than patient with me during these travails. Thank you, guys.

A good portion of my time in graduate school was spent at DESY in Hamburg, Germany, where I was fortunate to meet and to work with many wonderful physicists, whose myriad talents I respect and admire. Many discussions on the physics of vector meson electroproduction (among other things) were held with Eric Belz, Tom O'Neill, Sasha Borissov, Machiel Kolstein, Falk Meißner, and Michael Tytgat. Other people I would like to thank from my time at DESY are Antje Brüll, Johan Blouw, Balijeet Bains, Jan Visser, Pam Chumney, Bryan Tipton, Jeff Martin, Brynnen Owen, Elke Aschenauer, Erik Volk, James Ely, Andrea Belz (Dvoredsky), Kalen Martens, Chiara Simani, Philipp Geiger, and Marc-André Funk. With your help, I have finally become aware that positrons, in fact, do not travel backwards through time.

Lunch time is the best time of day. This mantra was thoroughly reinforced by the NPL lunch crew, including Derek van Westrum, Ken Knowles, Jeff Brack, Jeff Patterson, Gertjan Hofman, Andy Saunders, Horst Muller, Dale Prull, and Don Edmonds. I will miss the NPL and the tranquil antiquity it proclaims with verve.

I thank all my buds in Colorado from the other side of normal, who have encouraged me throughout the years to take mini-detours from the physics shenanigans through the activities of skiing, golfing, and hanging loose. You have helped me maintain some semblance of sanity during my time in Boulder: Brooks L'Amie, Matt Bromley, Burt Arnold, Joe Miller, and Aaron Burns, to name a few. In addition, there will always be a special spot in my heart for Mary Jane, the place where I discovered that bumps plus trees plus skis equals a truly exquisite experience. She rocks!

Finally, I'd like to thank my parents, who brought me into this world and instilled in me the value that hard work is a good thing. I appreciate the love and support I have received from you guys.

May Peace be with you all. I wish you the best.

CONTENTS

TABLES

TABLE

FIGURES

FIGURE

CHAPTER 1

INTRODUCTION

One of the goals of high energy and nuclear physics research is to understand the properties of "matter", that is, the properties of fundamental particles and the ways these particles interact with each other. Experimentally, this information is obtained by crashing particles or conglomerations of particles together at large energies and observing the characteristics of the reaction products. Careful comparison of measured quantities with theoretical predictions throughout the last century has led to the quite successful Standard Model of the physical world. In this model, there are two general types of particles, those particles which comprise matter, called leptons and quarks, and those particles which mediate the exchange forces between the leptons and quarks, called gauge bosons. The exchange forces described by the Standard Model are the electromagnetic, weak, and strong interactions.

Leptons are particles which do not undergo strong interactions, and have been observed to fall into three families: electron, muon, and tau leptons (written in order of increasing mass). The data indicate that leptons have no structure, that is, that they can be thought of as point particles. Quarks are particles which do undergo strong interactions, and are classified into different 'flavors' of quark, q, including the u, d, s, c, b, and t. In contrast to leptons, quarks have never been observed to exist alone in a free state. In other words, quarks display the property of confinement, where a single quark always appears bound together with at least one other quark within a state that is called a hadron. Specifically, a $q\bar{q}$ state is called a meson, and a qqq state is called a baryon. The properties of quarks, then, are inferred from data on hadronic reactions. For example, the data from deeply-inelastic scattering of electrons on protons, first observed in the late 1960's, indicated, among other things, that the quarks inside the proton are point particles when probed at high energy scales. [1]

Leptons and quarks interact via the exchange of gauge bosons in the Standard Model. The description of the interaction is separated into two distinct theories: electroweak theory, which describes the electromagnetic and the weak forces, and Quantum Chromodynamics (QCD), which describes the strong force. The electroweak theory describes the interactions of leptons and quarks via the exchange of four particles: the photon, γ^*, and the massive charged and neutral bosons, $W^\pm$ and Z^0, respectively. The exchange of photons is called the electromagnetic interaction, and is characterized by the small coupling constant, $\alpha_{e.m.} \approx 1/137$, of the photon to electrically charged leptons and hadrons. The exchange of massive vector bosons is called the weak interaction, and occurs much less frequently than does the electromagnetic interaction at low energy. The effective coupling constant of the weak interaction is on the order of $G_F \approx 10^{-5}\,\mathrm{GeV}^{-2}$, driven primarily by the large mass of the exchanged virtual $W^\pm$ or Z boson. In an uncertainty principle picture, the interaction length for the weak interaction must be very short, so that the energy fluctuation allowed by the uncertainty principle could be large enough so that the exchange of a massive vector boson can take place.

The other part of the Standard Model is QCD, which describes the strong interactions of quarks via the exchange of gluons, g, which couple with the "color" charge of the quarks. The strong interaction is effectively a short range interaction, and it has the property that the coupling constant of gluons with quarks is small at high energies, on the order of $\alpha_S \approx 0.1$ at $M_Z \approx 90\,\mathrm{GeV}$, but at low energies, the coupling becomes large.

The interactions in the Standard Model are formulated in terms of a relativistic quantum field theory, which combines the uncertainty principle and particle-wave duality of quantum mechanics together with the laws of special relativity. When the coupling of the gauge bosons to the leptons and quarks is small, transition probabilities of the interaction can be calculated perturbatively, that is, as small disturbances to the normal forward motion of a free lepton or quark. For example, using perturbative techniques with the theory of Quantum Electrodynamics (QED), electromagnetic interactions can be calculated quite precisely in the Standard Model. Perturbative QED calculations provide a description of, among other things, the total cross sections for $e^-e^- \to e^-e^-$ (Møller scattering), for $e^+e^- \to e^+e^-$ (Bhabha scattering), for $e^+e^- \to \mu^+\mu^-$ (muon production) [1], and many other processes. For strong interaction physics processes, some success has been achieved in describing experimental data by calculations using perturbative techniques with QCD (pQCD) at high energies, where the quark-gluon coupling constant is small. For example, the detailed dependence of the structure functions of the proton as a function of the momentum transfer is well-described by pQCD. [1] In addition, the Drell-Yan process, where a high-mass lepton pair emerges from the q-$\bar{q}$ annihilation process in hard proton-proton scattering, has also been fairly well-described by pQCD. [2] At smaller energies, however, where the strong coupling constant becomes large, calculations using a perturbative expansion formalism do not work. At these energies, a non-perturbative approach is typically used in the models, using "effective" degrees of freedom to describe the hadron-hadron interaction, for example, quark and gluon degrees of freedom might be replaced by meson or baryon degrees of freedom. The topic of the present work is a study of strong interaction physics in the Standard Model.

A well-established method to study the quark and gluon structure, collectively called parton structure, of hadrons is the technique of scattering high energy leptons from nuclear targets. The lepton scattering takes place via the exchange of a virtual photon, whose properties can be calculated precisely with QED. In this picture, the virtual photon is the well-understood tool with which we probe the unknown structure of the target. By changing the energy and scattering angle of the scattered lepton, the wavelength of the virtual photon can be varied over a large range, from distances comparable to the size of nuclei down to distances comparable to the size of quarks. The small value of the electromagnetic coupling constant of the photon to charged particles allows the photon to traverse well inside the target before it interacts, so that the inner structure of the hadron can be easily accessed. Numerous experiments on the deeply inelastic scattering (DIS) of leptons from nuclei have measured the structure functions of the nucleon over a large range of photon energy and wavelength. A wealth of information has been learned about these structure functions, including the momentum distributions of partons inside the nucleon, and the structure of these distributions in nuclei. [3] Double-spin asymmetry measurements with polarized leptons on polarized targets have recently begun to reveal information on the distribution of the spin polarization components of partons within the nucleon. [4–6]

Another technique by which features of the strong interaction can be studied is the scattering of hadrons from hadrons. In high energy "diffractive" hadron-proton scattering, the differential cross-section has been observed to be dominated by scattering at forward angles. At small angles, the data are described well by a fit of the form

$$\frac{d\sigma}{dt} \propto e^{-b|t'|}, \tag{1.1}$$

where t' is the squared transverse momentum exchanged from the hadron to the proton. Applying an optical model to elastic hadron scattering likens this reaction to absorption by a disc of radius b, so that b can be interpreted as the geometrical "size" of the hadron-proton interaction. [7,8] An example of the differential cross-section data from $\pi^- + p \to \pi^- + p$ elastic scattering can be seen in the left plot in Figure 1.1.

The total cross section of the $h + p \to X$ reaction as a function of center-of-momentum energy for several different hadrons can be seen in Figure 1.2. The reaction cross sections of the different hadrons on protons exhibit similar features as a function of energy, namely, a "resonance" region where the cross section varies strongly as a function of energy, followed by a region where the cross section becomes nearly independent of energy. The total hadron-proton reaction cross section data, together with the hadron-proton scattering differential cross section data, are consistent with the idea that hadron-hadron reactions are dominated by a short-range strong interaction with myriad open channels.

There are two different types of models which have had reasonable success in describing the features of diffractive hadron-proton cross section data. One approach is based on QCD, where quarks and gluons are the fundamental quanta which are exchanged in the reaction. The total vector meson photoproduction cross section data at high energy, for example, are fairly well-described by pQCD models of $2g$ exchange. [10,11] Another approach to describe the data is Regge theory, a phenomenological approach which uses hadronic degrees of freedom to describe the process. In Regge theory, the reaction is considered to proceed via the exchange of groups of mesons in the t-channel which have similar quantum numbers, *i.e.*, they lie along the same Regge trajectory. [12] Such a reaction is said to have occurred via Reggeon exchange. The energy dependence of the π-p elastic scattering cross section, for example, is well-described in Regge theory by the exchange of a particular Regge trajectory which has the quantum numbers of the vacuum, called Pomeron exchange. [13] The Regge model is a phenomenological model which has had a lot of success in describing the energy dependence of the total cross section for many

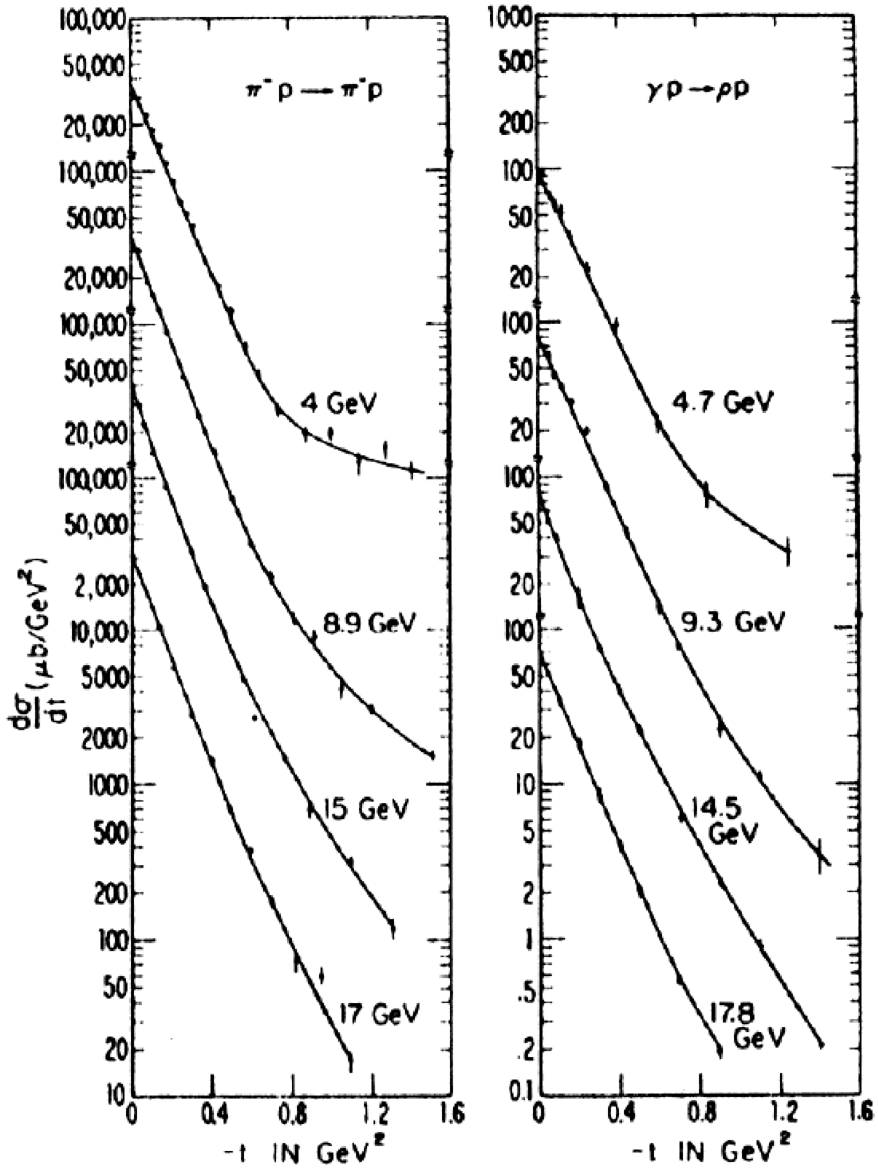

Figure 1.1. The differential cross sections for $\pi^- p \rightarrow \pi^- p$ elastic scattering and for $\gamma p \rightarrow \rho^0 p$ photoproduction plotted as a function of $-t$. These plots are taken from Reference [9] and references therein. At small t, the differential cross section drops steeply for both processes.

12 ***38. Plots of cross sections and related quantities***

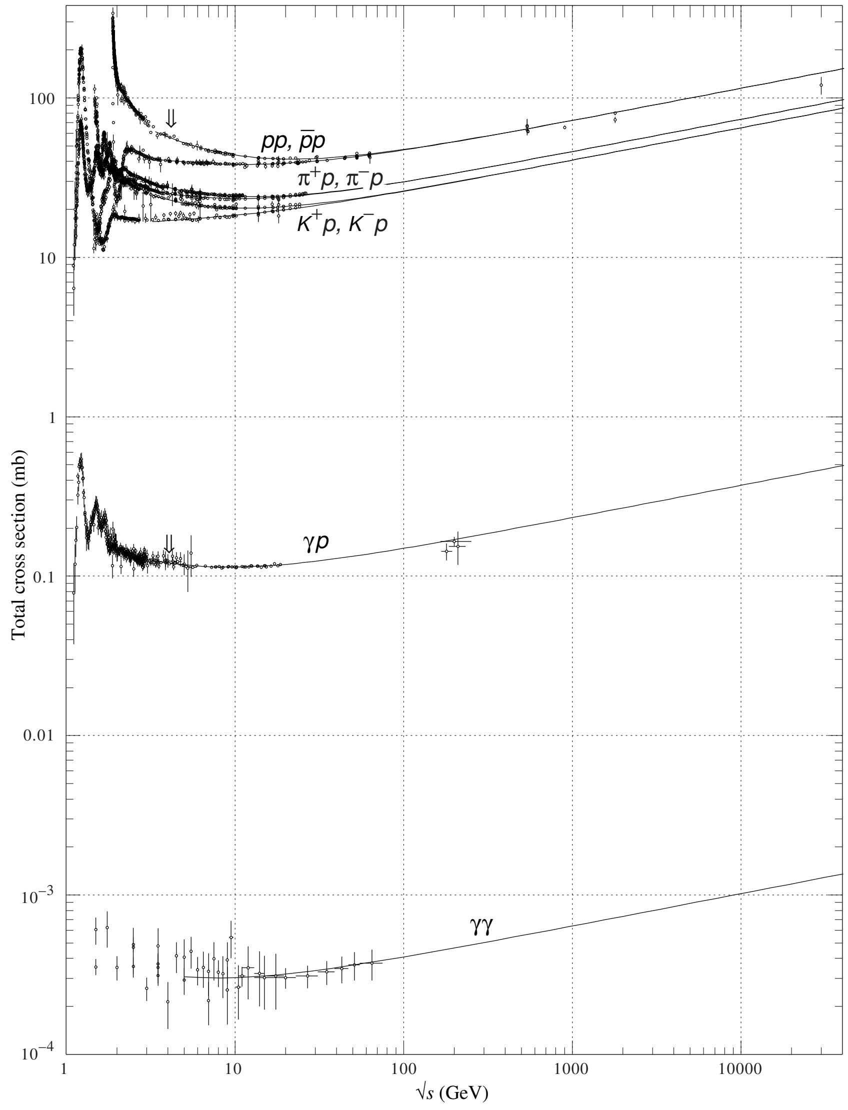

Figure 38.17: Summary of hadronic, γp, and $\gamma\gamma$ total cross sections. Corresponding computer-readable data files may be found at `http://pdg.lbl.gov/xsect/contents.html` (Courtesy of the COMPAS group, IHEP, Protvino, Russia, April 1998.)

Figure 1.2. The total cross section for various h-p and γ-p reactions as a function of energy in the h-p (γ-p) center-of-momentum frame. The lines represent Regge fits to the data. It is clear that the behavior of the reaction cross section as a function of energy does not depend strongly on the type of incident particle, since, in all cases, there is a resonance region followed by a region where it becomes independent of energy. This plot is taken from the Particle Data Group, and references therein.

hadronic reactions. [14] In a QCD picture, it is conjectured that Reggeon exchange would be $2q$ exchange, and Pomeron exchange would be $2g$ exchange. Some attempts to link Pomeron exchange to $2g$ exchange in vector meson electroproduction have met with limited success. [15]

The present work is a combination of lepton-proton scattering and diffractive hadron-proton interactions, two seemingly disjoint approaches to study strong interactions which are actually closely connected. This connection could be suggested by the observation that the photon-hadron reaction cross sections display similar features as those seen in hadron-hadron reactions. In Figure 1.2, the total $\gamma + p \rightarrow X$ reaction cross section is plotted as a function of the energy. The similarity of the shape of the photon-proton reaction cross section to that of the hadron-proton reaction cross sections is striking. In particular, the photon-proton cross section demonstrates a resonance structure at low energies and becomes nearly independent of energy at higher energies. The major difference between the photon-proton and the hadron-proton cross sections is that the photon-proton cross section is simply smaller in magnitude by approximately the fine structure constant, $\alpha_{e.m.}$. In addition, it has been observed that the differential cross section for ρ^0 photoproduction as a function of t' behaves according to Equation 1.1, as has been observed in hadron-proton elastic scattering. [9] For example, compare the left and right plots in Figure 1.1. Thus, both the total and differential cross section data for the photon processes can be interpreted to be suggestive that the photon acts like a hadron as a probe of the proton.

This idea of a hadronic component of the photon is quantified in the Vector Meson Dominance (VMD, sometimes called VDM) model of the photon. [9,16] The VMD model of the photon is a quantum mechanical picture of the photon where the wave function consists of two components: the normal "bare" photon state that interacts electromagnetically with the target, and hadronic states that interact

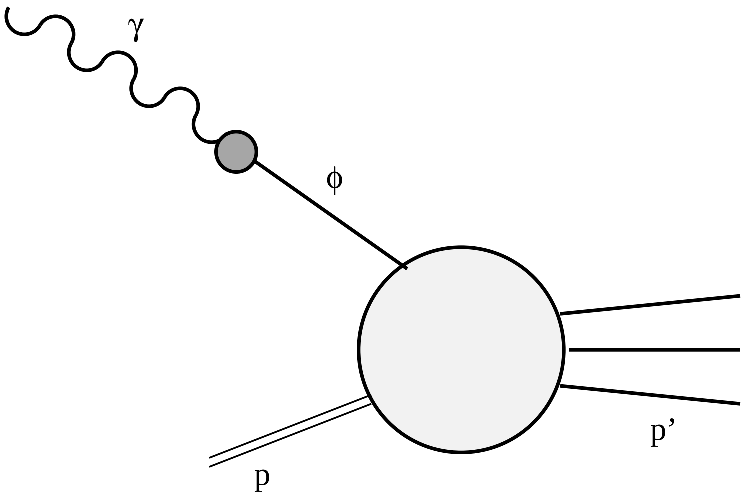

Figure 1.3. A pictorial description of the Vector Meson Dominance (VMD) model. Time moves from left to right in the picture. The photon fluctuates quantum mechanically into a ϕ vector meson a significant time before it interacts strongly with the target. With sufficient energy, the photon could fluctuate into any vector meson with quantum numbers $J^{PC} = 1^{--}$, in addition to this particular channel.

strongly with the target. Since the quantum numbers of the photon are $J^{PC} = 1^{--}$, the meson states which comprise the hadronic component of the photon should also have quantum numbers $J^{PC} = 1^{--}$, *i.e.*, they are vector mesons. In models which describe photon reactions, the VMD model is usually thought of as it is depicted in Figure 1.3. The (virtual) photon fluctuates into a vector meson (or quark-antiquark pair, depending on the degrees of freedom in the model), which then proceeds to interact as a hadron with the target. At small photon energies, the small-mass vector meson states are expected to dominate the hadronic component of the wave function, namely, the $\rho^0(770)$, $\omega(782)$, $\phi(1020)$, and J/$\psi(3097)$. In the quark model, the ρ^0 is $(u\bar{u} - d\bar{d})/\sqrt{2}$, the ω is primarily $(u\bar{u} + d\bar{d})/\sqrt{2}$ with a small admixture of $s\bar{s}$, the ϕ is primarily $s\bar{s}$, and the J/ψ is primarily $c\,\bar{c}$.

One of the biggest successes predicted by the VMD model is the quantitative relation between the $\gamma + N \rightarrow X$ total reaction cross section and the $\gamma + N \rightarrow \rho^0 + N$ forward photoproduction cross section [17]. In the VMD model, the rate of the fluctuation of a γ into a ρ^0 is governed by the $\gamma - \rho^0$ coupling constant which is measurable in experiments of the ρ^0 leptonic width in the decay $\rho^0 \to e^+e^-$. Thus, in the VMD model, the $\gamma + N \to X$ total reaction cross section is related to the $\rho^0 + N \to X$ total reaction cross section by this $\gamma - \rho^0$ coupling constant. Also, the $\gamma + N \to \rho^0 + N$ forward photoproduction cross section is related to the $\rho^0 + N \to \rho^0 + N$ forward elastic scattering cross section by the same coupling constant. Then, with the use of the optical theorem, one can relate the $\rho^0 + N \to X$ total reaction cross section to the $\rho^0 + N \to \rho^0 + N$ forward elastic scattering amplitude, thereby establishing the desired relation between the total photon reaction cross section and the forward ρ^0 photoproduction cross section, which is in agreement with experiment. [17] Note that the value of the $\rho^0 - N$ total reaction cross section computed in this VMD calculation is on the order of 25 mb—a value that would be typical for hadronic reactions. The total photon reaction cross section and the total photoproduction cross sections for several vector mesons, including the ρ^0, can be seen plotted in Figure 1.4. Nowadays, the VMD model is used in some form or another in nearly every calculation of the vector meson photoproduction process. See, for example, References [10,13,16,19–24].

Experiments began to report results on the total photoproduction cross sections of the ρ^0, ω, and ϕ vector mesons in the late 1960's [9]. As a function of photon-proton center-of-momentum energy, the cross sections of a few vector mesons are plotted in Figure 1.4. The total vector meson photoproduction cross section data can be described well by using the VMD model together with the exchange of Regge trajectories. At high energy, the slow decrease of the ρ^0, ω, and ϕ production cross sections as one decreases in energy is attributed to Pomeron exchange. As we approach even lower energies, the ρ^0 and the ω cross sections are observed to increase dramatically, attributed to the increasing prominence of Reggeon exchange amplitudes for these reactions. The ϕ cross section, on the other hand, is not observed

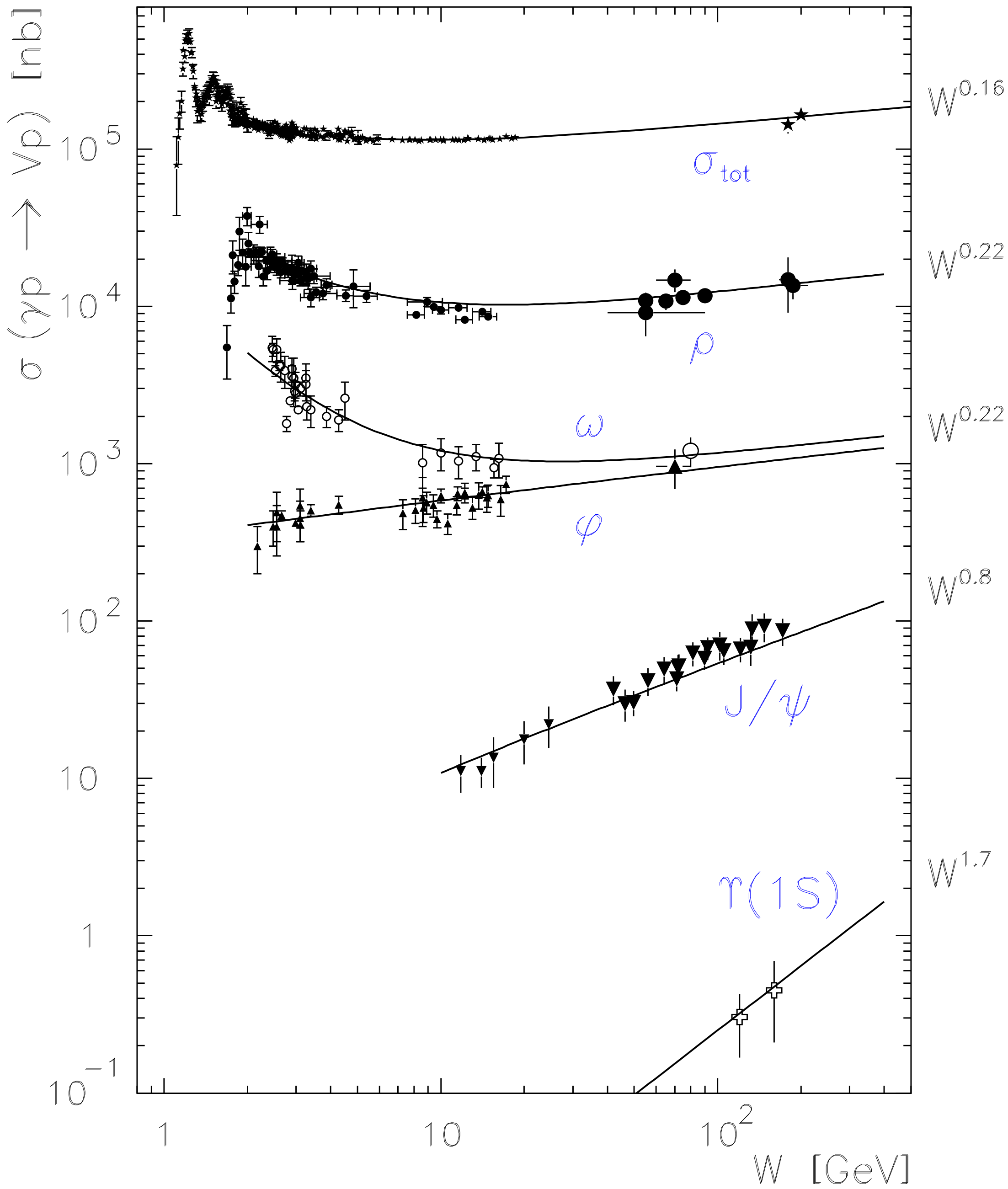

Figure 1.4. The total photon-proton absorption and photoproduction cross sections for several vector mesons plotted as a function of W, the center-of-momentum energy. This plot is taken from [12], [18], and references therein. The small-mass vector meson photoproduction cross sections are well-described using VMD and the Regge exchange model. The lines indicate these Regge-based power law fits to the data in [16,18].

to increase as it does for the ρ^0 and ω. As the ϕ is made up primarily of $s\bar{s}$ quarks, Reggeon exchange amplitudes are expected to be suppressed in their production. [25]

The specific topic of this work is the virtual photoproduction and decay of ϕ vector mesons in the reaction $(\vec{e}, e'\phi)$, then $\phi \to K^+K^-$, on nuclear targets. In particular, we will study the spin polarization properties of this reaction. The spin angular momentum of a quantum mechanical particle can be specified by the total spin quantum number and one component of the spin along a specified axis, called the spin quantization axis. The spin quantization axis may be chosen to point in any direction, and is typically chosen to be that which simplifies the description of the reaction. Following convention, we choose the spin quantization axis of each of the particles in the ϕ photoproduction reaction to be along the direction of motion of the particle. The component of angular momentum along the direction of motion is called the helicity quantum number of the particle.

The ϕ decays via the decay channel $\phi \to K^+K^-$ with a branching ratio of $\approx 50\%$. The width of the ϕ mass peak is on the order of $4\,\mathrm{MeV}$, indicating that the ϕ has a longer lifetime than the ρ^0, for example, which has a decay width of $\approx 150\,\mathrm{MeV}$. As the kaons have zero spin, the spin information of the ϕ is contained in the spatial distribution of the K^+K^- pair. Hence, measurements of the decay angular distributions of the K^+K^- give information about the helicity of the ϕ. In principle, the helicity properties of the final state ϕ in this electroproduction reaction could come from either the virtual photon or the target, or some combination of both.

There are very few data published on the helicity structure of ϕ mesons. A review of vector meson photoproduction and decay through 1975 can be found in Reference [9], and a more recent review can be found in Reference [18]. An early measurement of the ratio of longitudinal to transverse ϕ photoproduction cross sections was reported by an experiment at Cornell in Reference [26], published in 1977. In the 1990's, measurements of the longitudinal polarization of electroproduced

ϕ mesons were reported by the New Muon Collaboration (NMC) [27] at CERN and the ZEUS Collaboration [28] at DESY. Preliminary results on more of the ϕ spin-density matrix elements have recently become available from H1 and ZEUS in References [29] and [30], respectively.

Most of the data available from the decay angular distributions of vector mesons come from measurements of the $(e, e'\rho^0)$, then $\rho^0 \to \pi^+\pi^-$, reaction, first measured in the late 1960's. Experiments of note which have measured the helicity structure of the ρ^0 include a low-energy experiment at DESY [31] in the 1970's, experiments by the E665 Collaboration at Fermilab [32] in the late 1980's, experiments by the European Muon Collaboration [33] and NMC [27] at CERN in the 1980's and 1990's, and recent measurements by the HERMES [34], H1 [35, 36], and ZEUS [37] Collaborations at DESY. In these experiments, it was observed that the helicity of the ρ^0 is approximately equal to the helicity of the virtual photon. The preservation of the photon's helicity by the vector meson in photoproduction reactions has come to be known as s-channel helicity conservation, or SCHC. Hence, the measurement of the helicity structure of the ρ^0 (or ϕ) is often referred to as a "test of SCHC."

If SCHC were observed, it could be inferred that none of the helicity information of the ϕ is coming from the target. This would be a very important observation that would greatly constrain the possible reaction mechanisms in the models. In the VMD model of the photon, SCHC is assumed implicitly. In Regge models, amplitudes resulting from Pomeron exchange exhibit SCHC by construction, while amplitudes from Reggeon exchange need not. A pQCD model of the reaction based on quark and gluon degrees of freedom interprets the test of SCHC as a sensitive probe of the quark wave function of the vector meson, through the geometrical configuration of these quarks' interactions with two target gluons. [19] This model, in particular, makes a prediction for the measurement of specific SCHC-violating amplitudes at high W.

The decay angular distributions of vector mesons produced from an unpolarized lepton beam allow the measurement of up to 15 different spin-density matrix elements. [38] As mentioned before, in experiments on the ρ^0 meson, the helicity of the ρ^0 was observed to be approximately equal to the helicity of the photon. However, precision measurements of the 15 spin-density matrix elements for the ρ^0 meson have revealed that at high energy, there do exist small but significant non-zero amplitudes which violate SCHC, on the order of $\approx 10\%$. [36,37] Preliminary results on the ϕ meson at high energy indicate the presence of the same SCHC violating amplitudes as those observed for the ρ^0. [29,30]. These SCHC violations observed at high energy are consistent with the pQCD model of $2g$ exchange mentioned in the previous paragraph. At lower energy, violations of SCHC have been observed in ρ^0 photoproduction which are different than those seen at high energy. [31]

In this work, we will analyze the decay distributions of ϕ mesons produced by a longitudinally polarized positron beam at intermediate photon-proton center-of-momentum energy ($4 < W < 7\,\mathrm{GeV}$). With a longitudinally polarized beam, eight more spin-density matrix elements can be measured from the decay angular distributions, for a total of 23 measurable quantities. This is the first measurement of the complete set of 23 matrix elements which is available to the decay angular distribution analysis for any vector meson, allowing an unprecedented comparison of the spin-density matrix elements of the ϕ meson with the predictions of SCHC. In addition, these spin-density matrix elements will be compared with the prediction of the pQCD model of $2g$ exchange which has shown success at higher energy.

The results presented in this work on the ϕ meson will also be compared with published results from the ρ^0 meson. In the case of SCHC, the longitudinal polarization of a vector meson, V, measured with decay angular distributions, can be used to compute R_V, the ratio of cross sections for the production of V by longitudinal and transverse photons. The results from a fit to data on R_ϕ will be compared with the results from a fit to data on R_ρ. The function with which we will fit these data will be based on the VMD model, which predicts that the cross section ratio is inversely proportional to the vector meson mass. [39]

A synopsis of this work follows. In Chapter 2, the theory used to describe vector meson electroproduction and decay is described in detail, including a discussion of VMD, SCHC, and a pQCD model of $2g$ exchange. In Chapter 3, the HERMES detector which was used to collect the exclusive ϕ data sample is described. In Chapter 4, the extraction of the spin-density matrix elements from the measured quantities is discussed, as well as the estimates of the statistical and systematic uncertainties. In Chapter 5, the results of the spin-density matrix elements for ϕ mesons are compared with predictions from SCHC and the pQCD model of $2g$ exchange. In addition, the ϕ data are compared with ρ^0 data in this chapter. Finally, in Chapter 6, we summarize and make conclusions from this work, as well as speculate on subsequent research one might want to pursue as a result.

CHAPTER 2

VECTOR MESON ELECTROPRODUCTION PHYSICS

The physics of exclusive, diffractive vector meson electroproduction and decay is discussed.

2.1 Definitions and Polarization Formalism

2.1.1 Kinematics We assume the Born approximation, whereby the inelastic scattering of positrons, $e + N \to e + N + \phi$, is assumed to occur via the exchange of a single photon, as depicted in Figure 2.1. Using the system of units where $\hbar = c = 1$, we denote space-time four-vectors by $p = (E, \vec{p}) = (E, p_x, p_y, p_z)$, with the Lorentz-invariant metric $m^2 \equiv p^2 = E^2 - |\vec{p}|^2$.

The positron is scattered into the spectrometer at polar and azimuthal lab angles θ_e and φ_e through the exchange of a virtual photon. Neglecting the rest mass relative to the energy, the four-momenta of the initial and final positrons in the lab frame are $e = E(1, 0, 0, 1)$ and $e' = E'(1, \sin\theta_e \cos\varphi_e, \sin\theta_e \sin\varphi_e, \cos\theta_e)$, respectively. The positron information is used to compute the virtual photon's four-momentum $q = e - e' = (\nu, \vec{q})$. The negative mass-squared of the photon is computed in the lab frame as

$$Q^2 \equiv -q^2 \approx 4EE' \sin^2 \frac{\theta_e}{2} \geq 0, \tag{2.1}$$

where the assumption $m_e \approx 0$ has been made. A photon with $Q^2 = 0$ is called a real photon, and a photon with $Q^2 \neq 0$ is called a virtual photon. The invariant center-of-momentum energy squared of the photon-nucleon system is given by the

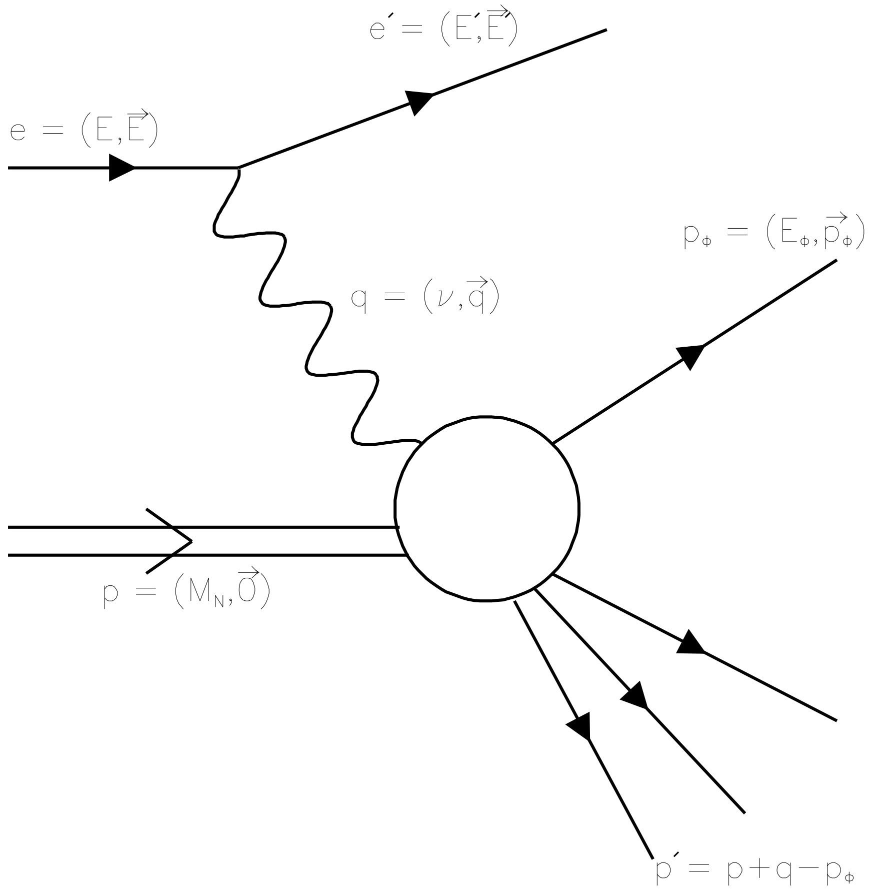

Figure 2.1. Diagram describing ϕ electroproduction. The undetected baryonic final state is denoted p'.

expression

$$W^2 \equiv (q+p)^2 = M_N^2 + 2\nu M_N - Q^2, \tag{2.2}$$

where the initial target nucleon, $p = (M_N, \vec{0})$, is assumed to be at rest in the lab frame. Often the variable Bjorken-x is used to describe deep-inelastic positron scattering, defined by

$$x = \frac{Q^2}{2M_p \nu}. \tag{2.3}$$

The ϕ is detected via the decay channel $\phi \to K^+K^-$, so that $p_\phi = (E_\phi, \vec{p}_\phi) = (E_+ + E_-, \vec{p}_+ + \vec{p}_-)$. The invariant mass squared of the di-kaon system is

$$M_{2K}^2 = p_\phi^2 = (E_+ + E_-)^2 - (\vec{p}_+ + \vec{p}_-)^2 > 4M_K^2. \tag{2.4}$$

Note that for production of a di-kaon state of mass M_{2K}, the minimum energy necessary in the photon-nucleon system is

$$W^2 \geq (M_N + M_{2K})^2. \tag{2.5}$$

The final baryonic state, p', is unmeasured in this experiment, and must be computed from the measured variables $p' = p + q - p_\phi$.

The polar angle of the produced ϕ relative to the virtual photon is given implicitly in terms of the four-momentum transfer to the target squared, the Mandelstam variable

$$t = (p' - p)^2 = (q - p_\phi)^2 < 0. \tag{2.6}$$

In the t-channel of the reaction, the progression from a virtual photon to a real ϕ is via the exchange of energy and 3-momentum with the target, as seen in Figure 2.2. The value of t closest to zero where this reaction is kinematically allowed is called

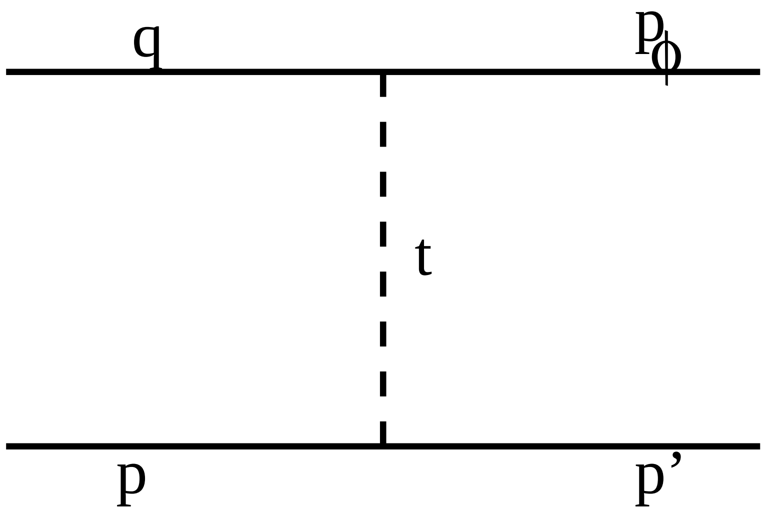

Figure 2.2. Tree-level diagram defining the kinematic variables for a t-channel exchange process. This diagram is contained within the circle in Figure 2.1.

t_{min}, defined by

$$t_{min} = M_{2K}^2 - Q^2 + 2(|\vec{q}_{c.m.}||\vec{p}_{\phi,c.m.}| - E_{\gamma^*,c.m.}E_{\phi,c.m.}) < 0, \tag{2.7}$$

evaluated in the photon-nucleon center-of-momentum frame, hereafter called the hadronic frame. As is t, t_{min} is invariant under Lorentz transformations. In the hadronic frame, the case $t = t_{min}$ corresponds to the case where the ϕ is produced collinear to the γ^*, so that defining

$$t' \equiv t - t_{min} \leq 0 \tag{2.8}$$

gives a measure of the transverse four-momentum transfer squared. Of the possible solutions to scatter from the virtual photon to the real ϕ, the case $t = t_{min}$ corresponds to the case where the energy-momentum transfer is closest to light-like, *i.e.* to lying parallel to the world line oriented at 45° ($t = 0$), with the constraint that the recoiling target remain on-shell. ZEUS and H1 [18] report t_{min} values for their ρ analysis of $-t_{min} < 10^{-4}\,\mathrm{GeV}^2$. The exclusive ϕ candidates in this analysis have an average $\langle -t_{min}\rangle \approx 0.1\,\mathrm{GeV}^2$, about three orders of magnitude larger. The

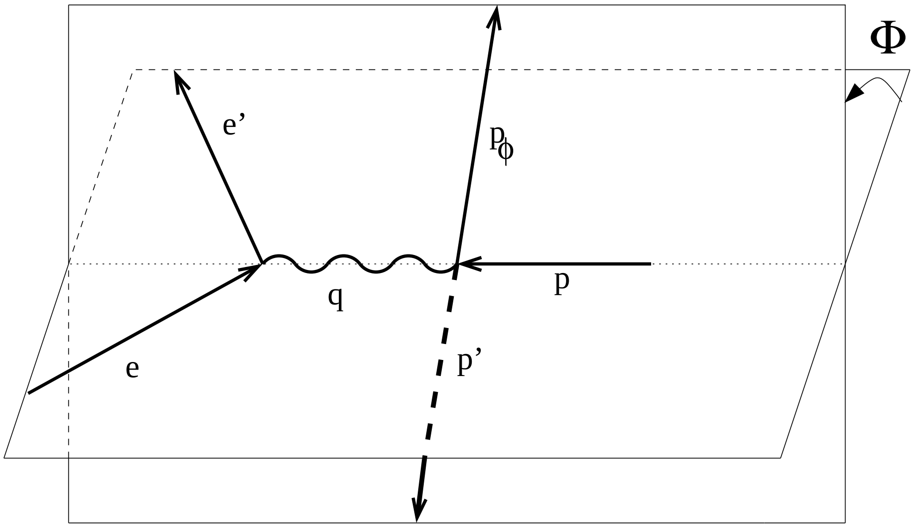

Figure 2.3. Diagram defining the azimuthal production angle, Φ. This angle is defined in the photon-proton center-of-momentum frame (hadronic frame).

much larger $-t_{min}$ is due to the much smaller virtual photon energy available to the reaction at HERMES, $\langle\nu\rangle = 14\,\mathrm{GeV}$, compared to $400 - 40,000\,\mathrm{GeV}$ at ZEUS and H1. Thus, t_{min} should not be ignored in our evaluation of t'.

The azimuthal production angle of the ϕ around the photon is denoted by Φ, and is depicted in Figure 2.3. It is defined as the angle between the positron scattering plane and the ϕ production plane, evaluated in the hadronic frame. In terms of momentum vectors,

$$\begin{aligned} \cos\Phi &= \frac{(\vec{q}\times\vec{p}_\phi)\cdot(\vec{e}\times\vec{e}\,')}{|\vec{q}\times\vec{p}_\phi|\;|\vec{e}\times\vec{e}\,'|}, \text{ and} \\ \sin\Phi &= \frac{[(\vec{q}\times\vec{p}_\phi)\times(\vec{e}\times\vec{e}\,')]\cdot\vec{q}}{|\vec{q}\times\vec{p}_\phi|\;|\vec{e}\times\vec{e}\,'|\;|\vec{q}|}. \end{aligned} \tag{2.9}$$

The boost from the lab frame to the hadronic frame is via $\vec{\beta} = \vec{q}/(\nu + M_p)$, *i.e.* along the direction of the virtual photon. As Φ is the azimuthal angle around this momentum vector of virtual photon, its value evaluated in the lab frame is the same as its value evaluated in the hadronic frame, where it is defined.

The decay of the ϕ into a K^+K^- pair is described, in the ϕ rest frame, by

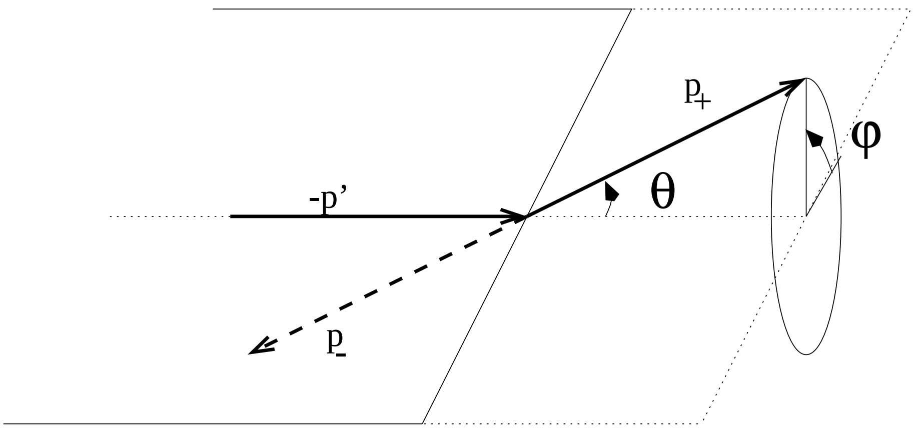

Figure 2.4. Diagram defining the polar and azimuthal decay angles, $\cos\theta$ and φ, of the K^+ relative to the ϕ spin quantization axis. These angles are defined in the ϕ rest frame. The plane shown is the ϕ production plane from Figure 2.3, and defines $\varphi = 0$.

the polar and azimuthal angles $\cos\theta$ and φ, respectively, of the K^+ relative to the ϕ spin quantization axis. The ϕ spin quantization is defined in the hadronic frame to be along the ϕ direction of motion. In the ϕ rest frame, where $\cos\theta$ is defined, the ϕ spin quantization axis is along the direction opposite the direction of the recoiling target, $-p'$. See Figure 2.4. In terms of momentum vectors, the polar angle is given by

$$\cos\theta = \frac{-\vec{p}\,' \cdot \vec{p}_+}{|\vec{p}\,'|\ |\vec{p}_+|}, \tag{2.10}$$

and the azimuthal angle is given by

$$\begin{aligned} \cos\varphi &= \frac{(\vec{q} \times -\vec{p}\,') \cdot (-\vec{p}\,' \times \vec{p}_+)}{|\vec{q} \times -\vec{p}\,'|\ |-\vec{p}\,' \times \vec{p}_+|} \text{ and} \\ \sin\varphi &= \frac{-[(\vec{q} \times -\vec{p}\,') \times -\vec{p}\,'] \cdot (-\vec{p}\,' \times \vec{p}_+)}{|(\vec{q} \times -\vec{p}\,') \times -\vec{p}\,'|\ |-\vec{p}\,' \times \vec{p}_+|}. \end{aligned} \tag{2.11}$$

Note that expressions 2.9, 2.10, and 2.11 are the definitions given in P. Joos, *et al.* [31] They are identical in content, but simpler in form, than the expressions given in Schilling and Wolf. [38]

2.1.2 Helicity The topic of this work involves the polarization properties of relativistic particles. In standard non-relativistic treatments, the possible polarization states of a particle are classified by the component of angular momentum along a fixed axis. We, however, use the helicity formalism to classify the possible polarization states of a particle, for reasons which will become evident soon enough. A particle's helicity, λ, is defined by its component of angular momentum (spin) in the direction of motion of the particle. [1] The particle helicity operator is $\frac{1}{2}(\vec{S} \cdot \hat{p})$, where $\vec{S}$ are the spin matrices of the particle and $\hat{p} = \vec{p}/|\vec{p}|$ is the direction of motion of the particle. For particles moving at the speed of light, such as real photons or neutrinos, the direction of motion of the particle is invariant under Lorentz transformations along or against said direction. Therefore, helicity is well-defined for massless particles. For massive particles, a definite frame must be chosen in which to evaluate the helicity.

A photon is a spin-1 particle, and so in principle has three helicity states $\lambda = +1,\ 0,\ -1$. The polarization state of the photon is called transverse if $\lambda = \pm 1$ and longitudinal if $\lambda = 0$. Note that this nomenclature is leftover from optics, and refers to the component of the $\vec{E}$-field vector relative to the Poynting vector of the photon. Hence, a "longitudinal photon" actually has spin polarization transverse to the direction of motion of the photon. For virtual photons, both transverse and longitudinal components must be considered. Real photons ($Q^2 = 0$), however, are polarized 100% transverse. [40]

The helicity states are a natural choice of basis with which to describe relativistic electromagnetic interactions of leptons, since helicity is conserved in such processes. [1] To show this, we introduce the right- and left-handed chiral projection operators (normally introduced in the context of neutrinos), defined on the electron spinors u with the Dirac-Pauli representation:

$$\begin{aligned} u_R &= P_R u = \frac{1}{2}(1+\gamma^5)u, \text{ and} \\ u_L &= P_L u = \frac{1}{2}(1-\gamma^5)u. \end{aligned} \tag{2.12}$$

Taking the ultra-relativistic limit ($E \cong |\vec{p}|$), we notice that

$$\gamma^5 u \simeq \begin{pmatrix} \vec{\sigma}\cdot\hat{p} & 0 \\ 0 & \vec{\sigma}\cdot\hat{p} \end{pmatrix} u, \tag{2.13}$$

so that right- and left-handed projections of u correspond to electron states of positive and negative helicity, respectively. Helicity conservation in electromagnetic processes then follows from the properties of γ-matrices. We would like to show that $\bar{u}_L \gamma^\mu u_R = 0$. We write

$$\bar{u}_L = u^\dagger \gamma^0 = u^\dagger \frac{1}{2}(1-\gamma_5)\gamma^0 = \bar{u}\frac{1}{2}(1+\gamma_5), \tag{2.14}$$

where the last two equal signs are because $\gamma_5 = \gamma_5^\dagger$ and $\gamma_5\gamma_0 = -\gamma_0\gamma_5$. So then

$$\bar{u}_L \gamma^\mu u_R = \frac{1}{4}\bar{u}(1+\gamma_5)\gamma_\mu(1+\gamma_5)u = \frac{1}{4}\bar{u}\gamma_\mu(1-\gamma_5)(1+\gamma_5)u, \tag{2.15}$$

the last step following from $\gamma_5\gamma_\mu = -\gamma_\mu\gamma_5$. The conclusion $\bar{u}_L\gamma^\mu u_R = 0$ follows immediately from the observation that $(\gamma_5)^2 = 1$. Therefore, the helicity of relativistic, point-like, spin-1/2 particles is preserved in interactions with vector coupling.

2.1.3 Photon Helicity We follow the formalism from Schilling and Wolf to obtain the spin-density matrix of the photon. [38] They use the Born approximation, discussed in Subsection 2.1.1. In this case, the cross-section then takes the form [41]

$$\frac{d\sigma_{eN\to eN\phi}}{dE' d\Omega_e d\Phi dt} \propto \frac{1}{Q^4} L_{\mu\nu} T^{\mu\nu}, \tag{2.16}$$

where $L_{\mu\nu}$ is the leptonic tensor and $T^{\mu\nu}$ is the hadronic tensor. The leptonic tensor $L_{\mu\nu}$ contains all the information regarding the polarization state of the virtual photon, and so is called the spin-density matrix of the photon. It can be calculated exactly using the theory of Quantum Electrodynamics (QED) in our choice of Lorentz frame. As is usual in physics, the interpretation of the reaction depends on the Lorentz frame chosen.

The frame in which we choose to calculate $L_{\mu\nu}$ is the Breit frame, or "brick-wall" frame, defined from either the lab frame or the hadronic frame by a boost along $\vec{q}$. In the brick-wall frame, the positron is scattered elastically backwards with the same energy as before the reaction. [42] If the positron is unpolarized (equal population of states with $\lambda = \pm 1/2$), helicity conservation dictates that the photon must be emitted with equal population of states with $\lambda = \pm 1$, but with no $\lambda = 0$ state. Hence, the spin-density matrix of the virtual photon is the same as that of unpolarized real photons. We choose the virtual photon scattering cross section normalization in the Breit frame to be the same as that in real photoproduction. Then the relative amount of transverse and longitudinal components resulting from subsequent boosts is fixed. This particular separation of the transverse and longitudinal strengths is known as the Hand convention.

Using the Hand convention, and boosting from the Breit frame to the lab frame, the positron deep-inelastic scattering differential cross section is given by [43]

$$\frac{d\sigma}{d\cos\theta_e \, d\varphi_e \, dE'} = \Gamma_T(\sigma_T + \epsilon\sigma_L), \tag{2.17}$$

where the transverse photon flux is given by

$$\Gamma_T = \frac{\alpha}{4\pi^2}\frac{W^2 - M_p^2}{2M_p}\frac{1}{Q^2}\frac{E'}{E}\frac{2}{1-\epsilon}. \tag{2.18}$$

The unpolarized transverse photon component of the total cross section is given by σ_T, while σ_L refers to the longitudinal component. The polarization parameter is

$$\epsilon = \left[1 + 2\frac{\nu^2 + Q^2}{4EE' - Q^2}\right]^{-1}, \tag{2.19}$$

and gives the flux of longitudinal photons normalized to unit flux of transverse photons. Inspection of Equation 2.19 reveals that for a fixed Q^2, ν, and beam energy, ϵ is uniquely determined. Therefore, the ratio of longitudinal to transverse contributions to the total cross-section is also uniquely determined. Hence, with a single beam energy, it is not possible to separate the contributions from transverse photons and longitudinal photons, it is only possible to measure the sum, $\sigma_T + \epsilon\sigma_L$.

The frame in which to study the helicity properties of ϕ's is called the s-channel helicity frame. The s-channel helicity frame is defined in the photon-proton center-of-momentum system, where the spin-polarization axis of the ϕ is taken to be the direction of the ϕ.

In an early experiment on ρ^0 decay distributions, one of the goals was specifically to determine what frame to use to describe the spin-polarization properties of the process $\gamma + N \rightarrow \rho^0 + N$. [44] There were three competing frames at the time, differing essentially in the choice of ρ^0 spin-quantization axis, depicted in Figure 2.5. These three frames each had the ρ^0 spin-quantization axis chosen to be sensitive to a different mechanism by which angular momentum could be transferred to the ρ^0 final state. [9] The Gottfried-Jackson frame was defined in the ρ^0 rest frame, where the z-axis was taken to be the direction of the photon. This frame was well-suited to a reaction mechanism where no spin would be transferred through the t-channel exchange with the target. The Adair frame was defined in the hadronic system (the $\gamma^* - N$ center-of-momentum frame), where the z-axis was taken to be the direction of the photon. This frame was well-suited to a model whereby spin-projection would be conserved in the assumed s-channel system of Figure 2.5. As mentioned before, the helicity frame is defined in the hadronic frame like the Adair frame, but the z-axis is taken to be the direction of the ρ^0. This frame is suited to a reaction mechanism where the helicity of the photon is preserved by the helicity of the ρ^0 meson in the s-channel system of Figure 2.5. For forward produced ρ^0's ($t' \approx 0$), the quantization axes of the ρ^0 in all three frames coincide. In Reference [44], the ρ^0 spin-density matrix elements were measured in each of the above three frames, and plotted as a function of t. It turned out that the s-channel helicity frame was the only frame in which the spin-density matrix elements did not vary strongly with t. [44] This

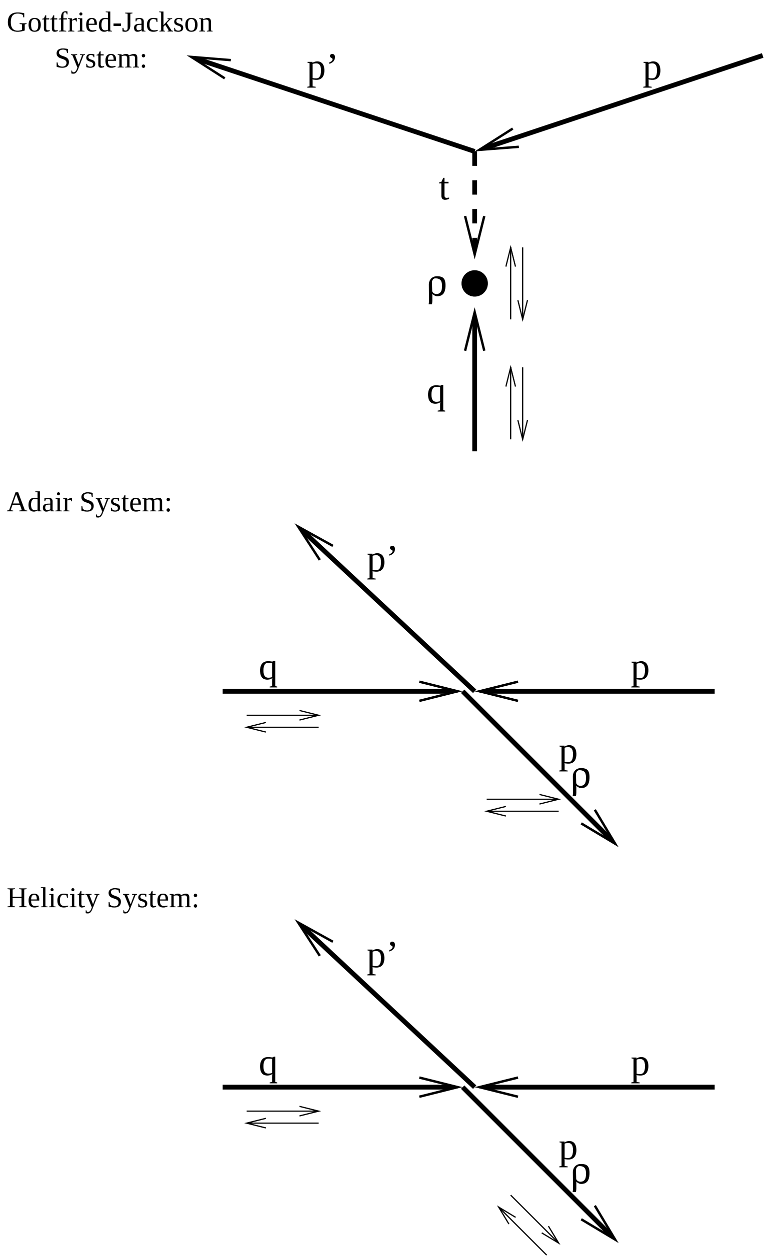

Figure 2.5. A schematic diagram showing the different systems of reference which would be appropriate for different scenarios of spin transfer to the ρ^0 state. [9]

is evidence that the s-channel helicity frame is the preferred choice of frame which simplifies the description of the reaction mechanism, and implies that the helicity basis is an efficient basis in which to think about this reaction. As such, this observation of the preservation of the photon helicity by the ρ^0 meson quickly acquired an acronym: SCHC, or s-Channel Helicity Conservation. It should be noted that SCHC is a phenomenon that is observed only in the s-channel helicity frame. The s-channel frame has an implicit assumption made on the hadronic frame, that there is no orbital angular momentum in the $\gamma^* - N$ system. With this assumption, the γ^* and the N collide head-on, as it is depicted in Figure 2.3.

We boost our $L_{\mu\nu}$ from the Breit frame to the helicity frame by a Lorentz transformation along $\vec{q}$. While the transverse polarizations remain unchanged under boosts along $\vec{q}$, the longitudinal (z) and scalar (time) components transform into each other. They are therefore treated as a single entity through current conservation, which reduces $L_{\mu\nu}$ from a 4×4 matrix to a 3×3 matrix. [38] In addition, we make a change of basis from the basis of spatial coordinates, (x, y, z), to the basis of photon helicity states, $(+1, 0, -1)$. Then the photon spin-density matrix reads (for $Q^2 \gg m_e^2$):

$$L_{\lambda\lambda'} \sim \begin{pmatrix} 1 & \sqrt{\epsilon(1+\epsilon)}\, e^{-i\Phi} & -\epsilon\, e^{-2i\Phi} \\ \sqrt{\epsilon(1+\epsilon)}\, e^{i\Phi} & 2\epsilon & -\sqrt{\epsilon(1+\epsilon)}\, e^{-i\Phi} \\ -\epsilon\, e^{2i\Phi} & -\sqrt{\epsilon(1+\epsilon)}\, e^{i\Phi} & 1 \end{pmatrix}, \tag{2.20}$$

where $\lambda,\ \lambda' = -1,\ 0,\ +1$ is the photon helicity, with the polarization parameter, ϵ.

The spin-density matrix $L_{\lambda\lambda'}$ in equation 2.20 is for an unpolarized positron beam. For a longitudinally polarized positron beam, the photon density matrix, $\rho(\gamma)$, is given by the sum of the unpolarized and polarized density matrices,

$$\rho(\gamma)_{\lambda\lambda'} \sim [L_{\lambda\lambda'} + M_{\lambda\lambda'}], \tag{2.21}$$

where the polarized spin-density matrix is

$$M_{\lambda\lambda'} \sim P \begin{pmatrix} \sqrt{1+\epsilon} & \sqrt{\epsilon}\, e^{-i\Phi} & 0 \\ \sqrt{\epsilon}\, e^{i\Phi} & 0 & \sqrt{\epsilon}\, e^{-i\Phi} \\ 0 & \sqrt{\epsilon}\, e^{i\Phi} & -\sqrt{1+\epsilon} \end{pmatrix}. \tag{2.22}$$

It is possible to write $\rho(\gamma)$ as a linear combination of an orthogonal set of matrices Σ^α:

$$\rho(\gamma) = \frac{1}{2}\sum_{\alpha=0}^{8} \Pi_\alpha \Sigma^\alpha, \tag{2.23}$$

where

$$\Sigma^0 = \begin{pmatrix} 1 & 0 & 0 \\ 0 & 0 & 0 \\ 0 & 0 & 1 \end{pmatrix},\ \Sigma^1 = \begin{pmatrix} 0 & 0 & 1 \\ 0 & 0 & 0 \\ 1 & 0 & 0 \end{pmatrix},\ \Sigma^2 = \begin{pmatrix} 0 & 0 & -i \\ 0 & 0 & 0 \\ i & 0 & 0 \end{pmatrix},$$

$$\Sigma^3 = \begin{pmatrix} 1 & 0 & 0 \\ 0 & 0 & 0 \\ 0 & 0 & -1 \end{pmatrix},\ \Sigma^4 = 2\begin{pmatrix} 0 & 0 & 0 \\ 0 & 1 & 0 \\ 0 & 0 & 0 \end{pmatrix},\ \Sigma^5 = \frac{1}{\sqrt{2}}\begin{pmatrix} 0 & 1 & 0 \\ 1 & 0 & -1 \\ 0 & -1 & 0 \end{pmatrix},$$

$$\Sigma^6 = \frac{1}{\sqrt{2}}\begin{pmatrix} 0 & -i & 0 \\ i & 0 & i \\ 0 & -i & 0 \end{pmatrix},\ \Sigma^7 = \frac{1}{\sqrt{2}}\begin{pmatrix} 0 & 1 & 0 \\ 1 & 0 & 1 \\ 0 & 1 & 0 \end{pmatrix},\ \text{and } \Sigma^8 = \frac{1}{\sqrt{2}}\begin{pmatrix} 0 & -i & 0 \\ i & 0 & -i \\ 0 & i & 0 \end{pmatrix}. \tag{2.24}$$

The matrices Σ^α are density matrices representing pure states of photon polarization. Matrices $\Sigma^0 - \Sigma^3$ correspond to contributions from transverse photons, Σ^4 represents purely longitudinal photons, and $\Sigma^5 - \Sigma^8$ represent longitudinal-transverse interference terms. The transverse terms are further classified according to the conventions of real photons: an unpolarized component ($\alpha = 0$), two components of linear polarization ($\alpha = 1,\ 2$), and a circularly polarized component ($\alpha = 3$). As previously mentioned, with a constant beam energy, the unpolarized transverse ($\alpha = 0$) and the longitudinal ($\alpha = 4$) components of the photon cannot be separated.

2.1.4 Vector Meson Helicity and Decay Distributions The reaction $e + N \to e + N + \phi$ was reduced to the two-body reaction $\gamma^* + N \to \phi + N$ in the previous subsection. We describe the production amplitudes of this two-body reaction with the helicity amplitudes of Jacob and Wick, defined by [45]

$$T_{\lambda_\phi \lambda_{N'} \lambda_\gamma \lambda_N} = \langle \lambda_\phi \lambda_{N'} | J_{\lambda_\gamma} | \lambda_N \rangle. \tag{2.25}$$

The summation over nucleon helicities is always implied, and will not be indicated hereafter. These helicity amplitudes were developed in the 1950's for the formalism of relativistic four-body reactions, using a helicity basis in which to calculate collision amplitudes instead of a standard spin-projection basis.

In terms of the helicity amplitudes and the photon spin-density matrix, the spin-density matrix of the vector meson is given by

$$\rho(\phi) = \frac{1}{2} T \rho(\gamma) T^\dagger, \tag{2.26}$$

which has been obtained from the photon spin-density matrix by a change of basis transformation. As with the photon spin-density matrix, the ϕ spin-density matrix can be expressed in terms of a linear combination of matrices:

$$\rho(\phi) = \sum_{\alpha=0}^{8} \Pi_\alpha \rho^\alpha, \tag{2.27}$$

where

$$\rho^\alpha_{\lambda_\phi \lambda'_\phi} = \sum_{\lambda_\gamma, \lambda'_\gamma} T_{\lambda_\phi \lambda_\gamma} \Sigma^\alpha_{\lambda_\gamma \lambda'_\gamma} T^*_{\lambda'_\phi \lambda'_\gamma}. \tag{2.28}$$

From Expression 2.28, it is clear how the different components of the photon spin-density matrix, Σ^α, contribute to the ϕ spin-density matrix. We keep track of these separate contributions with the superscript α. The vector meson spin-density matrices, ρ^α, are explicitly expressed in terms of the Jacob and Wick helicity amplitudes in Appendix A.

The vector meson decay angular distribution can be written in terms of the spin-one Wigner D functions as

$$W(\cos\theta,\varphi) = \frac{3}{4\pi}\sum_{\lambda,\lambda'} D^1_{\lambda 0}(\theta,\varphi)^*\rho(\phi)_{\lambda\lambda'}D^1_{\lambda' 0}(\theta,\varphi). \tag{2.29}$$

The quantity $|D^j_{mm'}(\theta,\varphi)|^2$ describes a state of total angular momentum j, and gives the probability of scattering into angle (θ,φ) when making the transition from a state with spin-polarization m to one with m'. So $W(\cos\theta,\varphi)$ is the probability of a spin-one ϕ decaying into two spin-zero kaons at angles $(\cos\theta,\varphi)$. Because it is a probability density, the condition $W(\cos\theta,\varphi) \geq 0$ must be true for all $(\cos\theta,\varphi)$.

As discussed at the end of Subsection 2.1.3, we cannot separate the unpolarized transverse and the longitudinal components of the photon. Thus, instead of measuring $\rho(\phi)_{ij}$ in Equation 2.29, we measure the sum of spin-density matrix elements, defined by:

$$\begin{aligned} r^{04}_{ij} &= \frac{\rho^0_{ij} + \epsilon R\rho^4_{ij}}{1+\epsilon R}, \\ r^{\alpha}_{ij} &= \begin{cases} \frac{\rho^{\alpha}_{ij}}{1+\epsilon R} & \text{for } \alpha = 1-3, \\ \frac{\sqrt{R}\rho^{\alpha}_{ij}}{1+\epsilon R} & \text{for } \alpha = 5-8, \end{cases} \end{aligned} \tag{2.30}$$

where $R = \sigma_L/\sigma_T$ is the ratio of cross-sections for production from longitudinal and transverse photons. In the limit $Q^2 \gg m_e^2$, the decay angular distributions for ϕ's produced by a mono-energetic, longitudinally-polarized positron beam is

$$W(\cos\theta,\varphi,\Phi) = W_{unpol}(\cos\theta,\varphi,\Phi) + W_{LongPol}(\cos\theta,\varphi,\Phi), \tag{2.31}$$

where

$$
\begin{aligned}
&W_{unpol}(\cos\theta, \varphi, \Phi) = \\
&\quad \frac{3}{4\pi}\left[\frac{1}{2}(1 - r^{04}_{00}) + \frac{1}{2}(3r^{04}_{00} - 1)\cos^2\theta - \sqrt{2}\,\mathrm{Re}\, r^{04}_{10}\sin 2\theta\cos\varphi\right. \\
&\qquad - r^{04}_{1-1}\sin^2\theta\cos 2\varphi \\
&\qquad - \epsilon\cos 2\Phi\,\big(r^1_{11}\sin^2\theta + r^1_{00}\cos^2\theta \\
&\qquad\qquad\qquad -\sqrt{2}\,\mathrm{Re}\, r^1_{10}\sin 2\theta\cos\varphi - r^1_{1-1}\sin^2\theta\cos 2\varphi\big) \\
&\qquad - \epsilon\sin 2\Phi\left(\sqrt{2}\,\mathrm{Im}\, r^2_{10}\sin 2\theta\sin\varphi + \mathrm{Im}\, r^2_{1-1}\sin^2\theta\sin 2\varphi\right) \\
&\qquad + \sqrt{2\epsilon(1+\epsilon)}\cos\Phi \\
&\qquad\qquad \times\big(r^5_{11}\sin^2\theta + r^5_{00}\cos^2\theta \\
&\qquad\qquad\qquad -\sqrt{2}\,\mathrm{Re}\, r^5_{10}\sin 2\theta\cos\varphi - r^5_{1-1}\sin^2\theta\cos 2\varphi\big) \\
&\qquad + \sqrt{2\epsilon(1+\epsilon)}\sin\Phi \\
&\qquad\qquad \times\left.\left(\sqrt{2}\,\mathrm{Im}\, r^6_{10}\sin 2\theta\sin\varphi + \mathrm{Im}\, r^6_{1-1}\sin^2\theta\sin 2\varphi\right)\right], \qquad (2.32)
\end{aligned}
$$

and

$$
\begin{aligned}
&W_{LongPol}(\cos\theta, \varphi, \Phi) = \\
&\quad \frac{3}{4\pi}P_b\left[\sqrt{1-\epsilon^2}\left(\sqrt{2}\,\mathrm{Im}\, r^3_{10}\sin 2\theta\sin\varphi + \mathrm{Im}\, r^3_{1-1}\sin^2\theta\sin 2\varphi\right)\right. \\
&\qquad + \sqrt{2\epsilon(1-\epsilon)}\cos\Phi \\
&\qquad\qquad \times\left(\sqrt{2}\,\mathrm{Im}\, r^7_{10}\sin 2\theta\sin\varphi + \mathrm{Im}\, r^7_{1-1}\sin^2\theta\sin 2\varphi\right) \\
&\qquad + \sqrt{2\epsilon(1-\epsilon)}\sin\Phi \\
&\qquad\qquad \times\big(r^8_{11}\sin^2\theta + r^8_{00}\cos^2\theta \\
&\qquad\qquad\qquad \left.-\sqrt{2}\,\mathrm{Re}\, r^8_{10}\sin 2\theta\cos\varphi - r^8_{1-1}\sin^2\theta\cos 2\varphi\big)\right]. \qquad (2.33)
\end{aligned}
$$

The beam may be either positively or negatively polarized: $-1 < P_b < +1$. The goal of the analysis described in Chapter 4 is to extract the values of the spin-density matrix elements, r^{α}_{ij}, from the decay angular distributions of ϕ mesons.

2.2 Description of ϕ Data

In this section, we describe the helicity structure and the kinematic dependencies of the cross section of the observed ϕ electroproduction data, along with a model which has had reasonable success describing the $e + A \to e + A + \phi$ data. Note that most of the presently available data on vector meson electroproduction are from the ρ^0 vector meson. In this work, we will refer to general vector meson production as ϕ production.

2.2.1 Differential Cross Section We assume that the positron scatters via a single photon. As was previously discussed in Subsection 2.1.3, the Hand convention is used, so that the differential cross section in the positron variables for ϕ meson electroproduction is written,

$$\frac{d\sigma}{d\cos\theta_e \, d\varphi_e \, dE'} = \Gamma_T \sigma_T(Q^2, W^2)(1 + \epsilon R_\phi(Q^2, W^2)), \tag{2.34}$$

where $R_\phi(Q^2, W^2) = \sigma_L/\sigma_T$ is the ratio of total cross sections for production of ϕ mesons from longitudinal and transverse polarized photons, Γ_T is the transverse photon flux, and ϵ is the ratio of the fluxes of longitudinal and transverse photons, normalized to unit transverse flux.

2.2.2 VMD Model's Prediction of the Cross Section Ratio The Vector Meson Dominance model (VMD, sometimes called VDM) is a model of how the photon interacts with hadrons. [9] The VMD model asserts that, with high enough energy, the electromagnetic photon state fluctuates into a hadronic state with appropriate quantum numbers, which then interacts via the strong force with the target. The VMD picture of relating photon-hadron processes to hadron-hadron processes is used in nearly all modern theories discussing the photoproduction of vector mesons. It implies a definite separability of the reaction, in the sense that the fluctuation of the photon into a vector meson should occur on time scales much longer than that of the vector meson's subsequent reaction with the target. It should be noted that recently, this simple VMD picture of the reaction has been observed to be consistent with data from the HERMES experiment on nuclear shadowing in ρ^0 electroproduction from nuclear targets. [46]

The original VMD model [47] included the additional assumption that the photon cross section is totally dominated by its ρ^0 component, *i.e.*, that there are no other vector meson terms in the photon wave function, such as the ω, ϕ, or J/Ψ. Although this assumption is dubious, in this subsection we will nevertheless use the original VMD model in order to gain insight on polarization phenomena in virtual photon reactions. At the end of this subsection, we will comment on the inclusion of the other vector mesons into the VMD framework, and discuss the photoproduction of ρ^0 and ϕ mesons.

The original VMD model can be used to predict the form of the ratio of total cross sections for electromagnetic positron scattering via scalar and transverse polarized virtual photons, $R_{\gamma^* p} = \sigma_S/\sigma_T$. We follow the derivation in [47]. In $R_{\gamma^* p}$, σ_S is the total cross section for scattering via scalar photons, and σ_T is the total cross section for scattering via transverse polarized photons. [43] We will see below that the scalar component of the total cross section is related to the longitudinal component of the total cross section by electromagnetic current conservation. This equivalence has the consequence that in today's nomenclature, the scalar component of the cross section usually has the label of the "longitudinal" component, and is denoted σ_L. However, in this subsection, we keep the scalar and longitudinal distinction, as it is essential to the discussion.

Using the Hand convention, the differential cross section for positron scattering in the lab frame is written,

$$\frac{d\sigma}{dQ^2\, dE'} = \frac{1}{2EE'}\Gamma_T(\sigma_T + \epsilon\, \sigma_S), \tag{2.35}$$

with the photon flux given by

$$\Gamma_T = \frac{\alpha}{2\pi} K \frac{1}{Q^2} \frac{E'}{E} \frac{2}{1-\epsilon}, \tag{2.36}$$

where $K = (W^2 - M_p^2)/2M_p$. Note that Equation 2.35 and 2.36 differ from Equation 2.17 and 2.18 by a Jacobian and an integral over the azimuthal positron angle. We would like to write σ_T and σ_S in terms of sandwiches of the transverse and the longitudinal components of the electromagnetic current density, ej_μ. The transverse and longitudinal polarization vectors of a massive vector particle are given by [1]

$$\epsilon^{(\lambda=\pm1)} = \mp\frac{1}{\sqrt{2}}(0, 1, \pm i, 0) \text{ and} \tag{2.37}$$

$$\epsilon^{(\lambda=0)} = \frac{1}{M}(|\vec{p}|, 0, 0, E), \tag{2.38}$$

respectively. Denoting the initial proton state by $|p\rangle$ and the final hadronic state by $|A\rangle$, the transverse photon amplitude is given by,

$$e\langle A|\epsilon^{(\lambda=\pm1)} j_\mu|p\rangle = e\langle A| \mp (j_x \pm i j_y)/\sqrt{2}|p\rangle = e\langle A|j_\perp^{(1,2)}|p\rangle, \tag{2.39}$$

where $ej_\perp^{1,2}$ refer to the $\pm$ circularly polarized components of the electromagnetic current density perpendicular to the virtual-photon three momentum, $\vec{q}$. Similarly, the longitudinal photon current is given by

$$\epsilon^{(\lambda=0)} j_\mu = \frac{1}{\sqrt{Q^2}}(|\vec{q}| j_0 - \nu j_{||}), \tag{2.40}$$

where j_0 is the scalar component of the current density and $j_{||}$ is the component parallel to $\vec{q}$. As a result of current conservation, the scalar and longitudinal components of current are related by $\partial_\mu j^\mu = q_\mu j^\mu = 0$, so that we can write

$$j_0 = \frac{|\vec{q}|}{\nu} j_{||}, \tag{2.41}$$

which, when inserted into Equation 2.40, yields the expression for the longitudinal photon current,

$$\epsilon^{(\lambda=0)} j_\mu = \frac{\sqrt{Q^2}}{\nu} j_{||}. \tag{2.42}$$

Hence, we can write the photon cross sections in terms of the squares of matrix elements,

$$\sigma_T = \left(\frac{2\pi\alpha}{K}\right)(2\pi)^4 \sum_A |\langle A|j_\perp|p\rangle|^2 \delta^{(4)}(p+q-p') \text{ and} \tag{2.43}$$

$$\sigma_S = \frac{Q^2}{\nu^2}\left(\frac{2\pi\alpha}{K}\right)(2\pi)^4 \sum_A |\langle A|j_{||}|p\rangle|^2 \delta^{(4)}(p+q-p'), \tag{2.44}$$

where $\sum_A$ is meant to signify both the average over initial polarization states and the sum over final polarization states.

The transverse and scalar components of the cross section for the $\rho^0 + p \to A$ reaction can be expressed in a similar way as the photon cross sections. In the VMD model, the assumption is made that the ρ^0 couples to a conserved source, the photon, so that the current conservation equation 2.41 can be applied to the neutral ρ^0 current density, $J_\mu^{(\rho)}$. [48] Therefore, the longitudinal component of the ρ^0 current can be written analogously to Equation 2.42,

$$\epsilon^{(\lambda=0)} J_\mu^{(\rho)} = \frac{\sqrt{M_\rho^2}}{E_\rho} J_{||}^{(\rho)}, \tag{2.45}$$

where E_ρ is the laboratory energy of the ρ^0. The transverse and scalar ρ^0 scattering cross sections can be written analogously to the photon cross sections,

$$\sigma_T^{(\rho p)} = \left(\frac{1}{2|\vec{q}|}\right)(2\pi)^4 \sum_A |\langle A|J_\perp^{(\rho)}|p\rangle|^2 \delta^{(4)}(p+q-p'), \text{ and} \tag{2.46}$$

$$\sigma_S^{(\rho p)} = \frac{M_\rho^2}{E_\rho^2}\left(\frac{1}{2|\vec{q}|}\right)(2\pi)^4 \sum_A |\langle A|J_{||}^{(\rho)}|p\rangle|^2 \delta^{(4)}(p+q-p'), \tag{2.47}$$

where $\vec{q}$ is the 3-momentum of the ρ^0.

The fundamental hypothesis of the original VMD model [49] relates the electromagnetic matrix element, $\langle A|j_\mu|p\rangle$, to the hadronic matrix element, $\langle A|J_\mu^{(\rho)}|p\rangle$, via

$$\langle A|j_\mu|p\rangle(Q^2, W) = \frac{M_\rho^2}{f_\rho}\frac{1}{M_\rho^2 + Q^2}\langle A|J_\mu^{(\rho)}|p\rangle(W^2), \tag{2.48}$$

where the γ-ρ^0 coupling constant, f_ρ, is determined from the decay $\rho^0 \to e^+e^-$. The original VMD model assumes that the Q^2 dependence of the electromagnetic matrix element is dominated by the ρ^0 propagator, *i.e.*, that there is no other Q^2 dependence in the process, for example, in the hadronic form factors. Using this hypothesis and the expressions for $\sigma_S^{(\rho\, p)}$ and $\sigma_T^{(\rho\, p)}$, we can write

$$(2\pi)^4 \sum_A |\langle A|j_\perp|p\rangle|^2 \delta^{(4)}(p+q-p') = 2|\vec{q}| \left(\frac{M_\rho^2}{f_\rho} \frac{1}{M_\rho^2 + Q^2} \right)^2 \sigma_T^{(\rho\, p)}(W), \text{ and} \quad (2.49)$$

$$(2\pi)^4 \sum_A |\langle A|j_{||}|p\rangle|^2 \delta^{(4)}(p+q-p') = 2|\vec{q}| \left(\frac{M_\rho^2}{f_\rho} \frac{1}{M_\rho^2 + Q^2} \right)^2 \frac{E_\rho^2}{M_\rho^2} \sigma_S^{(\rho\, p)}(W^2). \quad (2.50)$$

Substituting these expressions into the photon cross sections, we obtain the simple result,

$$\begin{aligned} R_{\gamma^* p}(Q^2, W^2) &= \frac{\sigma_S}{\sigma_T} = \xi(W^2) \frac{Q^2}{M_\rho^2} \frac{E_\rho^2}{\nu^2} \\ &\approx \xi(W^2) \frac{Q^2}{M_\rho^2} \end{aligned} \quad (2.51)$$

where $\xi(W^2) = \sigma_S^{(\rho\, p)}/\sigma_T^{(\rho\, p)}$. The value of $E_\rho^2/\nu^2 \approx 1$ in diffractive scattering, and can be treated as a correction to the prediction of the original VMD model that $R_{\gamma^* p} \propto Q^2/M_\rho^2$.

The original Vector Meson Dominance model was extended in Reference [39] to describe the electroproduction of vector mesons, a subprocess of positron scattering. In that work, the contributions of the ρ^0, ω, and ϕ mesons to the virtual photon amplitude were included in the VMD calculation. These days, the technique of including several vector meson channels into the hadronic component of the photon is referred to as Generalized Vector Dominance (GVD). Applying GVD to the photoproduction of vector mesons, the analog of Equation 2.48 is

$$T_{\mu\nu}(\gamma^* A \to VA) = \sum_{V'=\rho,\omega,\phi} \frac{M_{V'}^2}{f_{V'}} \frac{1}{M_{V'}^2 + Q^2} T_{\mu\nu}(V'A \to VA). \quad (2.52)$$

In GVD models, it is often assumed that the interaction is "diagonal" in the vector mesons, that is, that terms with $V' \neq V$ are negligible, so that the coherent sum in Equation 2.52 collapses to a single term, as it does in Equation 2.48. With the "diagonal" GVD assumption, the vector meson production cross section ratios were calculated in Reference [39] to be

$$R_\rho = \xi_\rho(W^2)\frac{Q^2}{M_\rho^2}, \text{ and} \tag{2.53}$$

$$R_\phi = \xi_\phi(W^2)\frac{Q^2}{M_\phi^2}, \tag{2.54}$$

where $\xi_V(W^2) = \sigma_L^{(V\,p)}/\sigma_T^{(V\,p)}$ is the ratio of the V-p scattering cross sections. For an idea of how good this assumption of "diagonal" GVD is in ρ^0 and ϕ production, we look at an analogous pseudoscalar reaction. The forward differential cross section for $\pi^- p \to \pi^- p$ elastic scattering has been observed to be on the order of $\approx 50\,\text{mb}$, as can be seen in Figure 1.1, while the forward differential cross section for $\pi^- p \to \eta n$ inelastic scattering is on the order of $\approx 0.5\,\text{mb}$ [50]

2.2.3 Diffractive Production

In the previous subsection, we used the VMD model to reduce the problem of vector meson photoproduction:

$$\gamma^* + N \to \phi + N, \tag{2.55}$$

to one of hadronic production:

$$\begin{aligned} &\rho^0 + N \to \phi + N, \\ &\omega + N \to \phi + N, \quad \text{or} \\ &\phi + N \to \phi + N. \end{aligned} \tag{2.56}$$

In this section we want to explore briefly the phenomenology associated with these types of hadronic reactions.

Data from high energy hadron-proton collisions have been observed to show the following features in several reaction channels [9]: a total cross-section that is nearly independent of energy above the resonance region, and a differential production cross-section dominated by scattering at forward angles, *i.e.* at small

$-t' \lesssim 0.8\,\mathrm{GeV}^2$. These are features of a diffractive production mechanism, as will be described below. It should be noted that similar features were observed also in high energy photon-proton data, lending confidence to VMD as the picture of the hadronic nature of photons.

The diffractive peak is defined as data in the small $-t'$ region, where the differential cross-section can be fit with an exponential [51],

$$\frac{d\sigma(Q^2, W^2, t')}{d\,|t'|} = \sigma(Q^2, W^2) b\, e^{-b|t'|}, \tag{2.57}$$

where b is called the exponential slope. The term "diffractive" is left over from optics, there used for describing the far-field scattering of light from a black target of comparable size to the wavelength. [40] Applying an optical model to elastic hadron scattering likens this reaction to absorption by a disc of radius R. Expanding in Legendre polynomials yields a cross-section of the form of Equation 2.57, with b related to the size of the disc by $b \simeq R^2$. [8] In this way, the exponential slope can be related to the hadronic "size" of the initial hadron-proton state by [7]

$$b_{hp} = \frac{1}{3}(\langle r_h^2 \rangle + \langle r_p^2 \rangle), \tag{2.58}$$

where r_h and r_p are the "size" of the hadron and proton, respectively. At the energies we are considering in this work ($W \approx 5\,\mathrm{GeV}$), typical values are $b_{\rho p} \approx 7\ \mathrm{GeV}^{-2}$ [9], and $b_{\phi p} \approx 4\,\mathrm{GeV}^{-2}$ [26] [52]. These results are interpreted as indicative that the ρ^0 is a spatially larger state than the ϕ.

The data in this thesis were collected from nuclear as well as proton targets. In the nuclear ($A \neq 1$) case, we expect there to be two contributions to the differential cross-section:

$$\frac{d\sigma}{d\,|t'|} \propto \left(\sigma_A b_A\, e^{-b_A|t'|} + \sigma_p b_p\, e^{-b_p|t'|}\right), \tag{2.59}$$

where the first term represents elastic scattering from the entire nucleus and the second term represents quasi-elastic scattering from individual nucleons within the nucleus.

2.2.4 Total Cross Section The differential cross section for ϕ electroproduction is

$$\frac{d\sigma}{d\cos\theta_e\, d\varphi_e\, dE'} = \Gamma_T \sigma_T(1+\epsilon R), \tag{2.60}$$

where the total transverse photoproduction cross section of ϕ mesons is denoted $\sigma_T(Q^2, W^2)$. In the original VMD model, Equation 2.48, the Q^2 dependence of photoproduction matrix elements is assumed to be contained entirely in the propagator of the vector meson. Thus, the Q^2 dependence of the total transverse ϕ production cross-section is predicted to behave as

$$\sigma_T(Q^2, W^2) = \sigma(Q^2=0, W^2)\left(\frac{1}{1+Q^2/M_\phi^2}\right)^2. \tag{2.61}$$

In a recent work by Hüfner and Kopeliovich, they propose an extension to the original VMD model to describe the photoproduction of J/Ψ mesons. [53] In their calculation, they include the original VMD production channel, $\gamma^* \to J/\Psi$ followed by $J/\Psi + N \to J/\Psi + N$, as well as the additional channel $\gamma^* \to \Psi'$ followed by $\Psi' + N \to J/\Psi + N$. Assuming that the elastic scattering amplitude is proportional to the transverse size of the $q\bar{q}$-dipole, and using harmonic oscillator wave functions for the hadronic basis, they obtain a correction to the Q^2 dependence of the total electroproduction cross section predicted by the original VMD model:

$$\sigma_T(Q^2, W^2) = \sigma(Q^2=0, W^2)\left(\frac{1}{1+Q^2/M_{J/\Psi}^2}\right)^2 \left(\frac{M_{\Psi'}^2 - M_{J/\Psi}^2}{M_{\Psi'}^2 - Q^2}\right)^2. \tag{2.62}$$

The small size of the ϕ meson (relative to the ρ^0, for example; see Subsection 2.2.3) make the application of Equation 2.62 to ϕ photoproduction at HERMES energies plausible, with the substitutions $J/\Psi \to \phi$ and $\Psi' \to \phi'$. [17] The values of $M_{\phi'} = 1.680\,\mathrm{GeV}$ and $M_\phi = 1.019\,\mathrm{GeV}$ are from the Particle Data Group. It will be seen in Subsection 4.2.3 that Equation 2.62 does indeed approximately describe the Q^2 dependence of the data. Note that Equation 2.62 is a correction to the original VMD prediction of the total photoproduction cross section of ϕ mesons. As such, the original VMD prediction of the ratio $R = \sigma_L/\sigma_T$ from Equation 2.51 is not affected. [17]

Using the VMD model, the W^2 dependence of the total photoproduction cross section, $\sigma(W^2) = \sigma(Q^2 = 0, W^2)$, is typically compared with models where the vector meson scattering from the nucleus is assumed to take place via the exchange of various particles in the t-channel. These models are usually based on the exchange of either hadrons or quarks and gluons, with the appropriate total quantum numbers to allow the couplings at the vertices with the vector meson and the target nucleus.

In an approach based on the phenomenological Regge theory, hadron-hadron scattering is considered to proceed via the exchange of mesons in the t-channel which lie along the same Regge trajectory. [12] A Regge trajectory is defined as a group of particles which all have the same isospin, baryon, and strangeness quantum numbers. The $\rho(770)$ and the $\rho(1700)$ lie along the isospin-1 trajectory, while the $\omega(782)$ and $\phi(1020)$ lie along the isospin-0 trajectory. It is found that if one plots the spin of the particle versus the invariant mass of the particle, called a Chew-Frautschi plot, the particles in a given Regge trajectory lie along a straight line with intercept $\alpha(0)$. In Regge theory, the cross section for hadron-hadron total cross sections via the exchange of such a Reggeon trajectory would be given by

$$\sigma_{tot}(W^2) \sim (W^2)^{\alpha(0)-1}. \tag{2.63}$$

There exists a Regge trajectory for particles with the quantum numbers of the vacuum which has no physical particles lying along it. The exchange of this vacuum trajectory is called Pomeron exchange, and the exchange of any other trajectory is called Reggeon exchange.

As an example, Regge theory predicts that the W^2 dependence of the total ρ^0 photoproduction cross section has the form, [14]

$$\sigma = a\ (W^2)^{\epsilon} + b\ (W^2)^{-\eta}, \tag{2.64}$$

where a and b are fit to data, and the arguments on the exponents come from the intercepts of the Pomeron and the isospin-1 Reggeon exchange trajectories. Using the intercepts which are fit from the Chew-Frautschi plots, $\epsilon \approx 0.08$ and $\eta \approx 0.45$, the W^2 dependence of the total ρ^0 photoproduction cross section from Equation 2.64 is consistent with the observed ρ^0 data, as can be seen in Figure 2.6.

The world data on the photoproduction cross sections of various vector mesons is plotted as a function of $W = \sqrt{W^2}$ in Figure 2.6. We concentrate on the cross sections for the low-lying mass vector mesons, *i.e.*, the ρ^0, ω, and ϕ. At high energies, such as those seen at the HERA collider experiments H1 and ZEUS ($W \approx 100\,\mathrm{GeV}$), the cross sections for ρ^0, ω, and ϕ photoproduction are observed to slowly decrease as W decreases, interpreted as the dominance of Pomeron exchange. [54] As we decrease further to lower energies ($W \approx 5\,\mathrm{GeV}$), both the ρ^0 cross-section and the ω begin to increase dramatically, which is ascribed to the increasing strength of Reggeon exchange amplitudes. The ϕ cross section data are observed to not increase as we move to lower energies. In the Regge exchange model, this continued slow decrease of the ϕ cross section at low energies is attributed to a suppression of the Reggeon amplitudes in ϕ production relative to ρ^0 and ω production. [25] Note that Pomeron exchange is constructed necessarily to exhibit SCHC, while Reggeon exchange would not necessarily exhibit SCHC.

Work has been done to connect the Regge exchange model with models based on quark and gluon degrees of freedom. [15] In the quark-gluon description, the exchange of a Pomeron becomes the exchange of a pair of gluons, while the exchange of a Reggeon becomes the exchange of a quark-antiquark pair. For the analysis considered in this work, the Regge parameterization of the photoproduction cross section data will suffice.

2.2.5 SCHC and NPE As mentioned in Section 2.1.3, it was observed in ρ^0 photoproduction data that the helicity of the photon is approximately

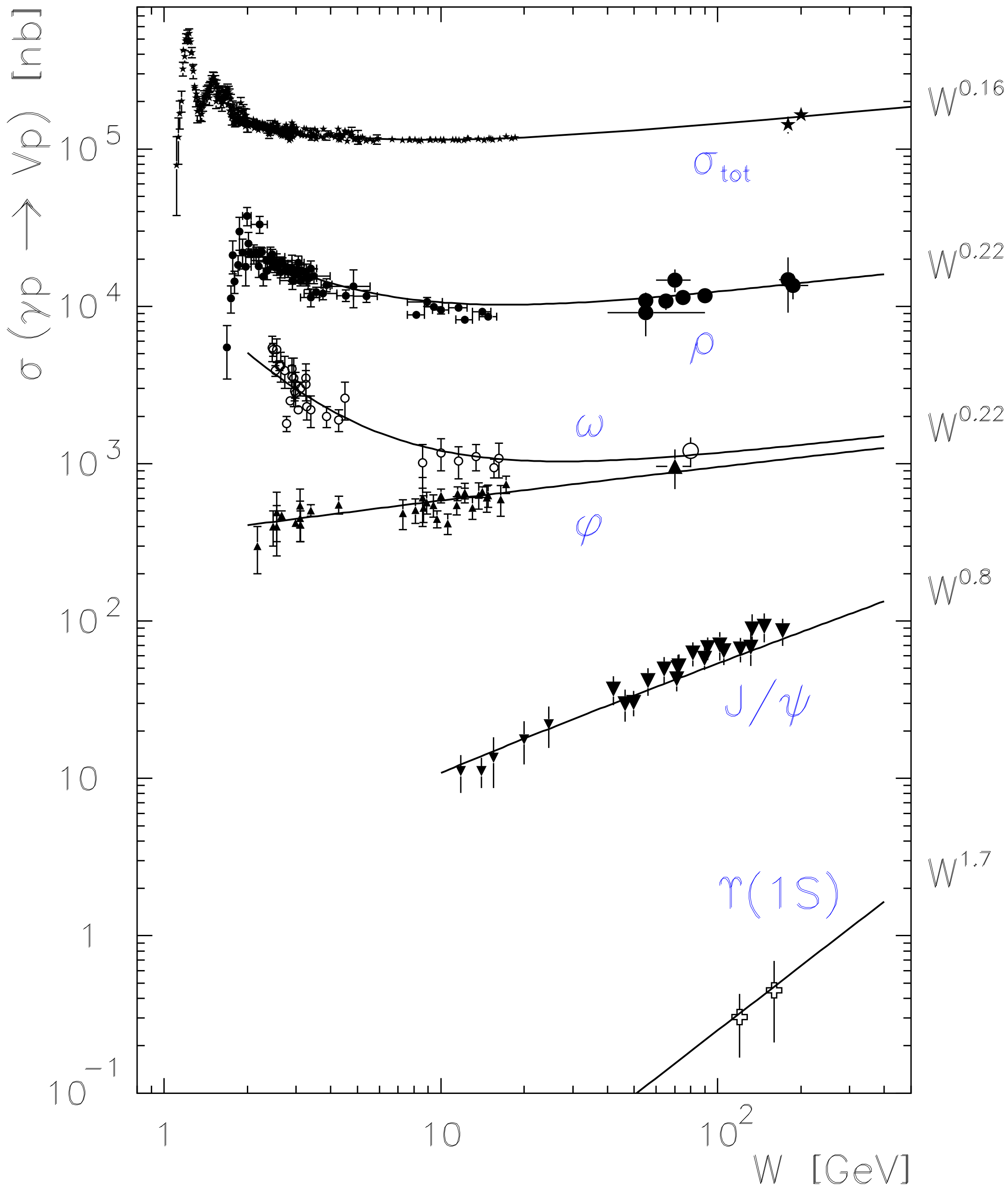

Figure 2.6. Repeat of Figure 1.4. The total photon-proton absorption and production cross sections for several vector mesons plotted as a function of W, the center-of-momentum energy. This plot is taken from [12], [18], and references therein. The vector meson production cross sections can be well described using VMD and the Regge exchange model. The lines indicate the Regge-based power law fits to the data in [16,18].

preserved by the helicity of the ρ^0 in the s-channel helicity frame, a phenomenon called s-Channel Helicity Conservation, or SCHC. We want to explore the ramifications of SCHC on the measured spin density matrix elements, r^{α}_{ij}.

Recall the helicity amplitudes introduced in Section 2.1.4, expression 2.25,

$$T_{\lambda_\phi \lambda_{N'} \lambda_\gamma \lambda_N} = \langle \lambda_\phi \lambda_{N'} | J_{\lambda_\gamma} | \lambda_N \rangle.$$

Hereafter we will implicitly sum over nucleon helicities. The observation of SCHC is that helicity changing amplitudes are zero: [36]

$$T_{\lambda_\phi \lambda_\gamma} = T_{\lambda_\phi \lambda_\gamma} \delta_{\lambda_\phi \lambda_\gamma}, \tag{2.65}$$

so that

$$T_{-10} = T_{0-1} = T_{10} = T_{01} = 0, \text{ and} \tag{2.66}$$

$$T_{-11} = T_{1-1} = 0. \tag{2.67}$$

The helicity-conserving amplitudes, T_{-1-1}, T_{00}, and T_{11}, are not zero. This reduction in the number of non-zero matrix elements considerably simplifies the picture of the production in the helicity basis, making it an efficient basis in which to think about the reaction.

The angular distribution in Equations 2.32 and 2.33 is given in terms of the 23 spin density matrix elements r^{α}_{ij}, not the helicity amplitudes $T_{\lambda_\phi \lambda_\gamma}$. These spin-density matrix elements are defined as bilinear combinations of the helicity amplitudes in Equation 2.28, and are written out explicitly in Appendix A. From these expressions, we can see the effect of SCHC on the spin-density matrix elements. With SCHC, sixteen matrix elements are zero, leaving only r^{04}_{00}, r^{1}_{1-1}, $\mathrm{Im}(r^{2}_{1-1})$, $\mathrm{Re}(r^{5}_{10})$,

$\mathrm{Im}(r^6_{10})$, $\mathrm{Im}(r^7_{10})$, and $\mathrm{Re}(r^8_{10})$ to be (possibly) non-zero. Furthermore, SCHC restricts the value of three of these spin density matrix elements,

$$\begin{aligned} \mathrm{Im}(r^2_{1-1}) &= -r^1_{1-1}, \\ \mathrm{Im}(r^6_{10}) &= -\mathrm{Re}(r^5_{10}), \text{ and} \\ \mathrm{Re}(r^8_{10}) &= \mathrm{Im}(r^7_{10}), \end{aligned} \tag{2.68}$$

reducing the total number of independent non-zero matrix elements to four: r^{04}_{00}, r^1_{1-1}, $\mathrm{Re}(r^5_{10})$, and $\mathrm{Im}(r^7_{10})$.

The longitudinal polarization of ϕ's is given by r^{04}_{00}. Note that with SCHC, the only term that survives in the expression for r^{04}_{00} is the $|T_{00}|^2$ term. Also with SCHC, r^1_{1-1} simplifies to the product of transverse amplitudes, $T_{11}T^{\dagger}_{-1-1}$, while $\mathrm{Re}(r^5_{10})$ and $\mathrm{Im}(r^7_{10})$ are the real and imaginary parts of $T_{11}T^{\dagger}_{00}$.

In terms of the four remaining spin-density matrix elements, the decay angular distribution, in the case of SCHC, reads

$$\begin{aligned} W(\cos\theta,\psi) &= \frac{3}{4\pi}\left[\frac{1}{2}(1+r^{04}_{00}) + \frac{1}{2}(3r^{04}_{00}-1)\cos^2\theta\right. \\ &+ \epsilon\, r^1_{1-1}\sin^2\theta\cos 2\psi \\ &- 2\sqrt{\epsilon(1+\epsilon)}\,\mathrm{Re}(r^5_{10})\sin 2\theta\cos\psi \\ &+ \left. P_b\, 2\sqrt{\epsilon(1-\epsilon)}\,\mathrm{Im}(r^7_{10})\sin 2\theta\sin\psi\right], \end{aligned} \tag{2.69}$$

where the angular dependence on the azimuthal production angle, Φ, and the azimuthal decay angle, φ, has been reduced to a dependence on $\psi = \varphi - \Phi$. This simplification of the azimuthal angular dependence can be understood in terms of the following picture of the reaction. [55] When the positron scatters via the (transverse) photon, the $\vec{E}$-field of this photon oscillates in the $(ee'\gamma^*)$ plane. With SCHC, no further $\vec{E}$-fields come from the interaction with the target. So when the ϕ is produced, viewed as a resonant $s\bar{s}$-pair, these charged particles will naturally line up in a dipole along the $\vec{E}$-field from the photon. The formation of decay products, K^+

and K^-, will tend to follow the direction of this dipole, as they are the products of hadronization of the $\bar{s}$ and s. This leads to the observed correlation between φ, the decay products' azimuth, and the $(ee'\gamma^*)$ plane, which defines $\Phi = 0$.

The general shape of the decay angular distributions in the case of SCHC can be seen from Equation 2.69, namely, a flat distribution of events as a function of Φ and φ, and a $\cos 2\psi$ dependence of the ψ distribution from transverse ϕ's. The shape of the $\cos\theta$ distribution will be parabolic (independent of SCHC), with the degree of curvature given by the longitudinal polarization, r^{04}_{00}. This is a result of the use of the spin-one Wigner D functions in Equation 2.29.

In terms of the exchange of particles with the target, the test of SCHC is a measure of the (lack of) helicity contribution of this exchange to the ϕ final state. We can further use the measured spin-density matrix elements to give us information on the parity of this exchange. The exchange is said to have natural parity if its quantum numbers are $J^P = 0^+,\ 1^-,\ 2^+, 3^-,\ \ldots$. The exchange is said to have unnatural parity if its quantum numbers are $J^P = 0^-,\ 1^+,\ 2^-, 3^+,\ \ldots$. [55] In terms of helicity amplitudes, natural and unnatural parity exchange manifest themselves by the relations [38]

$$T_{-\lambda_\phi -\lambda_\gamma} = \pm(-1)^{\lambda_\phi - \lambda_\gamma} T_{\lambda_\phi \lambda_\gamma}, \tag{2.70}$$

where the $+\,(-)$ case refers to natural (unnatural) parity exchange. In the case of SCHC and Natural Parity Exchange (NPE),

$$r^1_{1-1} \propto T_{11} T^\dagger_{-1-1} = |T_{11}|^2, \tag{2.71}$$

and we can write

$$r^{04}_{00} + 2r^1_{1-1} = 1. \tag{2.72}$$

This condition for SCHC and NPE has been observed to be true for ρ^0 data. [34]

Note that in the case of unnatural parity exchange,

$$r^1_{1-1} \propto T_{11} T^\dagger_{-1-1} = -|T_{11}|^2, \tag{2.73}$$

and so Equation 2.72 would not be expected to be valid.

An important consequence of SCHC is that one may easily compute the longitudinal- to transverse-photon ϕ production cross-section ratio, R_ϕ, via the measurement of the longitudinal polarization of the ϕ,

$$R_\phi \equiv \frac{\sigma_L}{\sigma_T} = \frac{1}{\epsilon} \frac{r^{04}_{00}}{1 - r^{04}_{00}}. \tag{2.74}$$

The ratio of total cross sections has been reduced to the ratio of longitudinal to transverse ϕ polarization, divided by the ratio of the flux of longitudinal to transverse photons, normalized to unit transverse photon flux.

Note that in ρ^0 electroproduction, at both small and large virtual photon energies, small violations of SCHC have been reported. [31] [37] [36]

2.2.6 pQCD Model of $2g$ Exchange In this section, we describe a calculation of the spin-density matrix elements, r^α_{ij}, in diffractive ρ^0 electroproduction by D. Yu. Ivanov and R. Kirschner. [19] It is a model which uses quark and gluon degrees of freedom, and is based on perturbative Quantum Chromodynamics (pQCD). It uses a wave function for the vector meson constructed from current quarks, and, as such, is intended for use in the hard, diffractive regime, that is, where $W^2 \gg Q^2$ and $Q^2 \gg M^2_\rho$. The validity of the pQCD model in the calculation of the longitudinal SCHC amplitude, T_{00}, has been shown in Reference [56], and the calculation was actually performed in References [23] and [57]. In Reference [10], the pQCD approach was extended to calculate the transverse SCHC amplitude, T_{11}. The calculation described here is an extension of the model used in [10].

The amplitude of ρ^0 photoproduction from a proton target, depicted in Figure 2.7, occurs via the exchange of two gluons in the t-channel, and can be

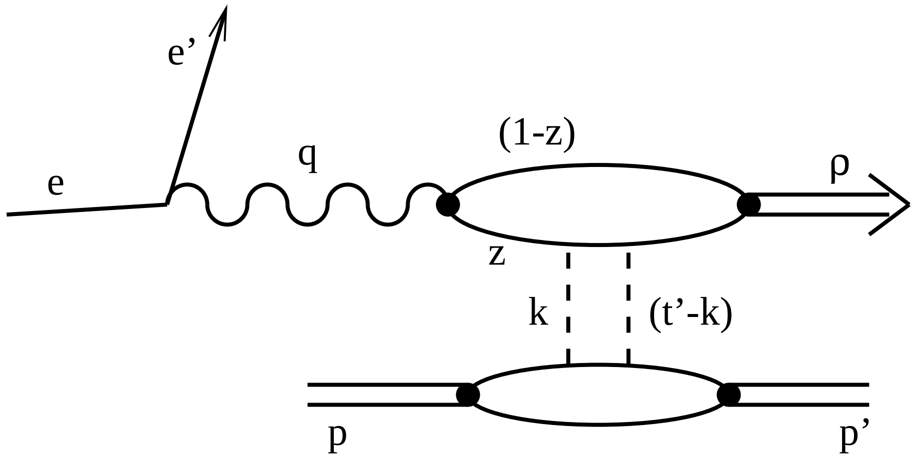

Figure 2.7. Simple diagram to define the variables in the $2g$ exchange model of Ivanov and Kirschner. In the calculation, terms where the gluons couple to the $\bar{q}$ are also included.

represented as the integral over the (transverse) momenta, $\vec{k}$, of said gluons:

$$T_{\gamma^* p \to \rho p} = i\ W^2 \int \frac{d^2 k}{\vec{k}^2 (\vec{t}' - \vec{k})^2}\ J_{\gamma^* \rho}(\vec{k}, \vec{t}') J_p(\vec{k}), \tag{2.75}$$

where $\vec{t}'$ is the net (transverse) 3-momentum transfer to the target. $J_{\gamma^* \rho}$ is the photon to ρ^0 current and J_p is the proton current. Assuming NPE in the t-channel, there are five independent helicity amplitudes to be calculated. Two of them are helicity conserving amplitudes: T_{00} and T_{11}, two of them are helicity "single-flip" amplitudes: T_{10} and T_{01}, and one is a helicity "double-flip" amplitude: T_{1-1}.

The space-time picture of the reaction in this model is that from VMD, where the virtual photon fluctuates into a $q\bar{q}$-pair a long time before and the $q\bar{q}$ converts into a ρ^0 a long time after the interaction with the target. Thus, the calculation is factorized into three parts: the split of the photon into a $q\bar{q}$-pair, the interaction of the target gluons with the $q\bar{q}$ dipole, and, finally, the formation of the ρ^0. Thus, the $\gamma^* \to \rho^0$ transition current in Equation 2.75 can be written as the convolution of the gluon-quark dipole interaction with the wave functions of the incoming virtual photon and outgoing vector meson. In spatial coordinates,

$$J_{\gamma^*\to\rho}(\vec{k},\vec{t}) \propto \int d^2\vec{r}dz\ \Psi_{\gamma^*}(\vec{r},z) f(\vec{r},\vec{k},\vec{t},z)\Psi_\rho(\vec{r},z), \tag{2.76}$$

where $\vec{r}$ is the transverse separation between the quarks, and z is the longitudinal momentum fraction of the photon carried by the q. The $\bar{q}$ carries momentum fraction $(1-z)$.

To represent the wave function of the photon to $q\bar{q}$-pair transition, the light cone wave function of the photon is used. In pQCD, the wave function of the quarks goes as $z(1-z)$. [58] This pQCD wave function is constructed in such a way that the total helicity of the $q\bar{q}$-pair is zero, *i.e.*, if the q has $\lambda = +1/2$, then the $\bar{q}$ has $\lambda' = -1/2$. Therefore, the helicity of the photon is retained by the spatial distribution of the $q\bar{q}$ dipole, that is, the projection of the orbital angular momentum of the $q\bar{q}$-pair onto the z-axis. Note that this is in contrast to the vector meson wave function which would be used in the old quark model, where the meson is purely s-wave, and the polarization retained by the spin components of the wave function. The transverse and longitudinal photon wave functions are given by

$$\Psi^T_{\gamma^*} \propto \delta_{\lambda,-\lambda'} K_1\left(rQ\sqrt{z(1-z)}\right) \text{ and} \tag{2.77}$$

$$\Psi^L_{\gamma^*} \propto \delta_{\lambda,-\lambda'} K_0\left(rQ\sqrt{z(1-z)}\right), \tag{2.78}$$

where λ and λ' are the helicities of the q and $\bar{q}$, $Q=\sqrt{Q^2}$, and $K_{0,1}(mr)$ are Bessel functions.

Now the q and $\bar{q}$ quarks interact with two target gluons. As shown at the end of Section 2.1.2, the helicity of relativistic leptons is preserved when scattering via gauge bosons with vector coupling. Therefore, the interaction of these t-channel gluons with the $q\bar{q}$-pair does not change the helicity states of the quarks. The pQCD quark-dipole interaction with gluons is written in this model as

$$f(\vec{r},\vec{k},\vec{t}',z) \propto e^{i\vec{t}'\cdot\vec{r}z}(1-e^{-i\vec{k}\cdot\vec{r}})(1-e^{-i(\vec{t}'-\vec{k})\cdot\vec{r}}), \tag{2.79}$$

where a color factor has been included in the proportion. Note there are no helicity indices in expression 2.79. This dipole interaction factor vanishes if the momentum of either of the t-channel gluons vanishes, $\vec{k}$ or $(\vec{t}' - \vec{k})$, or if the transverse separation of the quarks, $\vec{r}$, goes to zero. Thus, it describes the interaction of a $q\bar{q}$ dipole with two gluons.

Finally, the transverse and longitudinal ρ^0 wave functions, $\Psi_\rho^{T,L}$, are constructed analogously to the photons, and by projecting the $q\bar{q}$ onto the ρ^0 basis by the Wigner D-functions, introduced in Section 2.2.5. As for the wave function of the photon, the wave function of the ρ^0 is assumed to go as $z(1-z)$.

The integral of the proton current over the transverse momenta of the t-channel gluons in Equation 2.75 is estimated to be proportional to the gluon distribution in the proton at $t' = 0$,

$$\int \frac{d^2k}{k^2} J_p \propto x\, G(x, Q^2). \tag{2.80}$$

This relation was shown in the analysis of J/Ψ electroproduction using the leading-log approximation of pQCD. [23]

The main idea of the calculation of the helicity amplitudes follows. The photon fluctuates into a $q\bar{q}$ pair as in VMD, whose helicity information is contained in the spatial Bessel functions, $K_{0,1}(mr)$. The interaction of the target gluons with the $q\bar{q}$ dipole is written as an integral over the ingoing and outgoing $q\bar{q}$ Bessel functions, convoluted by the interaction with $2g$ also written in spatial coordinates. The helicity state of the final produced ρ^0 coincides with the orbital angular momentum projection of the outgoing quark pair. Therefore, in this model, the way to have a single-flip or double-flip helicity transition is for the target gluons to change the spatial wave function of the $q\bar{q}$-pair.

The helicity amplitudes in this model for ϕ photoproduction are calculated to be

$$\alpha = \frac{T_{11}}{T_{00}} = \frac{\langle M\rangle}{Q}\frac{1+\gamma}{\gamma}, \tag{2.81}$$

$$\beta = \frac{T_{10}}{T_{00}} = \frac{\sqrt{|t'|}}{Q}\frac{1}{\sqrt{2}\gamma}, \tag{2.82}$$

$$\delta = \frac{T_{01}}{T_{00}} = -\frac{\langle M\rangle\sqrt{|t'|}}{Q^2}\frac{\sqrt{2}}{\gamma}, \text{ and} \tag{2.83}$$

$$\eta = \frac{T_{1-1}}{T_{00}} = \eta^0 + \eta^1, \tag{2.84}$$

where

$$\eta^0 = -\frac{\bar{\alpha}_S^2\,|t'|\langle M\rangle}{\pi\alpha_S Q m_\phi^2}\frac{1}{\{4\gamma[\Gamma^2(\gamma+1)/\Gamma(2\gamma+2)]x\,G(x,Q^2/4)\}}, \text{ and} \tag{2.85}$$

$$\eta^1 = \frac{|t'|\langle M\rangle}{Q^3}\frac{2(\gamma+2)}{\gamma}. \tag{2.86}$$

In these equations, $x\,G(x,Q^2)$ is the gluon distribution in the proton. If one were to evolve the gluon distribution in Q^2, the pQCD evolution equations of Altarelli and Parisi would be used. With this evolution, the gluon distribution scales like

$$G(x,Q^2) \sim (Q^2)^\gamma, \tag{2.87}$$

where γ is called the effective anomalous dimension of gluon density, and can be obtained from the parameterization of the parton distribution functions of the proton. [10] The effective gluon anomalous dimension was assumed to be constant for this calculation.

It should be noted that in Ivanov and Kirschner's calculation [19], the above formulae were calculated for the case of ρ^0 vector meson production at HERA collider kinematics, *i.e.* higher W^2 and Q^2, where two-gluon exchange is expected to dominate. In this kinematic region, the model predicts small SCHC violations, in agreement with the ρ^0 and ϕ data recently measured in this region. [37] [36] The predictions of this model for the ϕ vector meson in our kinematic range will be evaluated and compared with the data in Subsection 5.2.

CHAPTER 3

EXPERIMENTAL APPARATUS

The data analyzed in this thesis were acquired at the DESY (Deutsches Elektronen SYnchrotronen) laboratory in Hamburg, Germany during the 1995, 1996, and 1997 running periods. Data were collected using the positron beam of the HERA (Hadron Elektron Ring Anlage) positron-proton collider ring, incident on a gas target internal to the positron beam line. Reaction products from the beam-target interaction are collected into the HERMES magnetic spectrometer, located in the East Hall of the ring. The HERA positron beam and HERMES spectrometer are well described in many places, including the theses [59], [6], and [60]. Also, a detailed description exists in the article [61]. Therefore, in this thesis, we will keep the discussion of these topics brief, focusing on features specific to the measurement of the $(\vec{e}, e'K^+K^-)$ reaction.

3.1 Beam and Target

As it travels around the HERA ring, the 27.5 GeV positron beam becomes polarized transverse to its direction of motion as a result of asymmetric spin-flip interaction probabilities of the beam with its own synchrotron radiation [62], an effect known as the Sokolov-Ternov effect [63]. The polarization of the beam builds up exponentially from an initial value of zero to an asymptotic value of 50-60%, with a rise time on the order of 0.5 hours. Spin rotators before and after the HERMES interaction point rotate the spin vector of the positrons so that the beam is longitudinally polarized as it travels through the target. Note that a longitudinally polarized positron has its spin vector pointed along the direction of motion, while a longitudinally polarized photon, discussed in Subsection 2.1.2, has its spin vector pointed transverse to the direction of motion. The value of the positron current during a typical fill of 8 hours would begin at a value of $\approx 30\,\mathrm{mA}$ and drop to a value of $\approx 10\,\mathrm{mA}$ before the beam was finally dumped.

At the HERMES interaction point, the longitudinally polarized positron beam traverses the gas target. Gas is injected through a feed tube on the side of the 40 cm long, elliptical target storage cell internal to the positron beam line. At different times during the data collection periods used in this analysis, the target contained different polarized and unpolarized gases. In 1995, data were collected only on a target of polarized $^3\vec{\mathrm{He}}$. In 1996, data were collected on polarized $^1\vec{\mathrm{H}}$, as well as unpolarized ^{1}H, ^{2}H, and ^{3}He, while in 1997, data were collected on polarized $^1\vec{\mathrm{H}}$, in addition to unpolarized ^{1}H, ^{2}H, and ^{14}N. The data taken on different nuclei are combined together in this analysis. It will be shown later in this work that the results of the analysis on spin-density matrix elements do not depend strongly on the type of target gas used, justifying this technique of simply combining these data.

The form of the decay angular distribution, $W(\cos\theta, \varphi, \Phi)$, is obtained by averaging over target nucleon polarization states, assuming that the target is unpolarized. Approximately 1/3 of the data used in this analysis were taken on polarized targets. The polarized targets used at HERMES have their polarization state changed frequently (on the order of a few minutes) during the course of data taking. Therefore, by using the $(\vec{e}, e'K^+K^-)$ data taken on polarized targets in this analysis regardless of the target's polarization state, this effectively averages over the target polarization states. The areal densities of the internal targets were on the order of $\sim 10^{15}$ nucleons/cm^2 for both the 1995 running and the 1996-1997 unpolarized running, and $\sim 10^{14}$ nucleons/cm^2 for the polarized $^1\vec{\mathrm{H}}$ target. As a result, approximately 25% of the ϕ data presented here come from 1995 running, approximately 68% come from 1996-1997 running on unpolarized targets, and only 7% come from

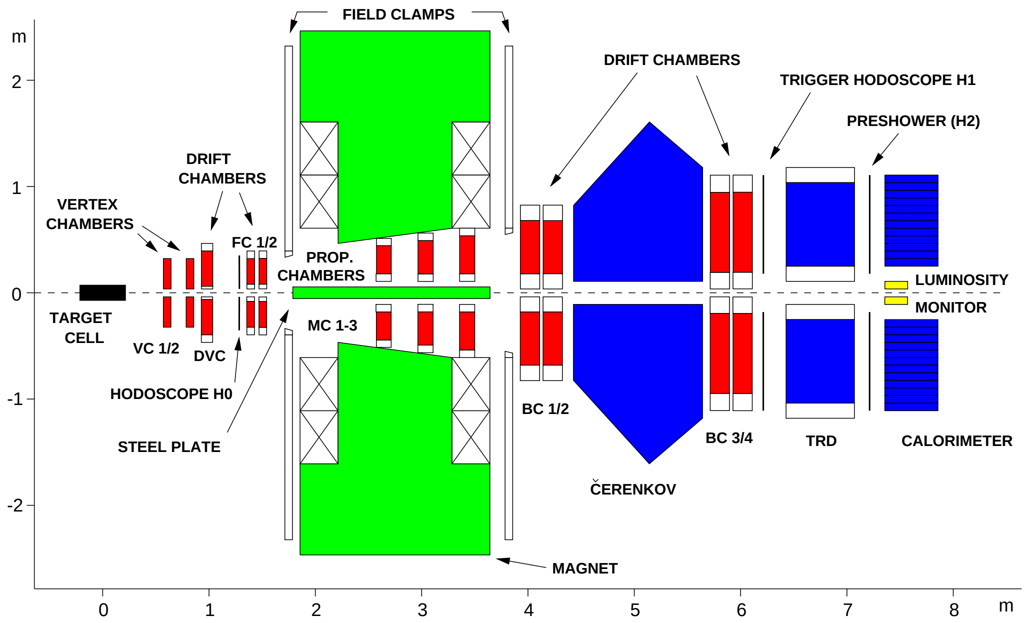

Figure 3.1. Schematic diagram of the HERMES spectrometer viewed from the side. In this picture, the positron beam travels through the spectrometer from left to right.

1996-1997 polarized running.

3.2 Spectrometer

The HERMES spectrometer is depicted schematically in Figure 3.1. The HERMES coordinate system is right-handed, where the z-axis points in the positron beam direction (to the right in Figure 3.1), the x-axis points away from the center of the ring (into the page in the figure), and the y-axis points up (up in the figure). It is identically instrumented in the upper and lower halves, with an open geometry providing angular coverage of $-170 < \theta_x < +170\,\mathrm{mrad}$ and $40 < |\theta_y| < 140\,\mathrm{mrad}$. This open geometry allows the detection of the multiple particle final state in which we are interested.

The magnetic field of the HERMES spectrometer magnet points in the $+y$ direction, has a "deflecting power" of $\int |\vec{B}|d\vec{l} = 1.3\,\text{Tesla-m}$, and is split by the positron and proton beam lines in the xz-plane. In order that the beams are not affected too much by this magnet, the beams pass through a massive iron plate, called the septum plate, which exists in the xz-symmetry plane to reduce the field seen by the beams. This is the cause of the angular restriction $|\theta_y| > 40\,\mathrm{mrad}$.

3.2.1 Trigger As the positron beam passes through the target, various particles are scattered into the spectrometer acceptance, and occasionally an $(\vec{e}, e'K^+K^-)$ scattering event takes place which we would like to analyze. In this instance, the data acquisition system of the experiment must be triggered to write information from the various detector components to tape for later processing.

The main trigger at HERMES in 1995-1997 was designed to trigger on events with a deeply inelastic scattered positron in the acceptance, called the DIS trigger. [64] The DIS trigger is defined by the coincidence measurement of a minimum ionizing signal in a hodoscope located in front of the spectrometer magnet (H0), a hodoscope located behind the magnet (H1), a preshower hodoscope (H2) located behind, and a localized energy deposition of at least 1.5(3.5) GeV in 1996-7(95) in the electromagnetic calorimeter (CALO), also located behind. The coincident signal between H1 and H2 reduces the rate of unwanted triggers from random accidental signals that would occur by using just one hodoscope. Including H0 into the coincidence reduces the background of "backwards-going" charged particles and the background resulting from electromagnetic showers, both coming from the HERA proton beam. Requiring a localized energy deposition of 1.5(3.5) GeV in the CALO is an indication that the charged particle which fired the hodoscopes is a high energy positron. In addition to the coincident signals from the hodoscopes and the calorimeter, the timing of the RF system for the HERA positron beam is monitored and included into the trigger logic. This so-called HERA clock tightens up the timing of the H0*H1*H2*CALO coincidence signal, in the sense that the trigger can be precisely timed to be coincident with the timing for a positron bunch passing through the target. Depending on the beam conditions, the frequency of DIS triggers with the dense target was typically $50 - 200\,\mathrm{Hz}$, resulting in a frequency of measured DIS positrons on the order of approximately $3\,\mathrm{Hz}$. The trigger is estimated to detect positrons with an efficiency in excess of 99%. [65] In 1996-1997, the DIS trigger described above was called trigger 21. In 1995, the DIS trigger did not include H0, but was otherwise identical, and was called trigger 18.

In this work, we use the DIS trigger to choose events of the type $(\vec{e}, e')$, of which our desired event topology, $(\vec{e}, e' K^+ K^-)$, is a subset.

3.2.2 Tracking The tracking detectors in the HERMES spectrometer are comprised of drift chambers to track the two positively and one negatively charged particles before and after the spectrometer magnet. By measuring the bend of the charged particle as it travels through the magnetic field, these drift chambers measure the particle's 3-momentum (times the electric charge). The physical principles underlying the operation of a drift chamber are discussed in many places, for example, in References [66] and [67].

There are two drift chambers per spectrometer half in front of the magnet, called the Front Chambers (FC), while there are four drift chambers per spectrometer half behind the magnet, called the Back Chambers (BC). In addition, there is a set of proportional chambers within the spectrometer magnet, called the Magnet Chambers (MC), to track the charged particles as they travel through the magnet. Part of the work done by the author as a collaborator on this experiment included installing and calibrating the FC's. In Reference [67], the efficiency and spatial resolution of each FC plane were determined to be 99% and 220μm, respectively.

The computer algorithm used by the collaboration to construct the tracks from the FC and BC spatial information is called the HERMES Reconstruction Code, or HRC. [59] With a drift chamber planar spatial resolution of 220μm, the tracking algorithm is estimated to reconstruct the momentum of the particle with an accuracy of $\delta|\vec{p}|/|\vec{p}| \approx 1\%$, while the angular resolution of the track is estimated to be approximately 300μrad. In a simple calculation of the effect of the momentum and angular resolution of the tracks on the decay angle $\cos\theta$, the momentum resolution is found to dominate the resolution in $\cos\theta$, an effect which smears the measured value of $\cos\theta$ on the order of 0.05. The systematic uncertainty in the spin-density matrix elements due to the effect of the spectrometer resolution on the data (smearing) will be estimated more precisely in Subsection 4.3.2.

Note that during the 1997 data collection period, two additional tracking detectors were installed in the front region to better pinpoint the track in this region: one more set of drift chambers, called the Drift Vertex Chambers (DVC), and a silicon tracking detector, called the Vertex Chambers (VC). [6] However, in order to maintain a consistent tracking algorithm throughout the entire 1995-1997 ϕ data sample, the DVC's and VC's are not used for the reconstruction of 1997 data in this analysis.

En route to our goal of obtaining a data sample of $(\vec{e}, e'K^+K^-)$ events, we require our sample of DIS trigger events collected in Subsection 3.2.1 to have exactly three tracks from HRC: two with positive charge and one with negative charge.

3.2.3 Particle Identification In addition to tracking detectors, the HERMES spectrometer has detectors designed to identify the type of particle that has been tracked, called particle identification (PID) detectors. The PID detectors at HERMES were designed with the intention to identify DIS positrons or electrons. Each charged particle is identified as either a lepton or hadron, where here "lepton" means positron (or electron). The detectors include a threshold Čerenkov detector, a transition radiation detector (TRD), the preshower hodoscope (H2), and the electromagnetic calorimeter (CALO), listed in the order in which the particle sees them. The physical principles underlying the operation of these detectors are described in [40] and [68]. Using a likelihood technique based on the combined responses of these four detectors, the track is identified as most probably a lepton or a hadron.

The efficiency of this likelihood technique to identify positrons over the kinematic range available at HERMES is $\approx 99\%$, with a contamination of the positron sample by positive hadrons on the order of $< 1\%$. [61] [69]

Having identified candidate three-track events of the type $(\vec{e}, e'h^+h^-)$, we would like to restrict further the sample to events of the type $(\vec{e}, e'K^+K^-)$. We do this indirectly, by using the threshold Čerenkov detector to eliminate events where either the $h+$ or the h^- is a pion. The physical principle underlying the operation of the Čerenkov detector is Čerenkov radiation. Čerenkov radiation occurs when a charged particle traverses a medium with speed larger than that of the velocity of light in the medium, in which case the particle will radiate photons, called Čerenkov photons. [40] The minimum speed necessary for a particle to radiate Čerenkov photons is

$$\beta = \frac{1}{n}, \tag{3.1}$$

where n is the index of refraction of light in the medium. For a given momentum, the speed decreases as the mass increases. Hence, in a given medium, a positron with momentum above the positron momentum threshold will radiate Čerenkov photons, while a pion must have momentum above the larger pion momentum threshold—larger since the pion is slower. The Čerenkov detector is filled with a gas whose composition has an index of refraction such that pions just begin to radiate Čerenkov photons in the HERMES kinematic range, so that pion identification is possible.

Therefore, for our $(\vec{e}, e'K^+K^-)$ event sample, we require that either the h^+ or the h^- has momentum above the pion momentum threshold in the Čerenkov, and not exhibit any signal in this detector. The gas used in the Čerenkov in 1995 was pure N_2 at atmospheric pressure, whose index of refraction results in a pion momentum threshold of 5.7 GeV. The gas used in the Čerenkov in 1996 and 1997 was 70%/30% N_2/C_4F_{10} at atmospheric pressure, which has a pion momentum threshold of 4.0 GeV. [70] The amount of the contamination of the exclusive di-kaon sample by pion background will be different for the different years' pion momentum thresholds. In addition, there will be contamination of the di-kaon sample by heavier hadrons, as well as the contamination by pions due to the measurement inefficiency of the Čerenkov detector, all of which will be sources of non-exclusive background underneath the exclusive ϕ signal. All of these issues will be addressed by the background correction in Subsection 4.3.4.

CHAPTER 4

ANALYSIS

4.1 Extraction of r^{α}_{ij} from the Exclusive ϕ Signal

4.1.1 Spectrometer Specific Information For exclusive ϕ candidates, three charged track $(\vec{e}, e'h^+h^-)$ events from the HERMES μDST production are used from the 1995-1997 data collection periods on polarized and unpolarized nuclear targets, including $^1\vec{\mathrm{H}}$, $^3\vec{\mathrm{He}}$, ^{1}H, ^{2}H, ^{3}He, and ^{14}N. The data analyzed are from DIS triggers 18 and 21 described in Subsection 3.2.1.

In its data production, HERMES uses different tracking methods to accommodate the different years' front-region tracking detector configuration. (See chapter 3.) To have a consistent tracking algorithm throughout the entire ϕ data set, we choose the NOVC HRC reconstruction algorithm, located in `version 95e5`, `version 96c1`, `version 97c0` (polarized) and `version 97b2` (unpolarized) μDST's. The first two digits in the μDST version number refer to the year of data collection. The third digit is the counter of HRC production; this records HRC production information, such as the tracking algorithm used. The fourth digit is the counter of μDST production; this mainly records changes in slow control information. At the time of this writing, the μDST versions used in this analysis were the most recent NOVC HRC productions available.

Positrons and hadrons are defined by a likelihood technique, depending on the combined responses of the TRD, the Čerenkov, the preshower, and the calorimeter. [71] For 1996/97 data, the positrons (hadrons) are defined by

$$g1Track.rPID3 + g1Track.rPID5 > (<) 0. \tag{4.1}$$

For 1995 data, a downshifting scheme is used: when the TRD is operating well, positrons (hadrons) are defined by

$$g1Track.rPID3 + 0.31 * g1Track.rTRD > (<)5.48. \tag{4.2}$$

When the TRD is not operating well, positrons (hadrons) are defined by [60]

$$g1Track.rPID3 > (<)0. \tag{4.3}$$

In Reference [34] it was found that misidentification between positrons and hadrons had a negligible effect on the results of the ρ^0.

In order to make edge-effect corrections to the data more easily facilitated, we require the events to occur within the well-understood part of the spectrometer. We make horizontal and vertical angular fiducial constraints,

$$\begin{aligned} \left|\frac{dX}{dZ}\right| &< 170\,\text{mrad and} \\ 40 < \left|\frac{dY}{dZ}\right| &< 140\,\text{mrad}, \end{aligned} \tag{4.4}$$

on all three particles, where X, Y, and Z refer to the directions in the lab coordinate system described in Section 3.2. We also make calorimeter fiducial constraints on the positron:

$$\begin{aligned} |rXpos + 463 * rXslope| &< 175\,\text{cm, and} \\ |rYpos + 463 * rYslope| &> 30\,\text{cm}. \end{aligned} \tag{4.5}$$

The sensitivity of the spin-density matrix elements to the fiducial constraints will be included into the systematic uncertainty in Subsection 4.3.2.

At HERMES energies, the scattered positron and the K^+K^- pair from the ϕ decay should come from the same vertex, [72]

$$\left|\frac{z_{vtx}^{h^+} + z_{vtx}^{h^-}}{2} - z_{vtx}^{e^+}\right| < 7\,\text{cm}, \tag{4.6}$$

and each of these tracks should come from the target region, so there are constraints placed on the transverse and longitudinal components of the vertex position:

$$t_{vtx} < 0.75\,\text{cm for all data;} \tag{4.7}$$

$$-18 < z_{vtx} < 18\,\text{cm for 1996/97 data, and} \tag{4.8}$$

$$-30 < z_{vtx} < 30\,\text{cm for 1995 data.} \tag{4.9}$$

The energies of the h^+ and h^- are computed assuming the hadrons are kaons. To reduce pion contamination, we require that one of the hadron pair exceed the 1996/97 pion momentum threshold in the Čerenkov counter (4.0 GeV) and exhibit no signal in the counter (< 0.2 photoelectrons). It was confirmed that the Čerenkov counter also did not fire on the second hadron for nearly all the events considered in the exclusive ϕ sample. The gas actually used in the Čerenkov counter was different in 1995, with an increased pion momentum threshold of 5.7 GeV for these data. The mismatch between the pion momentum threshold used in the analysis and the actual 1995 experimental pion momentum threshold will increase the background for the 1995 exclusive ϕ data sample. This background will be corrected for in Section 4.2.1. Runlists are used to reject runs in which the Čerenkov detector is known to be not operating properly.

The spectrometer specific constraints on the data are summarized in Table 4.1. These constraints are applied to all data analyzed in this thesis.

4.1.2 ϕ Mass and Exclusivity Constraints As mentioned before, the energies of the h^+ and h^- are computed from the measured momenta of the charged tracks, assuming the hadrons are kaons. For each event, the invariant mass of the two hadron system is computed (see Equation 2.4),

$$M_{2K}^2 = \sqrt{(p_+ + p_-)^2},$$

and the distribution of such events is seen in Figure 4.1. The ϕ resonance is clearly

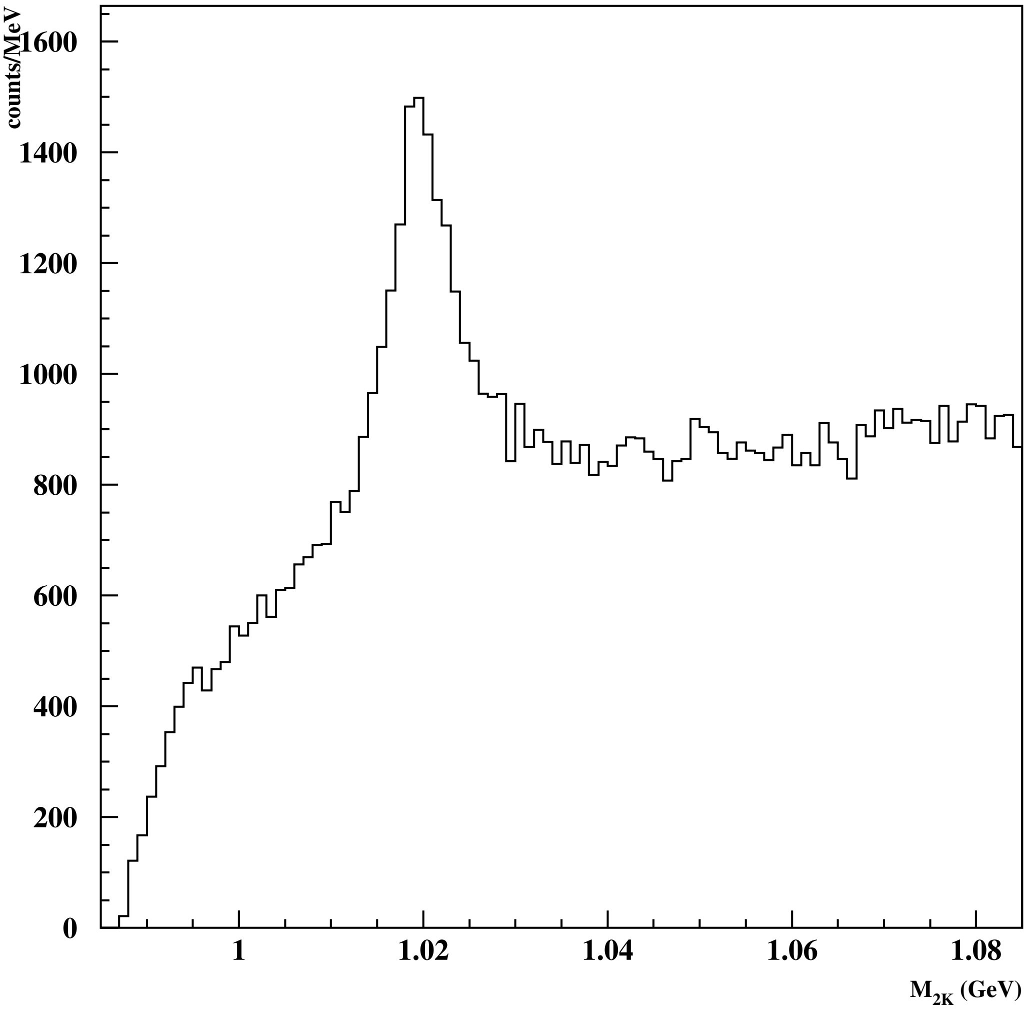

Figure 4.1. Distribution of events as a function of M_{2K}, with no constraint on ΔE. The ϕ resonance is clearly visible.

Table 4.1. Spectrometer specific constraints on the data to restrict the exclusive $(e, e'\phi)$ candidate events to well-understood regions of the spectrometer. These constraints are for the 1996/97 data samples. See text for changes for 1995 data.

Constraint	Description
exactly $(e'h^+h^-)$	NOVC 3-track event
$rPID35 > (<)0$	e/h identification (see text)
$\left\lvert\frac{dX}{dZ}\right\rvert < 170\,\text{mrad}$	fiducial cut on e', h^+, h^-
$40 < \left\lvert\frac{dY}{dZ}\right\rvert < 140\,\text{mrad}$	fiducial cut on e', h^+, h^-
$\lvert rXpos + 463 * rXslope\rvert < 175\,\text{cm}$	$e+$ calorimeter fiducial cut
$\lvert rYpos + 463 * rYslope\rvert > 30\,\text{cm}$	$e+$ calorimeter fiducial cut
$\left\lvert\frac{z_{vtx}^{h^+} + z_{vtx}^{h^-}}{2} - z_{vtx}^{e^+}\right\rvert < 7\,\text{cm}$	similar vertex
$t_{vtx} < 0.75\,\text{cm}$	transverse vertex cut on e', h^+, h^-
$-18 < z_{vtx} < 18\,\text{cm}$	z-vertex cut on e', h^+, h^-
$\vec{p}_h > 4.0\,\text{GeV}$ and Č$< 0.2\,$p.e.	pion decontamination on one hadron

visible in this distribution. For our event sample, we look at events only within the ϕ mass region, $1.012 < M_{2K} < 1.028\,\text{GeV}$. The sensitivity of the spin-density matrix elements to the ϕ mass constraint is included into the systematic uncertainty in Subsection 4.3.4.

In the center-of-mass frame of the ϕ, the K^+K^--pair fly out back-to-back with equal and opposite momenta of 0.127 GeV. In the lab, the average energy of the ϕ is on the order of the energy of the photon, approximately 12 GeV. As a result, the boost from the ϕ center-of-mass frame to the lab frame is large, so that it compresses the opening angle between the K^+K^- in the lab frame. Therefore, in the lab, the maximum opening angle between the K^+ and the K^- is still too small so that the K^+ and K^- cannot go each into a separate half of the spectrometer. Hence, the event topology for the $(e, e'\phi \to K^+K^-)$ events in the HERMES spectrometer is such that when the positron goes into one of the halves of the spectrometer, the K^+K^--pair from the ϕ decay will always go together into the other half.

We would like the final state of our reaction to consist exclusively of a ϕ and a nucleon in the ground state, however, the limited acceptance of the HERMES spectrometer prevents us from measuring the complete final state. Only an indirect measurement of the excitation energy of the recoiling target can be made,

$$\Delta E \equiv \frac{p'^2 - M_p^2}{2M_p} = \nu - E_\phi + t/2M_p \tag{4.10}$$

in the lab frame. We define exclusive events as those having $\Delta E = 0\,\text{GeV}$, *i.e.* where the target is not dissociated and no additional particles are created. The distribution of events as a function of ΔE for events within the ϕ mass region is seen in Figure 4.2. The finite resolution of the spectrometer smears the exclusive peak, so in this analysis we define exclusive candidates as those with $\Delta E < 1.0\,\text{GeV}$. The effect of requiring this exclusivity constraint on the M_{2K} spectrum can be seen in Figure 4.3. The sensitivity of the spin-density matrix elements to the exclusivity constraint will be included into the systematic uncertainty in Subsection 4.3.4.

With the constraints from Table 4.1, the ϕ mass constraint, $1.012 < M_{2K} < 1.028\,\text{GeV}$, and the exclusivity constraint, $\Delta E < 1.0\,\text{GeV}$, the 1995-1997 data from all targets yield approximately 2200 candidate exclusive ϕ events. Note that this number agrees with the yield obtained in an independent analysis of these data in the extraction of the ϕ total photoproduction cross section. [74]

4.1.3 The Method of Moments and its Statistical Uncertainty

With the exclusive ϕ candidates from Subsection 4.1.2, we want to measure the spin-density matrix elements, r_{ij}^{α}, in the decay angular distribution of ϕ's, $W(\cos\theta, \varphi, \Phi)$, given in Equation 2.31. In Reference [38], Schilling and Wolf describe a technique to measure r_{ij}^{α} that we will use, called the method of moments. [36]

We assume there are no acceptance effects in the measured angular distributions. In this case, to measure a moment of a function, $F(\theta, \varphi, \Phi)$, one simply takes the average value of F over the data,

$$\langle F(\theta, \varphi, \Phi) \rangle = \frac{1}{N_{events}} \sum_{i=1}^{N_{events}} F(\theta_i, \varphi_i, \Phi_i). \tag{4.11}$$

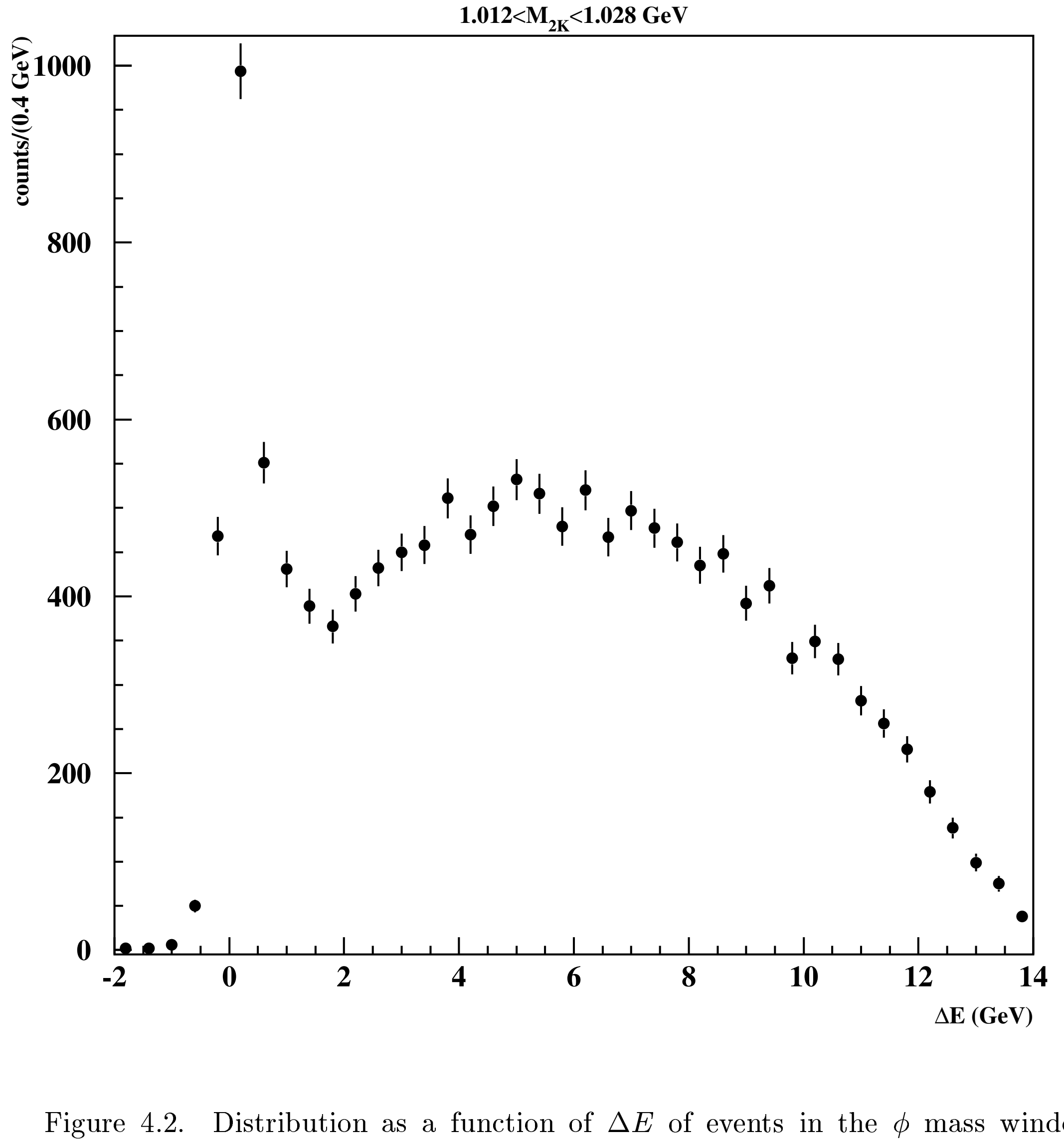

Figure 4.2. Distribution as a function of ΔE of events in the ϕ mass window, $1.012 < M_{2K} < 1.028\,\mathrm{GeV}$. The exclusive peak can be seen at $\Delta E < 1.0\,\mathrm{GeV}$.

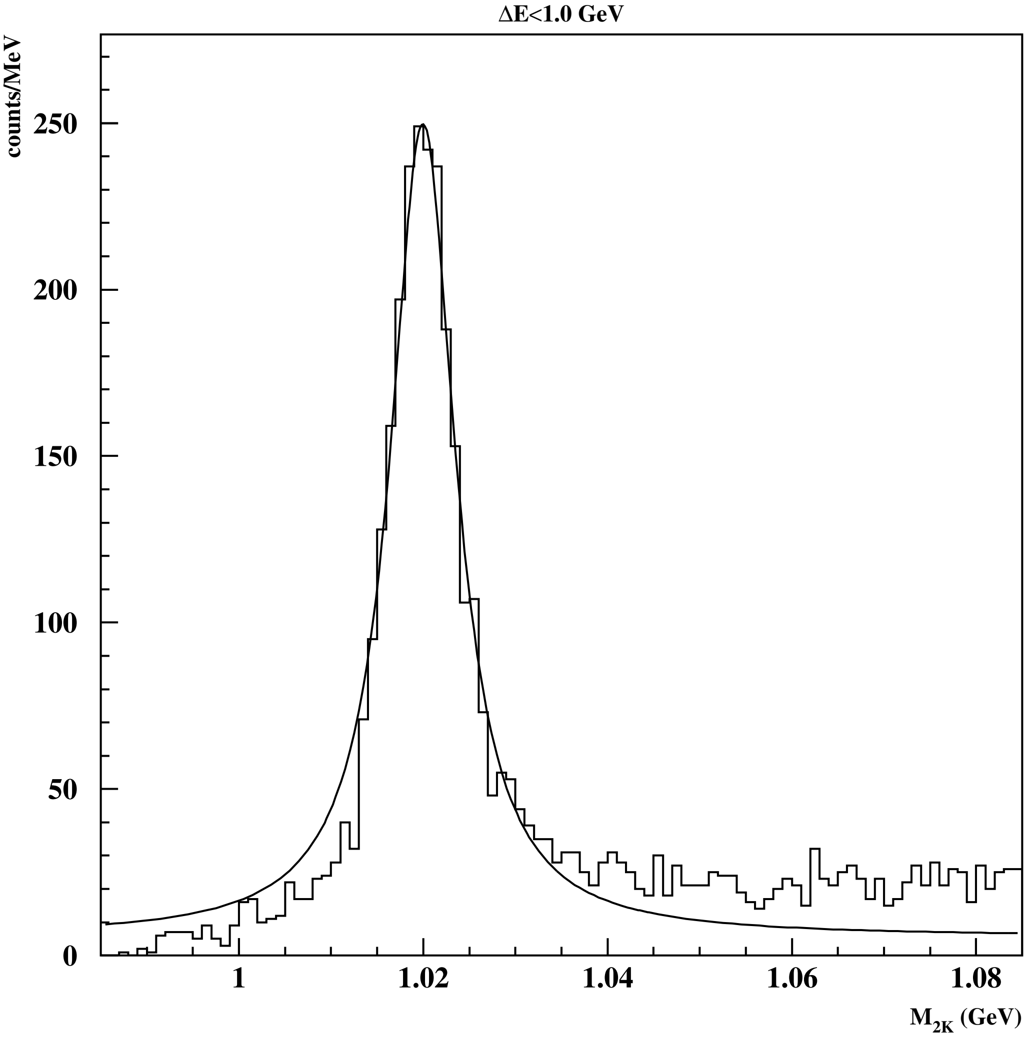

Figure 4.3. Distribution of events as a function of M_{2K} which satisfy the exclusivity constraint, $\Delta E < 1.0\,\mathrm{GeV}$. Compared with Figure 4.1, the ϕ resonance is more pronounced. The solid line is a relativistic p-wave Breit-Wigner fit to the distribution, $N_\phi \propto \frac{M_{2K} M_\phi \Gamma}{(M_{2K}^2 - M_\phi^2)^2 + M_\phi^2 \Gamma^2}$, with a constant width, Γ. [73] Also included is a linear background term. Not included in the fit is the resolution of the spectrometer, but the fitted parameters are $M_\phi \approx 1.020\,\mathrm{GeV}$ and $\Gamma \approx .009\,\mathrm{GeV}$, which compare fairly well with the values from the Particle Data Group: $M_\phi = (1019.413 \pm 0.008)\,\mathrm{MeV}$ and $\Gamma = (4.43 \pm 0.06)\,\mathrm{MeV}$. The Breit-Wigner shape seems to fit the data distribution well in the resonance region, but the background is clearly not well described by the simple linear background term.

Another way to think of this equation is, if we bin the data in a histogram as a function of F, the measured moment of F is the average value of this histogram,

$$\langle F \rangle = \frac{\sum_j F_j N_j}{\sum_j N_j}, \tag{4.12}$$

where N_j is the number of events in the histogram bin j with value F_j. The real variable analog of Expression 4.12 is written in terms of the data probability distribution, $W(\cos\theta, \varphi, \Phi)$, as the weighted average of F,

$$\langle F(\theta, \varphi, \Phi) \rangle = \frac{\int d\cos\theta \, d\varphi \, d\Phi \;\; F(\theta, \varphi, \Phi) W(\cos\theta, \varphi, \Phi)}{\int d\cos\theta \, d\varphi \, d\Phi \;\; W(\cos\theta, \varphi, \Phi)}, \tag{4.13}$$

and the method of moments follows from this definition in the following way. Inspection of Equation 2.31 for $W(\cos\theta, \varphi, \Phi)$ reveals that each r^{α}_{ij} is multiplied by an orthogonal trigonometric function of $(\cos\theta, \varphi, \Phi)$. Therefore, the measurement of a particular spin-density matrix element can be simply obtained by a measurement of the moment of its corresponding trigonometric function, according to Equation 4.13. As an example, we have the expression

$$\mathrm{Im}(r^3_{1-1}) = \frac{1}{P_b} \frac{1}{\sqrt{1-\epsilon^2}} \frac{5}{4} \langle \sin^2\theta \sin 2\varphi \rangle, \tag{4.14}$$

where $1/\sqrt{1-\epsilon^2} = \langle 1/\sqrt{1-\epsilon^2} \rangle$. The distribution of data events as a function of ϵ is plotted in Figure 4.4. In Appendix B, the explicit expressions of all 23 spin-density matrix elements in terms of their corresponding moments are given.

Special note should be paid to the factor of $1/P_b$ in Expression 4.14. The distribution of exclusive ϕ candidate events as a function of longitudinal beam polarization can be seen in Figure 4.5. We want to represent this distribution by a number, P_b, to use in the evaluation of Expression 4.14—clearly this cannot be done for the entire data set appropriately with the use of only one value. There are two regions in this distribution where, in each, the average beam polarization can be well-represented by single number: $P_b < -0.4$, which contains 695 events with a negative average polarization $\langle P_b \rangle = -0.531$, and $P_b > 0.4$, which contains 1050 events with a

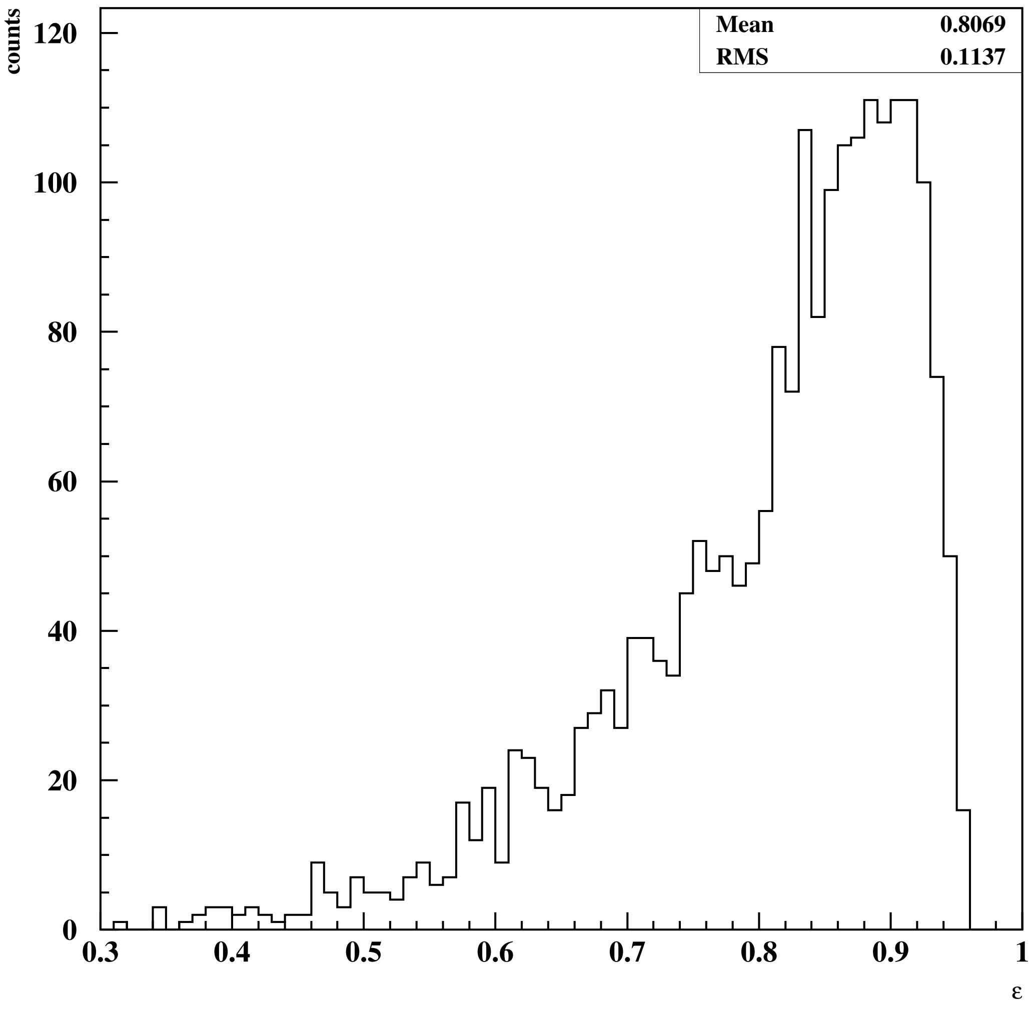

Figure 4.4. The distribution of ϕ data events as a function of the polarization parameter, ϵ. The average values of the functions of ϵ used in the method of moments to extract the spin-density matrix elements are: $1/\epsilon = 1.28$, $1/\sqrt{1-\epsilon^2} = 1.86$, $1/\sqrt{2\epsilon\,(1+\epsilon)} = 0.60$, and $1/\sqrt{2\epsilon\,(1-\epsilon)} = 1.96$.

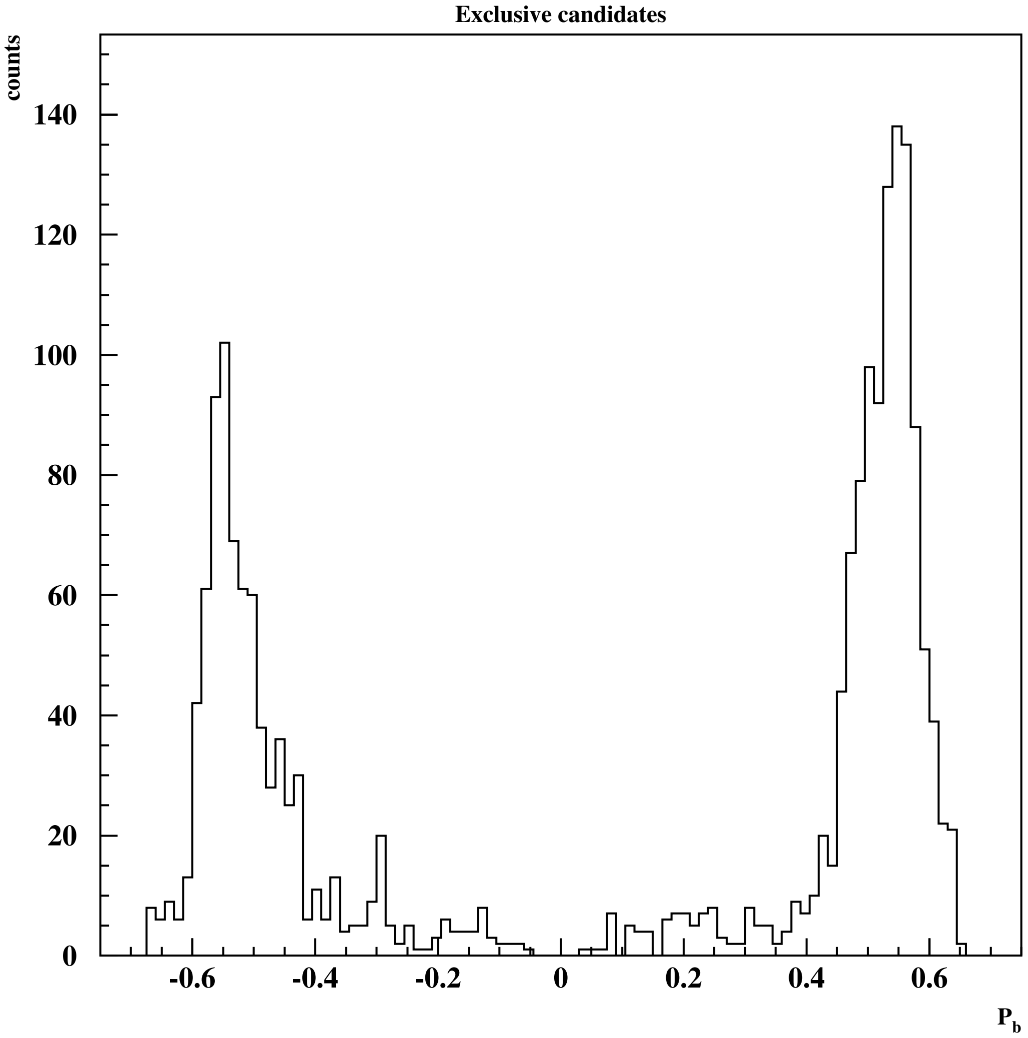

Figure 4.5. Distribution of events as a function of longitudinal beam polarization for the exclusive ϕ candidates. There are two regions in this distribution where, in each, the average beam polarization is well-represented by single number, $P_b < -0.4$ and $P_b > 0.4$.

positive average polarization $\langle P_b \rangle = 0.533$. Therefore, to determine the spin-density matrix elements which depend on P_b, we make separate measurements for positive and negative beam polarizations, and combine the results by the expression,

$$\mathrm{Im}(r^3_{1-1}) = \frac{\frac{\mathrm{Im}(r^3_{1-1})_+}{\sigma_+^2} + \frac{\mathrm{Im}(r^3_{1-1})_-}{\sigma_-^2}}{\frac{1}{\sigma_+^2} + \frac{1}{\sigma_-^2}}, \tag{4.15}$$

where $\mathrm{Im}(r^3_{1-1})_\pm$ are the extracted values of the spin-density matrix element with positive and negative beam polarizations, and $\sigma_\pm$ are the statistical uncertainties.

The statistical uncertainty in r^α_{ij} from the method of moments can be estimated in the following way. Any factors in front of the moment, such as $1/P_b$ and $1/\sqrt{1-\epsilon^2}$ in Equation 4.14, are assumed to be constant in the evaluation of the statistical uncertainty of r^α_{ij}. Including the statistical uncertainty of such factors has been checked to have a negligible effect on the statistical uncertainty of r^α_{ij}. Therefore, to estimate the statistical uncertainty on a spin density matrix element, we only need to evaluate the statistical uncertainty on the average value, $\langle F \rangle$, of the histogrammed angular distribution, Equation 4.24.

We assume that the number of counts in a particular bin, N_j, is a quantity independent of the number of counts in any other bin. The systematic uncertainty effects from smearing will be discussed in Subsection 4.3.2. By propagation of independent uncertainties, the statistical uncertainty in $\langle F \rangle$ can be written

$$(\delta\langle F \rangle)^2 = \sum_j \left(\frac{\partial \langle F \rangle}{\partial N_j}\, \delta N_j \right)^2 = \sum_j \left(\frac{F_j - \langle F \rangle}{\sum_i N_i} \right)^2 (\delta N_j)^2, \tag{4.16}$$

where δN_j is the statistical uncertainty in the number of counts in bin j, and $\langle F \rangle$ is from Equation 4.24. To validate Equation 4.16, we assume we have enough counts in each bin so that the statistical uncertainty in the number of counts is governed by counting statistics ($\delta N_j = \sqrt{N_j}$). Then Equation 4.16 becomes

$$(\delta\langle F \rangle)^2 = \frac{1}{N_{tot}} \times \left(\frac{1}{N_{tot}} \sum_j (F_j - \langle F \rangle)^2 \, N_j \right) \approx \frac{1}{N_{tot}}\, \sigma_F^2, \tag{4.17}$$

where $N_{tot} = \sum_i N_i$, and σ_F is the standard deviation of F. [75] This shows that Equation 4.16 reduces appropriately to the standard expression for the standard deviation of the mean. [76] In Subsection 4.3.1, we will show that the statistical uncertainty from Equation 4.16 agrees with the statistical uncertainty estimated from the standard χ^2 for one-dimensional histograms.

A word should be said about the statistical uncertainty for the matrix elements $r_{00}^{1,5,8}$ and $r_{11}^{1,5,8}$. In Appendix B, the expressions for each of these spin-density matrix elements are given by the linear combinations of the average values from two histograms. For example, the expressions for the spin-density matrix elements r_{00}^{5} and r_{11}^{5} are

$$r_{00}^{5} = a\left[-\langle\cos\Phi\rangle + 5\langle\cos^2\theta\,\cos\Phi\rangle\right], \text{ and} \tag{4.18}$$

$$r_{11}^{5} = a\left[\frac{3}{2}\langle\cos\Phi\rangle - \frac{5}{2}\langle\cos^2\theta\,\cos\Phi\rangle\right], \tag{4.19}$$

which are both functions of the two angular distributions $A = \langle\cos\Phi\rangle$ and $B = \langle\cos^2\theta\,\cos\Phi\rangle$. To estimate the statistical uncertainty for either r_{00}^{5} or r_{11}^{5}, we use the error propagation formula,

$$(\delta r_{00}^{5})^2 = \left|\frac{\partial r_{00}^{5}}{\partial A}\right|^2 (\sigma_A)^2 + \left|\frac{\partial r_{00}^{5}}{\partial B}\right|^2 (\sigma_B)^2 + 2\frac{\partial r_{00}^{5}}{\partial A}\frac{\partial r_{00}^{5}}{\partial B}\sigma_{AB}^2, \tag{4.20}$$

where σ_A and σ_B are the statistical uncertainties of the means of the histograms A and B from Equation 4.16, and σ_{AB} is the covariance between the means of the histograms A and B. To estimate the covariance between the means of the histograms, we compute the linear correlation coefficient, c_{AB} between the distributions of data used to compute $\langle A\rangle$ and $\langle B\rangle$. It is defined by [75]

$$c_{AB} = \frac{s_{AB}^2}{\sqrt{s_{AA}^2}\sqrt{s_{BB}^2}}, \tag{4.21}$$

where s_{AA}^2 is the standard deviation, or variance, of the distribution of data from

Table 4.2. The values and statistical uncertainties of the spin-density matrix elements for ϕ's, integrated over all kinematic variables, uncorrected for effects that will be described in Section 4.2. The uncertainty is the estimate of the statistical uncertainty from Equation 4.16.

Unpolarized beam		Polarized beam	
r^{04}_{00}	0.349 ± 0.016	$\mathrm{Im}(r^3_{10})$	-0.017 ± 0.039
r^1_{1-1}	0.202 ± 0.024	$\mathrm{Im}(r^3_{1-1})$	-0.086 ± 0.055
$\mathrm{Im}(r^2_{1-1})$	-0.177 ± 0.023	$\mathrm{Im}(r^7_{10})$	-0.030 ± 0.056
$\mathrm{Re}(r^5_{10})$	0.150 ± 0.008	$\mathrm{Im}(r^7_{1-1})$	0.126 ± 0.083
$\mathrm{Im}(r^6_{10})$	-0.158 ± 0.008	r^8_{11}	0.036 ± 0.083
$\mathrm{Re}(r^{04}_{10})$	-0.083 ± 0.010	r^8_{00}	-0.052 ± 0.123
r^{04}_{1-1}	0.003 ± 0.014	$\mathrm{Re}(r^8_{10})$	-0.033 ± 0.057
r^1_{11}	-0.017 ± 0.025	r^8_{1-1}	-0.034 ± 0.082
r^1_{00}	0.048 ± 0.037		
$\mathrm{Re}(r^1_{10})$	0.060 ± 0.018		
$\mathrm{Im}(r^2_{10})$	-0.091 ± 0.018		
r^5_{11}	-0.142 ± 0.011		
r^5_{00}	-0.061 ± 0.017		
r^5_{1-1}	0.013 ± 0.011		
$\mathrm{Im}(r^6_{1-1})$	-0.040 ± 0.011		

which we calculate the mean of A. It is defined as a sum over data events

$$s^2_{AA} = \frac{1}{N_{events} - 1} \sum_i [A_i - \langle A \rangle]^2 > 0. \tag{4.22}$$

The covariance between the distributions of data used to compute $\langle A \rangle$ and $\langle B \rangle$ is

$$s^2_{AB} = \frac{1}{N_{events} - 1} \sum_i [A_i - \langle A \rangle][B_i - \langle B \rangle] \tag{4.23}$$

which, contrary to its notation, may be < 0. The values of the linear correlation coefficients between the histograms which make up $r^{1,5,8}_{00}$ and $r^{1,5,8}_{11}$ are all on the order of $c_{AB} \approx +0.5$. Then the value of σ_{AB} used in Equation 4.20 is $\sigma_{AB} = c_{AB}\,\sigma_A\,\sigma_B$.

The values and statistical uncertainties of the uncorrected spin density matrix elements measured with the exclusive ϕ candidate events from the HERMES data are tabulated in Table 4.2. As an example, the distribution of data used to compute the moment for $\mathrm{Im}(r^6_{10})$ can be seen in Figure 4.6.

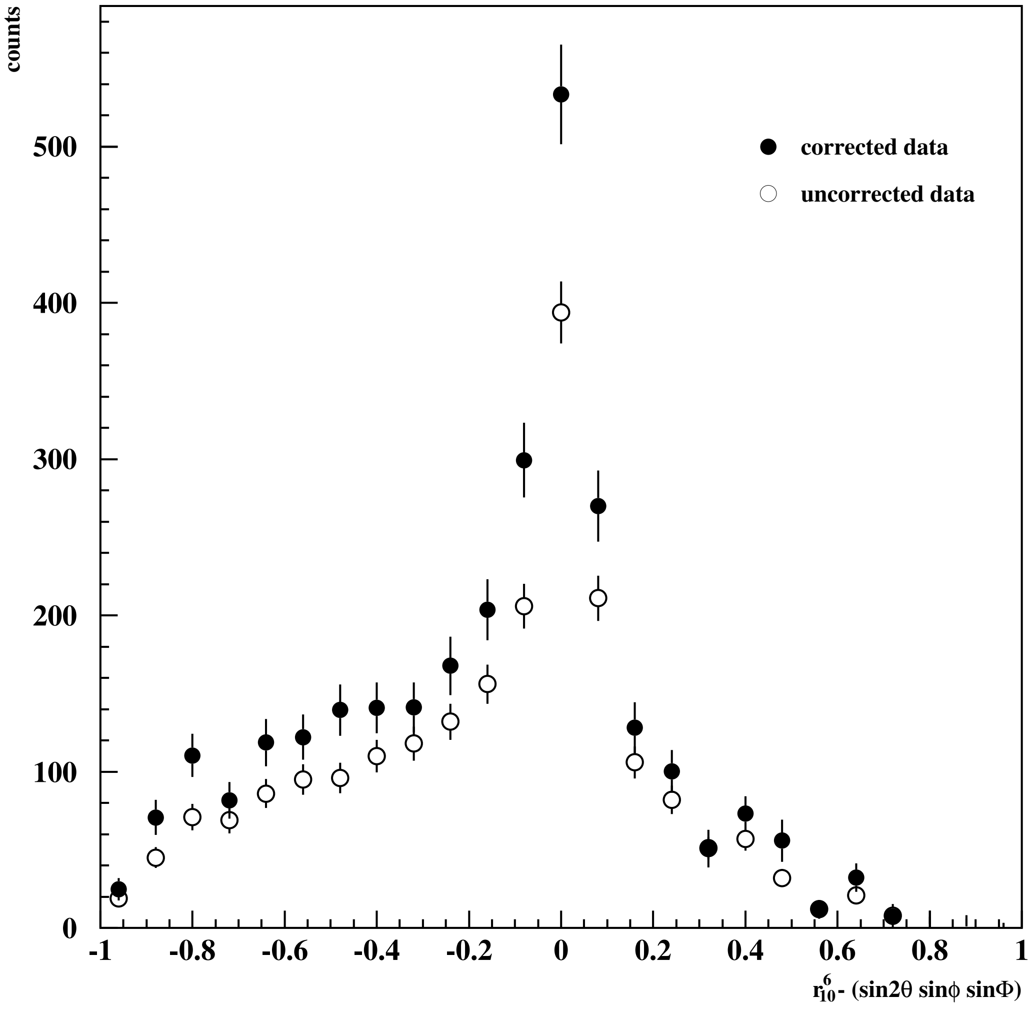

Figure 4.6. The distribution of data used to calculate $\mathrm{Im}(r^6_{10})$ before and after the corrections from Section 4.2 have been applied. The overall normalization of the corrected data is arbitrary, as $\mathrm{Im}(r^6_{10})$ depends only on the mean of this distribution. What is important is that the corrections applied increase the left side of the distribution relative to the right side.

4.2 Corrections to Data

In the experiment, we measure the number of counts in a given angular bin, N_j, which needs to be corrected for several effects before the moments can be finally evaluated. These corrections will be performed on the one-dimensional histograms of data before we calculate the moments,

$$\langle F \rangle = \frac{\sum_j F_j N_j^{corr}}{\sum_j N_j^{corr}}, \tag{4.24}$$

where N_j^{corr} is the corrected number of data events in histogram bin j with value F_j. The present section describes all the corrections performed in this analysis to obtain N_j^{corr} from N_j, the observed number of counts.

4.2.1 Background Effects For us, an exclusive ϕ event is defined as one with a final state consisting only of a scattered positron, a K^+K^--pair resulting from a ϕ decay, and a recoiling ground state nucleon. In this subsection, we describe a correction that is applied to the data to account for deviations of the data from this definition, called the background correction. We want to estimate two things about this background, namely, the total amount of background compared to the size of the exclusive ϕ signal, and the shape of this background as a function of F for each moment.

There are several sources of background expected to contaminate the exclusive ϕ sample, coming from either non-diffractive or diffractive origin. Some non-diffractive sources of background include,

- deeply-inelastic scattering from quarks which then fragment into hadrons with kinematics such that the event satisfies the exclusive ϕ constraints; and
- $s\bar{s}$-knockout from the nucleus.

In the spin-density matrix element analysis of the ρ^0 meson from HERMES [34], the largest source of background was estimated to be the DIS-fragmentation background, which was corrected for with a Monte Carlo simulation of the DIS process using

LEPTO, and the subsequent hadronization treated with the LUND model. [77] This study estimated the amount of background contaminating the exclusive ρ^0 yields to be on the order of 6-15%. A similar study on the ϕ yields gives an estimate of $\approx 9\%$ DIS-fragmentation background. Note that no other sources of background were explicitly addressed in this ρ^0 analysis. A calculation of the $s\bar{s}$-knockout process has found that the yield in ϕ production from the knockout process is expected to be at least 10 times smaller than that from the VMD-diffractive ϕ production process. [78]

Some diffractive sources of background include,

- diffractive $\rho^0 \to \pi^+\pi^-$ contamination;
- double-dissociative diffractive production, where the target remains intact for the production of the ϕ, and thereafter breaks up; [79]
- diffractive non-resonant K^+K^- production; and
- diffractive $\omega \to \pi^+\pi^-$ contamination.

Note that the contamination of the K^+K^- sample by e^+e^- events is negligible. [34, 71] In principle, to estimate the background under the exclusive ϕ peak with Monte Carlo methods, one would need models which describe the relative strengths and angular dependences of all of the listed non-diffractive and diffractive processes. We choose, instead, to estimate the background with a technique called the sideband method, whereby data in kinematic sidebands are used to estimate the size and shape of the background underneath our exclusive ϕ peak. The data, then, would automatically have contributions included from all of the processes listed above.

The distribution of three track events which satisfy all the constraints in Table 4.1 can be seen in Figure 4.7 as a scatter plot of ΔE vs. M_{2K}. The regions partitioned in this plot are defined by

- Region I, 192 events - $\Delta E < 1.0\,\mathrm{GeV}$, $0.994 < M_{2K} < 1.010\,\mathrm{GeV}$,
- Region II, 2188 events - $\Delta E < 1.0\,\mathrm{GeV}$, $1.012 < M_{2K} < 1.028\,\mathrm{GeV}$,
- Region III, 437 events - $\Delta E < 1.0\,\mathrm{GeV}$, $1.030 < M_{2K} < 1.046\,\mathrm{GeV}$, and

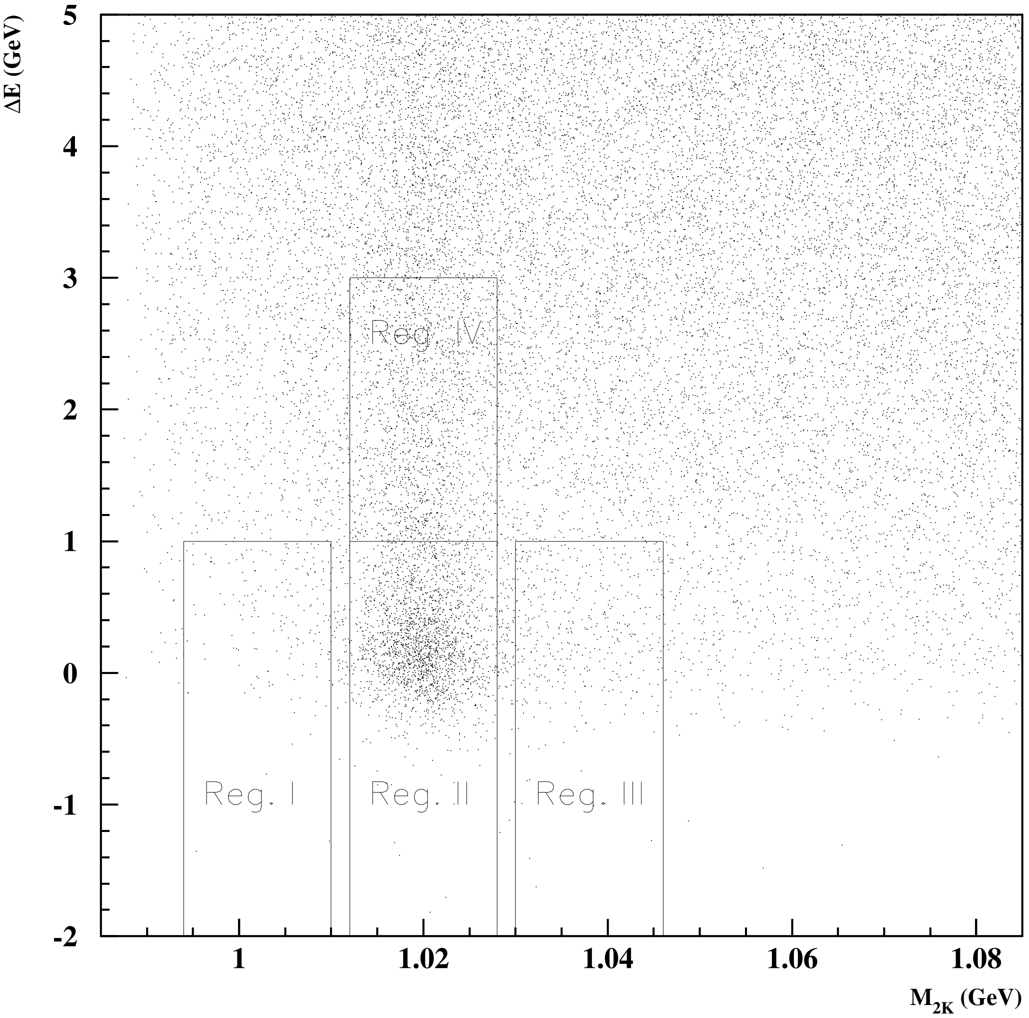

Figure 4.7. Scatter plot of ΔE vs. M_{2K} for data which have satisfied all the constraints in Table 4.1. The exclusive ϕ peak can be seen in the exclusive Region II, while Regions I, III, and IV are dominated by background events.

- Region IV, 1822 events - $1.0 < \Delta E < 3.0\,\mathrm{GeV}$, $1.012 < M_{2K} < 1.028\,\mathrm{GeV}$.

Region II is our exclusive region, dominated by the exclusive ϕ peak, contaminated by background. In Regions I, III, and IV, the data primarily consist of background events. The idea of the sideband method of background subtraction is to infer the size and shape of the background contaminating the exclusive peak in Region II by using the data from Region I, III, or IV, or some combination of these.

We want to discern which of the data regions, I, III, or IV, best resembles the background in Region II. To do so, we evaluate the differences of each moment of F, as well as the differences in the average value of $1/\epsilon$, a, $1/\sqrt{1-\epsilon^2}$, and b, between regions I, III, and IV. In Figure 4.8 is plotted the differences of these values between the regions. Most of the moments differ very little in value between regions, as can be seen by the preponderance of differences clustered around zero. However, for r^5_{00}, r^5_{11}, $1/\sqrt{1-\epsilon^2}$, and b, the value in Region IV significantly differs from both that in Region I and that in Region III. This is evidence that the shape or size, or both, of the background distribution is a stronger function of ΔE than M_{2K}. Unfortunately, it is not clear from this study how much of the background in Region II is from the contribution which would resemble the data in Region IV and how much is from the contribution which would resemble the data in Regions I and III. Therefore, for this analysis, we will use the data in Regions I and III for our background correction, and simply ascribe a systematic uncertainty to account for any background error, using the results from Regions I, III, and IV (described in Subsection 4.3.4).

A comparison of the sideband data with the LEPTO/LUND MC that was used in the ρ^0 spin-density matrix element analysis can be seen in Figure 4.9, plotted as a function of $\cos\theta$, φ, Φ, and ψ. This comparison is for the range $\Delta E < 3.0\,\mathrm{GeV}$ and $M_{2K} < 1.012\,\mathrm{GeV}$, approximately covering Region I. Although the statistics for the MC background run are limited, the shape of the MC agrees qualitatively with the data. In particular, the events are clustered at $\cos\theta \approx 0$ and at $\Phi = \pm\pi$. The

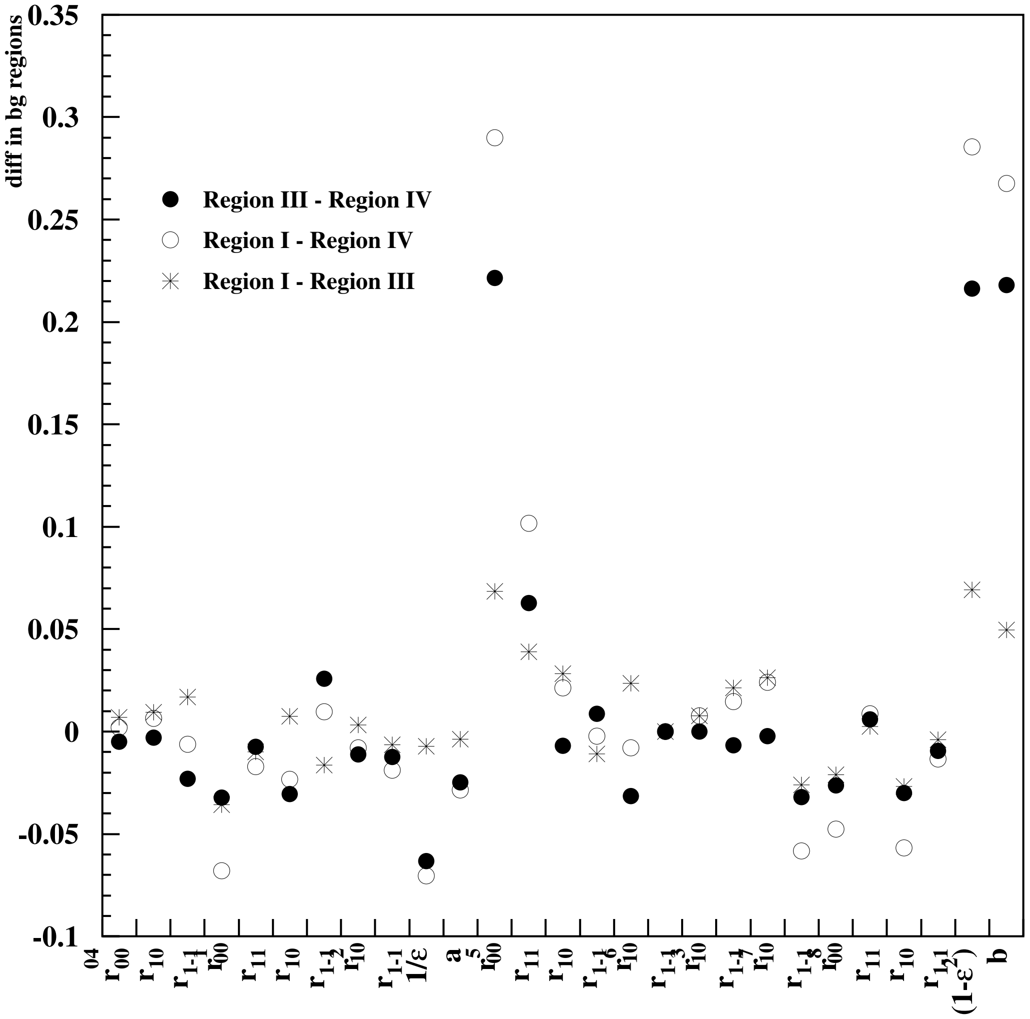

Figure 4.8. The differences between the average values of data for Region I, III, and IV is plotted versus moment. The labels for the abscissa of this plot refer to the moment used to calculate the r^{α}_{ij}. When there is no superscript on the label, the nearest superscript to the left is to be inferred. Most of the moments differ very little in value between Regions I, III, and IV. However, for r^5_{00}, r^5_{11}, $1/\sqrt{1-\epsilon^2}$, and b, the value in Region IV significantly differs from both that in Region I and that in Region III.

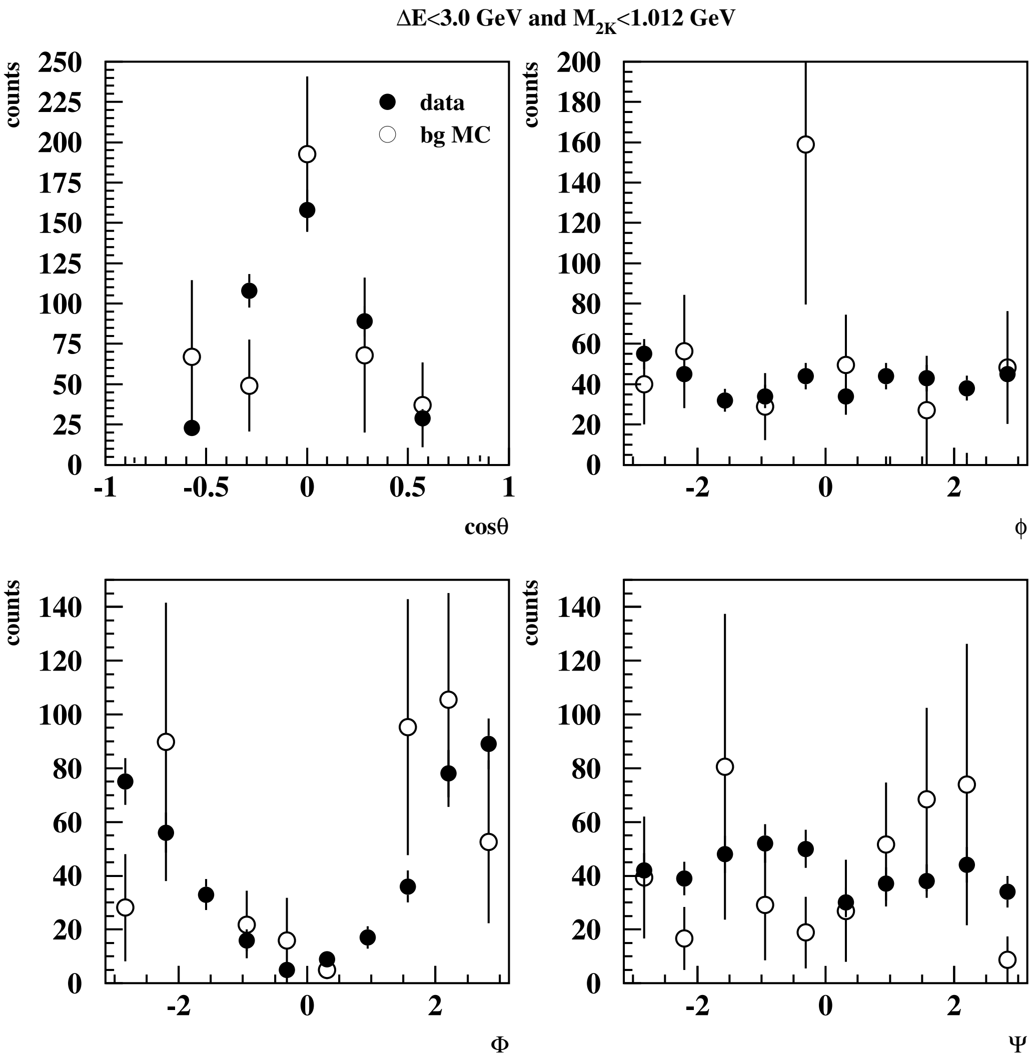

Figure 4.9. The distributions of data and the non-diffractive MC model used for the ρ^0 r^{α}_{ij} background correction in the region $\Delta E < 3.0\,\mathrm{GeV}$ and $M_{2K} < 1.012\,\mathrm{GeV}$. The error bars indicate the statistical uncertainty. Within the limited MC statistics presently available, the MC agrees with the data, in particular, the events are clustered at $\cos\theta \approx 0$ and at $\Phi = \pm\pi$. In order to facilitate comparison with the ρ^0 background MC, the decay angles in these plots were computed in the ρ^0 center-of-mass frame.

agreement between the data and the MC is comparable in the other regions of the $(\Delta E, M_{2K})$ phase space.

Region I and Region III are sidebands on either side of the ϕ peak in the M_{2K} distribution, of equal width as the ϕ data sample. To estimate the total amount of background in Region II, we take the average number of counts in Region I and Region III divided by the number of counts in Region II, which yields an estimate of $\approx 14\%$. Recall that the estimate of the DIS-fragmentation process for the background contaminating the ϕ mesons is $\approx 9\%$. The size of the background varies in Q^2 from 10-19% from the lowest to the highest Q^2 bins. It varies in $-t'$ from 11-19%, and in $\sqrt{W^2}$ from 20-10%. The distribution of data as a function of ΔE can be seen in Figure 4.10, where the crosses represent the data in the ϕ peak, and the circles represent the data in the sidebands, normalized to 14% underneath the exclusive peak.

To estimate the shape of the background, we combine the shapes from Region I and Region III with equal weights. So, in terms of histogram bins, j,

$$N_j^{bg} = B \times \left(N_j^I + \frac{N_{tot}^I}{N_{tot}^{III}} N_j^{III} \right), \tag{4.25}$$

where $N_{tot}^{I(III)}$ is the total number of counts in Region I (III), and B is the overall normalization such that $\sum_j N_j^{bg} / \sum_j N_j = 0.14$. Examples of uncorrected data and the background correction, N_j and N_j^{bg}, can be seen in Figure 4.11 for three of the spin-density matrix elements which are measured in this work to be significantly different from zero. In order to correct the data for the non-exclusive background, we subtract it from the data:

$$N_j^{bg\ corr} = N_j - N_j^{bg}. \tag{4.26}$$

The size of the effect of the background correction on each of the spin-density matrix elements is tabulated in Table 4.3. The effect of the background correction on r_{ij}^{α} is

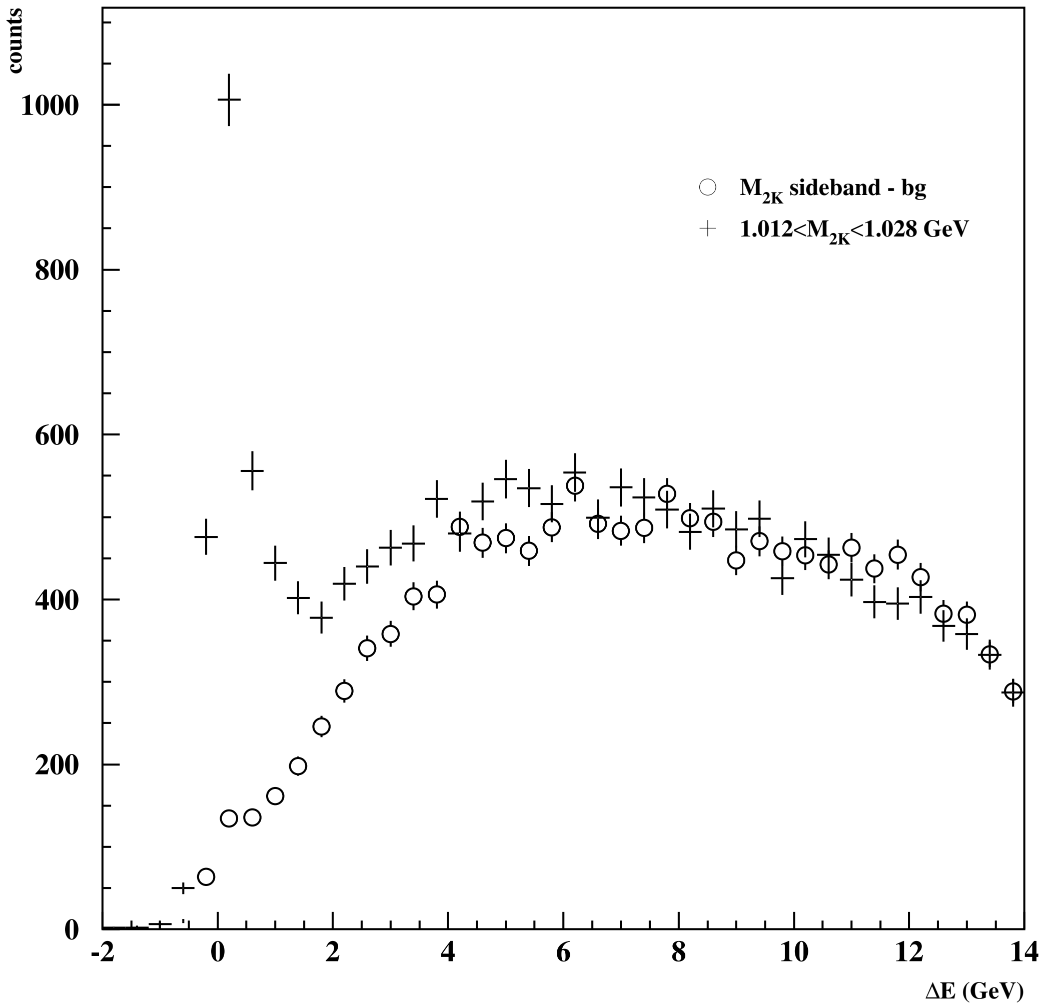

Figure 4.10. The distribution of data as a function of ΔE. The error bars indicate the statistical uncertainty. The crosses represent the data in the ϕ mass region: $1.012 < M_{2K} < 1.028\,\mathrm{GeV}$, while the circles represent the data in sidebands of M_{2K}. The sideband data are normalized to 14% of the data in the region $\Delta E < 1.0\,\mathrm{GeV}$.

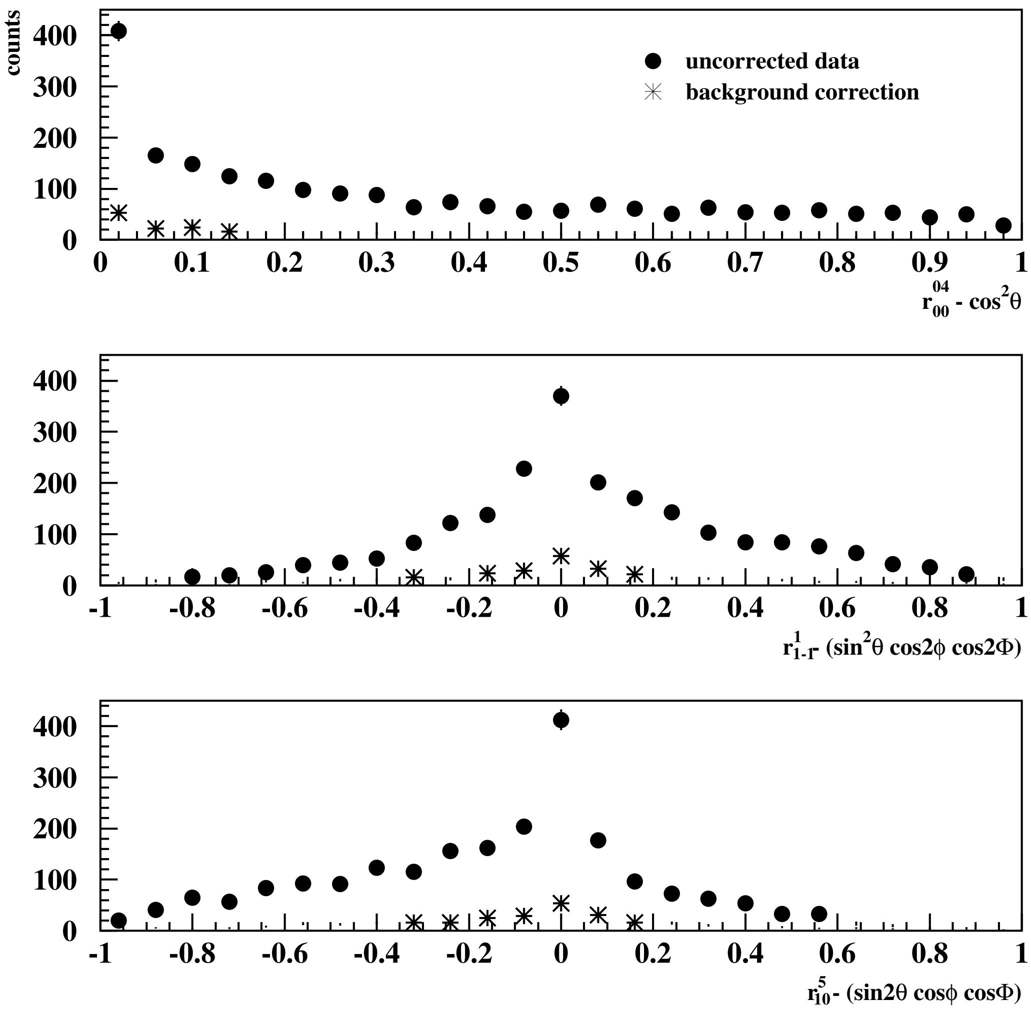

Figure 4.11. The distributions of data and the non-exclusive background correction used to compute the spin-density matrix elements r^{04}_{00}, r^{1}_{1-1}, and $\mathrm{Re}(r^{5}_{10})$. The bars on the points represent the statistical uncertainty. The background is normalized to $\approx 14\%$ of the data, integrated over the entire range.

Table 4.3. The effect of the background correction on the spin-density matrix elements. The size column is the difference in r_{ij}^{α} evaluated with and without the background correction: r_{ij}^{α}(with bg)$-r_{ij}^{\alpha}$(without bg), where r_{ij}^{α}(without bg) are from Table 4.2. The % uncertainty is the absolute value of this difference divided by the final values for r_{ij}^{α} in this thesis, that is, the values after having been corrected for all the effects described in the present section, Table 4.7. The large size of the % effect for several of the matrix elements is due to the small values of the matrix elements, themselves.

r_{ij}^{α}	size	%	r_{ij}^{α}	size	%
r_{00}^{04}	-0.008	3	$\mathrm{Im}(r_{10}^{3})$	-0.002	9
r_{1-1}^{1}	0.026	8	$\mathrm{Im}(r_{1-1}^{3})$	-0.014	16
$\mathrm{Im}(r_{1-1}^{2})$	-0.035	13	$\mathrm{Im}(r_{10}^{7})$	-0.009	29
$\mathrm{Re}(r_{10}^{5})$	0.014	10	$\mathrm{Im}(r_{1-1}^{7})$	0.028	19
$\mathrm{Im}(r_{10}^{6})$	-0.017	10	r_{11}^{8}	0.011	33
$\mathrm{Re}(r_{10}^{04})$	-0.004	21	r_{00}^{8}	-0.011	22
r_{1-1}^{04}	0.001	9	$\mathrm{Re}(r_{10}^{8})$	-0.014	39
r_{11}^{1}	-0.005	18	r_{1-1}^{8}	-0.006	10
r_{00}^{1}	0.001	4			
$\mathrm{Re}(r_{10}^{1})$	0.007	74			
$\mathrm{Im}(r_{10}^{2})$	-0.009	1421			
r_{11}^{5}	-0.014	64			
r_{00}^{5}	-0.003	10			
r_{1-1}^{5}	-0.002	12			
$\mathrm{Im}(r_{1-1}^{6})$	-0.005	21			

estimated to be $< 10\%$ for the r_{ij}^{α} which are measured to be significantly different from zero, and smaller than the statistical uncertainty for the other r_{ij}^{α}.

Since N_j and N_j^{bg} come from independent sets of data, we can compute the statistical uncertainty of $N_j^{bg\ corr}$ by adding their statistical uncertainties in quadrature,

$$\delta N_j^{bg\ corr} = \sqrt{(\delta N_j)^2 + (\delta N_j^{bg})^2}, \tag{4.27}$$

where we estimate the uncertainty on the number of counts in a given bin from counting statistics, so $\delta N_j = \sqrt{N_j}$ and $\delta N_j^{bg} = \sqrt{N_j^{bg}}$.

4.2.2 The Acceptance Correction Now our exclusive ϕ data sample needs to be corrected for effects coming from the limited acceptance of the spectrometer. We write the acceptance corrected data in terms of the background corrected data in the form

$$N_j^{acc\ corr} = A_j\, N_j^{bg\ corr}, \tag{4.28}$$

where $N_j^{bg\ corr}$ is from Equation 4.26, and A_j is the acceptance correction. Correlations between the angular variables in the acceptance require that the acceptance correction be performed simultaneously in the three variables $\cos\theta$, φ, and Φ. In Figures 4.12, 4.13, and 4.14 are the data events as scatter plots of $\cos\theta$ vs. φ, Φ vs. φ, and Φ vs. $\cos\theta$, respectively. The acceptance does not create any "holes" in the data, so that entire phase space of the angular variable can be used in the method of moments. It has been checked that the values of the moments of the acceptance corrected histograms change negligibly under a change of the number of angular bins, j.

In expression 4.28, A_j represents the ratio of the number of events expected in bin j, in the absence of any spectrometer effects, divided by the number of events

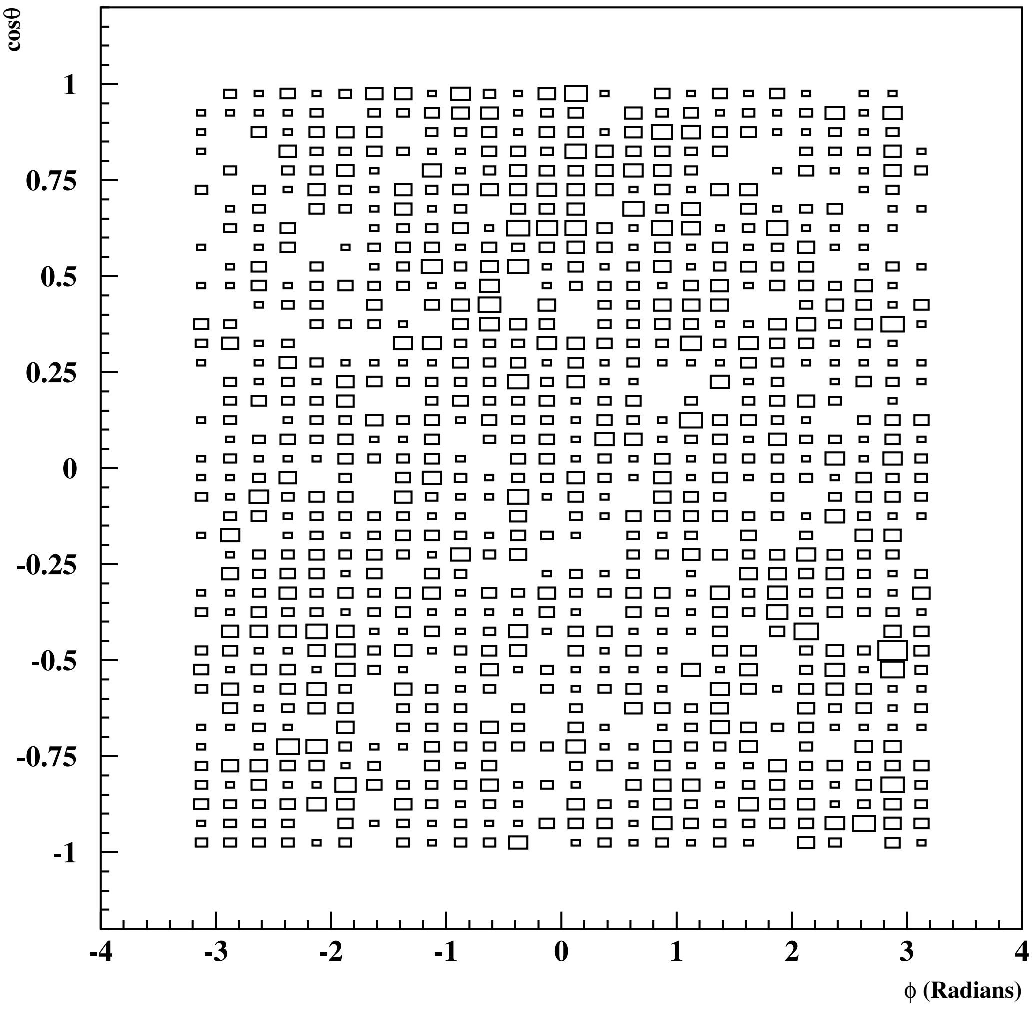

Figure 4.12. Exclusive ϕ events in a scatter plot of $\cos\theta$ vs. φ. In this plot, the size of the box indicates the number of counts in the bin relative to the other boxes. The entire phase space is very well covered by the data.

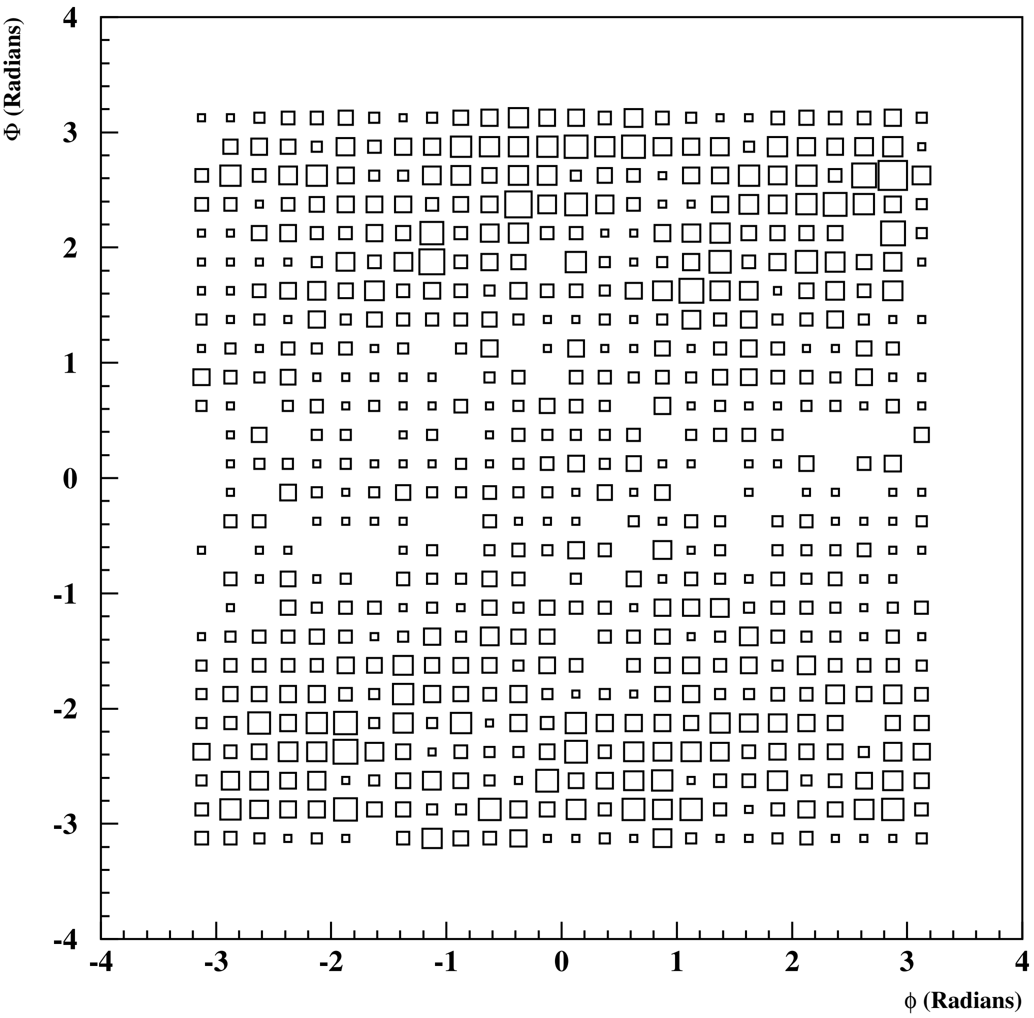

Figure 4.13. Exclusive ϕ events in a scatter plot of Φ vs. φ. Although there are fewer data along the contour $\Phi = 0$, there are enough to correct with the acceptance correction form of Equation 4.28. The suppression of data along $\Phi = 0$ will be discussed in Section 4.2.4.

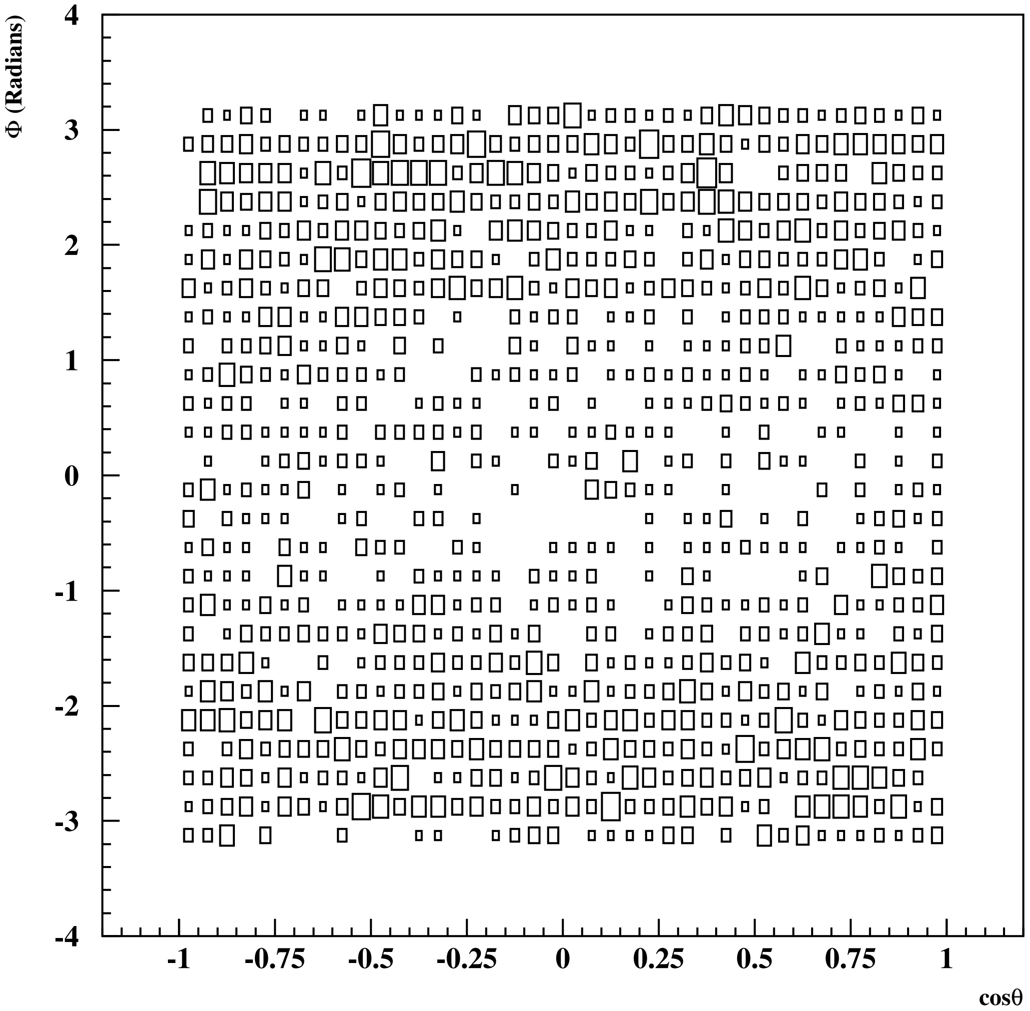

Figure 4.14. Exclusive ϕ events in a scatter plot of Φ vs. $\cos\theta$. As in Figure 4.13, there are fewer data along the contour $\Phi = 0$. However, there are enough to correct with the acceptance correction form of Equation 4.28.

actually observed in bin j:

$$A_j = \frac{N_{expected,j}}{N_{observed,j}}. \tag{4.29}$$

For this analysis, A_j will be determined using Monte Carlo (MC) techniques. MC events which are not affected by spectrometer effects are called generated MC events, $N_{gen,j}$. These events are generated according to a physics generator, in which is parameterized the dependence of the data on all of the kinematic variables. Details on the parameterization are given in Section 4.2.3. In Section 4.2.4, we describe the effects of the limited acceptance of the HERMES spectrometer on the distributions of decay distribution angular variables. The events which have passed through HMC and the analysis criteria are called the accepted MC events, $N_{acc,j}$. In terms of $N_{gen,j}$ and $N_{acc,j}$, the acceptance correction is given by

$$A_j = \frac{N_{gen,j}}{N_{acc,j}}. \tag{4.30}$$

Examples of the acceptance correction for three of the spin density matrix elements can be seen in Figure 4.15. Note that, given enough MC counts, the absolute normalization of the acceptance correction is unimportant, as it cancels in the evaluation of the moment, Equation 4.24.

The effect of the acceptance correction on the values of the spin density matrix elements are tabulated in Table 4.4. The acceptance correction is the largest correction performed on the data in this analysis. In particular, the values of $\mathrm{Re}(r^{04}_{10})$, $\mathrm{Re}(r^{1}_{10})$, $\mathrm{Im}(r^{2}_{10})$, r^{5}_{00}, r^{5}_{11}, and $\mathrm{Im}(r^{6}_{1-1})$, which were not zero before the acceptance correction, become consistent with zero after the acceptance correction.

To estimate the statistical uncertainty of the acceptance corrected data, we assume that the acceptance is known perfectly, so that the acceptance correction is simply a scale factor:

$$\delta N_j^{acc\ corr} = A_j\, \delta N_j^{bg\ corr}. \tag{4.31}$$

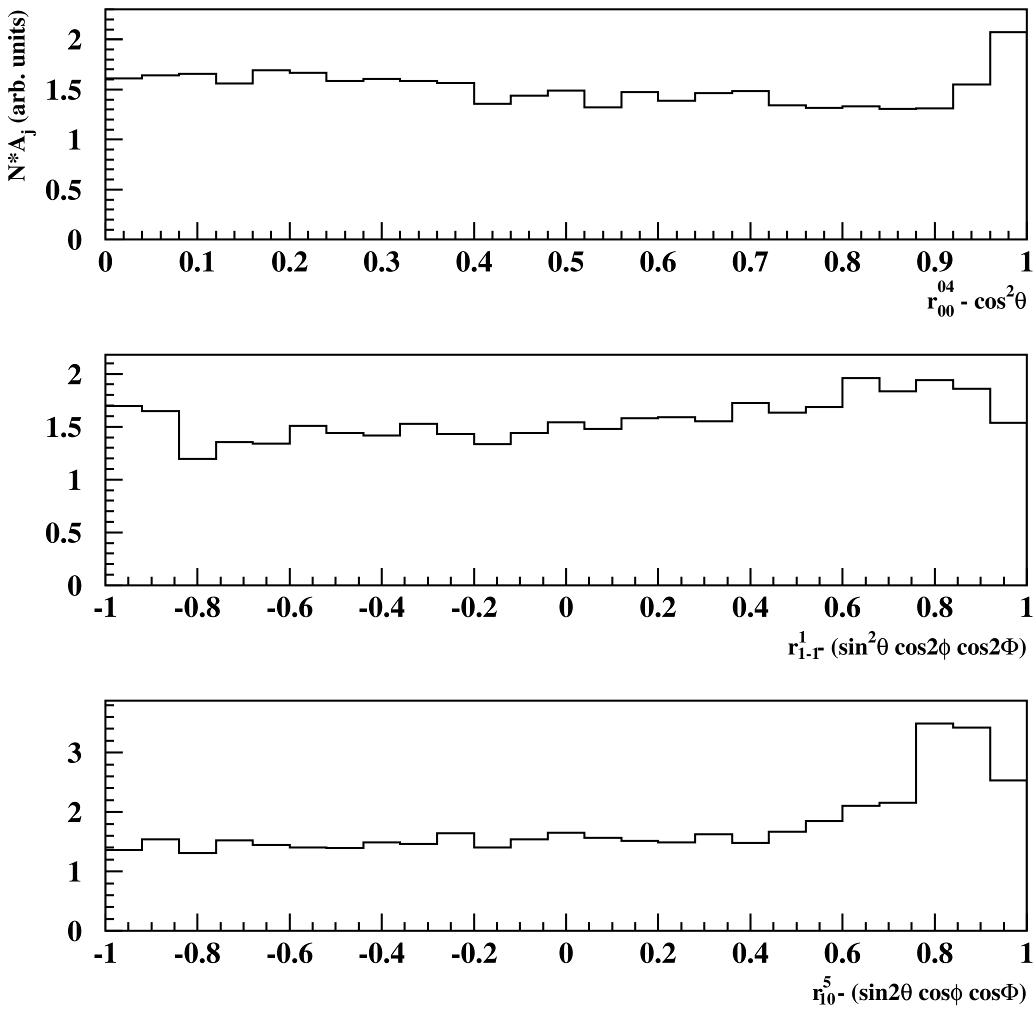

Figure 4.15. The distributions of the acceptance correction for the spin density matrix elements r^{04}_{00}, r^{1}_{1-1}, and $\mathrm{Re}(r^{5}_{10})$. As it drops out of the calculation of the mean, the overall normalization of the acceptance correction is arbitrary. The increase in the r^{04}_{00} acceptance correction at $\cos^2\theta = 1$ is due to the inability of the tracking algorithm to distinguish barely separated tracks in the front region. The increase in the $\mathrm{Re}(r^{5}_{10})$ acceptance correction is due to the correlations of the acceptance of the spectrometer in $\psi = \varphi - \Phi$. See Subsection 4.2.4.

Table 4.4. The effect of the acceptance correction on the spin-density matrix elements. The size column is the difference in the background corrected r_{ij}^{α} evaluated with and without the acceptance correction: $r_{ij}^{\alpha}(\text{with})-r_{ij}^{\alpha}(\text{without})$. The % uncertainty is the absolute value of this difference divided by the final values for r_{ij}^{α} in this thesis, from Table 4.7.

r_{ij}^{α}	effect	%	r_{ij}^{α}	effect	%
r_{00}^{04}	-0.034	11	$\mathrm{Im}(r_{10}^{3})$	-0.003	16
r_{1-1}^{1}	0.081	26	$\mathrm{Im}(r_{1-1}^{3})$	0.012	14
$\mathrm{Im}(r_{1-1}^{2})$	-0.067	24	$\mathrm{Im}(r_{10}^{7})$	0.002	8
$\mathrm{Re}(r_{10}^{5})$	-0.024	17	$\mathrm{Im}(r_{1-1}^{7})$	-0.011	8
$\mathrm{Im}(r_{10}^{6})$	0.004	3	r_{11}^{8}	-0.015	47
$\mathrm{Re}(r_{10}^{04})$	0.076	433	r_{00}^{8}	0.012	23
r_{1-1}^{04}	0.011	94	$\mathrm{Re}(r_{10}^{8})$	0.009	24
r_{11}^{1}	0.048	164	r_{1-1}^{8}	-0.018	31
r_{00}^{1}	-0.014	59			
$\mathrm{Re}(r_{10}^{1})$	-0.086	886			
$\mathrm{Im}(r_{10}^{2})$	0.110	16645			
r_{11}^{5}	0.150	685			
r_{00}^{5}	0.101	369			
r_{1-1}^{5}	-0.027	166			
$\mathrm{Im}(r_{1-1}^{6})$	0.022	85			

Uncertainty in the acceptance correction comes from the imprecision with which we model the data and the spectrometer. We will estimate the systematic uncertainty from our ignorance of the acceptance correction, including smearing, in Subsection 4.3.3.

4.2.3 Acceptance Correction: Model Assumptions The exclusive ϕ data sample is made up of three track $(e^+K^+K^-)$ events, the features of which we would like to mimic in our MC simulation. In Chapter 2, a lot of the machinery was discussed that describes the electroproduction and decay of ϕ mesons. We will use that machinery here for the model in our generator.

First, we need to specify the positron characteristics measured by the HERMES spectrometer, namely, its energy and momentum direction. The positron kinematic variables (E', $\cos\theta_e$, and φ_e) are generated with probability given by the differential virtual photoproduction cross-section of Hand, Equation 2.17, in the lab frame:

$$\frac{d\sigma}{dE'\,d\cos\theta_e\,d\varphi_e} = \Gamma_T\sigma_T(1+\epsilon R),$$

where the transverse photon flux is given by

$$\Gamma_T = \frac{\alpha}{4\pi^2}\frac{W^2-M_p^2}{2M_p}\frac{1}{Q^2}\frac{E'}{E}\frac{2}{1-\epsilon},$$

and the cross-section ratio, $R = \sigma_L/\sigma_T$, is given in terms of the longitudinal polarization of the ϕ, assuming SCHC, from Equation 2.74. The Q^2 dependence of the total cross-section is described by the modified VMD calculation of Hüfner and Kopeliovich, Equation 2.62,

$$\sigma_T(Q^2,W^2) = \sigma(Q^2=0,W^2)\left(\frac{1}{1+Q^2/M_\phi^2}\right)^2\left(\frac{M_{\phi'}^2-M_\phi^2}{M_{\phi'}^2-Q^2}\right)^2,$$

where $M_{\phi'} = 1.680\,\mathrm{GeV}$ and $M_\phi = 1.019\,\mathrm{GeV}$ from the Particle Data Group. The W^2 dependence of the total real photoproduction cross-section is given by the Regge fit in [18]: $\sigma(W^2) \sim \left(\sqrt{W^2}\right)^{0.32}$. The distribution of events as a function of the lepton variables Q^2, $\sqrt{W^2}$, and φ_e for the background corrected data and accepted MC events are in Figure 4.16. The accepted MC distributions agree very well with the background corrected data.

Next, we need to specify the energy and the momentum direction of the ϕ. The total amount of energy in the di-kaon system is M_{2K}, which is generated according to the relativistic p-wave Breit-Wigner resonance distribution described in the caption of Figure 4.3:

$$\frac{dN_\phi}{dM_{2K}} \propto \frac{M_{2K}M_\phi\Gamma}{(M_{2K}^2-M_\phi^2)^2+M_\phi^2\Gamma^2}, \tag{4.32}$$

where $M_\phi = 1.019\,\mathrm{GeV}$ and $\Gamma = 0.004\,\mathrm{GeV}$ from the Particle Data Group. The distribution of events as a function of M_{2K} for the data and accepted MC events are in Figure 4.17. The accepted MC distribution agrees well with the data in the ϕ mass region.

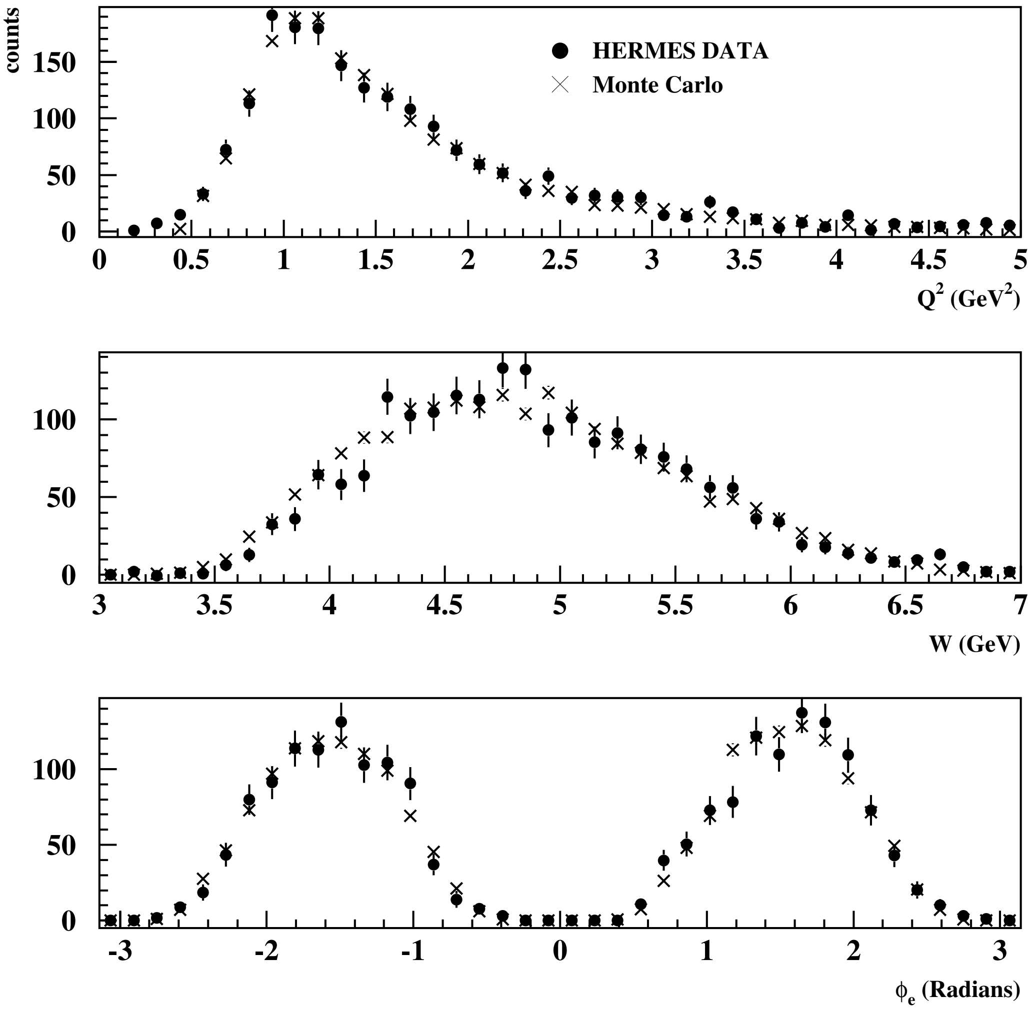

Figure 4.16. The distributions of the background corrected exclusive ϕ data and the accepted MC events used for the acceptance correction as a function of positron variables Q^2, $\sqrt{W^2}$, and φ_e. The MC has been normalized to have an equal number of counts as the data. The accepted MC distributions agree very well with the background corrected data, lending confidence to both the model used to parameterize the data and the model of the acceptance used.

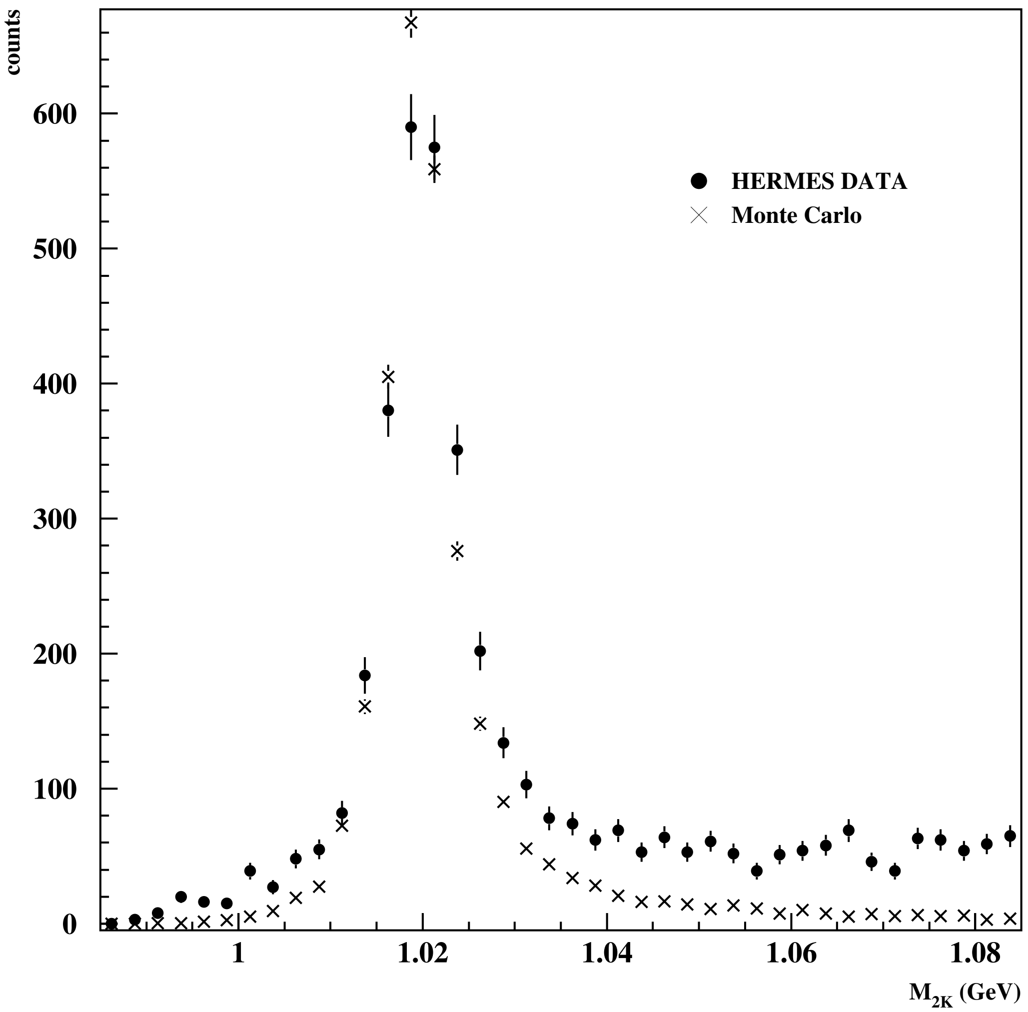

Figure 4.17. The distribution of exclusive ϕ data and the accepted MC events used for the acceptance correction as a function of the di-kaon mass, M_{2K}. The MC has been normalized to have an equal number of counts as the data in the ϕ mass region. The accepted MC distribution agrees well with the data in the ϕ mass region, lending confidence to both the model used to parameterize the data and the model of the acceptance used. Note that these data have not been corrected for non-exclusive background.

The polar production angle of the ϕ relative to the virtual photon is generated diffractively, *i.e.* implicitly according to an exponential in t', Equation 2.59:

$$\frac{dN}{d\,|t'|} \propto \left(\frac{\sigma_A}{\sigma_p} b_A\, e^{-b_A |t'|} + b_p\, e^{-b_p |t'|} \right),$$

where $\sigma_A/\sigma_p = 0.22$ is the ratio of total cross-sections to scatter coherently from the nucleus and incoherently from nucleons. $b_A = 34\,\mathrm{GeV}^{-2}$ is the coherent and $b_p = 3.81\,\mathrm{GeV}^{-2}$ is the incoherent slope parameter. These values were determined by iteratively fitting in the regions $|t'| < 0.05\,\mathrm{GeV}^2$ (with fixed b_p), to determine b_A and σ_A/σ_p, and $|t'| > 0.05\,\mathrm{GeV}^2$ (with fixed σ_A/σ_p and b_A), to determine b_p. The distribution of events as a function of $-t'$ for the data and accepted MC events are in Figure 4.18. The accepted MC distribution agrees well with the background corrected data.

The azimuthal production angle of the ϕ around the virtual photon is given by Φ, defined in the helicity frame in Figure 2.3. The back-to-back decay of the ϕ into the K^+K^- in the center-of-mass frame completely restricts the energy and angles of the K^-, once the ϕ characteristics have been determined. The energy of the K^+ is also restricted. The final two quantities used to describe the measured final state are the polar and azimuthal decay angles of the K^+, $\cos\theta$ and φ, defined in the ϕ center-of-mass frame in Figure 2.4. The distribution of MC events in the angles $\cos\theta$, φ, and Φ, depend on the input spin-density matrix elements, r^{α}_{ij}.

It turns out that the acceptance correction depends on the input values of r^{α}_{ij} assumed in the acceptance correction, values *a priori* unknown, values which we are attempting to determine here. Therefore, we use an iterative procedure to converge on the appropriate values to use for r^{α}_{ij} in the acceptance correction. Initially, a correction is computed, assuming a flat angular dependence as a function of $\cos\theta$, φ, Φ, and $\psi = \varphi - \Phi$, that is, with $r^{04}_{00}= 0.33$ and all other $r^{\alpha}_{ij}= 0$. Using this acceptance correction, a set of r^{α}_{ij} is extracted that is used as the input values to generate the next acceptance correction. By this iteration procedure, the correction

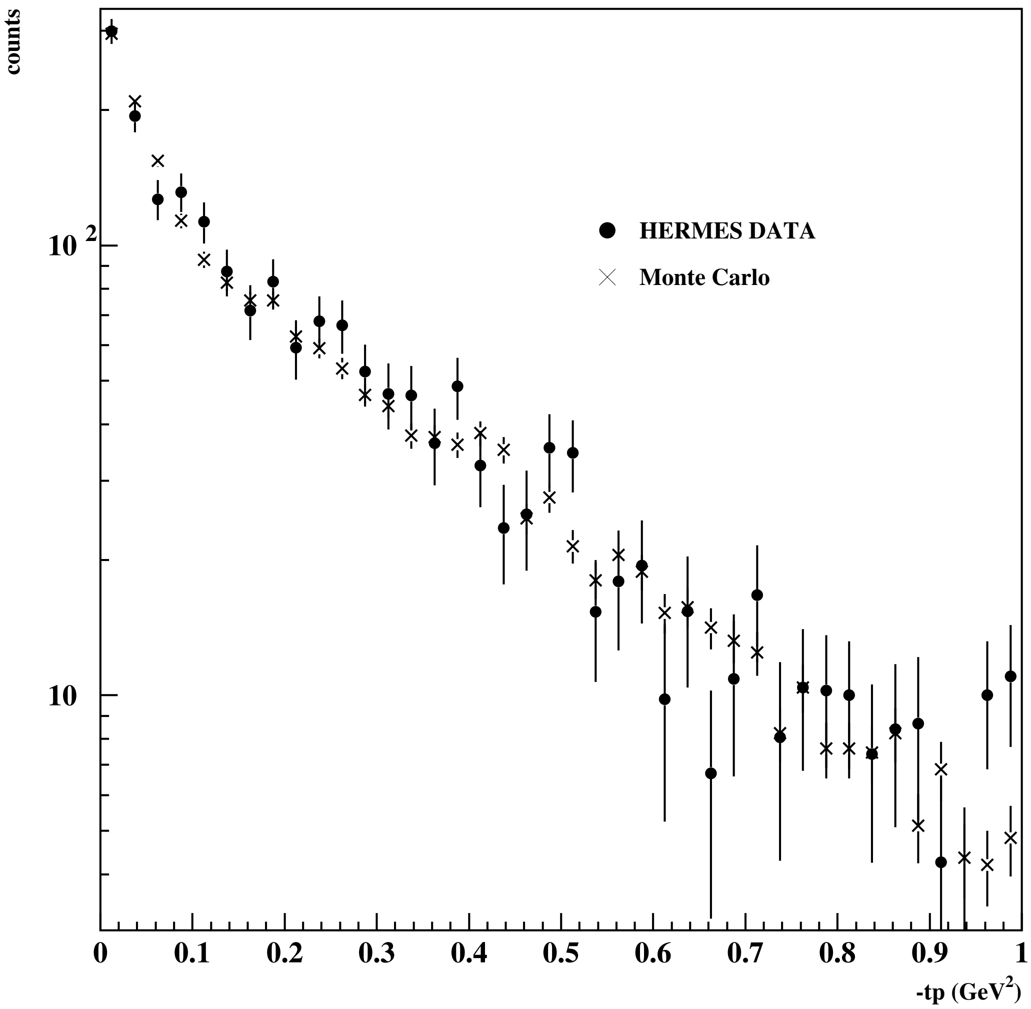

Figure 4.18. The distribution of background corrected exclusive ϕ data and the accepted MC events used for the acceptance correction as a function of the momentum transfer, $-t'$. The MC has been normalized to have an equal number of counts as the data. The accepted MC distribution agrees well with the background corrected data.

quickly converges to a stable set of values for r_{ij}^{α}, as can be seen in Figure 4.19.

MC events are generated in the angles $\cos\theta$, φ, and Φ, according to the decay angular distribution, $W(\cos\theta, \varphi, \Phi)$, from Equation 2.31, with the parameters r_{ij}^{α} given by the average values of r_{ij}^{α}, averaged over iteration numbers 2-5 in Figure 4.19. The distributions of events as functions of the angular variables $\cos\theta$, φ, Φ, and ψ (see the text surrounding Equation 2.69) for the data and accepted MC events are in Figure 4.20. The accepted MC distributions agree well with the data.

We would like to show that the values of r_{ij}^{α} to which the above iterative procedure converges are, in fact, the correct values that describe the data. To demonstrate this, we generate a set of exclusive ϕ MC "data" with r_{ij}^{α} values significantly different from the final results of the present analysis in Table 4.29. After three iterations, the extracted values of r_{ij}^{α} from the MC "data" are consistent with the input values within the statistics of the MC simulation, as can be seen in Table 4.5. The χ^2 of the extracted values from the input values is 39.4 for 23 degrees of freedom. This lends confidence to the entire acceptance correction procedure. The systematic uncertainty due to the ignorance of the parameterization of the data in the acceptance correction will be estimated in Subsection 4.3.3.

In this analysis, a total of 2.8×10^4 generated MC exclusive ϕ events are used in the acceptance correction.

4.2.4 Acceptance Correction: Spectrometer Effects In the previous section, we generated a sample of exclusive, diffractive $(e, e'\phi \to K^+K^-)$ MC events in 4π, of which we would like to see the effects from our measurement with the HERMES spectrometer. The considerable effort of some members of the HERMES collaboration has gone into modeling the response and geometrical features of the spectrometer, resulting in the HERMES Monte Carlo (HMC) program. It is described in Reference [77] and elsewhere. It is based on the GEANT package, wherein the passage of high-energy particles through matter is modeled. In this work, the

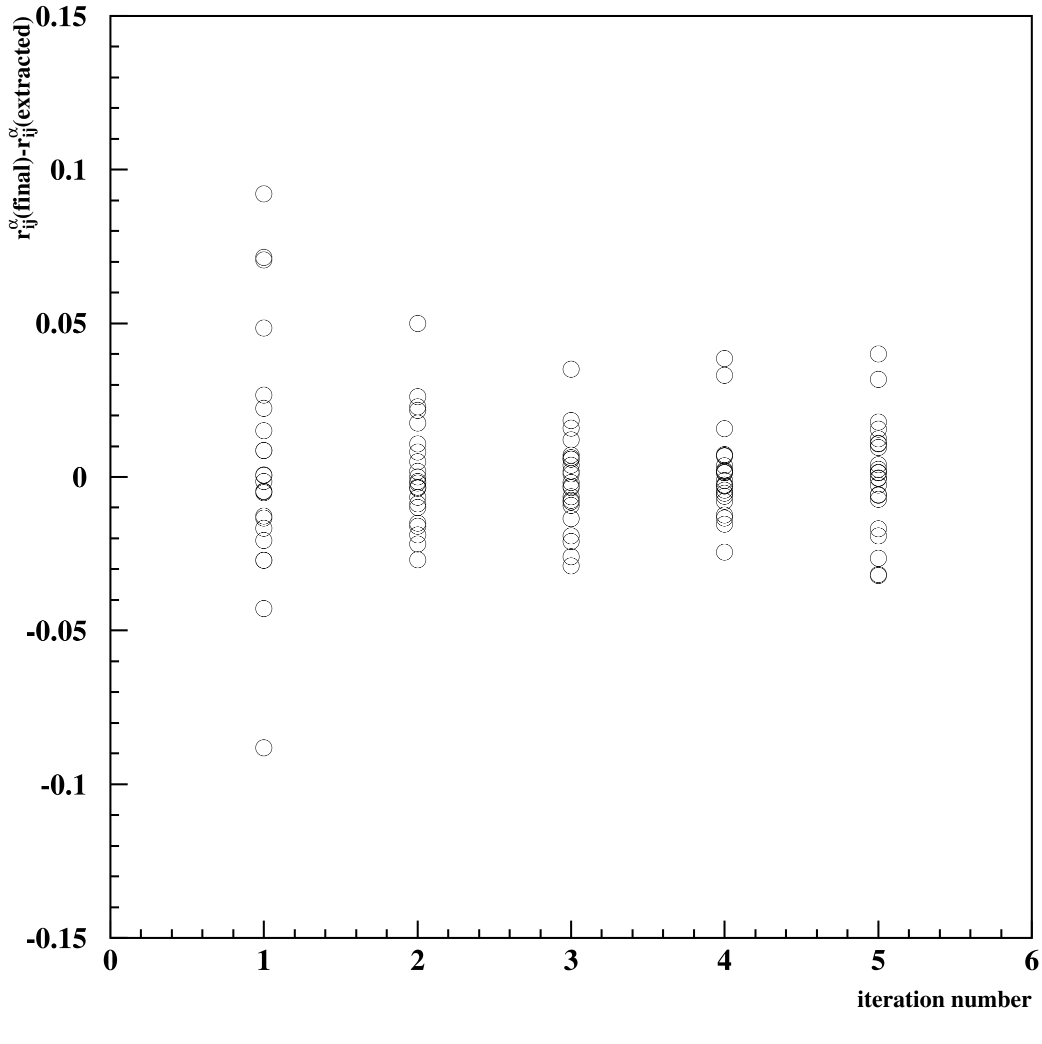

Figure 4.19. The difference between the extracted and final values of r_{ij}^{α} as a function of number of iterations of the acceptance correction. The first set of r_{ij}^{α}'s (iteration number=1) is extracted assuming an isotropic distribution of $(\cos\theta, \varphi, \Phi)$ in the acceptance correction. The vertical spread of the difference between the extracted and final values quickly shrinks and stays at a constant value, indicating convergence.

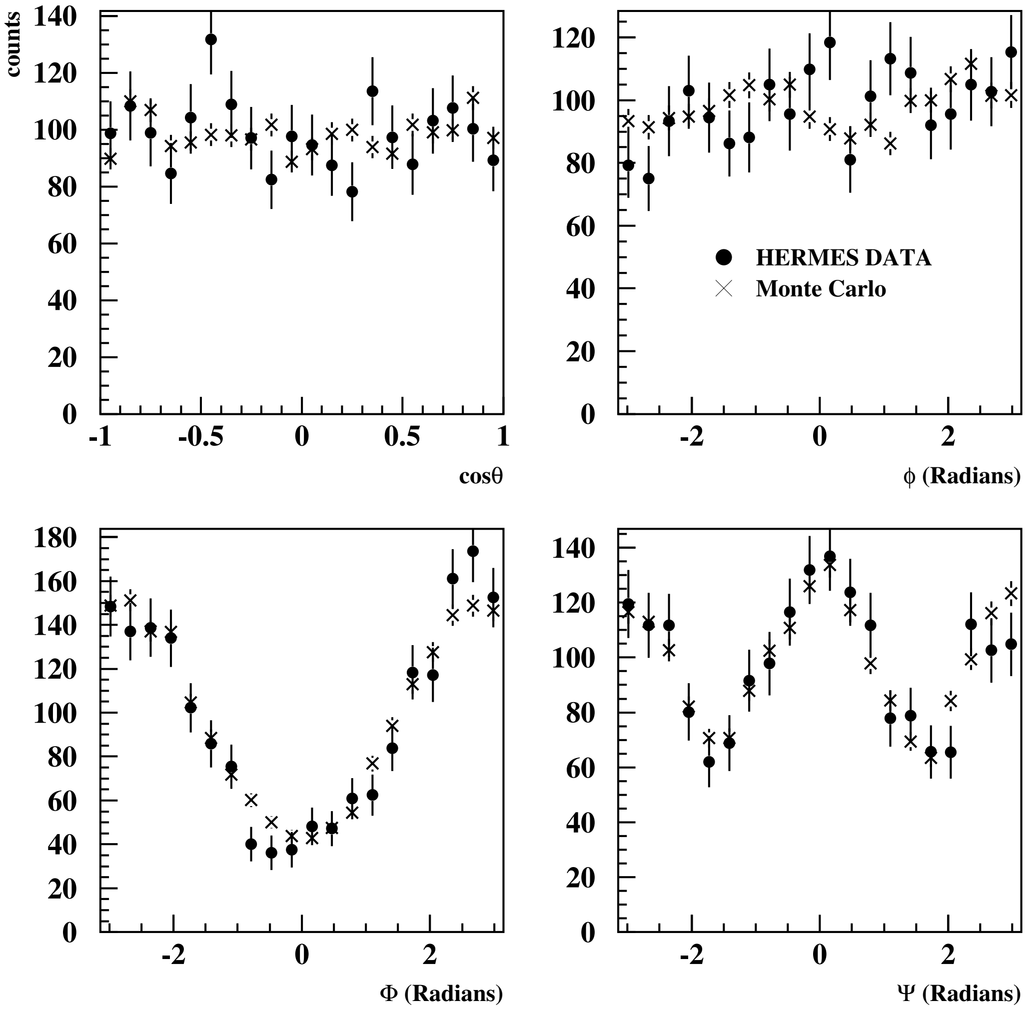

Figure 4.20. The distribution of background corrected exclusive ϕ data and the final set of accepted MC events used for the acceptance correction as a function of the decay angles, $\cos\theta$ and φ, the azimuthal production angle Φ, and $\psi = \varphi - \Phi$. The MC has been normalized to have an equal number of counts as the data. The accepted MC distributions agree well with the background corrected data.

Table 4.5. Comparison of the input and extracted values of r^{α}_{ij} for MC data. Note that although the input values of some of the matrix elements are significantly different from those extracted with real data, the acceptance correction procedure manages to converge to the correct values. A total of 2.3×10^3 MC events are used for these MC data.

r^{α}_{ij}	input	extracted	r^{α}_{ij}	input	extracted
r^{04}_{00}	0.045	0.451 ± 0.017	$\mathrm{Im}(r^{3}_{10})$	0.	0.041 ± 0.024
r^{1}_{1-1}	-0.200	-0.179 ± 0.023	$\mathrm{Im}(r^{3}_{1-1})$	0.	-0.023 ± 0.032
$\mathrm{Im}(r^{2}_{1-1})$	0.100	0.115 ± 0.023	$\mathrm{Im}(r^{7}_{10})$	0.	0.102 ± 0.036
$\mathrm{Re}(r^{5}_{10})$	-0.010	-0.009 ± 0.008	$\mathrm{Im}(r^{7}_{1-1})$	0.	-0.050 ± 0.047
$\mathrm{Im}(r^{6}_{10})$	0.050	0.051 ± 0.008	r^{8}_{11}	0.	-0.021 ± 0.079
$\mathrm{Re}(r^{04}_{10})$	0.	0.002 ± 0.010	r^{8}_{00}	0.	-0.021 ± 0.111
r^{04}_{1-1}	0.	-0.005 ± 0.013	$\mathrm{Re}(r^{8}_{10})$	0.	0.064 ± 0.037
r^{1}_{11}	0.	-0.029 ± 0.037	r^{8}_{1-1}	0.	0.030 ± 0.050
r^{1}_{00}	0.	0.079 ± 0.052			
$\mathrm{Re}(r^{1}_{10})$	0.	-0.029 ± 0.018			
$\mathrm{Im}(r^{2}_{10})$	0.	0.037 ± 0.017			
r^{5}_{11}	0.	-0.031 ± 0.018			
r^{5}_{00}	0.100	0.123 ± 0.025			
r^{5}_{1-1}	0.	-0.029 ± 0.011			
$\mathrm{Im}(r^{6}_{1-1})$	0.	-0.010 ± 0.011			

HMC version used was `84b8`, available on the `/hermes/r10/` software release.

A simple estimate of the effect of the septum plate on the yield of diffractive ϕ's can be made with a Monte Carlo simulation by comparing the total number of isotropically generated exclusive ϕ events to the number of these events which satisfy the constraints that the particles be within a "box" acceptance. In our kinematic range, $0.5 < Q^2 < 5.0\,\mathrm{GeV}^2$, approximately 25% of the exclusive, diffractive ϕ events have the scattered positron within the box. Of these, approximately 45% of the events have one of the $K^{\pm}$ pair within the box. Of these, approximately 55% have both the K^+ and the K^- within the box.

We actually want to understand the effects of the spectrometer acceptance on the ϕ decay angular distribution, which is a more complicated endeavor. The distribution is written in terms of the azimuthal production angle, Φ, and the decay angles, $\cos\theta$ and φ. The acceptance of the spectrometer available to detect the ϕ

changes from event to event, depending on both the polar and azimuthal scattering angle of the positron, as well as the polar scattering angle, t', of the ϕ relative to the γ^*. The acceptance of the spectrometer is well modeled in HMC, given the good agreement between the kinematic distributions of background corrected data and accepted MC events in Figures 4.16 through 4.20. To understand in detail how the HERMES acceptance affects the measured angular distributions, it is instructive to observe its effects on MC distributions generated isotropically in $(\cos\theta, \varphi, \Phi)$. Running HMC on an isotropically generated sample of MC events results in the one-dimensional distributions of isotropic accepted MC events in Figure 4.21.

The suppression of events near $\Phi = 0$ is a result of the septum plate which separates the top and bottom halves of the spectrometer. The case $\Phi = 0$ corresponds physically, in the helicity frame, to the case where the direction of the scattered e' relative to the initial e is the same as the direction of the ϕ relative to the γ^*. See the definition of Φ, Equation 2.9. As mentioned in Section 2.1.1, Φ has the same value when evaluated in the lab frame as it does in the helicity frame, where it is defined. Therefore, we ponder the case $\Phi = 0$ directly in the lab frame. The majority of detected positron events occurs at small angles around the beam pipe, so that a large portion of HERMES data comes from events with the e' detected directly above or below the beam pipe. We look at the case where the e' is scattered up relative to the beam pipe, into the acceptance of the upper spectrometer. The virtual photon emitted is emitted down, towards the acceptance of the lower spectrometer. The case $\Phi = 0$, then, means that the ϕ is produced up, relative to the γ^*, and hence, the decay K^+K^- pair will go up, towards the septum plate. The loss of such K^+K^- events into the septum plate leads to the observed suppression of events at $\Phi = 0$. This effect increases as $-t'$, the polar angle of the ϕ relative to the γ^*, increases.

This suppression of K^+K^- events at $\Phi = 0$ due to the septum plate also leads to the observed shape in the isotropic accepted MC $\psi = \varphi - \Phi$ distribution.

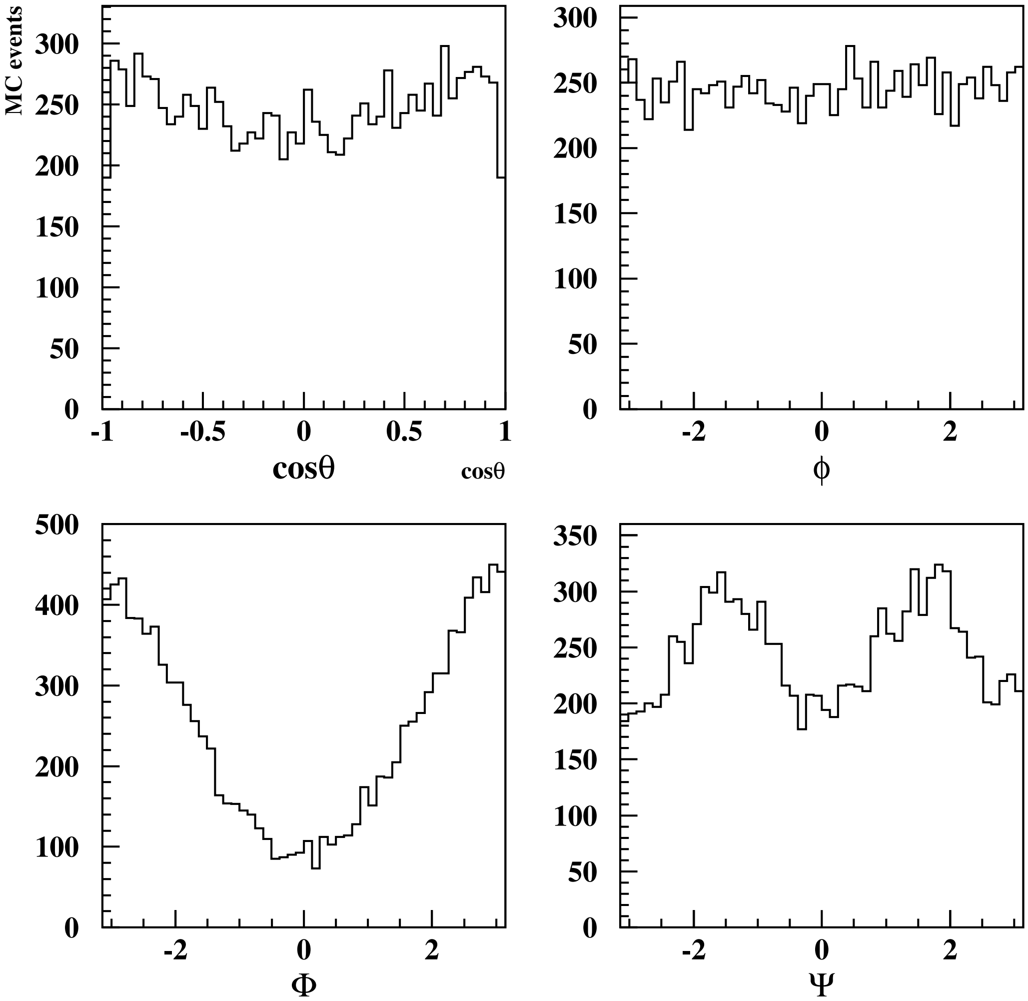

Figure 4.21. The distributions of isotropically generated MC events which have been accepted in the HERMES spectrometer. See text for details.

Picture, again, the same case where the e' scatters up into the spectrometer and $\Phi = 0$, so that the K^+K^- pair scatter up towards the septum plate. With $\Phi = 0$, ψ simply becomes $\psi = \varphi$, the azimuthal decay angle of the K^+. Assume that t' is small, so that the K^+K^- pair is going towards the upper edge of the lower half of the spectrometer acceptance. The only way for the spectrometer to detect both the K^+ and the K^- from this event is for the kaons to decay at angles such that they both miss the septum plate, that is, they must decay to the right and left at angles $\varphi = \pm\pi/2$. With $\Phi = 0$, this leads to the observed suppression of events at $\psi = 0, \pm\pi$.

The distribution of isotropic accepted MC events as a function of φ exhibits basically no effects due to acceptance. The aforementioned enhancement of events at $\varphi = \pm\pi/2$ results in an observable effect in the ψ distribution due to the interplay between φ, Φ, and the septum plate at $\Phi = 0$. This enhancement is not observed in the φ one-dimensional distribution directly, as the interplay between Φ and the septum plate only occurs at $\Phi = 0$, while the φ distribution is integrated over $-\pi < \Phi < \pi$, and so is washed out by the region $\Phi \neq 0$.

There are two features to note in the distribution of isotropic accepted MC events as a function of $\cos\theta$, namely, the suppression of events in the middle of the distribution around $\cos\theta \approx 0$, and the suppression of events at $\cos\theta = \pm 1$. In the lab frame, the events at $\cos\theta \approx 0$ correspond to those where the ϕ decays into a K^+K^- pair perpendicular to the direction of motion of the ϕ. In the lab, these events have the maximal spatial separation between the K^+ and the K^- allowed by kinematics. Therefore, the chance of losing one or the other out of the acceptance becomes observable. The events at $\cos\theta = \pm 1$ correspond to those where the $\phi \to K^+K^-$ decay is along the direction of motion of the ϕ in the lab frame. In the ϕ rest frame, where $\cos\theta$ is defined, the K^+ and K^- have equal and opposite momenta of $\approx 0.127\,\text{GeV}$. The boost from the ϕ rest frame to the lab frame (where E_ϕ is on the order of 10 GeV) is along the ϕ direction, and is large enough to fold the $K^{-(+)}$ momentum vector onto the $K^{+(-)}$ momentum vector in the lab frame, making them lay one on top of the other. The tracking algorithm is unable to distinguish two tracks which lay too close to each other in the front drift chamber. In this case, the event would not be tracked properly with our tracking algorithm, and such events would then be excluded from the analyzed data sample.

Note that the effect of smearing in the data from the spectrometer has already been included in our HMC acceptance correction, $N_{acc,j}$. Smearing is defined as the change of the values of the kinematic variables of a particle as it travels through the spectrometer on its way to detection. Smearing is due to interactions of the particle with the material that makes up the spectrometer, and manifests itself as either energy loss or multiple scattering through small angles, processes which have both been included into HMC, and are described by the Particle Data Group. We will need to estimate the systematic uncertainty on the smearing correction that is modeled in HMC, which will be done in Section 4.3.2.

In this analysis, a total of 1.2×10^4 accepted MC events in the exclusive ϕ region were used in the acceptance correction.

4.2.5 Radiative Effects In Subsection 2.1.3, the Born approximation is made, whereby the inelastic reaction $e + N \to e + \phi + N$ is assumed to take place via the exchange of a single virtual photon. In this section, we describe an estimate of the corrections to the deviations of the data from this assumption, called the radiative corrections. Our estimate comes from the output of the program `IDIFFRAD.F`, written by I. Akushevich. Of particular interest to the present decay angular distribution analysis is the calculation of the radiative corrections to the ϕ distribution as a function of Φ.

The model used in `IDIFFRAD.F` is described in Reference [80]. In Figure 4.22 are the lowest order Feynman diagrams of the observed electroproduction process.

The first diagram describes the Born amplitude, while the rest are corrections to this amplitude. The fourth and fifth diagrams describe the internal radiative corrections to the Born amplitude—internal in the sense that they have the same initial and final states as the Born amplitude, so that their contributions to the observed cross-section are added before squaring,

$$\begin{aligned} \sigma_{obs} &\sim |M_a + M_d + M_e|^2 \\ &\approx |M_a|^2 + 2M_a(M_d + M_e). \end{aligned} \tag{4.33}$$

The last two diagrams describe the external radiative corrections to the observed cross-section. These bremsstrahlung amplitudes do not have the same initial and final states as the Born amplitude, and so must be squared before their contribution can be added to that from internal amplitudes:

$$\sigma_{obs} \sim |M_a|^2 + 2M_a(M_d + M_e) + |M_b + M_c|^2. \tag{4.34}$$

Using QED, these terms are calculated, and the resulting observed cross-section takes the form,

$$\sigma_{obs} = \sigma_{Born} e^{\delta_{inf}} (1 + \delta_{VR} + \delta_{vac}) + \sigma_F, \tag{4.35}$$

where $e^{\delta_{inf}}(1 + \delta_{VR})$ represents the (infrared convergent) multiple soft photon radiation correction, δ_{vac} is the correction for the effects of vacuum polarization, and σ_F is the contribution from hard bremsstrahlung.

The output from running `IDIFFRAD.F` gives us the radiative corrections in the form,

$$\eta(\Phi) = \frac{\sigma_{obs}}{\sigma_{Born}}. \tag{4.36}$$

Therefore, to correct our data for corrections from radiative effects, we take the acceptance corrected data distributions from Equation 4.28, $N_j^{acc\ corr}$, and divide by

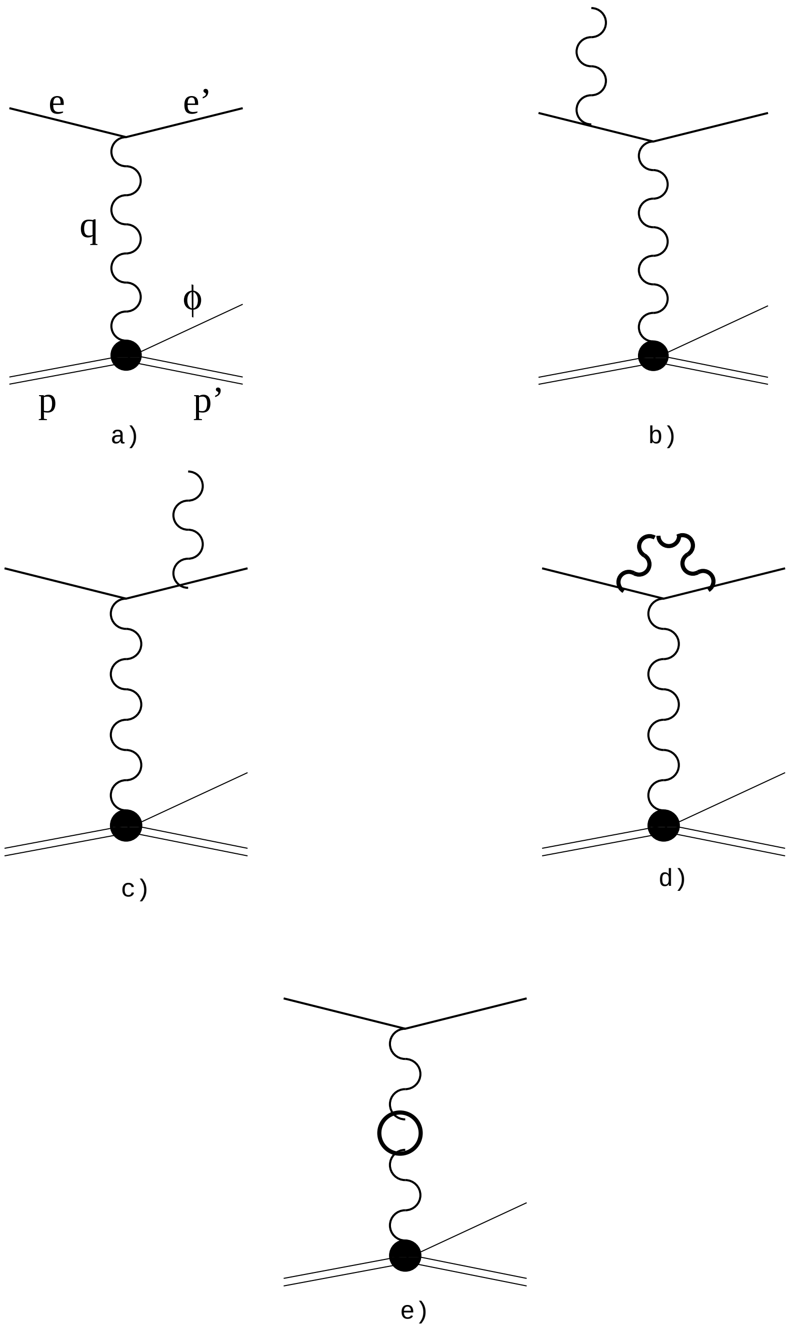

Figure 4.22. The Feynman diagrams contributing to the radiative corrections calculated in Reference [80].

Table 4.6. The effect of the radiative correction on the spin-density matrix elements. The size column is the difference in the background and acceptance corrected r^{α}_{ij} evaluated with and without the radiative correction: r^{α}_{ij}(with)$-r^{\alpha}_{ij}$(without). The % uncertainty is the absolute value of this difference divided by the final values for r^{α}_{ij} in this work, from Table 4.7. Any entry with 0 (or 0.000) means that the effect is smaller than the number of significant figures shown.

r^{α}_{ij}	size	%	r^{α}_{ij}	size	%
r^{04}_{00}	-0.004	1	$\mathrm{Im}(r^{3}_{10})$	0.000	0
r^{1}_{1-1}	0.001	0	$\mathrm{Im}(r^{3}_{1-1})$	-0.001	1
$\mathrm{Im}(r^{2}_{1-1})$	-0.002	1	$\mathrm{Im}(r^{7}_{10})$	-0.001	2
$\mathrm{Re}(r^{5}_{10})$	0.002	1	$\mathrm{Im}(r^{7}_{1-1})$	0.003	2
$\mathrm{Im}(r^{6}_{10})$	0.001	1	r^{8}_{11}	-0.000	1
$\mathrm{Re}(r^{04}_{10})$	-0.007	41	r^{8}_{00}	0.001	2
r^{04}_{1-1}	-0.001	8	$\mathrm{Re}(r^{8}_{10})$	0.001	2
r^{1}_{11}	-0.009	29	r^{8}_{1-1}	0.000	1
r^{1}_{00}	-0.002	9			
$\mathrm{Re}(r^{1}_{10})$	0.009	92			
$\mathrm{Im}(r^{2}_{10})$	-0.010	1518			
r^{5}_{11}	-0.013	59			
r^{5}_{00}	-0.011	40			
r^{5}_{1-1}	0.002	14			
$\mathrm{Im}(r^{6}_{1-1})$	-0.002	8			

the radiative correction:

$$N_j^{corr} = \frac{N_j^{acc\ corr}}{\eta(\Phi)}. \tag{4.37}$$

The radiative correction as a function of Φ for average HERMES ϕ kinematics is plotted in Figure 4.23. The effect of the radiative correction on the spin-density matrix elements is tabulated in Table 4.6. The effects of the radiative corrections on the extracted r^{α}_{ij} are small.

Note that there exists an alternative radiative correction procedure to the spin-density matrix element analysis which uses the same physics model, but is more complicated computationally than that described here, and is described in Reference [81]. In Subsection 4.3.5, we shall assign a systematic uncertainty to the simple radiative correction procedure used in this analysis.

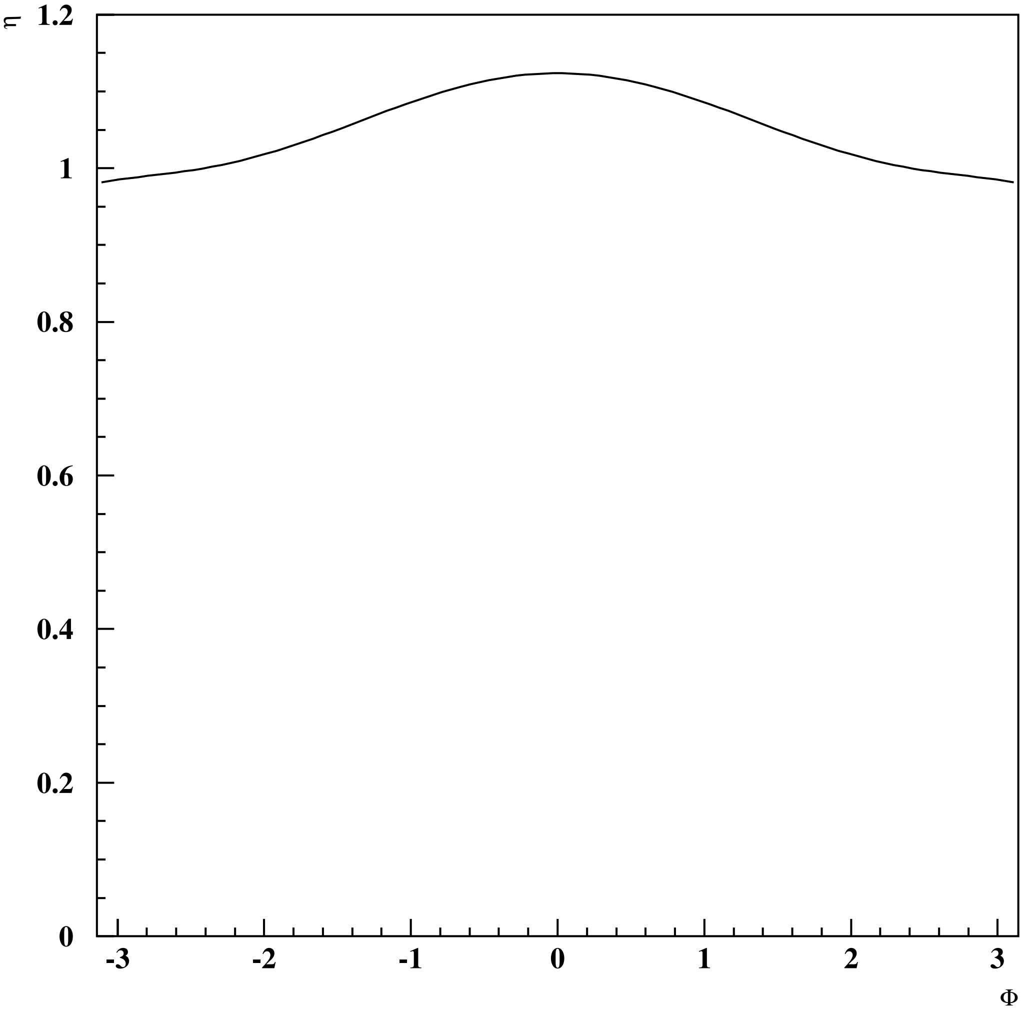

Figure 4.23. The radiative correction on ϕ electroproduction, η, plotted as a function of the azimuthal production angle, Φ. The correction is on the order of 10% in the production cross section. The effects of the correction on the measurements of r_{ij}^{α} are tabulated in Figure 4.6.

Table 4.7. The final results of the spin-density matrix elements for ϕ mesons, integrated over all kinematic variables. The uncertainty is statistical.

Unpolarized beam		Polarized beam	
r^{04}_{00}	0.304 ± 0.019	$\mathrm{Im}(r^3_{10})$	-0.022 ± 0.044
r^1_{1-1}	0.309 ± 0.030	$\mathrm{Im}(r^3_{1-1})$	-0.088 ± 0.066
$\mathrm{Im}(r^2_{1-1})$	-0.281 ± 0.029	$\mathrm{Im}(r^7_{10})$	-0.036 ± 0.060
$\mathrm{Re}(r^5_{10})$	0.143 ± 0.011	$\mathrm{Im}(r^7_{1-1})$	0.145 ± 0.098
$\mathrm{Im}(r^6_{10})$	-0.169 ± 0.010	r^8_{11}	0.031 ± 0.099
$\mathrm{Re}(r^{04}_{10})$	-0.018 ± 0.012	r^8_{00}	-0.051 ± 0.137
r^{04}_{1-1}	0.014 ± 0.017	$\mathrm{Re}(r^8_{10})$	-0.037 ± 0.065
r^1_{11}	0.017 ± 0.031	r^8_{1-1}	-0.057 ± 0.106
r^1_{00}	0.033 ± 0.042		
$\mathrm{Re}(r^1_{10})$	-0.010 ± 0.021		
$\mathrm{Im}(r^2_{10})$	-0.001 ± 0.022		
r^5_{11}	-0.017 ± 0.017		
r^5_{00}	0.024 ± 0.022		
r^5_{1-1}	-0.013 ± 0.014		
$\mathrm{Im}(r^6_{1-1})$	-0.026 ± 0.015		

As the effect of the radiative correction is small, we assume that the uncertainty on the radiative correction is also small, Hence, the statistical uncertainty on N_j^{corr} can be given by the expression

$$\delta N_j^{corr} = \frac{\delta N_j^{acc\ corr}}{\eta(\Phi)}, \tag{4.38}$$

with $\delta N_j^{acc\ corr}$ from Equation 4.31.

The radiative corrections are the final corrections performed on the data. The histograms N_j^{corr} in Equation 4.37 are the ones used in the final evaluation of the moments for the spin-density matrix elements in Equation 4.24. Hence, the final results of the spin-density matrix elements for ϕ's, corrected for non-exclusive background, the acceptance correction, and radiative effects, integrated over all data in the kinematic ranges $0.5 < Q^2 < 5.0\,\mathrm{GeV}^2$, $3.5 < \sqrt{W^2} < 6.5\,\mathrm{GeV}$, and $0 < -t' < 2.0\,\mathrm{GeV}^2$, are presented in Table 4.7 along with the statistical uncertainties.

To quantify the correlations between the 23 spin-density matrix elements, we compute the 23×23 matrix of sample linear-correlation coefficients, [75]

$$c_{kl} \equiv \frac{s_{kl}^2}{\sqrt{s_{kk}^2}\sqrt{s_{ll}^2}}. \tag{4.39}$$

In this equation, s_{kk}^2 is the standard deviation, or variance, of the distribution of the spin-density matrix element, $x_k = r_{ij,k}^{\alpha}$, obtained by calculating $r_{ij,k}^{\alpha}$ on an event-by-event basis from the expression in Appendix B. The standard deviation of the matrix element x_k is defined by a sum over acceptance corrected data events,

$$s_{kk}^2 = \frac{1/(N_{events}-1)\sum_i \left\{A_i[x_{ik} - \langle x_k\rangle]^2\right\}}{(1/N_{events})\sum_i A_i} > 0. \tag{4.40}$$

The covariance between two spin-density matrix elements, x_k and x_l, is defined as

$$s_{kl}^2 = \frac{1/(N_{events}-1)\sum_i \left\{A_i[x_{ik} - \langle x_k\rangle][x_{il} - \langle x_l\rangle]\right\}}{(1/N_{events})\sum_i A_i}, \tag{4.41}$$

which, contrary to its notation, may be < 0. To perform the acceptance correction on an event-by-event basis when computing these variances and covariances, A_i is calculated beforehand, using the same MC generated and MC accepted events as used for the final results in this work, although binned in $(\cos\theta, \varphi, \Phi)$.

The matrix of sample linear correlation coefficients is large enough to fit into two tables, Tables 4.8 and 4.9. It is defined a symmetric matrix normalized such that the diagonal elements are one. The off-diagonal elements give the estimate of the bias in the measurement of a moment of data, given the measurement of another moment of the same data. Most of the off-diagonal elements in the sample linear correlation coefficients are small (less than ≈ 0.2). The only ones of significant size are the ones describing the correlations between $r_{00}^{1,5,8}$ and $r_{11}^{1,5,8}$, all on the order of -0.4. If one were to study the expressions for these matrix elements in terms of moments from Appendix B, one might have expected these spin-density matrix elements to be largely negatively correlated.

Table 4.8. The matrix of linear-correlation coefficients between the distributions of moments. It is symmetric, and continues into the following table.

	r^{04}_{00}	$\mathrm{Re}(r^{04}_{10})$	r^{04}_{1-1}	r^{1}_{00}	r^{1}_{11}	$\mathrm{Re}(r^{1}_{10})$	r^{1}_{1-1}	$\mathrm{Im}(r^{2}_{10})$	$\mathrm{Im}(r^{2}_{1-1})$	$\mathrm{Im}(r^{3}_{10})$	$\mathrm{Im}(r^{3}_{1-1})$
r^{04}_{00}	1.000										
$\mathrm{Re}(r^{04}_{10})$	−0.009	1.000									
r^{04}_{1-1}	−0.019	−0.002	1.000								
r^{1}_{00}	−0.035	−0.005	−0.058	1.000							
r^{1}_{11}	0.013	0.001	0.234	−0.430	1.000						
$\mathrm{Re}(r^{1}_{10})$	−0.004	−0.063	−0.008	−0.040	−0.015	1.000					
r^{1}_{1-1}	−0.150	−0.009	0.044	−0.014	0.068	0.052	1.000				
$\mathrm{Im}(r^{2}_{10})$	−0.002	0.075	−0.008	0.026	−0.042	−0.026	−0.016	1.000			
$\mathrm{Im}(r^{2}_{1-1})$	0.103	0.030	0.030	0.022	−0.017	0.033	0.012	0.029	1.000		
$\mathrm{Im}(r^{3}_{10})$	−0.013	−0.003	0.026	−0.011	0.012	0.004	0.018	−0.017	−0.013	1.000	
$\mathrm{Im}(r^{3}_{1-1})$	0.016	0.013	−0.006	0.002	−0.009	0.006	0.061	−0.014	−0.017	−0.053	1.000
r^{5}_{00}	0.071	0.234	0.016	0.025	0.007	−0.158	−0.008	0.148	0.002	0.025	0.004
r^{5}_{11}	−0.028	0.155	−0.010	0.007	−0.002	−0.111	−0.040	0.110	0.068	−0.034	0.017
$\mathrm{Re}(r^{5}_{10})$	0.116	−0.047	−0.210	−0.161	−0.115	0.100	0.036	−0.041	−0.040	−0.023	0.032
r^{5}_{1-1}	0.017	−0.194	−0.009	−0.003	−0.042	0.107	0.013	0.181	0.023	−0.012	−0.065
$\mathrm{Im}(r^{6}_{10})$	−0.107	0.059	−0.240	−0.203	−0.129	0.023	−0.088	0.076	0.061	0.036	0.012
$\mathrm{Im}(r^{6}_{1-1})$	−0.015	0.189	0.000	−0.040	0.062	0.175	0.043	0.110	0.124	0.016	0.002
$\mathrm{Im}(r^{7}_{10})$	0.035	−0.022	−0.011	−0.032	0.032	−0.005	−0.002	−0.039	0.006	0.269	−0.217
$\mathrm{Im}(r^{7}_{1-1})$	−0.006	0.028	−0.065	0.021	−0.042	−0.038	0.061	0.008	−0.052	−0.205	0.254
r^{8}_{00}	−0.051	−0.022	−0.015	−0.039	0.031	0.010	−0.019	−0.007	−0.032	−0.247	−0.035
r^{8}_{11}	0.002	0.006	0.019	0.034	−0.048	−0.034	0.042	0.020	0.035	−0.201	0.013
$\mathrm{Re}(r^{8}_{10})$	−0.020	0.069	−0.015	0.010	−0.032	0.011	0.023	0.032	0.000	0.055	0.227
r^{8}_{1-1}	−0.020	−0.015	0.096	−0.024	0.048	0.020	−0.017	0.026	0.029	−0.244	−0.027

Table 4.9: The continuation of the matrix of linear-correlation coefficients between the distributions of moments.

	r^5_{00}	r^5_{11}	$\mathrm{Re}(r^5_{10})$	r^5_{1-1}	$\mathrm{Im}(r^6_{10})$	$\mathrm{Im}(r^6_{1-1})$	$\mathrm{Im}(r^7_{10})$	$\mathrm{Im}(r^7_{1-1})$	r^8_{00}	r^8_{11}	$\mathrm{Re}(r^8_{10})$	r^8_{1-1}
r^5_{00}	1.000											
r^5_{11}	−0.422	1.000										
$\mathrm{Re}(r^5_{10})$	−0.038	−0.002	1.000									
r^5_{1-1}	0.032	−0.139	0.027	1.000								
$\mathrm{Im}(r^6_{10})$	0.023	0.010	0.082	0.013	1.000							
$\mathrm{Im}(r^6_{1-1})$	−0.022	0.119	−0.014	−0.016	−0.001	1.000						
$\mathrm{Im}(r^7_{10})$	−0.003	0.006	−0.001	0.014	0.008	0.010	1.000					
$\mathrm{Im}(r^7_{1-1})$	0.010	−0.016	−0.002	−0.046	0.019	0.011	−0.083	1.000				
r^8_{00}	0.001	−0.006	0.001	−0.009	−0.029	0.013	−0.015	−0.033	1.000			
r^8_{11}	−0.007	0.030	−0.013	0.016	0.046	−0.030	−0.018	0.141	−0.393	1.000		
$\mathrm{Re}(r^8_{10})$	−0.007	0.005	0.026	−0.015	−0.005	0.014	−0.051	0.012	−0.011	0.042	1.000	
r^8_{1-1}	−0.009	0.016	−0.018	0.049	0.045	0.036	−0.025	−0.021	−0.033	0.207	−0.039	1.000

4.3 Systematic Uncertainty

The systematic uncertainty, in our case, is an estimate of the biases in our extraction of r_{ij}^{α}. In this work, we perform these studies on all data integrated over all kinematic variables.

4.3.1 Method of Moments We want to ascribe a systematic uncertainty to the method of moments technique by comparing it with another extraction technique, called the χ^2 technique. Often, the parameters that describe data are extracted by fitting the parameterization to data binned in histograms. Both the value and the statistical uncertainty of each parameter can be estimated by either a χ^2 or a maximum-likelihood technique, two techniques that are well understood and described in many places, for example, in the Particle Data Book or Reference [82]. Thus, to estimate the systematic uncertainty on a matrix element extracted with the method of moments technique, we will take the difference of the value obtained by the method of moments with that obtained by fitting the histogrammed data by a χ^2.

One would like to make an estimate of the systematic uncertainty of the method of moments for all the spin-density matrix elements, which would mean fitting the full three-dimensional distribution of data, $W(\cos\theta, \varphi, \Phi)$. However, in this work, we will make only a reduced statement about the systematic uncertainty, limiting it to an estimate of the uncertainty on those matrix elements which can be fitted with one-dimensional histograms. If one integrates the full decay angular distribution given by Equations 2.32 and 2.33 over φ and Φ, one obtains the one-dimensional distribution,

$$W(\cos\theta) = \frac{3}{4}\left[1 - r_{00}^{04} + (3r_{00}^{04} - 1)\cos^2\theta\right]. \tag{4.42}$$

Integrating W over $\cos\theta$ and Φ leaves

$$W(\varphi) = \frac{1}{2\pi}\left[1 - 2r_{1-1}^{04}\cos 2\varphi + P_b\sqrt{1-\epsilon^2}\,\mathrm{Im}\, r_{1-1}^{3}\sin 2\varphi\right]. \tag{4.43}$$

Integration over the decay angles gives the azimuthal production distribution,

$$
\begin{aligned}
W(\Phi) = \frac{1}{2\pi}\Big[& 1 - \epsilon\cos 2\Phi\,\mathrm{Tr}(r^1) \\
& + \sqrt{2\epsilon(1+\epsilon)}\cos\Phi\,\mathrm{Tr}(r^5) \\
& + P_b\sqrt{2\epsilon(1-\epsilon)}\sin\Phi\,\mathrm{Tr}(r^8)\Big],
\end{aligned}
\tag{4.44}
$$

where $\mathrm{Tr}(r^\alpha) = 2\,r^\alpha_{11} + r^\alpha_{00}$. Finally, if one assumes SCHC and integrates the resulting angular distribution (Equation 2.69) over $\cos\theta$, the decay angular distribution becomes

$$
W(\psi) = \frac{1}{2\pi}\left[1 + 2\epsilon\, r^1_{1-1}\cos 2\psi\right]. \tag{4.45}
$$

Using the fits to these one-dimensional distributions, we estimate the systematic uncertainty on the matrix elements r^{04}_{00}, r^{04}_{1-1}, $\mathrm{Im}(r^3_{1-1})$, and r^1_{1-1}. We do not use the one-dimensional Φ distribution to estimate the uncertainties on $r^{1,5,8}_{00}$ and $r^{1,5,8}_{11}$, as it is not clear how to best translate the measurement of the traces to the systematic uncertainty in the diagonal matrix elements.

In the χ^2 technique, we use the following procedure to simultaneously perform the acceptance correction and measure the one-dimensional matrix elements:

(1) Generate ϕ's according to the model described in Subsection 4.2.3 in the kinematic variables E', $\cos\theta_e$, φ_e, M_{2K}, and t'.

(2) Make these ϕ's decay isotropically in $d\Phi\,d\varphi\,d\cos\theta$, and track the e', h^+, h^- through the spectrometer with HMC.

(3) Weight each isotropically-generated event by the full angular distribution, $W(\cos\theta, \varphi, \Phi)$, varying the value of the matrix elements r^{04}_{00}, r^{04}_{1-1}, $\mathrm{Im}(r^3_{1-1})$, r^1_{1-1}, $\mathrm{Tr}(r^1)$, $\mathrm{Tr}(r^5)$, and $\mathrm{Tr}(r^8)$ until the HMC events best match the data.

For the matrix elements which are not observable in one-dimensional histograms, we assume SCHC values, where applicable:

$$\begin{aligned} \mathrm{Im}\,(r^2_{1-1}) &= -r^1_{1-1}, \\ r^{5,6,7,8}_{1-1} &= 0, \text{ and} \\ r^{1,2,3,04}_{10} &= 0. \end{aligned} \tag{4.46}$$

The matrix elements that describe the azimuthal production angle, Φ, are assumed to have the same longitudinal-to-transverse strength as when integrated over Φ:

$$\begin{aligned} r^{1,5,8}_{00} &= \mathrm{Tr}(r^{1,5,8}) \times r^{04}_{00} \\ r^{1,5,8}_{11} &= \mathrm{Tr}(r^{1,5,8}) \times \frac{1}{2}\left(1 - r^{04}_{00}\right). \end{aligned} \tag{4.47}$$

Finally, the matrix elements that are neither determined by SCHC nor observable in one-dimensional histograms are assumed to be zero,

$$\mathrm{Re}(r^5_{10}) = \mathrm{Im}(r^6_{10}) = \mathrm{Im}(r^7_{10}) = \mathrm{Re}(r^8_{10}) = 0. \tag{4.48}$$

We weight the MC events with $W(\cos\theta, \varphi, \Phi)$, using the generated values of ϵ (not corrected for acceptance effects), and the reconstructed values of $\cos\theta$, φ, and Φ. We define χ^2 as the normalized sum of squares of differences between the data and weighted MC, summing over all the bins in all four one-dimensional distributions,

$$\chi^2 = \sum_i \frac{(N_i - W(\cos\theta, \varphi, \Phi) \times MC_i)^2}{\sigma^2_{N,i} + \sigma^2_{MC,i}}, \tag{4.49}$$

where N_i and MC_i are the number of data and MC events in angular bin i, and $\sigma_{N,i}$ and $\sigma_{MC,i}$ are the statistical uncertainties of the data and weighted MC samples. The values of the seven parameters which simultaneously minimize the total χ^2 for the four one-dimensional distributions, $\cos\theta$, φ, Φ, and ψ, are the measured values of matrix elements from the χ^2 technique.

Table 4.10. The estimate of the systematic uncertainty due to the method of moments technique (m.m.). The m.m. values in this table are corrected for neither background nor radiative effects. Note that we use -$r^1_{1-1}(\chi^2)$ for $\mathrm{Im}(r^2_{1-1})(\chi^2)$. Since r^1_{1-1} and $\mathrm{Im}(r^2_{1-1})$ are combined by assuming SCHC in the χ^2 method, they are combined in the m.m. by averaging the absolute values before computing the differences. The $|\sigma_{syst}|/\sigma_{stat}$ column is the absolute value of the uncertainty divided by $(\delta\, r^{\alpha}_{ij})_{stat}$ from Table 4.7. The average value of this estimate of this systematic uncertainty relative to the statistical uncertainty is 0.51.

r^{α}_{ij}	$r^{\alpha}_{ij}(\chi^2)$	r^{α}_{ij}(m.m.)	$r^{\alpha}_{ij}(\chi^2)$-r^{α}_{ij}(m.m.)	$\lvert\sigma_{syst}\rvert/\sigma_{stat}$
r^{04}_{00}	0.305	0.320	-0.015	0.80
r^1_{1-1}	0.275	0.299	0.009	0.30
$\mathrm{Im}(r^2_{1-1})$	-0.275	-0.234	-0.009	0.31
r^{04}_{1-1}	0.001	0.006	-0.005	0.29
$\mathrm{Im}(r^3_{1-1})$	-0.021	-0.078	0.057	0.86

The differences of the r^{α}_{ij} measured with χ^2 technique and the r^{α}_{ij} measured with the method of moments technique are listed in Table 4.10. The systematic uncertainties are smaller than the statistical uncertainties.

The statistical uncertainty in r^{α}_{ij} in the χ^2 method is equal to the amount needed to change r^{α}_{ij} in order to change the total χ^2 defined in Equation 4.49 by one. If $\sigma_{MC} \ll \sigma_N$ in Equation 4.49, the interpretation of the statistical uncertainty is that repeated identical measurements of r^{α}_{ij} will yield results which lay within this uncertainty $\approx 1/e$ of the time. Using approximately 10k isotropic MC events in the χ^2 method, it has been checked that the statistical uncertainty obtained by the χ^2 technique agrees with the statistical uncertainty obtained by the method of moments technique. Hence, we can interpret the statistical uncertainty from the method of moments in the same way we do the statistical uncertainty from the χ^2 method.

4.3.2 Spectrometer Effects In this section, the systematic uncertainty is estimated for effects resulting from measuring data with the HERMES spectrometer. The effects considered here are acceptance edges, top-bottom alignment, and smearing.

First, we estimate the uncertainty on the spin-density matrix elements due to effects coming from the edges of the spectrometer acceptance. As described in Subsection 4.1.1, we place horizontal and vertical angular fiducial constraints on all three detected particles to ensure they are detected in a well-understood part of the spectrometer,

$$\begin{aligned} \left|\frac{dX}{dZ}\right| &< 170\,\mathrm{mrad} \text{ and} \\ 40 < \left|\frac{dY}{dZ}\right| &< 140\,\mathrm{mrad}. \end{aligned} \tag{4.50}$$

These constraints are also applied to the accepted MC events in the acceptance correction in order to implicitly correct for their effects. Thus, to estimate the uncertainty from these fiducial constraints, we repeat the analysis, changing these constraints for both the data and the accepted MC. As the event sample is dominated by scattering at small angles relative to the beam pipe, the largest edge effects will come from the spectrometer edges nearest the beam pipe, at $|dY/dZ| \approx 40\,\mathrm{mrad}$. Therefore, we reanalyze the data, changing the lower $|dY/dZ|$ constraint to $|dY/dZ| > 42\,\mathrm{mrad}$. The values of r^{α}_{ij} measured with $|dY/dZ| > 42\,\mathrm{mrad}$ minus those measured with $|dY/dZ| > 40\,\mathrm{mrad}$ are listed in Table 4.11. For all spin-density matrix elements, the systematic uncertainty estimated here is smaller than the statistical uncertainty.

Next, we estimate the systematic uncertainty due to possible misalignment between the top and bottom halves of the HERMES spectrometer. Alignment studies on the spectrometer have suggested that the relative alignment between the top and bottom halves of the spectrometer is not yet completely understood. [83] As discussed in Subsection 4.1.2, the event topology of the ϕ data at HERMES is such that when the scattered positron is detected in one half of the spectrometer, both the K^+ and K^- from the ϕ decay are detected in the other half. Thus, we can estimate the size of the effect of the top-bottom misalignment on the spin-density matrix elements by extracting r^{α}_{ij} with data from two scenarios: when the e' goes into the

Table 4.11. The systematic uncertainty due to effects from the edge of the spectrometer acceptance. The difference column is the estimate of the uncertainty, given by $r^{\alpha}_{ij}(|dY/dZ| > 42\,\mathrm{mrad})$-$r^{\alpha}_{ij}(|dY/dZ| > 40\,\mathrm{mrad})$. The $|\sigma_{syst}|/\sigma_{stat}$ column is the absolute value of the uncertainty divided by $(\delta\, r^{\alpha}_{ij})_{stat}$ from Table 4.7. The average value of this estimate of this systematic uncertainty relative to the statistical uncertainty is 0.33.

r^{α}_{ij}	diff.	$\|\sigma_{syst}\|/\sigma_{stat}$	r^{α}_{ij}	diff.	$\|\sigma_{syst}\|/\sigma_{stat}$
r^{04}_{00}	0.012	0.64	$\mathrm{Im}(r^{3}_{10})$	−0.038	0.86
r^{1}_{1-1}	−0.022	0.72	$\mathrm{Im}(r^{3}_{1-1})$	−0.005	0.07
$\mathrm{Im}(r^{2}_{1-1})$	−0.009	0.29	$\mathrm{Im}(r^{7}_{10})$	0.035	0.59
$\mathrm{Re}(r^{5}_{10})$	0.006	0.56	$\mathrm{Im}(r^{7}_{1-1})$	−0.004	0.04
$\mathrm{Im}(r^{6}_{10})$	0.002	0.21	r^{8}_{11}	0.018	0.13
$\mathrm{Re}(r^{04}_{10})$	−0.007	0.55	r^{8}_{00}	−0.017	0.10
r^{04}_{1-1}	−0.009	0.50	$\mathrm{Re}(r^{8}_{10})$	−0.025	0.38
r^{1}_{11}	−0.014	0.32	r^{8}_{1-1}	−0.022	0.21
r^{1}_{00}	0.008	0.14			
$\mathrm{Re}(r^{1}_{10})$	−0.001	0.06			
$\mathrm{Im}(r^{2}_{10})$	−0.002	0.09			
r^{5}_{11}	−0.003	0.11			
r^{5}_{00}	0.001	0.02			
r^{5}_{1-1}	0.006	0.43			
$\mathrm{Im}(r^{6}_{1-1})$	−0.009	0.57			

Table 4.12. The estimate of the systematic uncertainty due to the possible misalignment between the upper and lower halves of the spectrometer. The difference column is half of the absolute value of the difference of r^{α}_{ij} when the e' is detected in the upper and lower halves. The $|\sigma_{syst}|/\sigma_{stat}$ column is the absolute value of the uncertainty divided by $(\delta\, r^{\alpha}_{ij})_{stat}$ from Table 4.7. The average value of this estimate of this systematic uncertainty relative to the statistical uncertainty is 0.69.

r^{α}_{ij}	diff.	$\|\sigma_{syst}\|/\sigma_{stat}$	r^{α}_{ij}	diff.	$\|\sigma_{syst}\|/\sigma_{stat}$
r^{04}_{00}	0.027	1.45	$\mathrm{Im}(r^{3}_{10})$	0.004	0.09
r^{1}_{1-1}	0.025	0.84	$\mathrm{Im}(r^{3}_{1-1})$	0.044	0.66
$\mathrm{Im}(r^{2}_{1-1})$	0.016	0.55	$\mathrm{Im}(r^{7}_{10})$	0.005	0.09
$\mathrm{Re}(r^{5}_{10})$	0.004	0.34	$\mathrm{Im}(r^{7}_{1-1})$	0.093	0.94
$\mathrm{Im}(r^{6}_{10})$	0.000	0.02	r^{8}_{11}	0.029	0.21
$\mathrm{Re}(r^{04}_{10})$	0.014	1.13	r^{8}_{00}	0.046	0.26
r^{04}_{1-1}	0.014	0.81	$\mathrm{Re}(r^{8}_{10})$	0.073	1.13
r^{1}_{11}	0.044	1.03	r^{8}_{1-1}	0.047	0.44
r^{1}_{00}	0.032	0.59			
$\mathrm{Re}(r^{1}_{10})$	0.047	2.21			
$\mathrm{Im}(r^{2}_{10})$	0.028	1.29			
r^{5}_{11}	0.001	0.04			
r^{5}_{00}	0.013	0.43			
r^{5}_{1-1}	0.004	0.27			
$\mathrm{Im}(r^{6}_{1-1})$	0.016	1.06			

upper half of the spectrometer (K^+K^- in lower half), and when the e' goes into the lower half (K^+K^- in upper). The systematic uncertainty on r^{α}_{ij} is then estimated to be half the absolute value of the difference between the r^{α}_{ij}'s extracted with these two scenarios, the results of which are tabulated in Table 4.12. For many matrix elements, this estimate of the systematic uncertainty is larger than the estimate of the statistical uncertainty. The average value of the ratio of the systematic to the statistical uncertainty is 0.69.

Finally, we want to estimate the systematic uncertainty on the correction made for smearing effects. As discussed at the end of Subsection 4.2.4, smearing is defined as the change of the values of the kinematic variables of a particle as it travels through the spectrometer on its way to being detected. Smearing occurs as a result of interactions of the particle with the material that makes up the spectrometer, and manifests itself through energy loss and multiple scattering through small angles. These processes are well-understood at high energies, described by the Particle Data Group, and included in HMC, so that our acceptance correction already implicitly includes a correction for smearing effects. The distributions of exclusive ϕ data and accepted MC events as a function of ΔE in the exclusive region can be seen in Figure 4.24. The accepted MC events are generated at the interaction point with $\Delta E = 0$, so that the width of this peak is entirely due to the smearing modeled in HMC. The data peak is wider than the accepted MC peak, a discrepancy which we attribute to an underestimate of the smearing effects in HMC. The amount by which HMC underestimates the smearing correction can then be quantified by f, where

$$f = \frac{\sigma_{\Delta E,data} - \sigma_{\Delta E,MC}}{\sigma_{\Delta E,MC}} = 0.36, \tag{4.51}$$

given in terms of a fraction of the smearing correction already included in HMC.

The systematic uncertainty on the spin-density matrix elements due to this underestimate of the smearing correction can be estimated as follows. Take, as an example, the matrix element $\mathrm{Im}(r^3_{1-1})$, determined by

$$\mathrm{Im}(r^3_{1-1}) = \frac{1}{P_b}\frac{1}{\sqrt{1-\epsilon^2}}\frac{5}{4}\langle\sin^2\theta\sin 2\varphi\rangle. \tag{4.52}$$

Both the value $1/\sqrt{1-\epsilon^2}$ and the value $\langle\sin^2\theta\sin 2\varphi\rangle$ are smeared. The effect of the smearing modeled in HMC on the value of each of these averages can be quantified by simply taking the difference in the generated average and the reconstructed average after it has been through HMC (for the accepted MC events). For example,

$$\delta_s(\langle\sin^2\theta\sin 2\varphi\rangle) = \langle\sin^2\theta\sin 2\varphi\rangle_{HMC} - \langle\sin^2\theta\sin 2\varphi\rangle_{gen}. \tag{4.53}$$

Then the systematic uncertainty in $\mathrm{Im}(r^3_{1-1})$ due to the uncertainty in the smearing correction is given by

$$\begin{aligned}\delta_s\mathrm{Im}(r^3_{1-1}) = \Bigg[\frac{1}{P_b}&\left\{\frac{1}{\sqrt{1-\epsilon^2}} + f\cdot\delta_s\left(\frac{1}{\sqrt{1-\epsilon^2}}\right)\right\} \\ &\times\frac{5}{4}\{\langle\sin^2\theta\sin 2\varphi\rangle + f\cdot\delta_s(\langle\sin^2\theta\sin 2\varphi\rangle)\}\Bigg] - \mathrm{Im}(r^3_{1-1}),\end{aligned} \tag{4.54}$$

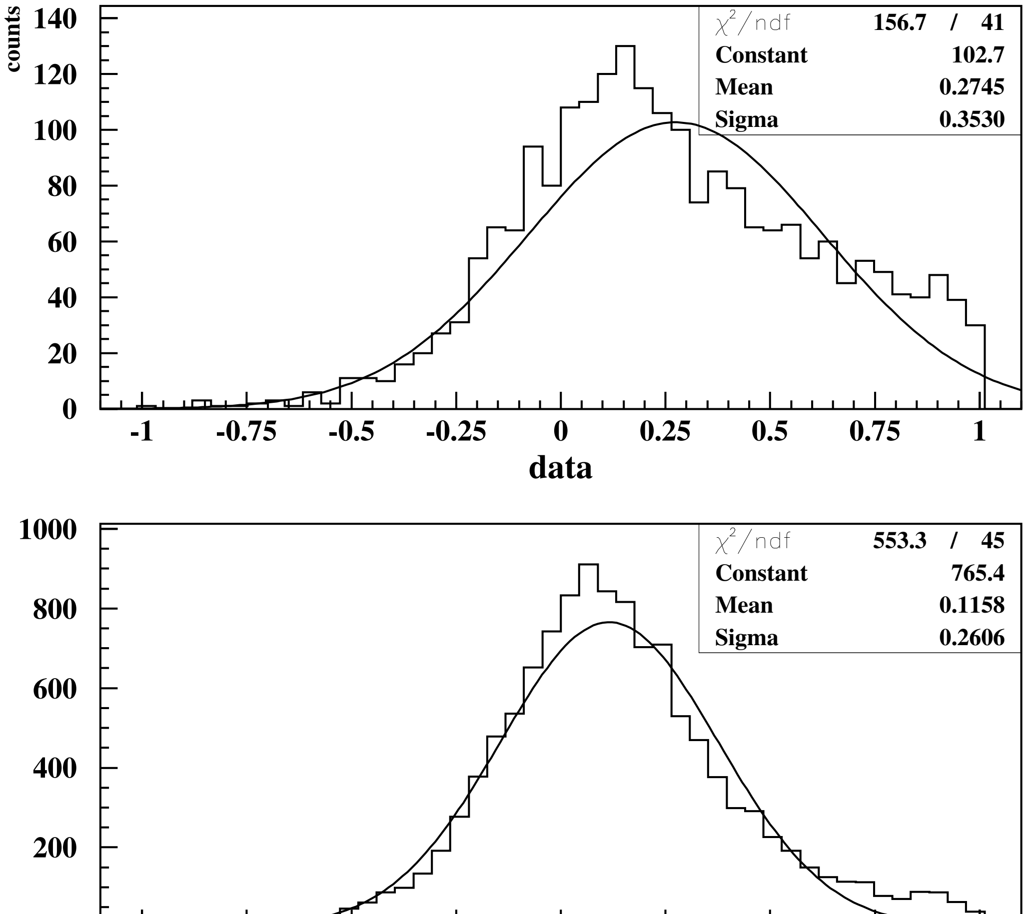

Figure 4.24. The distributions of uncorrected data and accepted MC events as a function of ΔE in the exclusive region. The accepted MC does not match the data well, especially at high ΔE, a feature we attribute to an underestimate of the smearing effects in HMC. The curves are Gaussian fits, and even though the fits do not follow the distribution well in either case, we use the fitted sigmas to represent the widths of the distributions.

Table 4.13. The estimate of the systematic uncertainty due to the smearing correction. The δ_s column gives the estimate of the uncertainty. The $|\sigma_{syst}|/\sigma_{stat}$ column is the absolute value of the uncertainty divided by $(\delta\, r^{\alpha}_{ij})_{stat}$ from Table 4.7. Any entry with 0.00 (or 0.000) means that the effect is smaller than the number of significant figures shown. The average value of this estimate of this systematic uncertainty relative to the statistical uncertainty is 0.54.

r^{α}_{ij}	δ_s	$\lvert\sigma_{syst}\rvert/\sigma_{stat}$	r^{α}_{ij}	δ_s	$\lvert\sigma_{syst}\rvert/\sigma_{stat}$
r^{04}_{00}	0.003	0.14	$\mathrm{Im}(r^{3}_{10})$	0.000	0.00
r^{1}_{1-1}	0.004	0.12	$\mathrm{Im}(r^{3}_{1-1})$	0.113	1.70
$\mathrm{Im}(r^{2}_{1-1})$	0.000	0.00	$\mathrm{Im}(r^{7}_{10})$	-0.025	0.42
$\mathrm{Re}(r^{5}_{10})$	0.002	0.19	$\mathrm{Im}(r^{7}_{1-1})$	-0.103	1.04
$\mathrm{Im}(r^{6}_{10})$	-0.001	0.09	r^{8}_{11}	0.178	1.28
$\mathrm{Re}(r^{04}_{10})$	-0.001	0.08	r^{8}_{00}	-0.086	0.49
r^{04}_{1-1}	-0.001	0.05	$\mathrm{Re}(r^{8}_{10})$	0.066	1.03
r^{1}_{11}	-0.036	0.84	r^{8}_{1-1}	0.278	2.61
r^{1}_{00}	-0.039	0.71			
$\mathrm{Re}(r^{1}_{10})$	0.002	0.08			
$\mathrm{Im}(r^{2}_{10})$	-0.001	0.03			
r^{5}_{11}	-0.017	0.72			
r^{5}_{00}	-0.023	0.81			
r^{5}_{1-1}	0.000	0.02			
$\mathrm{Im}(r^{6}_{1-1})$	0.000	0.01			

where $f \cdot \delta_s()$ is the amount that HMC underestimates the smearing correction. The results of this estimate of the systematic uncertainty from the smearing correction are tabulated in Table 4.13. For most of the spin-density matrix elements, the systematic uncertainties due to smearing estimated here are smaller than the statistical uncertainties.

4.3.3 Acceptance Correction We want to estimate the systematic uncertainty due to the uncertainty in the parameters used in the generation of our MC acceptance correction, described in Subsection 4.2.3.

First, we study the Q^2 dependence of the total cross-section, which is given in our acceptance correction MC by the modified VMD calculation of Hüfner and

Table 4.14. The estimate of the systematic uncertainty due to the uncertainty in the assumed Q^2 dependence of the cross-section used in the acceptance correction. The difference column gives the estimate of the uncertainty, r^{α}_{ij}(modified VMD)$-r^{\alpha}_{ij}$(VMD). The $|\sigma_{syst}|/\sigma_{stat}$ column is the absolute value of the uncertainty divided by $(\delta\, r^{\alpha}_{ij})_{stat}$ from Table 4.7. Any entry with 0.00 (or 0.000) means that the effect is smaller than the number of significant figures shown. The average value of this estimate of this systematic uncertainty relative to the statistical uncertainty is 0.42.

r^{α}_{ij}	diff.	$\lvert\sigma_{syst}\rvert/\sigma_{stat}$	r^{α}_{ij}	diff.	$\lvert\sigma_{syst}\rvert/\sigma_{stat}$
r^{04}_{00}	-0.005	0.28	$\mathrm{Im}(r^3_{10})$	0.007	0.15
r^1_{1-1}	0.015	0.49	$\mathrm{Im}(r^3_{1-1})$	-0.019	0.28
$\mathrm{Im}(r^2_{1-1})$	-0.014	0.49	$\mathrm{Im}(r^7_{10})$	0.018	0.30
$\mathrm{Re}(r^5_{10})$	-0.007	0.68	$\mathrm{Im}(r^7_{1-1})$	0.008	0.08
$\mathrm{Im}(r^6_{10})$	0.009	0.89	r^8_{11}	0.000	0.00
$\mathrm{Re}(r^{04}_{10})$	0.015	1.21	r^8_{00}	0.007	0.04
r^{04}_{1-1}	0.002	0.09	$\mathrm{Re}(r^8_{10})$	-0.008	0.13
r^1_{11}	0.024	0.56	r^8_{1-1}	-0.010	0.09
r^1_{00}	-0.009	0.17			
$\mathrm{Re}(r^1_{10})$	-0.008	0.40			
$\mathrm{Im}(r^2_{10})$	0.016	0.74			
r^5_{11}	0.026	1.10			
r^5_{00}	0.015	0.53			
r^5_{1-1}	-0.007	0.49			
$\mathrm{Im}(r^6_{1-1})$	0.005	0.37			

Kopeliovich,

$$\sigma_T(Q^2, W^2) = \sigma(Q^2 = 0, W^2)\left(\frac{1}{1 + Q^2/M^2_{\phi}}\right)^2 \left(\frac{M^2_{\phi'} - M^2_{\phi}}{M^2_{\phi'} - Q^2}\right)^2 . \tag{4.55}$$

To quantify the sensitivity of the spin-density matrix elements to the assumed Q^2 dependence of the cross-section, we redo the analysis, using the Q^2 dependence from standard VMD in the generated and accepted MC samples:

$$\sigma_T(Q^2, W^2) = \sigma(Q^2 = 0, W^2)\left(\frac{1}{1 + Q^2/M^2_{\phi}}\right)^2 . \tag{4.56}$$

The systematic uncertainty in r^{α}_{ij} due to the uncertainty in the Q^2 dependence of the cross-section used in the acceptance correction is then estimated by the difference of the extracted r^{α}_{ij}'s, the results of which are tabulated in Table 4.14. Note that this is actually an overestimate of the uncertainty, since the model from Hüfner and

Table 4.15. The estimate of the systematic uncertainty due to the uncertainty in the assumed $\sqrt{W^2}$ dependence of the cross-section used in the acceptance correction. The difference column is the estimate of the uncertainty, $|r_{ij}^{\alpha}((\sqrt{W^2})^{0.42}) - r_{ij}^{\alpha}((\sqrt{W^2})^{0.22})|/2$. The $|\sigma_{syst}|/\sigma_{stat}$ column is the absolute value of the uncertainty divided by $(\delta\, r_{ij}^{\alpha})_{stat}$ from Table 4.7. Any entry with 0.00 (or 0.000) means that the effect is smaller than the number of significant figures shown. The average value of this estimate of this systematic uncertainty relative to the statistical uncertainty is 0.11.

r_{ij}^{α}	diff.	$\|\sigma_{syst}\|/\sigma_{stat}$	r_{ij}^{α}	diff.	$\|\sigma_{syst}\|/\sigma_{stat}$
r_{00}^{04}	0.002	0.12	$\mathrm{Im}(r_{10}^{3})$	0.002	0.04
r_{1-1}^{1}	0.010	0.32	$\mathrm{Im}(r_{1-1}^{3})$	0.001	0.02
$\mathrm{Im}(r_{1-1}^{2})$	0.005	0.18	$\mathrm{Im}(r_{10}^{7})$	0.006	0.10
$\mathrm{Re}(r_{10}^{5})$	0.001	0.06	$\mathrm{Im}(r_{1-1}^{7})$	0.008	0.08
$\mathrm{Im}(r_{10}^{6})$	0.001	0.11	r_{11}^{8}	0.002	0.02
$\mathrm{Re}(r_{10}^{04})$	0.002	0.20	r_{00}^{8}	0.007	0.04
r_{1-1}^{04}	0.006	0.35	$\mathrm{Re}(r_{10}^{8})$	0.004	0.07
r_{11}^{1}	0.005	0.11	r_{1-1}^{8}	0.005	0.05
r_{00}^{1}	0.006	0.10			
$\mathrm{Re}(r_{10}^{1})$	0.001	0.06			
$\mathrm{Im}(r_{10}^{2})$	0.004	0.20			
r_{11}^{5}	0.001	0.04			
r_{00}^{5}	0.001	0.03			
r_{1-1}^{5}	0.000	0.02			
$\mathrm{Im}(r_{1-1}^{6})$	0.002	0.14			

Kopeliovich already matches the data well in Figure 4.16. For most of the spin-density matrix elements, this estimate is smaller than the statistical uncertainty.

Next, we examine the $\sqrt{W^2}$ dependence of the total cross-section, which in this analysis is given by the fit in [18]: $\sigma(Q^2 = 0, W^2) \sim \left(\sqrt{W^2}\right)^{\beta}$, with $\beta = 0.32$. To quantify the sensitivity of r_{ij}^{α} to this parameter, we redo the analysis twice, using the parameters $\beta = 0.22$ and $\beta = 0.42$ in the acceptance correction. The systematic uncertainty in r_{ij}^{α} due to the uncertainty in the $\sqrt{W^2}$ dependence of the cross-section used in the acceptance correction is then estimated by half the absolute value of the difference between these extracted r_{ij}^{α}'s, the results of which are tabulated in Table 4.15. The size of this effect is small compared to the statistical uncertainties.

Next, we examine the $-t'$ dependence of the differential cross-section, which in this analysis is given by the expression

$$\frac{dN}{d\,|t'|} \propto \left(\frac{\sigma_A}{\sigma_p} b_A\, e^{-b_A |t'|} + b_p\, e^{-b_p |t'|}, \right), \tag{4.57}$$

with $\sigma_A/\sigma_p = 0.22$, $b_A = 34\,\mathrm{GeV}^{-2}$, and $b_p = 3.81\,\mathrm{GeV}^{-2}$. These values were determined by iteratively fitting the acceptance corrected data distribution in the regions $|t'| < 0.05\,\mathrm{GeV}^2$ (with fixed b_p), to determine b_A and σ_A/σ_p, and $|t'| > 0.05\,\mathrm{GeV}^2$ (with fixed σ_A/σ_p and b_A), to determine b_p. To quantify the sensitivity of r^{α}_{ij} to these fitted parameters, we redo the analysis six times, using the parameters $\sigma_A/\sigma_p = 0.22 \pm 0.07$, $b_A = (34 \pm 8)\,\mathrm{GeV}^{-2}$, and $b_p = (3.81 \pm 0.13)\,\mathrm{GeV}^{-2}$ in the acceptance correction, the ranges corresponding to the statistical uncertainty of the fits. The systematic uncertainty in r^{α}_{ij} due to the uncertainty in each of the parameters of the $-t'$ differential cross-section used in the acceptance correction is estimated by half the absolute value of the difference between the extracted r^{α}_{ij}'s. The results of the studies on parameters σ_A/σ_p, b_A, and b_p are tabulated in Tables 4.16, 4.17, and 4.18, respectively.

Finally, we examine the dependence of the acceptance correction on the assumed values of r^{α}_{ij}. To estimate the systematic uncertainty on the dependence of the acceptance correction on the assumed values of r^{α}_{ij}, we take the difference of the extracted and the input values of r^{α}_{ij} in the MC "data" in Table 4.5. The difference of the extracted and the input values are tabulated in Table 4.19. This is the largest source of systematic uncertainty. Even so, the effect of varying r^{α}_{ij} in the acceptance correction on the extracted values of r^{α}_{ij} is generally smaller than the statistical uncertainty.

4.3.4 Background Correction We want to estimate the systematic uncertainty on the spin density matrix elements coming from the uncertainty in the background correction. As discussed in Subsection 4.2.1, we use the data in sidebands of M_{2K}, Regions I and III, to estimate the background underneath the exclusive ϕ peak. To quantify the uncertainty for the possible error of not using the data in the

Table 4.16. The estimate of the systematic uncertainty due to the uncertainty in the assumed σ_A/σ_p dependence of the differential cross-section used in the acceptance correction. The difference column is the estimate of the uncertainty, $|r^{\alpha}_{ij}(\sigma_A/\sigma_p = 0.29) - r^{\alpha}_{ij}(\sigma_A/\sigma_p = 0.15)|/2$. The $|\sigma_{syst}|/\sigma_{stat}$ column is this uncertainty divided by $(\delta\, r^{\alpha}_{ij})_{stat}$ from Table 4.7. Any entry with 0.00 (or 0.000) means that the effect is smaller than the number of significant figures shown. The average value of this estimate of this systematic uncertainty relative to the statistical uncertainty is 0.22.

r^{α}_{ij}	diff.	$\lvert\sigma_{syst}\rvert/\sigma_{stat}$	r^{α}_{ij}	diff.	$\lvert\sigma_{syst}\rvert/\sigma_{stat}$
r^{04}_{00}	0.010	0.53	$\mathrm{Im}(r^{3}_{10})$	0.000	0.00
r^{1}_{1-1}	0.012	0.38	$\mathrm{Im}(r^{3}_{1-1})$	0.002	0.04
$\mathrm{Im}(r^{2}_{1-1})$	0.000	0.01	$\mathrm{Im}(r^{7}_{10})$	0.000	0.00
$\mathrm{Re}(r^{5}_{10})$	0.004	0.37	$\mathrm{Im}(r^{7}_{1-1})$	0.000	0.00
$\mathrm{Im}(r^{6}_{10})$	0.001	0.06	r^{8}_{11}	0.015	0.11
$\mathrm{Re}(r^{04}_{10})$	0.004	0.35	r^{8}_{00}	0.018	0.10
r^{04}_{1-1}	0.010	0.55	$\mathrm{Re}(r^{8}_{10})$	0.005	0.08
r^{1}_{11}	0.007	0.17	r^{8}_{1-1}	0.007	0.07
r^{1}_{00}	0.007	0.14			
$\mathrm{Re}(r^{1}_{10})$	0.008	0.35			
$\mathrm{Im}(r^{2}_{10})$	0.002	0.11			
r^{5}_{11}	0.008	0.34			
r^{5}_{00}	0.002	0.07			
r^{5}_{1-1}	0.001	0.10			
$\mathrm{Im}(r^{6}_{1-1})$	0.017	1.15			

Table 4.17. The estimate of the systematic uncertainty due to the uncertainty in the assumed b_A dependence of the differential cross-section used in the acceptance correction. The difference column is the estimate of the uncertainty, $|r^{\alpha}_{ij}(b_A = 42) - r^{\alpha}_{ij}(b_A = 26)|/2$. The $|\sigma_{syst}|/\sigma_{stat}$ column is this uncertainty divided by $(\delta\, r^{\alpha}_{ij})_{stat}$ from Table 4.7. Any entry with 0.00 (or 0.000) means that the effect is smaller than the number of significant figures shown. The average value of this estimate of this systematic uncertainty relative to the statistical uncertainty is 0.22.

r^{α}_{ij}	diff.	$\lvert\sigma_{syst}\rvert/\sigma_{stat}$	r^{α}_{ij}	diff.	$\lvert\sigma_{syst}\rvert/\sigma_{stat}$
r^{04}_{00}	0.007	0.37	$\mathrm{Im}(r^{3}_{10})$	0.002	0.04
r^{1}_{1-1}	0.007	0.23	$\mathrm{Im}(r^{3}_{1-1})$	0.002	0.03
$\mathrm{Im}(r^{2}_{1-1})$	0.014	0.48	$\mathrm{Im}(r^{7}_{10})$	0.002	0.03
$\mathrm{Re}(r^{5}_{10})$	0.004	0.38	$\mathrm{Im}(r^{7}_{1-1})$	0.017	0.17
$\mathrm{Im}(r^{6}_{10})$	0.003	0.25	r^{8}_{11}	0.000	0.00
$\mathrm{Re}(r^{04}_{10})$	0.007	0.58	r^{8}_{00}	0.009	0.05
r^{04}_{1-1}	0.008	0.47	$\mathrm{Re}(r^{8}_{10})$	0.006	0.09
r^{1}_{11}	0.006	0.13	r^{8}_{1-1}	0.013	0.12
r^{1}_{00}	0.010	0.17			
$\mathrm{Re}(r^{1}_{10})$	0.011	0.52			
$\mathrm{Im}(r^{2}_{10})$	0.011	0.52			
r^{5}_{11}	0.002	0.09			
r^{5}_{00}	0.001	0.03			
r^{5}_{1-1}	0.004	0.28			
$\mathrm{Im}(r^{6}_{1-1})$	0.001	0.05			

Table 4.18. The estimate of the systematic uncertainty due to the uncertainty in the assumed b_p dependence of the differential cross-section used in the acceptance correction. The difference column is the estimate of the uncertainty, $|r^{\alpha}_{ij}(b_p = 3.94) - r^{\alpha}_{ij}(b_p = 3.68)|/2$. The $|\sigma_{syst}|/\sigma_{stat}$ column is this uncertainty divided by $(\delta\, r^{\alpha}_{ij})_{stat}$ from Table 4.7. Any entry with 0.00 (or 0.000) means that the effect is smaller than the number of significant figures shown. The average value of this estimate of this systematic uncertainty relative to the statistical uncertainty is 0.16.

r^{α}_{ij}	diff.	$\|\sigma_{syst}\|/\sigma_{stat}$	r^{α}_{ij}	diff.	$\|\sigma_{syst}\|/\sigma_{stat}$
r^{04}_{00}	0.008	0.43	$\mathrm{Im}(r^{3}_{10})$	0.003	0.07
r^{1}_{1-1}	0.005	0.17	$\mathrm{Im}(r^{3}_{1-1})$	0.009	0.14
$\mathrm{Im}(r^{2}_{1-1})$	0.000	0.00	$\mathrm{Im}(r^{7}_{10})$	0.005	0.09
$\mathrm{Re}(r^{5}_{10})$	0.001	0.09	$\mathrm{Im}(r^{7}_{1-1})$	0.004	0.04
$\mathrm{Im}(r^{6}_{10})$	0.001	0.10	r^{8}_{11}	0.013	0.09
$\mathrm{Re}(r^{04}_{10})$	0.001	0.09	r^{8}_{00}	0.007	0.04
r^{04}_{1-1}	0.004	0.21	$\mathrm{Re}(r^{8}_{10})$	0.001	0.01
r^{1}_{11}	0.003	0.07	r^{8}_{1-1}	0.003	0.02
r^{1}_{00}	0.010	0.18			
$\mathrm{Re}(r^{1}_{10})$	0.006	0.27			
$\mathrm{Im}(r^{2}_{10})$	0.006	0.29			
r^{5}_{11}	0.014	0.58			
r^{5}_{00}	0.010	0.34			
r^{5}_{1-1}	0.005	0.37			
$\mathrm{Im}(r^{6}_{1-1})$	0.001	0.04			

Table 4.19. The estimate of the systematic uncertainty in the extracted value of r^{α}_{ij} due to the uncertainty of r^{α}_{ij} used in the acceptance correction. The difference column is the difference between the extracted and input values of r^{α}_{ij} with MC "data" from Table 4.5. The $|\sigma_{syst}|/\sigma_{stat}$ column is this uncertainty divided by $(\delta\, r^{\alpha}_{ij})_{stat}$ from Table 4.7. The average value of this estimate of this systematic uncertainty relative to the statistical uncertainty is 0.73.

r^{α}_{ij}	diff.	$\|\sigma_{syst}\|/\sigma_{stat}$	r^{α}_{ij}	diff.	$\|\sigma_{syst}\|/\sigma_{stat}$
r^{04}_{00}	0.001	0.05	$\mathrm{Im}(r^{3}_{10})$	0.041	0.93
r^{1}_{1-1}	0.021	0.70	$\mathrm{Im}(r^{3}_{1-1})$	-0.023	0.35
$\mathrm{Im}(r^{2}_{1-1})$	0.015	0.52	$\mathrm{Im}(r^{7}_{10})$	0.102	1.69
$\mathrm{Re}(r^{5}_{10})$	0.001	0.09	$\mathrm{Im}(r^{7}_{1-1})$	-0.050	0.51
$\mathrm{Im}(r^{6}_{10})$	0.001	0.10	r^{8}_{11}	-0.021	0.15
$\mathrm{Re}(r^{04}_{10})$	0.002	0.16	r^{8}_{00}	-0.021	0.12
r^{04}_{1-1}	-0.005	0.29	$\mathrm{Re}(r^{8}_{10})$	0.064	0.99
r^{1}_{11}	-0.029	0.68	r^{8}_{1-1}	0.030	0.28
r^{1}_{00}	0.079	1.45			
$\mathrm{Re}(r^{1}_{10})$	-0.029	1.36			
$\mathrm{Im}(r^{2}_{10})$	0.037	1.71			
r^{5}_{11}	-0.031	1.32			
r^{5}_{00}	0.023	0.80			
r^{5}_{1-1}	-0.029	2.05			
$\mathrm{Im}(r^{6}_{1-1})$	-0.010	0.68			

Table 4.20. The estimate of the systematic uncertainty in the extracted value of r^{α}_{ij} due to the uncertainty in the background shape. The difference column is the estimate of the uncertainty, $|r^{\alpha}_{ij}(\text{Regions I and III}) - r^{\alpha}_{ij}(\text{Region IV})|/2$. The $|\sigma_{syst}|/\sigma_{stat}$ column is this uncertainty divided by $(\delta\, r^{\alpha}_{ij})_{stat}$ from Table 4.7. Any entry with 0.00 (or 0.000) means that the effect is smaller than the number of significant figures shown. The average value of this estimate of this systematic uncertainty relative to the statistical uncertainty is 0.23.

r^{α}_{ij}	diff.	$\|\sigma_{syst}\|/\sigma_{stat}$	r^{α}_{ij}	diff.	$\|\sigma_{syst}\|/\sigma_{stat}$
r^{04}_{00}	0.001	0.05	$\mathrm{Im}(r^{3}_{10})$	0.000	0.00
r^{1}_{1-1}	−0.006	0.20	$\mathrm{Im}(r^{3}_{1-1})$	0.002	0.03
$\mathrm{Im}(r^{2}_{1-1})$	−0.011	0.37	$\mathrm{Im}(r^{7}_{10})$	−0.002	0.03
$\mathrm{Re}(r^{5}_{10})$	0.003	0.32	$\mathrm{Im}(r^{7}_{1-1})$	0.008	0.08
$\mathrm{Im}(r^{6}_{10})$	0.002	0.15	r^{8}_{11}	0.007	0.07
$\mathrm{Re}(r^{04}_{10})$	0.001	0.08	r^{8}_{00}	−0.007	0.05
r^{04}_{1-1}	−0.004	0.21	$\mathrm{Re}(r^{8}_{10})$	−0.008	0.13
r^{1}_{11}	−0.011	0.36	r^{8}_{1-1}	−0.001	0.01
r^{1}_{00}	−0.002	0.04			
$\mathrm{Re}(r^{1}_{10})$	0.009	0.45			
$\mathrm{Im}(r^{2}_{10})$	−0.004	0.19			
r^{5}_{11}	−0.026	1.54			
r^{5}_{00}	−0.011	0.49			
r^{5}_{1-1}	−0.004	0.27			
$\mathrm{Im}(r^{6}_{1-1})$	−0.001	0.09			

sideband of ΔE, Region IV, to estimate the background underneath the peak, we redo the analysis, using Region IV to determine the shape of the background. The systematic uncertainty in r^{α}_{ij} due to the uncertainty in the shape of the background is the difference between the r^{α}_{ij}'s extracted when using Region I and III and those extracted when using Region IV, the results of which are tabulated in Table 4.20.

The constraints used to define the exclusive ϕ data sample that would affect the amount of non-exclusive background under the exclusive peak are the ϕ mass and exclusivity constraints, $1.012 < M_{2K} < 1.028\,\text{GeV}$ and $\Delta E < 1.0\,\text{GeV}$, as well as the pion decontamination constraint on the Čerenkov response for one of the hadrons, $\vec{p}_h > 4.0\,\text{GeV}$ with Č$< 0.2\,$photo-electrons. To study the sensitivity of r^{α}_{ij} to the background correction, we redo the analysis, modifying these constraint limits.

First, to quantify the sensitivity of r^{α}_{ij} to the ϕ mass constraint, we redo the

Table 4.21. The estimate of the systematic uncertainty in the extracted value of r^{α}_{ij} due to the choice of the ϕ mass constraint, $1.012 < M_{2K} < 1.028\,\text{GeV}$. The difference column is the estimate of the uncertainty, $|r^{\alpha}_{ij}(\text{wider}) - r^{\alpha}_{ij}(\text{narrower})|/2$. The $|\sigma_{syst}|/\sigma_{stat}$ column is this uncertainty divided by $(\delta\, r^{\alpha}_{ij})_{stat}$ from Table 4.7. Any entry with 0.00 (or 0.000) means that the effect is smaller than the number of significant figures shown. The average value of this estimate of this systematic uncertainty relative to the statistical uncertainty is 0.11.

r^{α}_{ij}	diff.	$\lvert\sigma_{syst}\rvert/\sigma_{stat}$	r^{α}_{ij}	diff.	$\lvert\sigma_{syst}\rvert/\sigma_{stat}$
r^{04}_{00}	0.005	0.26	$\mathrm{Im}(r^{3}_{10})$	0.009	0.21
r^{1}_{1-1}	0.006	0.19	$\mathrm{Im}(r^{3}_{1-1})$	0.009	0.13
$\mathrm{Im}(r^{2}_{1-1})$	0.008	0.29	$\mathrm{Im}(r^{7}_{10})$	0.005	0.07
$\mathrm{Re}(r^{5}_{10})$	0.000	0.01	$\mathrm{Im}(r^{7}_{1-1})$	0.001	0.01
$\mathrm{Im}(r^{6}_{10})$	0.000	0.04	r^{8}_{11}	0.011	0.08
$\mathrm{Re}(r^{04}_{10})$	0.001	0.12	r^{8}_{00}	0.015	0.08
r^{04}_{1-1}	0.002	0.09	$\mathrm{Re}(r^{8}_{10})$	0.010	0.15
r^{1}_{11}	0.003	0.07	r^{8}_{1-1}	0.014	0.13
r^{1}_{00}	0.010	0.18			
$\mathrm{Re}(r^{1}_{10})$	0.004	0.18			
$\mathrm{Im}(r^{2}_{10})$	0.001	0.04			
r^{5}_{11}	0.000	0.01			
r^{5}_{00}	0.002	0.07			
r^{5}_{1-1}	0.000	0.01			
$\mathrm{Im}(r^{6}_{1-1})$	0.001	0.06			

analysis twice, widening and narrowing this constraint to $1.010 < M_{2K} < 1.030\,\text{GeV}$ and $1.014 < M_{2K} < 1.026\,\text{GeV}$. Note that when changing the width of the M_{2K} region that defines the ϕ data sample like this, the width of data regions I and III which define the background correction must also be changed appropriately. With the wider mass constraint, there are 2353 exclusive ϕ candidates with an estimated 15% non-exclusive background, and with the narrower mass constraint, there are 1983 exclusive ϕ candidates with an estimated 13% non-exclusive background. The systematic uncertainty in r^{α}_{ij} due to the mass constraint of the ϕ is estimated by half the absolute value of the difference between the r^{α}_{ij}'s extracted with wider and narrower mass constraints, the results of which are tabulated in Table 4.21. The systematic uncertainties due to the ϕ mass constraint are small relative to the statistical uncertainties.

Table 4.22. The estimate of the systematic uncertainty in the extracted value of r^{α}_{ij} due to the exclusivity constraint, $\Delta E < 1.0\,\mathrm{GeV}$. The difference column is the estimate of the uncertainty, $|r^{\alpha}_{ij}(\Delta E < 0.8) - r^{\alpha}_{ij}(\Delta E < 1.2)|/2$. The $|\sigma_{syst}|/\sigma_{stat}$ column is this uncertainty divided by $(\delta\, r^{\alpha}_{ij})_{stat}$ from Table 4.7. Any entry with 0.00 (or 0.000) means that the effect is smaller than the number of significant figures shown. The average value of this estimate of this systematic uncertainty relative to the statistical uncertainty is 0.14.

r^{α}_{ij}	diff.	$\lvert\sigma_{syst}\rvert/\sigma_{stat}$	r^{α}_{ij}	diff.	$\lvert\sigma_{syst}\rvert/\sigma_{stat}$
r^{04}_{00}	0.000	0.01	$\mathrm{Im}(r^{3}_{10})$	0.009	0.20
r^{1}_{1-1}	0.009	0.30	$\mathrm{Im}(r^{3}_{1-1})$	0.004	0.06
$\mathrm{Im}(r^{2}_{1-1})$	0.003	0.10	$\mathrm{Im}(r^{7}_{10})$	0.002	0.03
$\mathrm{Re}(r^{5}_{10})$	0.001	0.12	$\mathrm{Im}(r^{7}_{1-1})$	0.017	0.17
$\mathrm{Im}(r^{6}_{10})$	0.002	0.15	r^{8}_{11}	0.012	0.09
$\mathrm{Re}(r^{04}_{10})$	0.000	0.02	r^{8}_{00}	0.021	0.12
r^{04}_{1-1}	0.001	0.06	$\mathrm{Re}(r^{8}_{10})$	0.019	0.29
r^{1}_{11}	0.012	0.27	r^{8}_{1-1}	0.021	0.20
r^{1}_{00}	0.007	0.12			
$\mathrm{Re}(r^{1}_{10})$	0.005	0.26			
$\mathrm{Im}(r^{2}_{10})$	0.007	0.30			
r^{5}_{11}	0.001	0.05			
r^{5}_{00}	0.001	0.04			
r^{5}_{1-1}	0.001	0.06			
$\mathrm{Im}(r^{6}_{1-1})$	0.003	0.20			

Next, to quantify the sensitivity of r^{α}_{ij} to the exclusivity constraint used on the data, we redo the analysis twice, tightening and loosening this constraint to $\Delta E < 0.8\,\mathrm{GeV}$ and $\Delta E < 1.2\,\mathrm{GeV}$. With the tighter exclusivity constraint, there are 1995 exclusive ϕ candidate events with an estimated 13% non-exclusive background, and with the looser exclusivity constraint, there are 2393 exclusive ϕ candidate events with an estimated 15% non-exclusive background. The systematic uncertainty in r^{α}_{ij} due to the exclusivity constraint is estimated by half the absolute value of the difference between the r^{α}_{ij}'s extracted with tighter and looser exclusivity constraints, the results of which are tabulated in Table 4.22. The systematic uncertainties due to the ϕ exclusivity constraint are small relative to the statistical uncertainties.

Finally, we want to study the sensitivity of r^{α}_{ij} to the pion decontamination constraint, that is, where one of the detected hadrons is required to be above the

Table 4.23. The estimate of the systematic uncertainty in the extracted value of r_{ij}^{α} due to the constraint made in order to reduce the contamination of the K^+K^- sample by pions, $\vec{p}_h > 4.0\,\mathrm{GeV}$ and $\check{\mathrm{C}} < 0.2\,\mathrm{p.e.}$ on one of the hadron pair. The difference column is the estimate of the uncertainty, $r_{ij}^{\alpha}(\vec{p}_h > 4.0) - r_{ij}^{\alpha}(\vec{p}_h > 5.0)$. The $|\sigma_{syst}|/\sigma_{stat}$ column is the absolute value of this uncertainty divided by $(\delta\, r_{ij}^{\alpha})_{stat}$ from Table 4.7. Any entry with 0.00 (or 0.000) means that the effect is smaller than the number of significant figures shown. The average value of this estimate of this systematic uncertainty relative to the statistical uncertainty is 0.28.

r_{ij}^{α}	diff.	$\|\sigma_{syst}\|/\sigma_{stat}$	r_{ij}^{α}	diff.	$\|\sigma_{syst}\|/\sigma_{stat}$
r_{00}^{04}	0.015	0.78	$\mathrm{Im}(r_{10}^{3})$	−0.003	0.07
r_{1-1}^{1}	0.003	0.09	$\mathrm{Im}(r_{1-1}^{3})$	−0.019	0.29
$\mathrm{Im}(r_{1-1}^{2})$	−0.010	0.35	$\mathrm{Im}(r_{10}^{7})$	0.018	0.30
$\mathrm{Re}(r_{10}^{5})$	−0.002	0.14	$\mathrm{Im}(r_{1-1}^{7})$	0.077	0.78
$\mathrm{Im}(r_{10}^{6})$	0.000	0.04	r_{11}^{8}	0.009	0.07
$\mathrm{Re}(r_{10}^{04})$	0.003	0.24	r_{00}^{8}	−0.004	0.02
r_{1-1}^{04}	−0.001	0.07	$\mathrm{Re}(r_{10}^{8})$	−0.019	0.29
r_{11}^{1}	0.005	0.12	r_{1-1}^{8}	0.003	0.03
r_{00}^{1}	0.029	0.53			
$\mathrm{Re}(r_{10}^{1})$	0.015	0.70			
$\mathrm{Im}(r_{10}^{2})$	−0.012	0.53			
r_{11}^{5}	−0.002	0.10			
r_{00}^{5}	0.004	0.15			
r_{1-1}^{5}	−0.009	0.67			
$\mathrm{Im}(r_{1-1}^{6})$	0.000	0.00			

pion momentum threshold in the Čerenkov detector, $\vec{p}_h > 4.0\,\mathrm{GeV}$, and exhibit no response in this detector ($\check{\mathrm{C}} < 0.2$ photo-electrons). To estimate the effect of the pion decontamination constraint on r_{ij}^{α}, we redo the analysis, increasing the minimum momentum requirement to $\vec{p}_h > 5.0\,\mathrm{GeV}$. With the higher momentum requirement, there are 1888 exclusive ϕ candidate events, with an estimated 12% non-exclusive background. The systematic uncertainty in r_{ij}^{α} due to the pion decontamination constraint is then the difference of r_{ij}^{α} extracted with the nominal minimum momentum minus r_{ij}^{α} extracted with the higher minimum momentum. The results of this estimate are tabulated in Table 4.23. The systematic uncertainty due to the pion decontamination constraint is generally smaller than the statistical uncertainty.

Table 4.24. The estimate of the systematic uncertainty in the extracted value of r^{α}_{ij} due to the radiative corrections performed on the data. The difference column is the estimate of the uncertainty, equal to half the value of the correction tabulated in Table 4.6. The $|\sigma_{syst}|/\sigma_{stat}$ column is the absolute value of this uncertainty divided by $(\delta\, r^{\alpha}_{ij})_{stat}$ from Table 4.7. Any entry with 0.00 (or 0.000) means that the effect is smaller than the number of significant figures shown. The average value of this estimate of this systematic uncertainty relative to the statistical uncertainty is 0.08.

r^{α}_{ij}	diff.	$\|\sigma_{syst}\|/\sigma_{stat}$	r^{α}_{ij}	diff.	$\|\sigma_{syst}\|/\sigma_{stat}$
r^{04}_{00}	-0.002	0.10	$\mathrm{Im}(r^{3}_{10})$	0.000	0.00
r^{1}_{1-1}	0.001	0.02	$\mathrm{Im}(r^{3}_{1-1})$	0.000	0.01
$\mathrm{Im}(r^{2}_{1-1})$	-0.001	0.03	$\mathrm{Im}(r^{7}_{10})$	0.000	0.00
$\mathrm{Re}(r^{5}_{10})$	0.001	0.10	$\mathrm{Im}(r^{7}_{1-1})$	0.001	0.01
$\mathrm{Im}(r^{6}_{10})$	0.001	0.06	r^{8}_{11}	0.000	0.00
$\mathrm{Re}(r^{04}_{10})$	-0.004	0.29	r^{8}_{00}	0.001	0.00
r^{04}_{1-1}	0.000	0.03	$\mathrm{Re}(r^{8}_{10})$	0.000	0.01
r^{1}_{11}	-0.004	0.10	r^{8}_{1-1}	0.000	0.00
r^{1}_{00}	-0.001	0.02			
$\mathrm{Re}(r^{1}_{10})$	0.004	0.21			
$\mathrm{Im}(r^{2}_{10})$	-0.005	0.23			
r^{5}_{11}	-0.006	0.28			
r^{5}_{00}	-0.006	0.19			
r^{5}_{1-1}	0.001	0.08			
$\mathrm{Im}(r^{6}_{1-1})$	-0.001	0.07			

4.3.5 Other Effects In this section, we discuss the systematic uncertainty associated with effects not yet covered in the previous subsections.

The first effect for which we will estimate the systematic uncertainty is the radiative correction, which was described in Subsection 4.2.5. As the radiative correction procedure we have used is quite simple, we estimate the systematic uncertainty due to the radiative correction is estimated to be half of the size of the correction, and is tabulated in Table 4.24. This is most likely an overestimate of the uncertainty. However, this systematic uncertainty is already very small compared to other effects.

The second effect to address is the technique by which we correct the data for acceptance effects. The acceptance correction used in this work is performed on histograms of data, one histogram for each spin-density matrix element. Both the data and the acceptance correction are binned as a function of F, the function associated with the r^{α}_{ij} of interest, these histograms are multiplied together, and the mean value of the resulting histogram is taken as the moment. The acceptance correction can also be performed on each data event individually, a technique alluded to when the matrix of linear-correlation coefficients was calculated at the end of section 4.2. In this technique, the acceptance correction is binned in the three-dimensional space of $(\cos\theta, \varphi, \Phi)$, and the moment is calculated by computing the average value of F over the data, weighing each event by the acceptance correction depending on its values of $(\cos\theta, \varphi, \Phi)$. We estimate the systematic uncertainty associated with the acceptance correction technique as the difference in r^{α}_{ij} obtained when correcting the data in histograms and when correcting the data events individually. The results of this study are tabulated in Table 4.25. For most of the matrix elements, the estimate of this systematic uncertainty is smaller than the statistical uncertainty.

The last systematic effect we would like to address is the stability of the results over time. The data presented in this work were collected over a couple of years, from August 1995 through November 1997. At two points during this time, in early 1996 and in early 1997, several components of the detector system were removed, repaired (or maintained), and subsequently replaced. It is conceivable that such changes to the detection apparatus during these "access periods" could significantly affect the results extracted from these data. To address this issue, we separate the data into three data-taking periods, split by the access periods, labeled by year: 1995, 1996, and 1997. The results of the spin-density matrix elements extracted from the data in each year are tabulated in Table 4.26. To estimate the effect of the time stability of the data, we compute the root-mean-square [75] (RMS) of the results from the three collection periods. Presumably, there are two effects which contribute to the value of the RMS: the statistical fluctuations which arise from using independent data sets, and the year-to-year changes in the running conditions.

Table 4.25. The estimate of the uncertainty due to the technique used to perform the acceptance correction. The difference column is the estimate of the uncertainty, the difference in r^{α}_{ij} obtained with the correction performed on data histograms and with the correction performed on each data event individually: $r^{\alpha}_{ij}(\text{histos}) - r^{\alpha}_{ij}(\text{events})$. The $|\sigma_{syst}|/\sigma_{stat}$ column is the absolute value of this uncertainty divided by $(\delta\, r^{\alpha}_{ij})_{stat}$ from Table 4.7. Any entry with 0.00 (or 0.000) means that the effect is smaller than the number of significant figures shown. The average value of this estimate of this systematic uncertainty relative to the statistical uncertainty is 0.52.

r^{α}_{ij}	diff.	$\lvert\sigma_{syst}\rvert/\sigma_{stat}$	r^{α}_{ij}	diff.	$\lvert\sigma_{syst}\rvert/\sigma_{stat}$
r^{04}_{00}	0.014	0.72	$\mathrm{Im}(r^{3}_{10})$	-0.026	0.60
r^{1}_{1-1}	0.047	1.56	$\mathrm{Im}(r^{3}_{1-1})$	-0.038	0.58
$\mathrm{Im}(r^{2}_{1-1})$	-0.052	1.82	$\mathrm{Im}(r^{7}_{10})$	0.016	0.26
$\mathrm{Re}(r^{5}_{10})$	-0.001	0.08	$\mathrm{Im}(r^{7}_{1-1})$	0.066	0.67
$\mathrm{Im}(r^{6}_{10})$	-0.002	0.22	r^{8}_{11}	-0.091	0.66
$\mathrm{Re}(r^{04}_{10})$	-0.011	0.91	r^{8}_{00}	0.032	0.18
r^{04}_{1-1}	-0.011	0.61	$\mathrm{Re}(r^{8}_{10})$	-0.010	0.15
r^{1}_{11}	0.010	0.22	r^{8}_{1-1}	-0.073	0.68
r^{1}_{00}	0.000	0.00			
$\mathrm{Re}(r^{1}_{10})$	-0.006	0.29			
$\mathrm{Im}(r^{2}_{10})$	0.025	1.15			
r^{5}_{11}	0.000	0.00			
r^{5}_{00}	0.005	0.16			
r^{5}_{1-1}	-0.004	0.28			
$\mathrm{Im}(r^{6}_{1-1})$	0.003	0.21			

Table 4.26. The spin-density matrix elements extracted from the three major periods of data collection. The 1995 sample contains 460 events, the 1996 sample contains 780 events, and the 1997 sample contains 950 events. The uncertainties are statistical.

r^{α}_{ij}	1995	1996	1997
r^{04}_{00}	0.338 ± 0.045	0.252 ± 0.030	0.331 ± 0.028
r^{1}_{1-1}	0.318 ± 0.071	0.301 ± 0.052	0.310 ± 0.043
$\mathrm{Im}(r^{2}_{1-1})$	-0.343 ± 0.065	-0.224 ± 0.049	-0.299 ± 0.043
$\mathrm{Re}(r^{5}_{10})$	0.145 ± 0.024	0.150 ± 0.017	0.137 ± 0.016
$\mathrm{Im}(r^{6}_{10})$	-0.183 ± 0.026	-0.175 ± 0.017	-0.158 ± 0.015
$\mathrm{Re}(r^{04}_{10})$	-0.040 ± 0.029	-0.007 ± 0.020	-0.015 ± 0.018
r^{04}_{1-1}	0.077 ± 0.040	-0.029 ± 0.030	0.020 ± 0.025
r^{1}_{11}	0.012 ± 0.073	0.013 ± 0.051	0.023 ± 0.045
r^{1}_{00}	0.075 ± 0.103	0.045 ± 0.067	0.004 ± 0.063
$\mathrm{Re}(r^{1}_{10})$	-0.054 ± 0.050	0.013 ± 0.036	-0.008 ± 0.031
$\mathrm{Im}(r^{2}_{10})$	-0.047 ± 0.050	-0.020 ± 0.035	0.036 ± 0.033
r^{5}_{11}	-0.028 ± 0.041	-0.025 ± 0.028	-0.007 ± 0.025
r^{5}_{00}	-0.013 ± 0.052	0.065 ± 0.036	0.008 ± 0.033
r^{5}_{1-1}	-0.011 ± 0.031	-0.012 ± 0.025	-0.015 ± 0.020
$\mathrm{Im}(r^{6}_{1-1})$	-0.037 ± 0.033	-0.008 ± 0.025	-0.036 ± 0.022
$\mathrm{Im}(r^{3}_{10})$	-0.084 ± 0.084	-0.030 ± 0.063	0.019 ± 0.065
$\mathrm{Im}(r^{3}_{1-1})$	-0.093 ± 0.119	-0.138 ± 0.097	-0.008 ± 0.097
$\mathrm{Im}(r^{7}_{10})$	-0.124 ± 0.113	-0.049 ± 0.085	0.055 ± 0.089
$\mathrm{Im}(r^{7}_{1-1})$	0.362 ± 0.178	0.137 ± 0.145	-0.052 ± 0.143
r^{8}_{11}	0.261 ± 0.183	0.064 ± 0.143	-0.148 ± 0.144
r^{8}_{00}	-0.353 ± 0.265	0.022 ± 0.190	0.061 ± 0.201
$\mathrm{Re}(r^{8}_{10})$	-0.038 ± 0.120	0.024 ± 0.094	-0.016 ± 0.094
r^{8}_{1-1}	-0.038 ± 0.192	0.166 ± 0.162	-0.256 ± 0.150

Table 4.27. The estimate of the uncertainty due to the stability of the detector apparatus over time. The Corr. RMS column is the estimate of the uncertainty, the square root of the RMS squared minus the average statistical uncertainty of r^{α}_{ij} squared using the data from each of the data collection periods from Table 4.26. Any entry with 0.00 (or 0.000) means that the computed RMS is smaller than the average statistical uncertainty. The $|\sigma_{syst}|/\sigma_{stat}$ column is this uncertainty divided by $(\delta\, r^{\alpha}_{ij})_{stat}$ from Table 4.7. The average value of this estimate of this systematic uncertainty relative to the statistical uncertainty is 0.48.

r^{α}_{ij}	Corr. RMS	$\lvert\sigma_{syst}\rvert/\sigma_{stat}$	r^{α}_{ij}	Corr. RMS	$\lvert\sigma_{syst}\rvert/\sigma_{stat}$
r^{04}_{00}	0.034	1.79	$\mathrm{Im}(r^{3}_{10})$	0.000	0.00
r^{1}_{1-1}	0.000	0.00	$\mathrm{Im}(r^{3}_{1-1})$	0.000	0.00
$\mathrm{Im}(r^{2}_{1-1})$	0.031	1.07	$\mathrm{Im}(r^{7}_{10})$	0.000	0.00
$\mathrm{Re}(r^{5}_{10})$	0.000	0.00	$\mathrm{Im}(r^{7}_{1-1})$	0.137	1.39
$\mathrm{Im}(r^{6}_{10})$	0.000	0.00	r^{8}_{11}	0.136	1.38
$\mathrm{Re}(r^{04}_{10})$	0.000	0.00	r^{8}_{00}	0.082	0.60
r^{04}_{1-1}	0.044	2.53	$\mathrm{Re}(r^{8}_{10})$	0.000	0.00
r^{1}_{11}	0.000	0.00	r^{8}_{1-1}	0.129	1.21
r^{1}_{00}	0.000	0.00			
$\mathrm{Re}(r^{1}_{10})$	0.000	0.00			
$\mathrm{Im}(r^{2}_{10})$	0.019	0.89			
r^{5}_{11}	0.000	0.00			
r^{5}_{00}	0.006	0.28			
r^{5}_{1-1}	0.000	0.00			
$\mathrm{Im}(r^{6}_{1-1})$	0.000	0.00			

In order to correct the RMS for the effect of the statistical fluctuations, we subtract the average statistical uncertainty (from the three columns in Table 4.26) squared from the RMS squared. The systematic uncertainty, then, is the square root of this difference. In the case that the computed RMS is smaller than the average statistical uncertainty, this means that the observed variation in the data is even less than that expected from normal statistical fluctuations. Therefore, for such matrix elements, we ascribe a systematic uncertainty of 0.000 for the year-to-year stability of the results. The results of this study are tabulated in Table 4.27.

The effects of the systematic studies performed in this section, averaged over all kinematic variables, are tabulated in Table 4.28. The largest source of systematic uncertainty for the spin-density matrix element analysis is the dependence of the

Table 4.28. Summary of effects included in the estimate of the systematic uncertainty. The $\langle|\sigma_{syst}|/\sigma_{stat}\rangle$ column is the average value of the estimate of this systematic uncertainty relative to the statistical uncertainty.

Description of study (subsection)	$\langle|\sigma_{syst}|/\sigma_{stat}\rangle$
Acceptance Correction: r_{ij}^{α} Dependence (4.3.3)	0.73
Top-Bottom Alignment (4.3.2)	0.69
Smearing (4.3.2)	0.54
Acceptance Correction Technique (4.3.5)	0.52
Extraction Technique (4.3.1)	0.51
Year-to-Year Variation (4.3.5)	0.48
Acceptance Correction: Q^2 Dependence (4.3.3)	0.42
Edge Effects (4.3.2)	0.33
π Decontamination Constraint (4.3.4)	0.28
Background Shape (4.3.4)	0.23
Acceptance Correction: σ_A/σ_p Dependence (4.3.3)	0.22
Acceptance Correction: b_A Dependence (4.3.3)	0.22
Acceptance Correction: b_p Dependence (4.3.3)	0.16
ΔE Constraint (4.3.4)	0.14
M_{2K} Constraint (4.3.4)	0.11
Acceptance Correction: $\sqrt{W^2}$ Dependence (4.3.3)	0.11
Radiative Correction (4.3.5)	0.08

results on the values of r_{ij}^{α} used in the acceptance correction.

The largest systematic uncertainties, that is, those estimated to be more than half of the statistical uncertainty, are due to effects which are independent from each other. As such, we will compute the total systematic uncertainty by simply adding all of the effects from all of the individual studies in quadrature for each matrix element. The final results for the spin-density matrix elements, including the statistical uncertainty and the total systematic uncertainty, are tabulated in Table 4.29. Tables of the results as a function of Q^2 and $-t'$, including the statistical uncertainties, are in Appendix C.

The results of the five spin-density matrix elements with systematic uncertainties estimated to be less than 50% of the measured values are plotted as a function of Q^2, $-t'$, and the target mass, A, in Figures 4.25, 4.26, 4.27, 4.28, 4.29, and 4.30. The results of the spin-density matrix elements which are less well-determined

Table 4.29. The final results of the spin-density matrix elements for ϕ's, integrated over all kinematic variables. The first uncertainty is statistical, the second, systematic. The kinematic ranges for these data are $0.5 < Q^2 < 5.0\,\mathrm{GeV}^2$ ($\langle Q^2\rangle = 1.67\,\mathrm{GeV}^2$), $3.5 < W < 6.5\,\mathrm{GeV}$ ($\langle W\rangle = 4.82\,\mathrm{GeV}$), and $0.0 < -t' < 2.0\,\mathrm{GeV}^2$ ($\langle -t'\rangle = 0.26\,\mathrm{GeV}^2$).

Unpolarized beam		Polarized beam	
r^{04}_{00}	$0.304 \pm 0.019 \pm 0.054$	$\mathrm{Im}(r^3_{10})$	$-0.022 \pm 0.044 \pm 0.064$
r^1_{1-1}	$0.309 \pm 0.030 \pm 0.067$	$\mathrm{Im}(r^3_{1-1})$	$-0.088 \pm 0.066 \pm 0.144$
$\mathrm{Im}(r^2_{1-1})$	$-0.281 \pm 0.029 \pm 0.071$	$\mathrm{Im}(r^7_{10})$	$-0.036 \pm 0.060 \pm 0.116$
$\mathrm{Re}(r^5_{10})$	$0.143 \pm 0.011 \pm 0.013$	$\mathrm{Im}(r^7_{1-1})$	$0.145 \pm 0.098 \pm 0.227$
$\mathrm{Im}(r^6_{10})$	$-0.169 \pm 0.010 \pm 0.011$	r^8_{11}	$0.031 \pm 0.099 \pm 0.200$
$\mathrm{Re}(r^{04}_{10})$	$-0.018 \pm 0.012 \pm 0.026$	r^8_{00}	$-0.051 \pm 0.137 \pm 0.119$
r^{04}_{1-1}	$0.014 \pm 0.017 \pm 0.051$	$\mathrm{Re}(r^8_{10})$	$-0.037 \pm 0.065 \pm 0.125$
r^1_{11}	$0.017 \pm 0.031 \pm 0.053$	r^8_{1-1}	$-0.057 \pm 0.106 \pm 0.322$
r^1_{00}	$0.033 \pm 0.042 \pm 0.078$		
$\mathrm{Re}(r^1_{10})$	$-0.010 \pm 0.021 \pm 0.061$		
$\mathrm{Im}(r^2_{10})$	$-0.001 \pm 0.022 \pm 0.062$		
r^5_{11}	$-0.017 \pm 0.017 \pm 0.043$		
r^5_{00}	$0.024 \pm 0.022 \pm 0.033$		
r^5_{1-1}	$-0.013 \pm 0.014 \pm 0.033$		
$\mathrm{Im}(r^6_{1-1})$	$-0.026 \pm 0.015 \pm 0.028$		

are plotted in Appendix C.

A final thing to note about the data presented here concerns the decay angular distribution, $W(\cos\theta,\varphi,\Phi)$, which is parameterized by r^{α}_{ij}. As discussed in Subsection 2.1.4, $W(\cos\theta,\varphi,\Phi)$ is a probability distribution, so that $W(\cos\theta,\varphi,\Phi) \geq 0$ should be true for all $(\cos\theta,\varphi,\Phi)$. Note that with the measured r^{α}_{ij} presented in Table 4.29, it turns out that there are regions of $(\cos\theta,\varphi,\Phi)$ phase space which yield a negative value for $W(\cos\theta,\varphi,\Phi)$. By varying the values of r^{04}_{00}, $\mathrm{Re}(r^{04}_{10})$, r^{04}_{1-1}, r^1_{1-1}, $\mathrm{Im}(r^2_{1-1})$, r^5_{00}, $\mathrm{Re}(r^5_{10})$, and $\mathrm{Im}(r^6_{10})$ within their listed systematic uncertainties, a positive-definite $W(\cos\theta,\varphi,\Phi)$ can be obtained.

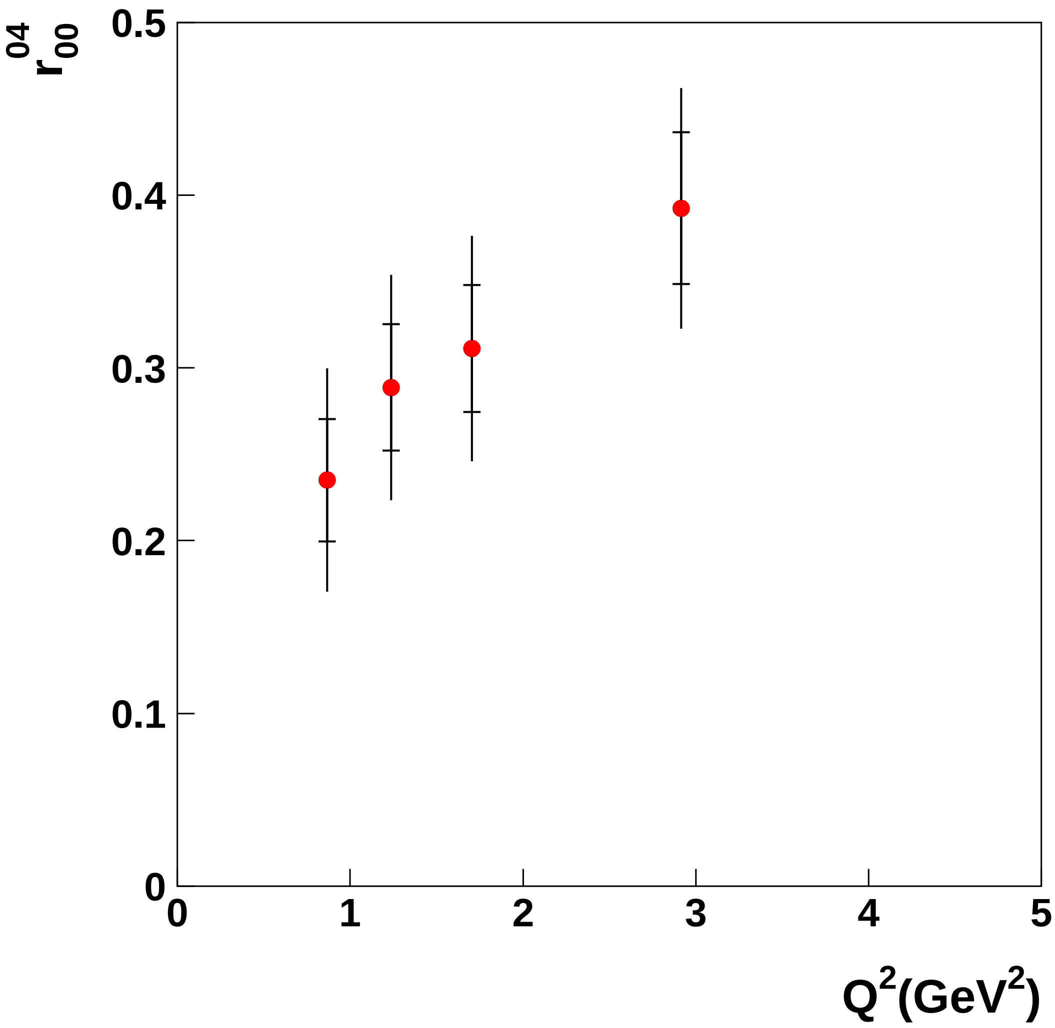

Figure 4.25. The longitudinal polarization of ϕ mesons plotted as a function of Q^2. The longitudinal polarization of ϕ's is seen to increase as Q^2 increases. The inner error bars on the points represent the statistical uncertainty, while the outer error bars indicate the statistical and systematic uncertainties added in quadrature. The systematic uncertainty for each kinematic bin is taken to be the average systematic uncertainty from Table 4.29.

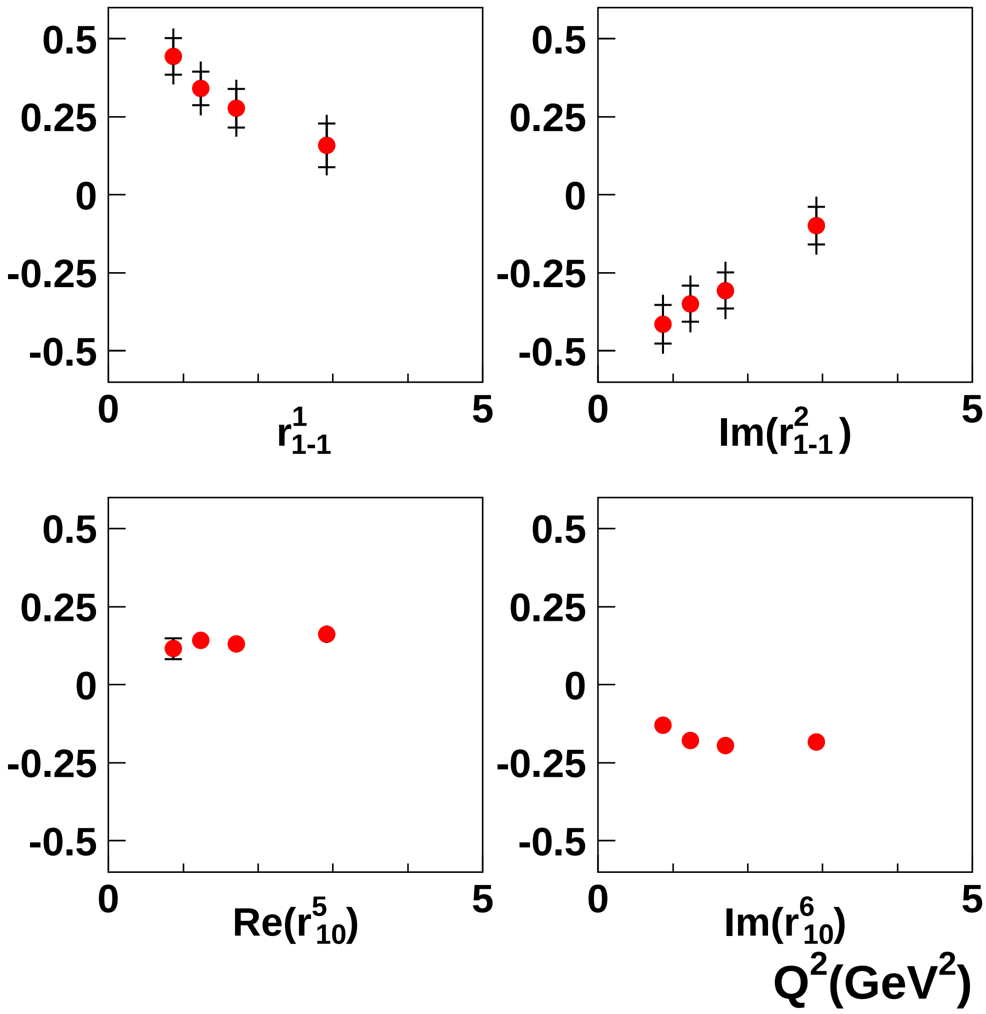

Figure 4.26. The spin-density matrix elements which have estimates for their systematic uncertainties that are less than 50% of the measured value, plotted as a function of Q^2. In the case of SCHC, $r^1_{1-1} = -\mathrm{Im}(r^2_{1-1})$, and this spin-density matrix element can be related to the transverse polarization of the ϕ. The observed decrease of r^1_{1-1} as Q^2 increases is matched by a corresponding increase in r^{04}_{00}, the longitudinal polarization of the ϕ, seen in Figure 4.25. The inner error bars on the points represent the statistical uncertainty, while the outer error bars indicate the statistical and systematic uncertainties added in quadrature. The systematic uncertainty for each kinematic bin is taken to be the average systematic uncertainty from Table 4.29.

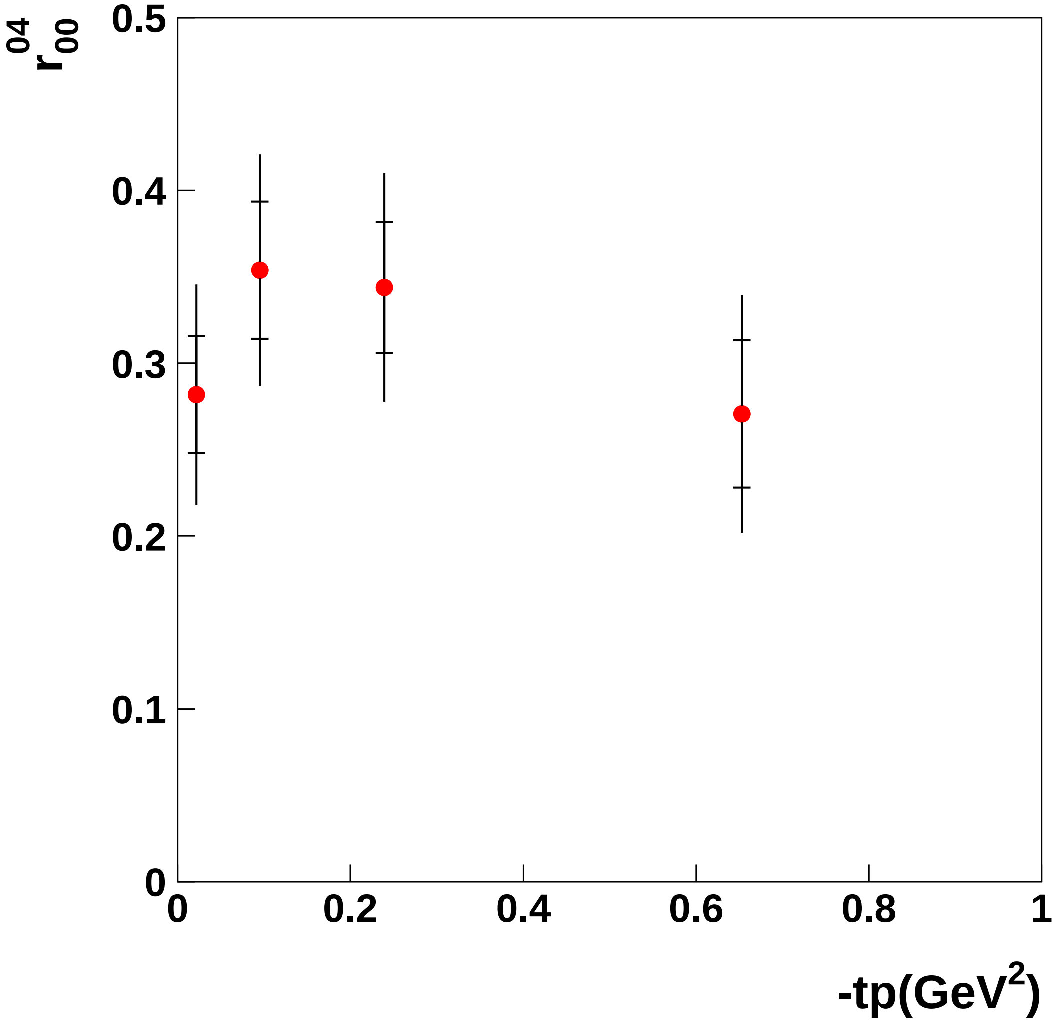

Figure 4.27. The longitudinal polarization of ϕ mesons plotted as a function of $-t'$. This matrix element does not depend strongly on $-t'$. The inner error bars on the points represent the statistical uncertainty, while the outer error bars indicate the statistical and systematic uncertainties added in quadrature. The systematic uncertainty for each kinematic bin is taken to be the average systematic uncertainty from Table 4.29.

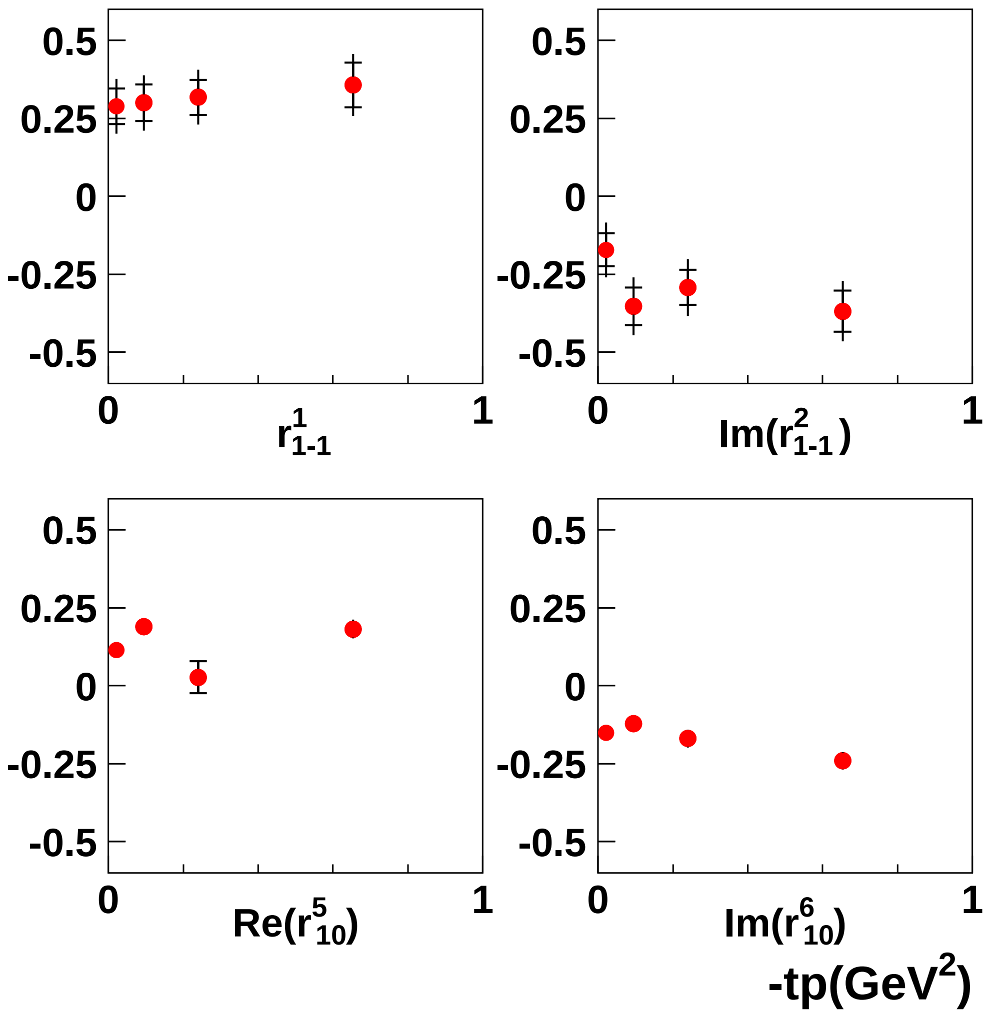

Figure 4.28. The spin-density matrix elements which have estimates for their systematic uncertainties that are less than 50% of the measured value, plotted as a function of $-t'$. None of these matrix elements are observed to depend strongly on $-t'$. The inner error bars on the points represent the statistical uncertainty, while the outer error bars indicate the statistical and systematic uncertainties added in quadrature. The systematic uncertainty for each kinematic bin is taken to be the average systematic uncertainty from Table 4.29.

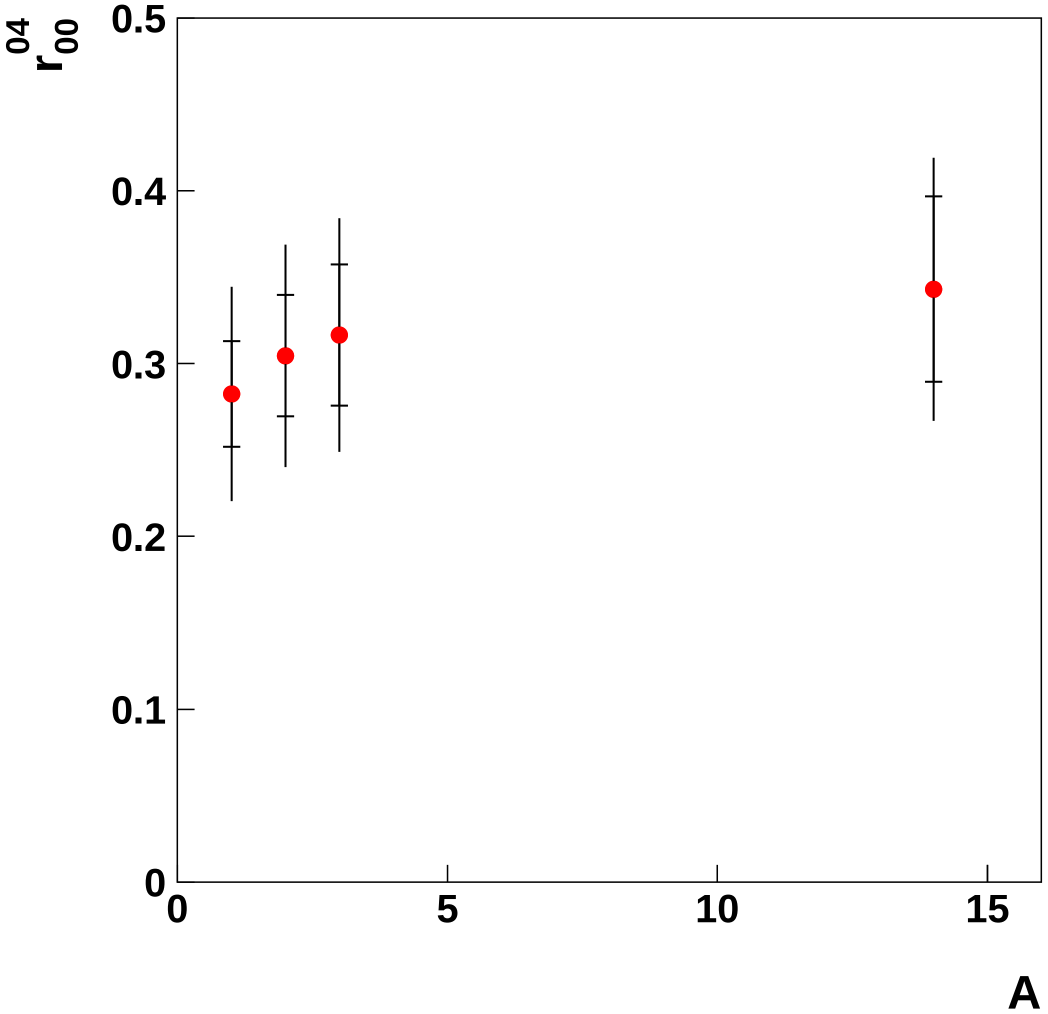

Figure 4.29. The longitudinal polarization of the ϕ meson plotted as a function of target mass, A, for the four types of target analyzed in this thesis. This matrix element does not have a strong dependence on A. The inner error bars on the points represent the statistical uncertainty, while the outer error bars indicate the statistical and systematic uncertainties added in quadrature. The systematic uncertainty for each target type is taken to be the average systematic uncertainty from Table 4.29.

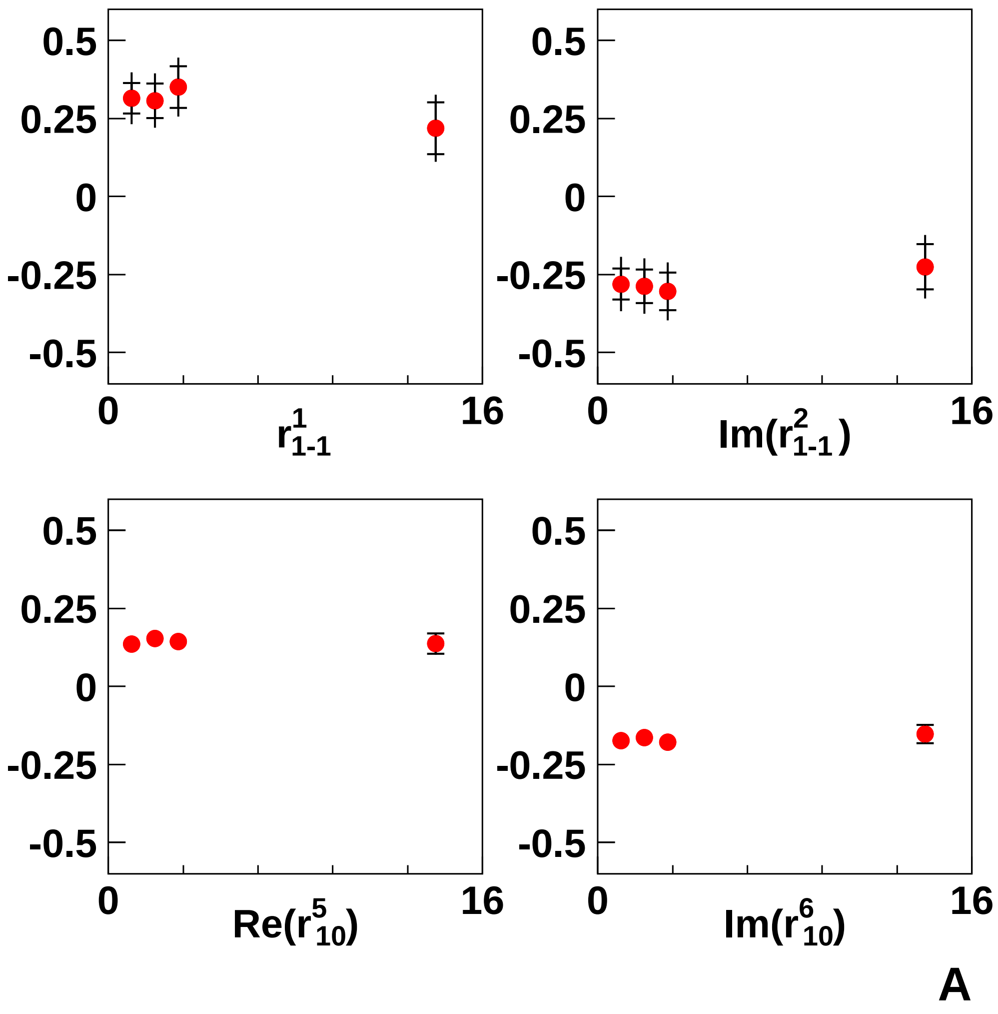

Figure 4.30. The spin-density matrix elements which have estimates for their systematic uncertainties that are less than 50% of the measured value, plotted as a function of A. None of these spin-density matrix elements depends strongly on A. The inner error bars on the points represent the statistical uncertainty, while the outer error bars indicate the statistical and systematic uncertainties added in quadrature. The systematic uncertainty for each target type is taken to be the average systematic uncertainty from Table 4.29.

CHAPTER 5

RESULTS

The final results from the spin-density matrix element analysis for ϕ vector mesons were presented in Table 4.29. In this section, we use these results to understand the helicity contributions of ϕ virtual photoproduction.

5.1 Helicity Amplitudes and Tests of SCHC and NPE

As described in Subsection 2.2.5, the phenomenon of s-channel helicity conservation (SCHC) predicts the following values of the helicity amplitudes:

$$T_{-10} = T_{0-1} = T_{10} = T_{01} = 0, \text{ and} \tag{5.1}$$

$$T_{-11} = T_{1-1} = 0. \tag{5.2}$$

In terms of the spin-density matrix elements, r^{α}_{ij}, SCHC manifests itself in that sixteen of them would be zero,

$$r^{04}_{10} = r^{04}_{1-1} = 0, \tag{5.3}$$

$$r^{1}_{00} = r^{1}_{11} = r^{1}_{10} = 0, \tag{5.4}$$

$$r^{2}_{10} = 0, \tag{5.5}$$

$$r^{3}_{10} = r^{3}_{1-1} = 0, \tag{5.6}$$

$$r^{5}_{00} = r^{5}_{11} = r^{5}_{1-1} = 0, \tag{5.7}$$

$$r^{6}_{1-1} = 0, \tag{5.8}$$

$$r^{7}_{1-1} = 0, \text{ and} \tag{5.9}$$

$$r^{8}_{00} = r^{8}_{11} = r^{8}_{1-1} = 0, \tag{5.10}$$

leaving only r^{04}_{00}, r^1_{1-1}, $\mathrm{Im}(r^2_{1-1})$, $\mathrm{Re}(r^5_{10})$, $\mathrm{Im}(r^6_{10})$, $\mathrm{Im}(r^7_{10})$, and $\mathrm{Re}(r^8_{10})$ to be (possibly) non-zero. Furthermore, SCHC would restrict the value of three of these spin-density matrix elements via the relations,

$$\begin{aligned} r^1_{1-1} &= -\mathrm{Im}(r^2_{1-1}), && (5.11) \\ \mathrm{Re}(r^5_{10}) &= -\mathrm{Im}(r^6_{10}), \text{ and} && (5.12) \\ \mathrm{Re}(r^8_{10}) &= \mathrm{Im}(r^7_{10}), && (5.13) \end{aligned}$$

reducing the total number of independent non-zero matrix elements to four: r^{04}_{00}, r^1_{1-1}, $\mathrm{Re}(r^5_{10})$, and $\mathrm{Im}(r^7_{10})$, about which SCHC says nothing. In total, there are 19 relations we want to test with the measurements from Table 4.29 in order to make a statistical statement about the validity of SCHC to describe these data. The statistical uncertainties are added in quadrature for the relations 5.11 to 5.13.

Using the table of r^α_{ij} in Table 4.29, the data have been measured such that out of the 19 relations expected with SCHC, 13 of them agree with the data within one sigma (statistical uncertainties, only), and 6 of them, within two sigma. Thus, we conclude that the ϕ data are consistent with SCHC. The three SCHC relations from Equations 5.11 to 5.13 are plotted as a function of Q^2 and $-t'$ in Figures 5.1 and 5.2, respectively. The sixteen matrix elements which have been measured to be consistent with zero are plotted as a function of Q^2 and $-t'$ in Appendix C. There are no clear systematic tendencies of these data to drift away from the predictions of SCHC. This indicates that the data are consistent with SCHC throughout the entire kinematic range studied here.

The consistency of these ϕ data with SCHC is in contrast to the measurements of r^α_{ij} for the ρ^0 meson at the high-energy collider experiments H1 [35] and ZEUS [37], who have reported significant deviations from zero for the matrix element r^5_{00}, and smaller deviations from zero for $\mathrm{Re}(r^{04}_{10})$, r^{04}_{1-1}, r^1_{11}, and $\mathrm{Im}(r^2_{10})$. At lower photon energies, an experiment at DESY in the early 1970's has reported non-zero

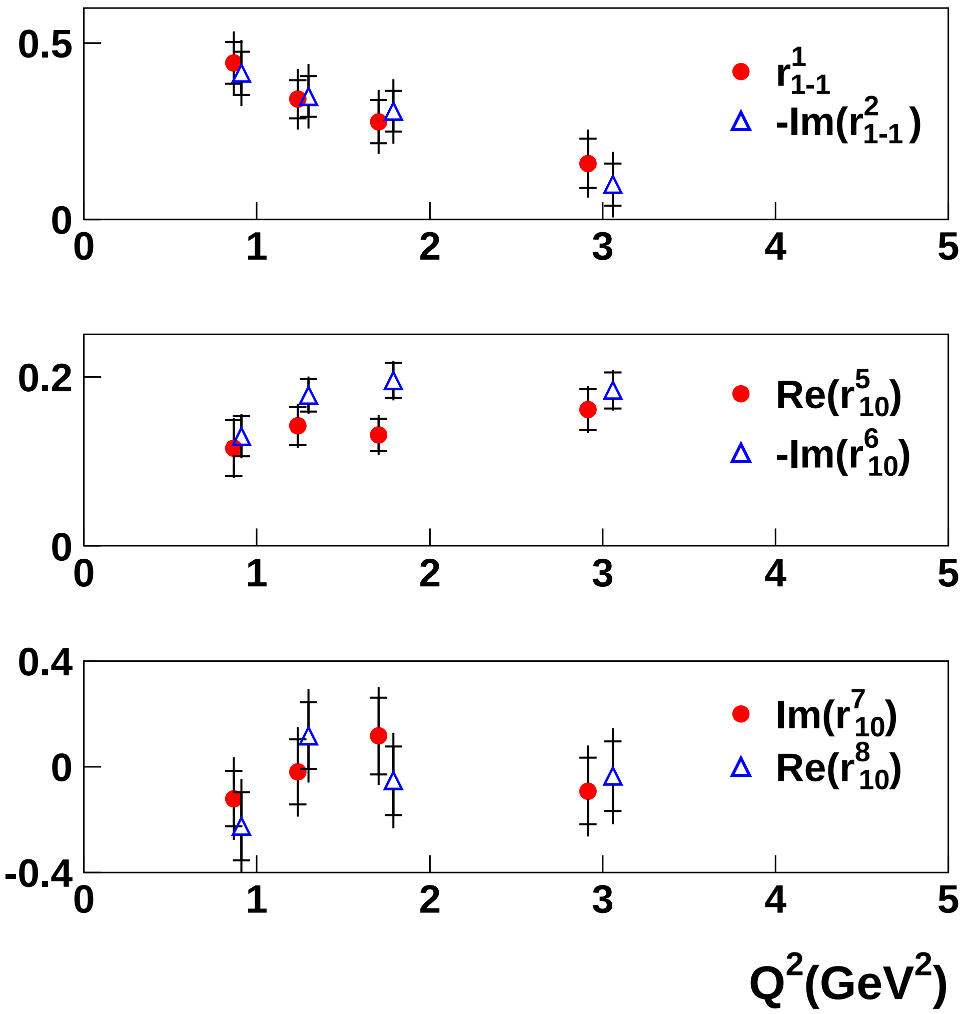

Figure 5.1. The data of the relations between r^{α}_{ij} predicted in the case of SCHC, plotted as a function of Q^2. The Q^2 values for the open points are shifted by 5% for ease of viewing. For the most part, the open and closed points lie on top of each other, indicating consistency with SCHC. The inner error bars on the points represent the statistical uncertainty, while the outer error bars indicate the statistical and systematic uncertainties added in quadrature. The systematic uncertainty for each kinematic bin is taken to be the average systematic uncertainty from Table 4.29.

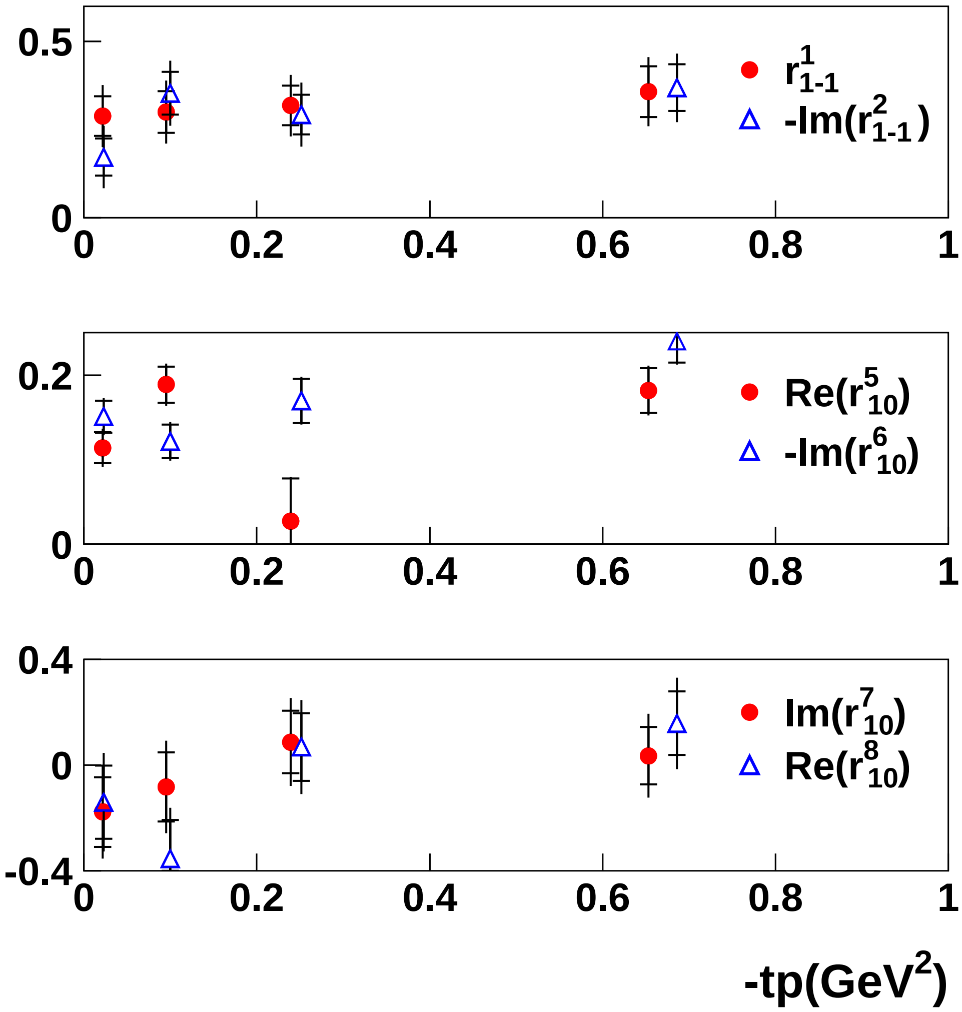

Figure 5.2: The same as Figure 5.1, only plotted versus $-t'$.

measurements of the SCHC-violating matrix elements $\mathrm{Re}(r^{04}_{10})$ and $\mathrm{Im}(r^{6}_{1-1})$. [31] The ϕ data measured here for r^{5}_{00} and $\mathrm{Re}(r^{04}_{10})$ are compared to the low and high-energy ρ^0 data in Figure 5.3. In addition, preliminary data from ZEUS and H1 on the ϕ vector meson indicates the presence of the same SCHC-violating matrix elements as observed for the ρ^0 at collider kinematics. [29] [30]

That the ϕ data presented in this work are more consistent with SCHC than the ρ^0 data suggests a simplification of the mechanisms in the models for ϕ production compared to ρ^0 production at our energies, since none of the helicity structure of the ϕ need come from the target. In a model of ϕ electroproduction where the $\gamma^* + p \rightarrow \phi + p$ reaction occurs via the exchange of a particle, or system of particles, with the target through the t-channel, the observation of SCHC implies that the total helicity of the exchanged system is zero. In Regge models, for example, these data would be in favor of models where the ϕ production reaction takes place via pure Pomeron exchange, *i.e.*, with no Reggeon exchange terms.

Another feature of the ϕ production data to be tested is the prediction of Natural Parity Exchange (NPE) in the t-channel. If the data were consistent with NPE, this would mean that the parity quantum numbers of the t-channel exchange match the angular momentum quantum numbers in the form $J^P = 0^+,\ 1^-,\ 2^+,\ 3^-, \ldots$. As discussed in Subsection 2.2.5, the observation of NPE, in coincidence with SCHC, would be manifest in the relation

$$r^{04}_{00} + 2r^{1}_{1-1} = 1. \tag{5.14}$$

Plots of this relation as a function of Q^2 and $-t'$ are in Figures 5.4 and 5.5, respectively. Within the sizable uncertainties, the ϕ data presented here are consistent with the predictions of both SCHC and NPE at lower Q^2, however, there may be a tendency of the data to move away from NPE at higher Q^2.

Another way to quantify the appropriateness of SCHC to describe these

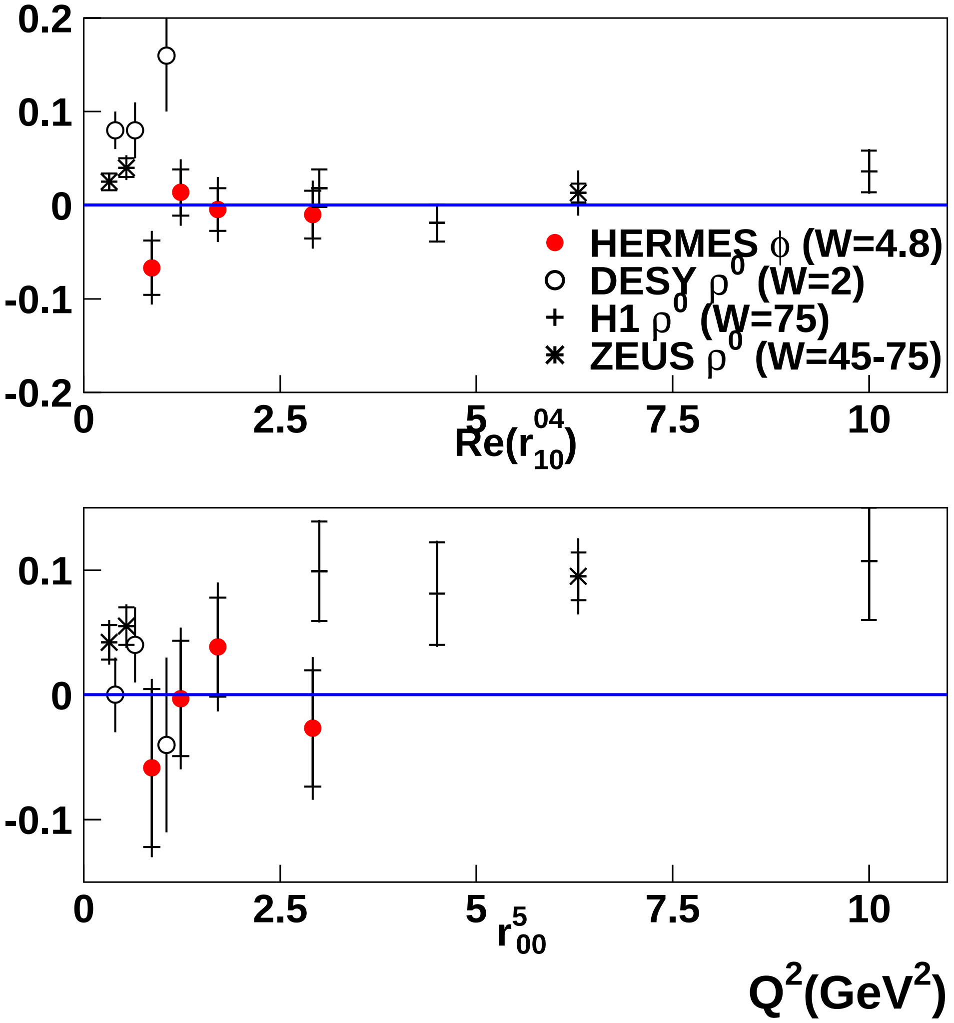

Figure 5.3. Comparison of ϕ and published ρ^0 data at low [31] and high-energy [35,37] for two of the spin-density matrix elements. On the DESY data, the error bars represent the statistical uncertainty, while on the other data, the inner error bars represent the statistical uncertainties and the outer error bars indicate the statistical and systematic uncertainties added in quadrature. The line indicates the prediction of SCHC. In the upper plot, the low energy ρ^0 data are not consistent with the predictions from SCHC. In the lower plot, the high energy ρ^0 data are not consistent with the predictions from SCHC. For both of these matrix elements, the ϕ data are consistent with SCHC.

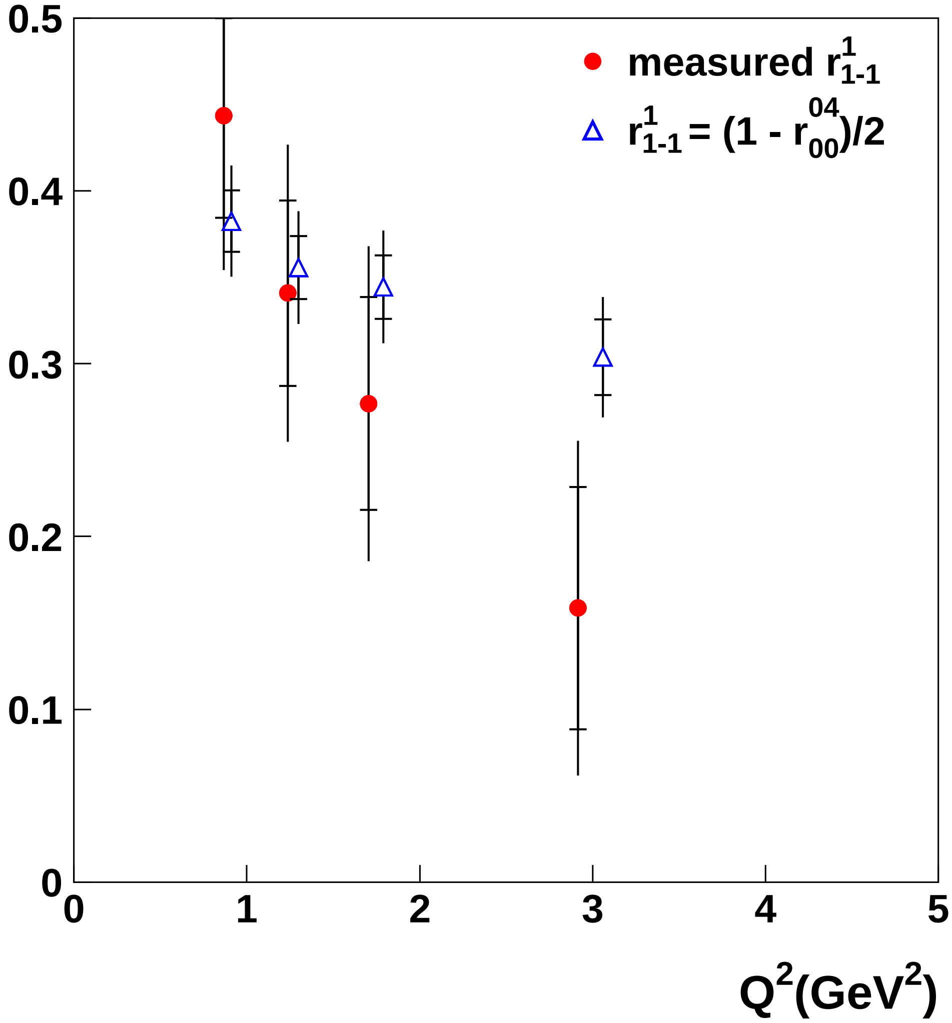

Figure 5.4. The test of the relation between r^{04}_{00} and r^1_{1-1} for the case of SCHC and NPE, plotted as a function of Q^2. The Q^2 values for the open points are shifted by 5% for ease of viewing. The inner error bars on the points represent the statistical uncertainty, while the outer error bars indicate the statistical and systematic uncertainties added in quadrature. The systematic uncertainty for each kinematic bin is taken to be the average systematic uncertainty from Table 4.29. Within the sizable uncertainties, the open and closed points lie on top of each other at low Q^2 indicating consistency with SCHC and NPE. As Q^2 increases, the open and closed points appear to become more disparate.

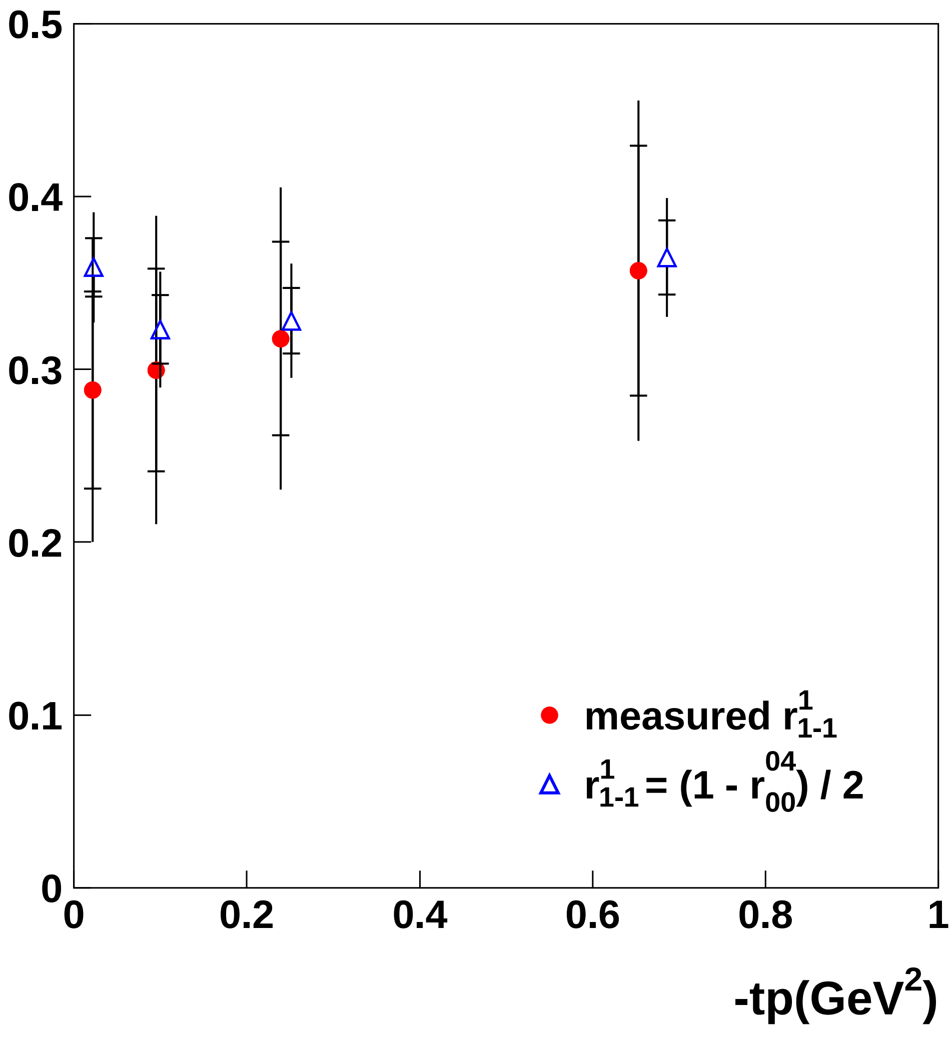

Figure 5.5: The same as Figure 5.4, only plotted versus $-t'$.

data is to look at the helicity amplitudes, themselves. In Appendix A, the spin-density matrix elements, r_{ij}^{α}, are written as the real or imaginary parts of the sums of bilinear combinations of the helicity amplitudes, $T_{\lambda_\phi \lambda_\gamma}$. Writing the helicity amplitudes as complex numbers in the form

$$T_{\lambda_\phi \lambda_\gamma} = |T_{\lambda_\phi \lambda_\gamma}| e^{i\varphi_{\lambda_\phi \lambda_\gamma}}, \tag{5.15}$$

where $|T_{\lambda_\phi \lambda_\gamma}|$ is the magnitude and $\varphi_{\lambda_\phi \lambda_\gamma}$ is the phase, we can use the measured values of r_{ij}^{α} from Table 4.29 to determine the magnitudes and phases of the helicity amplitudes.

We attempt to perform a fit to r_{ij}^{α}, using the fitting package MINUIT, as was done for preliminary ZEUS and H1 data in Reference [84]. For this fit, we assume NPE, so that there are only five independent helicity amplitudes to measure: T_{00}, T_{11}, T_{01}, T_{10}, and T_{1-1}, for a total of 10 independent parameters. We use the normalization $|T_{00}| = 1$ and $\varphi_{00} = 0$, and fit the magnitudes and phases of the other helicity amplitudes relative to these values. We perform the fit in three stages. First, we fit the magnitudes, $|T_{\lambda_\phi \lambda_\gamma}|$, and fix the values of the phases, $\varphi_{\lambda_\phi \lambda_\gamma}$, equal to some set of initial values. Next, we fit the phases, restricted to a range between $\pm 180°$, and fix the magnitudes equal to the values that were just fit. Finally, we fit both the phases and the magnitudes simultaneously, using the starting values of the parameters that have just been determined.

The best value for $|T_{11}|$ is approximately 1.3, regardless of the initial values of $\varphi_{\lambda_\phi \lambda_\gamma}$. The best values for $|T_{01}|$, $|T_{10}|$ and $|T_{1-1}|$ are all on the order of $<$ 0.3. However, it turns out that the fitted values of $|T_{01}|$, $|T_{10}|$, $|T_{1-1}|$, φ_{11}, φ_{01}, φ_{10}, and φ_{1-1} are highly correlated, and depend on the initial values of $\varphi_{\lambda_\phi \lambda_\gamma}$. A systematic study of the effect of changing the initial values of $\varphi_{\lambda_\phi \lambda_\gamma}$ on the χ^2 value of the fit shows that, depending on the initial values of $\varphi_{\lambda_\phi \lambda_\gamma}$, the fitting algorithm will converge to a set of one of approximately 15-20 possible "solutions", differing primarily in the fitted values of $\varphi_{\lambda_\phi \lambda_\gamma}$ (and χ^2). One group of these solutions to

Table 5.1. The magnitudes and phases of the helicity amplitudes, as obtained from fits to the measured spin-density matrix elements in Table 4.29. The two columns have different initial values for $\varphi_{\lambda_\phi\lambda_\gamma}$ in the fits. We shall take the set of parameters with $\chi^2 = 10.7$ as our best fit. The uncertainties are statistical.

	$\chi^2 = 10.7$		$\chi^2 = 17.9$	
Amplitude	$\lvert T_{\lambda_\phi\lambda_\gamma}\rvert$	$\varphi_{\lambda_\phi\lambda_\gamma}$ (deg.)	$\lvert T_{\lambda_\phi\lambda_\gamma}\rvert$	$\varphi_{\lambda_\phi\lambda_\gamma}$ (deg.)
T_{00}	1	0	1	0
T_{11}	1.28 ± 0.05	-29 ± 11	1.30 ± 0.06	4 ± 9
T_{01}	0.05 ± 0.08	32 ± 100	0.16 ± 0.11	-77 ± 18
T_{10}	0.14 ± 0.08	-119 ± 15	0.34 ± 0.11	98 ± 8
T_{1-1}	0.36 ± 0.14	65 ± 12	0.18 ± 0.11	-62 ± 28

which the fit converges has $\chi^2 \approx 25$, another slightly larger group of these solutions has $\chi^2 \approx 19$, a group of two solutions has $\chi^2 = 13.9$ and 13.2, and there is a single solution which has $\chi^2 = 10.7$ (out of 15 degrees of freedom). It is not clear which of these solutions is the proper solution. The values of the parameters from two fits, one with $\chi^2 = 10.7$ and another with $\chi^2 = 17.9$, are in Table 5.1, and are an example of the possible ranges of values that are obtained with these different "solutions." We shall take the set of magnitudes and phases corresponding to the fit with $\chi^2 = 10.7$ as our best fit values. The matrix of linear-correlation coefficients obtained from this fit is in Table 5.2. The significant correlations between the phases and the SCHC-violating magnitudes are clear from this table.

From the fitted values of the magnitudes of the helicity amplitudes, it is immediately clear that the SCHC-observing amplitudes are much larger than the SCHC-violating amplitudes, consistent with the conclusion reached earlier in this subsection. In addition, the transverse amplitude, T_{11}, is larger than the longitudinal amplitude, T_{00}, at these kinematics. The magnitudes of the individual SCHC-violating amplitudes are not well-constrained by this fit, nor are the phases of any of the amplitudes.

In the publications of the spin-density matrix elements for the ρ^0 meson from H1 [35] and ZEUS [37], they take a slightly different approach to determining

Table 5.2. The matrix of linear-correlation coefficients obtained by MINUIT for the best fit ($\chi^2 = 10.7$) of the magnitudes and the phases of the helicity amplitudes. This matrix is symmetric. The only parameter which is not significantly correlated with another is $|T_{11}|$.

	$\|T_{11}\|$	φ_{11}	$\|T_{01}\|$	φ_{01}	$\|T_{10}\|$	φ_{10}	$\|T_{1-1}\|$	φ_{1-1}
$\|T_{11}\|$	1.0							
φ_{11}	0.064	1.0						
$\|T_{01}\|$	0.150	0.485	1.0					
φ_{01}	0.130	0.591	0.847	1.0				
$\|T_{10}\|$	0.009	−0.131	−0.259	−0.388	1.0			
φ_{10}	0.032	0.627	0.323	0.401	0.364	1.0		
$\|T_{1-1}\|$	−0.054	0.763	0.292	0.420	−0.325	0.373	1.0	
φ_{1-1}	0.008	0.911	0.471	0.586	−0.281	0.503	0.812	1.0

the magnitudes of the helicity amplitudes, which we will now follow here. We make the assumption of SCHC for the following calculations, that is, we assume

$$|T_{00}|^2,\ |T_{11}|^2 \gg |T_{01}|^2,\ |T_{10}|^2,\ \text{and}\ |T_{1-1}|^2, \tag{5.16}$$

which is consistent with the fits from Table 5.1. We define

$$\tau_{01} = \frac{|T_{01}|}{\sqrt{|T_{11}|^2 + \epsilon\,|T_{00}|^2}}, \tag{5.17}$$

and, with SCHC and the additional assumption that $\varphi_{01} \approx \varphi_{00}$, we can write

$$\tau_{01} = \frac{|T_{01}|}{\sqrt{|T_{11}|^2 + \epsilon\,|T_{00}|^2}} \approx \sqrt{\epsilon}\frac{|r^5_{00}|}{\sqrt{2r^{04}_{00}}}. \tag{5.18}$$

Note that this expression differs from the one used by H1 and ZEUS only by the approximation $\epsilon \approx 1$, appropriate for their kinematics. Using Equation 5.18 with the results from Table 4.29, we obtain $\tau_{01} = 0.028 \pm 0.023$ (statistical uncertainty, only). This result is significantly smaller than the analogous quantities determined for the ρ^0 of $\tau_{01} = (8 \pm 3)\%$ (statistical only) and $\tau_{01} = (7.9 \pm 1.6\,(\text{stat.}) \pm 2.0\,(\text{syst.}))\%$ (DIS data) from References [35] and [37], respectively.

Along similar lines, we define

$$\tau_{10} = \frac{|T_{10}|}{\sqrt{|T_{11}|^2 + \epsilon\,|T_{00}|^2}}, \tag{5.19}$$

and, with SCHC and the additional assumption that $\varphi_{10} \approx \varphi_{00}$, we can write

$$\tau_{10} = \frac{|T_{10}|}{\sqrt{|T_{11}|^2 + \epsilon\,|T_{00}|^2}} \approx \frac{|\mathrm{Re}(r^{04}_{10}) + \mathrm{Re}(r^{1}_{10})|}{\sqrt{\epsilon\,r^{04}_{00}}}. \tag{5.20}$$

Using Equation 5.20 with the results from Table 4.29, we obtain $\tau_{10} = 0.057 \pm 0.049$ (statistical uncertainty, only). This result is comparable to the analogous quantity determined for the ρ^0 of $\tau_{10} = (2.7 \pm 1.9\,(\mathrm{stat.}) \pm 3.1\,(\mathrm{syst.}))\%$ (DIS data) from Reference [37]. Note that in Reference [85], it is shown that in the large Q^2 limit of pQCD, the produced vector meson is expected to be purely longitudinal, so that one might expect τ_{01} to be larger than τ_{10} in the large Q^2 limit, as has been observed for the ρ^0 for ZEUS kinematics. However, at HERMES kinematics, no such effect is observed for the ϕ.

Finally, we define

$$\tau_{1-1} = \frac{|T_{1-1}|}{\sqrt{|T_{11}|^2 + \epsilon\,|T_{00}|^2}}, \tag{5.21}$$

and, with SCHC and the additional assumption that $\varphi_{1-1} \approx \varphi_{00}$, we can write

$$\tau_{1-1} = \frac{|T_{1-1}|}{\sqrt{|T_{11}|^2 + \epsilon\,|T_{00}|^2}}, \approx \frac{|r^{1}_{11}|}{\sqrt{2\,r^{1}_{1-1}}}. \tag{5.22}$$

Using Equation 5.22 with the results from Table 4.29, we obtain $\tau_{1-1} = 0.022 \pm 0.036$ (statistical uncertainty, only). This result is comparable to the analogous quantity determined for the ρ^0 of $\tau_{1-1} = (1.4 \pm 2.7\,(\mathrm{stat.}) \pm 5.9\,(\mathrm{syst.}))\%$ (DIS data) from Reference [37].

5.2 Comparison of r^{α}_{ij} with pQCD Model

A model of ρ^0 electroproduction based on two gluon ($2g$) exchange by D. Ivanov and R. Kirschner [19] was discussed in Subsection 2.2.6. In this model, the photon fluctuates into a $q\bar{q}$ pair which subsequently interacts with the target via $2g$ exchange. The amplitude of this exchange was predicted to be proportional to the gluon distribution in the proton. [23] [86] The model is based on pQCD, meaning that the $q\bar{q}$ in the vector meson is written in terms of current quarks, and, as such, is meant to describe ρ^0 vector meson electroproduction in the hard, diffractive kinematic regime, where $W^2 \gg Q^2$ and $Q^2 \gg M_\rho^2$. We will compare the predictions of this model of r_{ij}^α to the data presented here on ϕ vector mesons at HERMES kinematics, where $\langle Q^2 \rangle = 1.7 \text{ GeV}^2 \approx M_\phi^2$ ($\langle W^2 \rangle = 24 \text{ GeV}^2$).

The recent data from HERMES on the ρ^0 total cross section are consistent with a model which predicts the dominance of $2q$ exchange amplitudes in this reaction at our kinematics. [87] Hence, it is not immediately obvious that the comparison of a $2g$ exchange model for the ρ^0 at high W is appropriate to compare with ϕ data at low W. To motivate this comparison, we look at the behavior of the total cross sections for ρ^0 and ϕ photoproduction as a function of W, the plot of which can be seen in Figure 2.6. At high energies, such as those at the HERA collider experiments, H1 and ZEUS ($W \approx 100\,\text{GeV}$), the total photoproduction cross sections for both the ρ^0 and the ϕ slowly decrease as W decreases. In terms of a Regge-based (parton-based) model, discussed in Subsection 2.2.4, the slow dependence of the cross section is interpreted to result from the diffractive exchange of a Pomeron ($2g$). As we decrease further in W to HERMES energies ($W \approx 5\,\text{GeV}$), the ρ^0 cross-section begins to increase dramatically, which is ascribed in these models to the increasing strength of Reggeon ($2q$) exchange amplitudes. The ϕ total cross section, however, does not increase as we move to lower W. The continued slow decrease of the ϕ cross section at low energies is interpreted as a result of the suppression of Reggeon amplitudes in ϕ production relative to ρ^0 production. Therefore, it may be reasonable to compare a $2g$ exchange model for the ρ^0 at high energies to ϕ production at HERMES kinematics, since $2q$ amplitudes are suppressed in ϕ production. It should be noted that, in the light-cone wave function formalism, the ρ^0 and the ϕ are treated identically. [88]

We must evaluate the predictions of this model for the helicity amplitudes at our kinematics. Recall that NPE is assumed, so that the only independent helicity amplitudes are T_{00}, T_{11}, T_{10}, T_{01}, and T_{1-1}. As discussed in Subsection 2.2.6, the ratios of these amplitudes are predicted to be given by the expressions,

$$\alpha = \frac{T_{11}}{T_{00}} = \frac{\langle M \rangle}{Q} \frac{1+\gamma}{\gamma}, \tag{5.23}$$

$$\beta = \frac{T_{10}}{T_{00}} = \frac{\sqrt{|t'|}}{Q} \frac{1}{\sqrt{2}\gamma}, \tag{5.24}$$

$$\delta = \frac{T_{01}}{T_{00}} = -\frac{\langle M \rangle \sqrt{|t'|}}{Q^2} \frac{\sqrt{2}}{\gamma}, \text{ and} \tag{5.25}$$

$$\eta = \frac{T_{1-1}}{T_{00}} = \eta^0 + \eta^1, \tag{5.26}$$

where

$$\eta^0 = -\frac{\bar{\alpha}_S^2 \, |t'| \langle M \rangle}{\pi \alpha_S Q m_\phi^2} \frac{1}{\{4\gamma[\Gamma^2(\gamma+1)/\Gamma(2\gamma+2)] x \, G(x, Q^2/4)\}}, \text{ and} \tag{5.27}$$

$$\eta^1 = \frac{|t'| \langle M \rangle}{Q^3} \frac{2(\gamma+2)}{\gamma}. \tag{5.28}$$

The average values of the kinematic variables for HERMES ϕ data to be used in the evaluation of these expressions are,

$$\langle M \rangle \approx M_\phi = 1.019\,\mathrm{GeV}, \tag{5.29}$$

$$|t'| = \langle |t'| \rangle = 0.34\,\mathrm{GeV}^2, \tag{5.30}$$

$$\sqrt{|t'|} = \langle \sqrt{|t'|} \rangle = 0.53\,\mathrm{GeV}, \tag{5.31}$$

$$Q = \langle \sqrt{Q^2} \rangle = 1.26\,\mathrm{GeV}, \tag{5.32}$$

$$Q^2 = \langle Q^2 \rangle = 1.67\,\mathrm{GeV}^2, \text{ and} \tag{5.33}$$

$$Q^3 = \langle (Q^2)^{3/2} \rangle = 2.39\,\mathrm{GeV}^3. \tag{5.34}$$

The gluon distribution of the proton, $x\,G(x, Q^2/4)$, is taken from the parameterizations of the parton distributions by Martin, Stirling, and Roberts, called the MRS fit. [86] The parameterization is of the form,

$$x\,G(x, Q_0^2) = A_g x^{-\lambda_g} (1-x)^{\eta_g} (1 + \epsilon_g \sqrt{x} + \gamma_g x), \tag{5.35}$$

and, for this calculation, we will use the values of the parameters from the fitted data evaluated at $Q^2 = Q_0^2 = 1\,\mathrm{GeV}^2$, explicitly given in [86], called the MRS(R2) fit: $A_g = 14.4$, $\lambda_g = -0.51$, $\eta_g = 5.51$, $\epsilon_g = -4.20$, and $\gamma_g = 6.47$. The average Bjorken-x of the ϕ data used in this expression is $\langle x \rangle = 0.073$. If one wanted to evolve the gluon distribution to a different (higher) Q^2, one would use the pQCD evolution formalism of Altarelli and Parisi, which evolves the gluon distribution according to $x\,G(x, Q^2) \sim (Q^2)^\gamma$. [10] The exponent γ is called the effective anomalous dimension of the gluon density, and has the value $\gamma \approx 0.5$ at HERMES kinematics. The strong coupling constant is taken to be $\alpha_S = 0.3$, and $\bar{\alpha}_S^2 = 0.87$ is empirically determined from a fit to pp scattering data. [19]

With these values of the parameters appropriate for HERMES kinematics, the ratios of the helicity amplitudes are computed in this model to be

$$\alpha = \frac{T_{11}}{T_{00}} = 2.43 \tag{5.36}$$

$$\beta = \frac{T_{01}}{T_{00}} = 0.59 \tag{5.37}$$

$$\delta = \frac{T_{10}}{T_{00}} = -0.91 \tag{5.38}$$

$$\eta^1 = \frac{T_{1-1}}{T_{00}} = 1.45, \text{ and} \tag{5.39}$$

$$\eta^0 = \frac{T_{1-1}}{T_{00}} = -0.32. \tag{5.40}$$

With these numerical values, the helicity amplitudes are predicted to exhibit the following hierarchy of dominance,

$$T_{11} > T_{1-1} > T_{00} > |T_{10}| > T_{01}. \tag{5.41}$$

$$(2.43 > 1.13 > 1.0 > 0.91 > 0.59)$$

Note that the prediction of this model for the relative sizes of the helicity amplitudes at HERMES energies is quite different from the calculation of the same model at

HERA collider energies, where [19]

$$T_{00} > T_{11} > T_{01} > |T_{10}| > |T_{1-1}|. \tag{5.42}$$

$$(1.0 > 0.59 > 0.12 > 0.06 > 0.02)$$

It should be noted that this model describes the HERA collider data fairly well. [58]

The spin-density matrix elements can be expressed in terms of $\alpha,\ \beta,\ \delta,$ and η by (see Appendix A)

$$\begin{aligned}
r^{04}_{00} &= B\left(\beta^2+\epsilon\right), \\
\mathrm{Re}(r^{04}_{10}) &= \frac{B}{2}\left[-\eta\beta+\alpha\beta+2\epsilon\,\delta\right], \\
r^{04}_{1-1} &= B\ \left(\alpha\eta-\epsilon\,\delta^2\right), \\
r^{1}_{11} &= B\eta\alpha, \\
r^{1}_{00} &= -B\beta^2, \\
\mathrm{Re}(r^{1}_{10}) &= \frac{B}{2}\beta\left[\eta-\alpha\right], \\
r^{1}_{1-1} &= \frac{B}{2}\ \left(\eta^2+\alpha^2\right), \\
\mathrm{Im}(r^{2}_{10}) &= \frac{B}{2}\beta\left[\eta+\alpha\right], \\
\mathrm{Im}(r^{2}_{1-1}) &= \frac{B}{2}\ \left(\eta^2-\alpha^2\right), \\
r^{5}_{11} &= \frac{B}{\sqrt{2}}\delta\left[\alpha-\eta\right], \\
r^{5}_{00} &= B\sqrt{2}\,\beta, \\
\mathrm{Re}(r^{5}_{10}) &= \frac{B}{2\sqrt{2}}\ \left[2\delta\beta+\alpha-\eta\right], \\
r^{5}_{1-1} &= \frac{B}{\sqrt{2}}\delta\left[\eta-\alpha\right], \\
\mathrm{Im}(r^{6}_{10}) &= -\frac{B}{2\sqrt{2}}\ \left[\alpha+\eta\right], \\
\mathrm{Im}(r^{6}_{1-1}) &= \frac{B}{\sqrt{2}}\delta\left[\eta+\alpha\right],\ \text{and} \\
r^{3,7,8}_{ij} &= 0,
\end{aligned} \tag{5.43}$$

where the helicity amplitudes have been assumed to be purely imaginary. In these equations, $B = N_T + \epsilon N_L$, with $N_L = 1 + 2\,\delta^2$ and $N_T = \alpha^2 + \beta^2 + \eta^2$.

The comparison of this pQCD prediction of r^{α}_{ij} with the HERMES ϕ data, averaged over all kinematic variables, can be seen in Figure 5.6. The χ^2 between the data and the theory is 140 for 15 degrees of freedom, where the uncertainties on the data are given by the statistical and systematic uncertainties added in quadrature. Hence, the ϕ data are not consistent with the predictions of this pQCD model of $2g$ exchange. This may have been foreseen, as the quark-gluon model presented here relies on the pQCD assumption that the separation between the quarks in the vector meson is small. [58] In other words, the $q\bar{q}$ pair are assumed to have not yet separated far enough apart to form into the full hadronic state before the gluons from the target interact with them. In this model, the quark separation typically goes as $\sim 1/(Q\sqrt{\gamma})$. This means that at HERMES kinematics, the grounds are shaky, at best, for the assumption about the dominance of small-distance physics.

At pQCD energies, the wave function of the current quarks in the vector meson is predicted to go as $\sim z\,(1-z)$, where z is the fraction of the photon momentum carried by the quark. [58] In this case, the pQCD model presented here predicts that the single spin-flip amplitude, T_{01}, becomes slightly enhanced compared to other SCHC violating amplitudes. At HERMES energies, it might be more meaningful to think of the meson in terms of an effective description, for instance in terms of constituent quarks. If the vector meson were a weakly bound state of constituent quarks, then their wave function would go as $\sim \delta(z - 1/2)$. In this case, the $2g$ model presented here would predict that the single spin-flip helicity amplitudes would be suppressed. Hence, the results reported here, *i.e.*, that the ϕ data are consistent with SCHC, may be interpreted in favor of a model with a narrow z-distribution for constituent quarks.

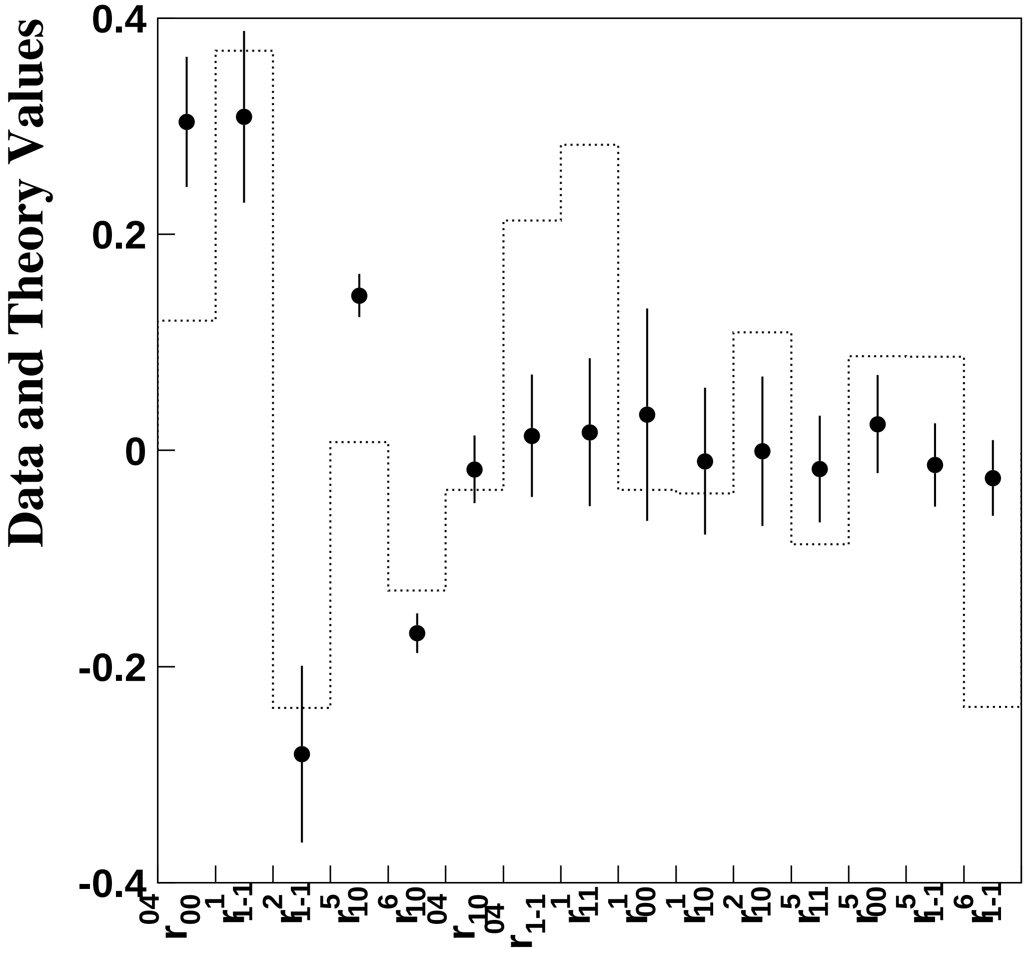

Figure 5.6. The comparison of the pQCD theory of Ivanov and Kirschner [19] with the HERMES ϕ data. It is clear that the theory does not match these data at HERMES kinematics. The bars on the points represent the statistical and the systematic uncertainties added in quadrature.

Table 5.3. The ratio of the longitudinal to transverse photoproduction cross section for ϕ mesons, computed from the measured longitudinal polarization of the ϕ, using Equation 5.44. The first uncertainty is statistical, the second, systematic.

$\langle Q^2 \rangle$	$\langle 1/\epsilon \rangle$	$R_\phi = \sigma_L/\sigma_T$
0.87	1.32	$0.405 \pm 0.080 \pm 0.122$
1.24	1.24	$0.504 \pm 0.090 \pm 0.133$
1.71	1.25	$0.567 \pm 0.097 \pm 0.143$
2.91	1.30	$0.841 \pm 0.155 \pm 0.191$

5.3 Cross-Section Ratio and Comparison with the ρ^0 Meson

As discussed in Subsection 2.2.5, with the assumption that the ϕ exhibits SCHC, one may compute the longitudinal- to transverse-photon ϕ production cross-section ratio from the measured longitudinal polarization of the ϕ,

$$R_\phi \equiv \frac{\sigma_L}{\sigma_T} = \frac{1}{\epsilon}\frac{r^{04}_{00}}{1 - r^{04}_{00}}. \tag{5.44}$$

As seen in Section 5.1, the ϕ data measured in this work are indeed consistent with SCHC, so that we may compute R_ϕ in this way. The data on R_ϕ, computed using Equation 5.44 from the r^{04}_{00} measured in this work, are plotted as a function of Q^2 in Figure 5.7, and are tabulated in Table 5.3. Since the statistical uncertainty on $1/\epsilon$ is small, the statistical and systematic uncertainties on R_ϕ can be estimated by simple error propagation,

$$\delta R_\phi = \left|\frac{\partial R_\phi}{\partial r^{04}_{00}}\right| \delta r^{04}_{00} = \left(\frac{1}{\epsilon}\frac{1}{(1 - r^{04}_{00})^2}\right) \delta r^{04}_{00}, \tag{5.45}$$

where $\delta r^{04}_{00}$is the uncertainty on r^{04}_{00}.

In Figure 5.8 are the results of R_ϕ from this analysis together with the collection of world data on R_ϕ, plotted as a function of Q^2. [26] [28] Note that the measurement of R_ϕ from Reference [27] is not included in this collection of world data, as it is statistically insignificant. We would like to compare these data to the world data on R_ρ for the ρ^0 meson. For this analysis, we choose to use data only from experiments which publish a numerical value of R_V (or a numerical value of r^{04}_{00},

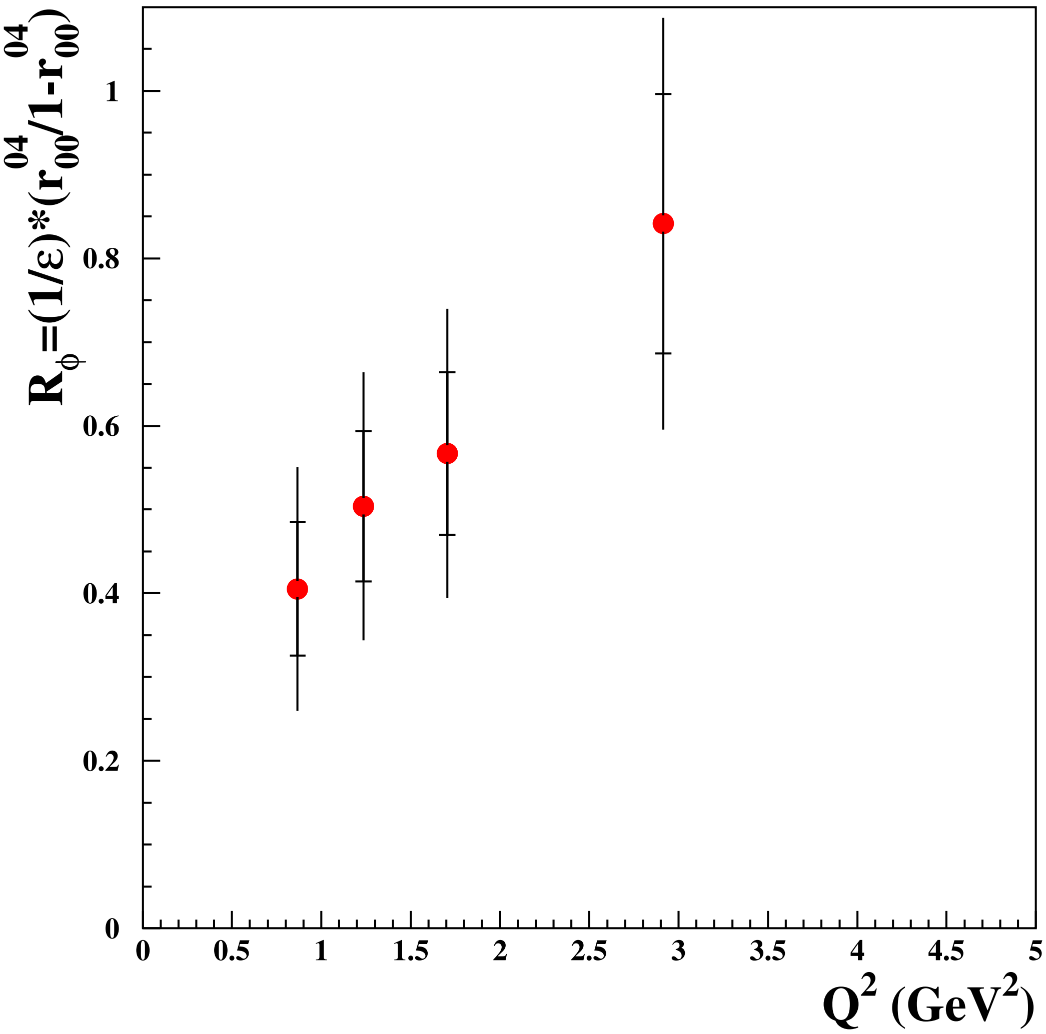

Figure 5.7. The longitudinal to transverse total ϕ photoproduction cross section ratio, $R_\phi = \sigma_L/\sigma_T$, plotted as a function of Q^2. Assuming SCHC, R_ϕ was computed from the measured values of $1/\epsilon$ and r^{04}_{00}, using Equation 5.44. The inner error bars on the points represent the statistical uncertainty, while the outer error bars indicate the statistical and systematic uncertainties added in quadrature. The systematic uncertainty on r^{04}_{00} for each Q^2 bin is taken to be the average systematic uncertainty from Table 4.29.

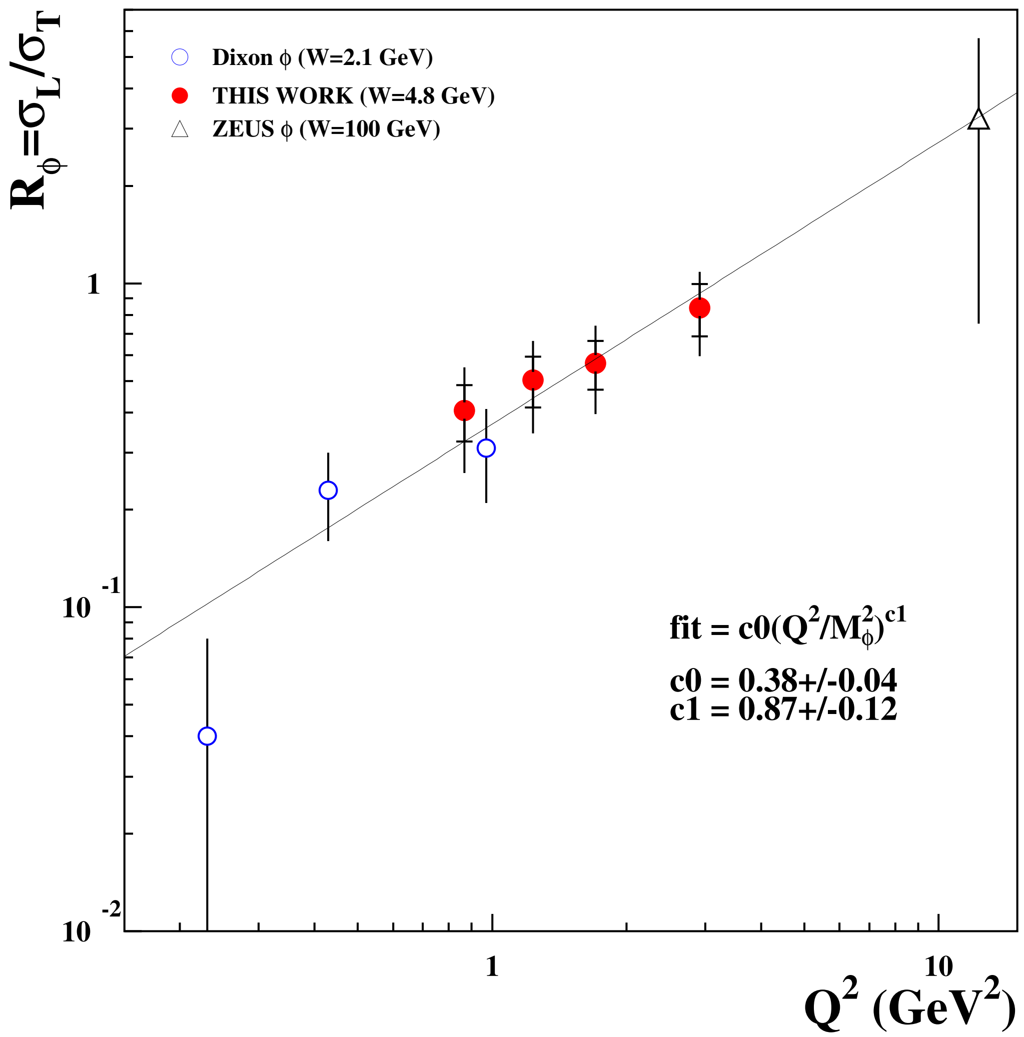

Figure 5.8. The world data on the longitudinal to transverse total photoproduction cross section ratio for ϕ vector mesons, $R_\phi = \sigma_L/\sigma_T$, plotted as a function of Q^2 on a log-log plot. The inner error bars on the points represent the statistical uncertainty, while the outer error bars indicate the statistical and systematic uncertainties added in quadrature. The systematic uncertainty on r^{04}_{00} for each Q^2 bin is taken to be the average systematic uncertainty from Table 4.29. The world data come from the published numerical values of R_ϕ in References [26] and [28], with only statistical uncertainties shown. The line is the fit to the data described in the text. The systematic uncertainties are not included in the fit, due to lack of information in the publications. The χ^2 of the fit is 5.1 for 6 degrees of freedom.

together with ϵ), so we need not estimate R_V from a plot. There are many more data on R_ρ than there are on R_ϕ. These include low energy measurements ($W < 4\,\mathrm{GeV}$) [31] [52] [89] [90], medium energy measurements ($4 < W < 7\,\mathrm{GeV}$) [91] [34], and high energy measurements ($W > 7\,\mathrm{GeV}$) [27] [92] [32] [93] [94] [95]. Our collection of world data on R_ρ can be seen, plotted as a function of Q^2, in Figure 5.9. In References [33] and [96], measured values of R_ρ are published, but are not included in this analysis. In Reference [33], the published value is presented at $Q^2 = 2\,\mathrm{GeV}^2$, obtained from measurements of the total cross section at higher Q^2 and propagated down, unnecessarily, to $2\,\mathrm{GeV}^2$ using the VMD model. In Reference [96], the values of $\langle Q^2 \rangle$ for the data are not available in the publication.

The form of the parameterization we intend to fit to these data warrants some discussion. The E665 experiment fits the Q^2 dependence of their data on R_ρ to the simple parameterization, [32]

$$R_V(Q^2) = a_0^V (Q^2)^{a_1^V}, \tag{5.46}$$

where $V = \rho^0$, ϕ. Fitting only to their data, the E665 experiment obtains the values $a_0^\rho = 0.66 \pm 0.05$ and $a_1^\rho = 0.61 \pm 0.09$. Using the fit function 5.46 on the world data we have collected for the ρ^0 and the ϕ, we obtain the values

$$a_0^\rho = 0.55 \pm 0.02, \qquad a_0^\phi = 0.36 \pm 0.03, \tag{5.47}$$

$$a_1^\rho = 0.68 \pm 0.03, \qquad a_1^\phi = 0.87 \pm 0.10, \tag{5.48}$$

where $\chi^2 = 92.1$ for 34 degrees of freedom in the ρ^0 fit and $\chi^2 = 5.1$ for 6 degrees of freedom in the ϕ fit. Note that only statistical uncertainties are used in these fits, as the systematic uncertainties are often impossible to estimate for many of the old data. The results of the fitted values to Equation 5.46 indicate that the ρ^0 and the ϕ data differ empirically. However, as a fit function, Equation 5.46 is unsavory, as the units of a_0^V depend on the fitted value of a_1^V.

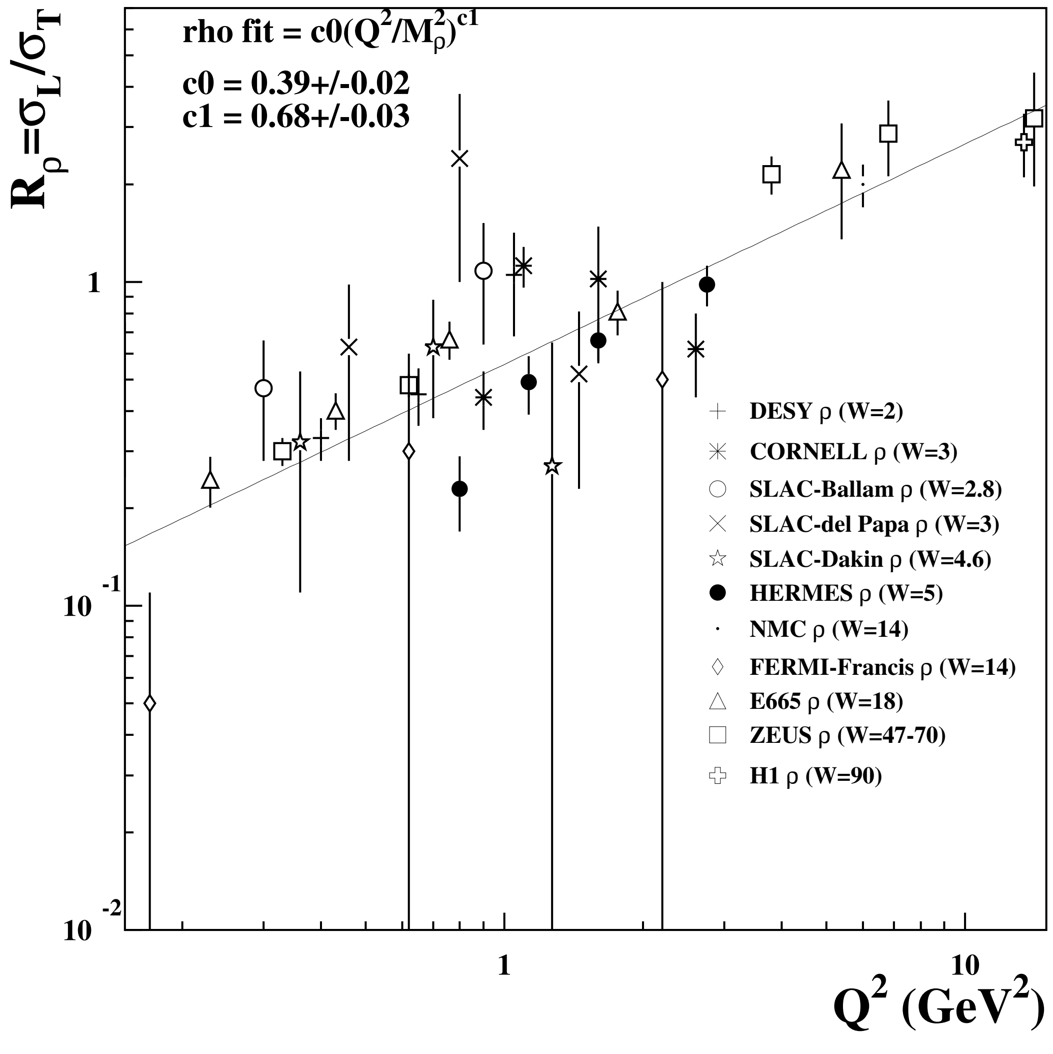

Figure 5.9. The world data on the longitudinal to transverse total photoproduction cross section ratio for ρ^0 vector mesons, $R_\rho = \sigma_L/\sigma_T$, plotted as a function of Q^2 on a log-log plot. The world data come from the published numerical values of R_ρ. The error bars represent the statistical uncertainty. The line is the fit to the data described in the text. The systematic uncertainties have not been included in the fit, due to lack of information in the publications.

We use the VMD model to motivate a modification to Equation 5.46 to use in the fit of R_V. In Subsection 2.2.2, a calculation of the longitudinal- to transverse-photon cross section ratio in the VMD model was discussed which predicts that

$$R_V = \xi_V(W^2)\,\frac{Q^2}{M_V^2}, \tag{5.49}$$

where $\xi_V(W^2) = \sigma_L^{(V\,p)}/\sigma_T^{(V\,p)}$ is the ratio of the V-p scattering cross sections, and could be different for different vector mesons. (Note that the multi-channel VMD model of Hüfner and Kopeliovich [53] does not change this VMD prediction of R_V. [17]) Inspired by this VMD prediction, we choose to fit the world data on R_ρ and R_ϕ with the fit function

$$R_V = c_0^V(W^2)\left(\frac{Q^2}{M_V^2}\right)^{c_1^V}, \tag{5.50}$$

where c_0^V is a function of W^2. This is the fit function used by the HERMES collaboration in their fit to R_ρ data. [34] Using fit function 5.50, integrated over all W^2, the values of the parameters of the fit to our collection of world data on R_ρ and R_ϕ are

$$c_0^\rho = 0.39 \pm 0.02, \qquad c_0^\phi = 0.38 \pm 0.04, \tag{5.51}$$

$$c_1^\rho = 0.68 \pm 0.03, \qquad c_1^\phi = 0.87 \pm 0.12, \tag{5.52}$$

with identical χ^2 as the fit with Equation 5.46. The fit parameters c_0^V and c_1^V are unitless, and are simply related to the fit parameters a_0^V and a_1^V by $c_0^V = a_0^V(M_V^2)^{c_1^V}$ and $c_1^V = a_1^V$.

The fits of R_ρ and R_ϕ indicate that c_0^ρ is consistent with c_0^ϕ within the statistical uncertainties. In the VMD model, this can be interpreted that the ratio of the longitudinal to transverse-polarized vector meson scattering cross sections from protons is equal for ρ^0 and ϕ vector mesons. This interpretation of c_0^V using the VMD model should be made with caution, however, since the VMD model also predicts that $c_1^V = 1$. This VMD prediction is in approximate agreement with the ϕ data, but is definitely not in agreement with the ρ^0 data.

A note about the integration of the data over W^2. A dependence of the fit value of $c_0^\rho(W)$ on W was indicated by the ρ data measured by the HERMES experiment. [34] They found,

$$c_0^\rho = \begin{cases} 0.33 \pm 0.03, & 4 < \langle W \rangle < 7\,\mathrm{GeV} \\ 0.48 \pm 0.03, & \langle W \rangle > 7\,\mathrm{GeV} \end{cases} \tag{5.53}$$

$$c_1^\rho = 0.61 \pm 0.04. \tag{5.54}$$

Re-fitting the data on R_ρ to Equation 5.50 in three bins of low, medium, and high $\langle W \rangle$ for c_0^ρ, we obtain

$$c_0^\rho = \begin{cases} 0.40 \pm 0.03, & \langle W \rangle < 4\,\mathrm{GeV} \\ 0.30 \pm 0.03, & 4 < \langle W \rangle < 7\,\mathrm{GeV} \\ 0.43 \pm 0.02, & \langle W \rangle > 7\,\mathrm{GeV} \end{cases} \tag{5.55}$$

$$c_1^\rho = 0.69 \pm 0.03, \tag{5.56}$$

with a $\chi^2 = 72.7$ for 32 degrees of freedom. The smaller $c_0^\rho(W)$ found by HERMES for medium energy data is confirmed, with the additional information that $c_0^\rho(W)$ for low energy data rises again to the same value as for high energy data. A fit to R_ϕ world data with Equation 5.50 gives

$$c_0^\phi = \begin{cases} 0.29 \pm 0.08, & \langle W \rangle < 4\,\mathrm{GeV} \\ 0.42 \pm 0.05, & 4 < \langle W \rangle < 7\,\mathrm{GeV} \\ 0.54 \pm 0.48, & \langle W \rangle > 7\,\mathrm{GeV} \end{cases} \tag{5.57}$$

$$c_1^\phi = 0.73 \pm 0.18, \tag{5.58}$$

with $\chi^2 = 3.9$ for 4 degrees of freedom. No marked dependence of c_0^ϕ on W is observed within the statistical uncertainty. Note that the data for R_ϕ at high energy are few and imprecise compared to R_ρ, resulting in the large statistical uncertainties for $c_0^\phi(W > 7\,\mathrm{GeV})$ and c_1^ϕ. In order to reduce the effects of the dependence of $c_0^\rho(W)$ on W in our comparison of ρ^0 and ϕ data, we have compared the values of c_0^ρ and c_0^ϕ fit to all the data, *i.e.*, using one value of c_0^V integrated over all W.

CHAPTER 6

CONCLUSIONS

We have studied the helicity structure of the production of exclusive, diffractive ϕ vector mesons by longitudinally polarized positrons at negative photon mass squared $0.5 < Q^2 < 5.0\,\mathrm{GeV}^2$ and γ^*-p center-of-mass energy $\langle W \rangle \approx 5\,\mathrm{GeV}$. The complete set of 23 spin-density matrix elements measurable from the decay and azimuthal production angular distributions of ϕ mesons has been presented. Previous data on the helicity structure of ϕ meson photoproduction are few, and this work is the first measurement of all 23 spin-density matrix elements available to the production of vector mesons by a longitudinally-polarized lepton beam.

At our kinematics, the data indicate that the helicity of the photon is preserved by the ϕ meson, *i.e.*, that the ϕ data are consistent with SCHC. Normalized to $|T_{00}| = 1$, the largest SCHC-violating helicity amplitude is measured to be $|T_{1-1}| = 0.36 \pm 0.14$, compared to the SCHC-observing amplitude, $|T_{11}| = 1.28 \pm 0.05$. This observation of SCHC for the ϕ meson at low W is in contrast to published data for the ρ^0 at both low and high W, and preliminary data for the ϕ meson at high W, where small but significant SCHC-violating amplitudes have been measured. In a Regge model, Pomeron exchange is constructed to exhibit SCHC, while Reggeon exchange need not. The result that the ϕ data exhibit SCHC is consistent with the idea that Reggeon exchange amplitudes are suppressed in ϕ photoproduction. [25]

A pQCD model of $2g$ exchange, whose predictions are in agreement with the measured violations of SCHC at high W, was evaluated at our kinematics and compared to the data. It is found that this pQCD model does not agree with the ϕ data measured here. The discrepancy between the data and the predictions of this model can be interpreted as evidence that writing the wave function of the ϕ in terms of the current quarks used in the light-cone formalism of pQCD may not be valid at our kinematics. In this model, the observation of SCHC in the ϕ data could be interpreted in favor of a wave function with a narrow momentum distribution for the quarks in the vector meson.

Exploiting the result of SCHC in the data, the ratio of total cross sections for the production of ϕ mesons by longitudinal- and transverse-polarized photons, $R_\phi = \sigma_L/\sigma_T$, was computed from the measured longitudinal polarization of the ϕ. The world data on R_ϕ were fit with a parameterization inspired by the VMD model,

$$R_\phi = c_0^\phi \left(\frac{Q^2}{M_\phi^2}\right)^{c_1^\phi}, \tag{6.1}$$

and the fit parameters were compared with those from an analogous fit to world data on R_ρ. The fits indicate that $c_0^\phi = c_0^\rho$ and $c_1^\phi \neq c_1^\rho$ within the statistical uncertainties. In the VMD model, the fit parameter c_0^ϕ is interpreted to be the ratio of scattering cross sections for longitudinally-polarized ϕ mesons from protons and transversely-polarized ϕ mesons from protons. The observation that $c_0^\phi = c_0^\rho$, within this model, would be evidence that the polarization properties of the total scattering cross sections are independent of the flavor of the quarks inside the vector meson, a conclusion which could be tested by measuring R_V for other vector mesons. However, a caveat to this interpretation of c_0^V should be noted. The same VMD model used for this interpretation of c_0^V also predicts that $c_1^V = 1$. We have fitted a value of $c_1^\phi = 0.87 \pm 0.12$ to the ϕ data in this work, so that the ϕ data are indeed consistent with this prediction of VMD. However, the fitted value to ρ^0 data was $c_1^\rho = 0.68 \pm 0.03$, clearly not consistent with VMD. Higher precision data for the ϕ meson on R_ϕ at higher Q^2 would be useful to better constrain the value of the exponent c_1^ϕ in this fit, and are forthcoming. [97]

To summarize, the data from ϕ mesons produced by virtual photons appear to exhibit SCHC and are approximately consistent with VMD. This is in contrast to ρ^0 meson data, which exhibit violations of SCHC and are not consistent with VMD. One could speculate that the differences observed in the helicity structure of ρ^0 and ϕ data could be due to the length of time the vector meson lives before it decays. The lifetime of the ρ^0 is much shorter than that of the ϕ (or ω), indicated by the much wider mass peak of the ρ^0. If the helicity amplitudes were to depend primarily on the spatial separation of the quarks in the vector meson, as is suggested in the pQCD model of $2g$ exchange presented in this work, the lifetime of the vector meson could conceivably have an effect.

It is also possible to speculate that the differences in the ρ^0 and ϕ data are due to the different quark composition of the ρ^0 and ϕ. In the quark model, the ρ^0 meson is comprised of $u\bar{u}$ and $d\bar{d}$ quark pairs, while the ϕ meson is predominately $s\bar{s}$. Since the proton target is made up of primarily u and d quarks, ρ^0 scattering could be expected to take place both by the exchange of u and d quark-pairs with the target (Reggeons) and by the exchange of gluon-pairs (Pomerons) with the target. Since s-quarks comprise a much smaller component of the proton wave function, the exchange of s-quarks with the proton might be expected to be suppressed in ϕ scattering, so that the Pomeron, or $2g$, term would dominate this reaction. Based on this idea, it would be interesting to measure the helicity structure of the ω and the J/Ψ vector mesons. Since the ω meson is comprised of mostly $u\bar{u}$ and $d\bar{d}$-pairs and the J/Ψ is predominately $c\bar{c}$, the helicity structure data from the ω meson might be expected to behave more like the ρ^0, while the J/Ψ might be expected to behave more like the ϕ.

In a sense, one can think of the study of the photoproduction of different vector mesons as a study of the properties of the particles which are exchanged with the target. In particular, the data from the diffractive production of different vector mesons could be thought of as measurements of different combinations of Reggeon

$(2q)$ and Pomeron $(2g)$ exchange amplitudes. In this picture, the ρ^0 photoproduction reaction is due to a certain combination of Pomeron and Reggeon amplitudes, the ω photoproduction reaction is due to a different combination of Pomeron and Reggeon amplitudes, and the ϕ photoproduction reaction is a particularly "clean" case of vector meson production, since only the Pomeron amplitude appears to contribute. Using ϕ photoproduction, then, one could study the properties of this Pomeron exchange, unencumbered by the extra complications coming from additional Reggeon interactions. For example, the ϕ photoproduction reaction may be a good testing ground for the comparison of $2g$ models with Pomeron models.

The subject of this work is currently an active field of research. In the near future, we look forward to measurements of the ϕ spin-density matrix at high energy from the H1 [29, 97] and ZEUS [30] Collaborations. These data should help constrain the models at high Q^2 and W, where no data exist at the moment. From the HERMES Collaboration, we look forward to data on the complete set of spin-density matrix elements for ρ^0 and ω mesons produced by a longitudinally polarized lepton beam. [98] At smaller energies, proposals to precisely measure the spin-density matrix of ρ^0 and ϕ mesons have been approved for the CLAS detector in Hall B at Jefferson Laboratory. [99, 100]

APPENDIX A

SPIN-DENSITY MATRIX ELEMENTS IN TERMS OF HELICITY AMPLITUDES

Here are the spin-density matrix elements expressed in terms of the helicity amplitudes. These expressions are the explicit forms of the equations given in Appendix A of Reference [38]. Note that parity conservation has been used to simplify these expressions. In this context, parity affects the bilinear combinations of helicity amplitudes by the relation

$$T_{-\lambda_\phi -\lambda_\gamma} T_{-\lambda'_\phi -\lambda'_\gamma} = (-1)^{\lambda_\phi - \lambda_\gamma + \lambda'_\phi - \lambda'_\gamma} T_{\lambda_\phi \lambda_\gamma} T_{\lambda'_\phi \lambda'_\gamma}, \tag{A.1}$$

which is another way to express Equation (72) from Reference [38].

$$r^{04}_{00} = B\left[|T_{01}|^2 + \epsilon\,|T_{00}|^2\right] \tag{A.2}$$

$$\mathrm{Re}(r^{04}_{10}) = B\frac{1}{2}\,\mathrm{Re}\left[(T_{1-1}T^{\dagger}_{0-1}) + (T_{11}T^{\dagger}_{01}) + 2\epsilon\,(T_{10}T^{\dagger}_{00})\right] \tag{A.3}$$

$$r^{04}_{1-1} = B\,\mathrm{Re}\left[(T_{11}T^{\dagger}_{-11}) + \epsilon\,(T_{10}T^{\dagger}_{-10})\right] \tag{A.4}$$

$$r^{1}_{11} = B\,\mathrm{Re}\left[(T_{1-1}T^{\dagger}_{11})\right] \tag{A.5}$$

$$r^{1}_{00} = B\,\mathrm{Re}\left[(T_{0-1}T^{\dagger}_{01})\right] \tag{A.6}$$

$$\mathrm{Re}(r^{1}_{10}) = B\frac{1}{2}\,\mathrm{Re}\left[(T_{1-1}T^{\dagger}_{01}) + (T_{11}T^{\dagger}_{0-1})\right] \tag{A.7}$$

$$r^{1}_{1-1} = B\frac{1}{2}\,\mathrm{Re}\left[(T_{1-1}T^{\dagger}_{-11}) + (T_{11}T^{\dagger}_{-1-1})\right] \tag{A.8}$$

$$\mathrm{Im}(r^{2}_{10}) = B\frac{1}{2}\,\mathrm{Re}\left[(T_{1-1}T^{\dagger}_{01}) - (T_{11}T^{\dagger}_{0-1})\right] \tag{A.9}$$

$$\mathrm{Im}(r^{2}_{1-1}) = B\frac{1}{2}\,\mathrm{Re}\left[(T_{1-1}T^{\dagger}_{-11}) - (T_{11}T^{\dagger}_{-1-1})\right] \tag{A.10}$$

$$\mathrm{Im}(r^{3}_{10}) = B\frac{1}{2}\,\mathrm{Im}\left[(T_{11}T^{\dagger}_{01}) - (T_{1-1}T^{\dagger}_{0-1})\right] \tag{A.11}$$

$$\mathrm{Im}(r^{3}_{1-1}) = B\frac{1}{2}\,\mathrm{Im}\left[(T_{11}T^{\dagger}_{-11})\right] \tag{A.12}$$

$$r^5_{11} = B\frac{1}{\sqrt{2}}\,\mathrm{Re}\left[(T_{10}T^\dagger_{11}) - (T_{10}T^\dagger_{1-1})\right] \tag{A.13}$$

$$r^5_{00} = B\sqrt{2}\,\mathrm{Re}\left[(T_{00}T^\dagger_{01})\right] \tag{A.14}$$

$$\mathrm{Re}(r^5_{10}) = B\frac{1}{2\sqrt{2}}\,\mathrm{Re}\left[(T_{10}T^\dagger_{01}) + (T_{11}T^\dagger_{00}) - (T_{10}T^\dagger_{0-1}) - (T_{1-1}T^\dagger_{00})\right] \tag{A.15}$$

$$r^5_{1-1} = B\frac{1}{\sqrt{2}}\,\mathrm{Re}\left[(T_{10}T^\dagger_{-11}) + (T_{11}T^\dagger_{-10})\right] \tag{A.16}$$

$$\mathrm{Im}(r^6_{10}) = B\frac{1}{2\sqrt{2}}\,\mathrm{Re}\left[(T_{10}T^\dagger_{01}) - (T_{11}T^\dagger_{00}) + (T_{10}T^\dagger_{0-1}) - (T_{1-1}T^\dagger_{00})\right] \tag{A.17}$$

$$\mathrm{Im}(r^6_{1-1}) = B\frac{1}{\sqrt{2}}\,\mathrm{Re}\left[(T_{10}T^\dagger_{-11}) - (T_{11}T^\dagger_{-10})\right] \tag{A.18}$$

$$\mathrm{Im}(r^7_{10}) = B\frac{1}{2\sqrt{2}}\,\mathrm{Im}\left[(T_{10}T^\dagger_{01}) + (T_{11}T^\dagger_{00}) + (T_{10}T^\dagger_{0-1}) + (T_{1-1}T^\dagger_{00})\right] \tag{A.19}$$

$$\mathrm{Im}(r^7_{1-1}) = B\frac{1}{\sqrt{2}}\,\mathrm{Im}\left[(T_{10}T^\dagger_{-11}) + (T_{11}T^\dagger_{-10})\right] \tag{A.20}$$

$$r^8_{11} = B\frac{1}{\sqrt{2}}\,\mathrm{Im}\left[(T_{10}T^\dagger_{1-1}) - (T_{10}T^\dagger_{11})\right] \tag{A.21}$$

$$r^8_{00} = -B\sqrt{2}\,\mathrm{Im}\left[(T_{00}T^\dagger_{01})\right] \tag{A.22}$$

$$\mathrm{Re}(r^8_{10}) = B\frac{1}{2\sqrt{2}}\,\mathrm{Im}\left[-(T_{10}T^\dagger_{01}) + (T_{11}T^\dagger_{00}) + (T_{10}T^\dagger_{0-1}) - (T_{1-1}T^\dagger_{00})\right] \tag{A.23}$$

$$r^8_{1-1} = B\frac{1}{\sqrt{2}}\,\mathrm{Im}\left[-(T_{10}T^\dagger_{-11}) + (T_{11}T^\dagger_{-10})\right] \tag{A.24}$$

In these equations,

$$B = \frac{1}{N_T + \epsilon N_L}, \tag{A.25}$$

with

$$N_T = |T_{11}|^2 + |T_{10}|^2 + |T_{1-1}|^2 \text{ and} \tag{A.26}$$

$$N_L = 2|T_{01}|^2 + |T_{00}|^2. \tag{A.27}$$

Under the assumption of Natural Parity Exchange (NPE) in the t-channel, these expressions can be further simplified. NPE is the condition on the amplitudes:

$$T_{-\lambda_\phi -\lambda_\gamma} = (-1)^{\lambda_\phi - \lambda_\gamma} T_{\lambda_\phi \lambda_\gamma}, \tag{A.28}$$

so that

$$T_{-1-1} = T_{11}, \tag{A.29}$$

$$T_{-10} = -T_{10}, \tag{A.30}$$

$$T_{0-1} = -T_{01}, \text{ and} \tag{A.31}$$

$$T_{-11} = T_{1-1}. \tag{A.32}$$

This leaves us with five independent amplitudes: the two helicity conserving amplitudes, T_{00} and T_{11}, the two single-flip amplitudes, T_{10} and T_{01}, and the double-flip amplitude, T_{1-1}. Assuming NPE, the spin-density matrix elements are given by

$$r^{04}_{00} = B\left(|T_{01}|^2 + \epsilon\,|T_{00}|^2\right), \tag{A.33}$$

$$\mathrm{Re}(r^{04}_{10}) = B\frac{1}{2}\,\mathrm{Re}\left[-(T_{1-1}T^{\dagger}_{01}) + (T_{11}T^{\dagger}_{01}) + 2\epsilon\,(T_{10}T^{\dagger}_{00})\right], \tag{A.34}$$

$$r^{04}_{1-1} = B\left(\mathrm{Re}(T_{11}T^{\dagger}_{1-1}) - \epsilon\,|T_{10}|^2\right), \tag{A.35}$$

$$r^{1}_{11} = B\,\mathrm{Re}\left[(T_{1-1}T^{\dagger}_{11})\right], \tag{A.36}$$

$$r^{1}_{00} = -B\,|T_{01}|^2, \tag{A.37}$$

$$\mathrm{Re}(r^{1}_{10}) = B\frac{1}{2}\,\mathrm{Re}\left[(T_{1-1}T^{\dagger}_{01}) - (T_{11}T^{\dagger}_{01})\right], \tag{A.38}$$

$$r^{1}_{1-1} = B\frac{1}{2}\left(|T_{1-1}|^2 + |T_{11}|^2\right), \tag{A.39}$$

$$\mathrm{Im}(r^{2}_{10}) = B\frac{1}{2}\,\mathrm{Re}\left[(T_{1-1}T^{\dagger}_{01}) + (T_{11}T^{\dagger}_{01})\right], \tag{A.40}$$

$$\mathrm{Im}(r^{2}_{1-1}) = B\frac{1}{2}\left(|T_{1-1}|^2 - |T_{11}|^2\right), \tag{A.41}$$

$$\mathrm{Im}(r^{3}_{10}) = B\frac{1}{2}\,\mathrm{Im}\left[(T_{1-1}T^{\dagger}_{01}) + (T_{11}T^{\dagger}_{01})\right], \tag{A.42}$$

$$\mathrm{Im}(r^{3}_{1-1}) = B\frac{1}{2}\,\mathrm{Im}\left[(T_{11}T^{\dagger}_{1-1})\right], \tag{A.43}$$

$$r^{5}_{11} = B\frac{1}{\sqrt{2}}\,\mathrm{Re}\left[(T_{10}T^{\dagger}_{11}) - (T_{10}T^{\dagger}_{1-1})\right], \tag{A.44}$$

$$r^{5}_{00} = B\sqrt{2}\,\mathrm{Re}\left[(T_{00}T^{\dagger}_{01})\right], \tag{A.45}$$

$$\mathrm{Re}(r^5_{10}) = B\frac{1}{2\sqrt{2}}\,\mathrm{Re}\left[2(T_{10}T^\dagger_{01}) + (T_{11}T^\dagger_{00}) - (T_{1-1}T^\dagger_{00})\right], \tag{A.46}$$

$$r^5_{1-1} = B\frac{1}{\sqrt{2}}\,\mathrm{Re}\left[(T_{10}T^\dagger_{1-1}) - (T_{11}T^\dagger_{10})\right], \tag{A.47}$$

$$\mathrm{Im}(r^6_{10}) = -B\frac{1}{2\sqrt{2}}\,\mathrm{Re}\left[(T_{11}T^\dagger_{00}) + (T_{1-1}T^\dagger_{00})\right], \tag{A.48}$$

$$\mathrm{Im}(r^6_{1-1}) = B\frac{1}{\sqrt{2}}\,\mathrm{Re}\left[(T_{10}T^\dagger_{1-1}) + (T_{11}T^\dagger_{10})\right], \tag{A.49}$$

$$\mathrm{Im}(r^7_{10}) = B\frac{1}{2\sqrt{2}}\,\mathrm{Im}\left[(T_{11}T^\dagger_{00}) + (T_{1-1}T^\dagger_{00})\right], \tag{A.50}$$

$$\mathrm{Im}(r^7_{1-1}) = B\frac{1}{\sqrt{2}}\,\mathrm{Im}\left[(T_{10}T^\dagger_{1-1}) - (T_{11}T^\dagger_{10})\right], \tag{A.51}$$

$$r^8_{11} = B\frac{1}{\sqrt{2}}\,\mathrm{Im}\left[-(T_{10}T^\dagger_{11}) + (T_{10}T^\dagger_{1-1})\right], \tag{A.52}$$

$$r^8_{00} = -B\sqrt{2}\,\mathrm{Im}\left[(T_{00}T^\dagger_{01})\right], \tag{A.53}$$

$$\mathrm{Re}(r^8_{10}) = B\frac{1}{2\sqrt{2}}\,\mathrm{Im}\left[-2(T_{10}T^\dagger_{01}) + (T_{11}T^\dagger_{00}) - (T_{1-1}T^\dagger_{00})\right], \text{ and} \tag{A.54}$$

$$r^8_{1-1} = -B\frac{1}{\sqrt{2}}\,\mathrm{Im}\left[(T_{10}T^\dagger_{1-1}) + (T_{11}T^\dagger_{10})\right]. \tag{A.55}$$

APPENDIX B

SPIN-DENSITY MATRIX ELEMENTS IN TERMS OF MOMENTS

Here are the spin-density matrix elements given in terms of moments. Note that this is just a copy of Appendix C in Reference [38]. With the standard definition of a moment of a distribution, Equation 4.13,

$$\langle F(\theta,\varphi,\Phi)\rangle = \frac{\int d\cos\theta\, d\varphi\, d\Phi\ F(\theta,\varphi,\Phi)W(\cos\theta,\varphi,\Phi)}{\int d\cos\theta\, d\varphi\, d\Phi\ W(\cos\theta,\varphi,\Phi)},$$

the spin-density matrix elements can be written:

$$r^{04}_{00} = \frac{5}{2}\langle\cos^2\theta\rangle - \frac{1}{2}, \tag{B.1}$$

$$\mathrm{Re}(\mathrm{r}^{04}_{10}) = -\frac{5}{4\sqrt{2}}\langle\sin 2\theta\ \cos\varphi\rangle, \tag{B.2}$$

$$r^{04}_{1-1} = -\frac{5}{4}\langle\sin^2\theta\ \cos 2\varphi\rangle, \tag{B.3}$$

$$r^{1}_{00} = \frac{1}{\epsilon}\left[\langle\cos 2\Phi\rangle - 5\langle\cos^2\theta\ \cos 2\Phi\rangle\right], \tag{B.4}$$

$$r^{1}_{11} = \frac{1}{\epsilon}\left[-\frac{3}{2}\langle\cos 2\Phi\rangle + \frac{5}{2}\langle\cos^2\theta\ \cos 2\Phi\rangle\right], \tag{B.5}$$

$$\mathrm{Re}(\mathrm{r}^{1}_{10}) = \frac{1}{\epsilon}\frac{5}{2\sqrt{2}}\langle\sin 2\theta\cos\varphi\cos 2\Phi\rangle, \tag{B.6}$$

$$r^{1}_{1-1} = \frac{1}{\epsilon}\frac{5}{2}\langle\sin^2\theta\cos 2\varphi\cos 2\Phi\rangle, \tag{B.7}$$

$$\mathrm{Im}(\mathrm{r}^{2}_{10}) = -\frac{1}{\epsilon}\frac{5}{2\sqrt{2}}\langle\sin 2\theta\sin\varphi\sin 2\Phi\rangle, \tag{B.8}$$

$$\mathrm{Im}(\mathrm{r}^{2}_{1-1}) = -\frac{1}{\epsilon}\frac{5}{2}\langle\sin^2\theta\sin 2\varphi\sin 2\Phi\rangle, \tag{B.9}$$

$$\mathrm{Im}(\mathrm{r}^{3}_{10}) = \frac{1}{P_b\sqrt{1-\epsilon^2}}\frac{5}{4\sqrt{2}}\langle\sin 2\theta\sin\varphi\rangle, \tag{B.10}$$

$$\mathrm{Im}(\mathrm{r}^{3}_{1-1}) = \frac{1}{P_b\sqrt{1-\epsilon^2}}\frac{5}{4}\langle\sin^2\theta\sin 2\varphi\rangle, \tag{B.11}$$

$$r^{5}_{00} = a\left[-\langle\cos\Phi\rangle + 5\langle\cos^2\theta\ \cos\Phi\rangle\right], \tag{B.12}$$

$$r^{5}_{11} = a\left[\frac{3}{2}\langle\cos\Phi\rangle - \frac{5}{2}\langle\cos^2\theta\ \cos\Phi\rangle\right], \tag{B.13}$$

$$\mathrm{Re}(\mathrm{r}^5_{10}) = -a\,\frac{5}{2\sqrt{2}}\,\langle\sin 2\theta\cos\varphi\cos\Phi\rangle, \tag{B.14}$$

$$r^5_{1-1} = -a\,\frac{5}{2}\,\langle\sin^2\theta\cos 2\varphi\cos\Phi\rangle, \tag{B.15}$$

$$\mathrm{Im}(\mathrm{r}^6_{10}) = a\,\frac{5}{2\sqrt{2}}\,\langle\sin 2\theta\sin\varphi\sin\Phi\rangle, \tag{B.16}$$

$$\mathrm{Im}(\mathrm{r}^6_{1-1}) = a\,\frac{5}{2}\,\langle\sin^2\theta\sin 2\varphi\sin\Phi\rangle, \tag{B.17}$$

$$\mathrm{Im}(\mathrm{r}^7_{10}) = \frac{1}{P_b}\,b\,\frac{5}{2\sqrt{2}}\langle\sin 2\theta\sin\varphi\cos\Phi\rangle, \tag{B.18}$$

$$\mathrm{Im}(\mathrm{r}^7_{1-1}) = \frac{1}{P_b}\,b\,\frac{5}{2}\langle\sin^2\theta\sin 2\varphi\cos\Phi\rangle, \tag{B.19}$$

$$r^8_{00} = \frac{1}{P_b}\,b\left[-\langle\sin\Phi\rangle + 5\langle\cos^2\theta\ \sin\Phi\rangle\right], \tag{B.20}$$

$$r^8_{11} = \frac{1}{P_b}\,b\left[\frac{3}{2}\langle\sin\Phi\rangle - \frac{5}{2}\langle\cos^2\theta\ \sin\Phi\rangle\right], \tag{B.21}$$

$$\mathrm{Re}(\mathrm{r}^8_{10}) = -\frac{1}{P_b}\,b\,\frac{5}{2\sqrt{2}}\langle\sin 2\theta\cos\varphi\sin\Phi\rangle, \text{ and} \tag{B.22}$$

$$r^8_{1-1} = -\frac{1}{P_b}\,b\,\frac{5}{2}\langle\sin^2\theta\cos 2\varphi\sin\Phi\rangle, \tag{B.23}$$

where

$$a = \frac{1}{\sqrt{2\epsilon(1+\epsilon)}}, \text{ and} \tag{B.24}$$

$$b = \frac{1}{\sqrt{2\epsilon(1-\epsilon)}}. \tag{B.25}$$

APPENDIX C

SPIN-DENSITY MATRIX ELEMENTS AS A FUNCTION OF KINEMATIC VARIABLES

The spin-density matrix elements measured with systematic uncertainty greater than 50% are presented here as a function of kinematic variables. Figures C.1 and C.2 are these spin-density matrix elements plotted against Q^2. Figures C.3 and C.4 are the same spin-density matrix elements plotted against $-t'$. Finally, Figures C.5 and C.6 are the spin-density matrix elements plotted against target mass, A.

The results of the complete set of spin-density matrix elements observable with a longitudinally polarized lepton beam are given in tabular form as a function of Q^2, $-t'$, and A in Tables C.1, C.2, and C.3, respectively.

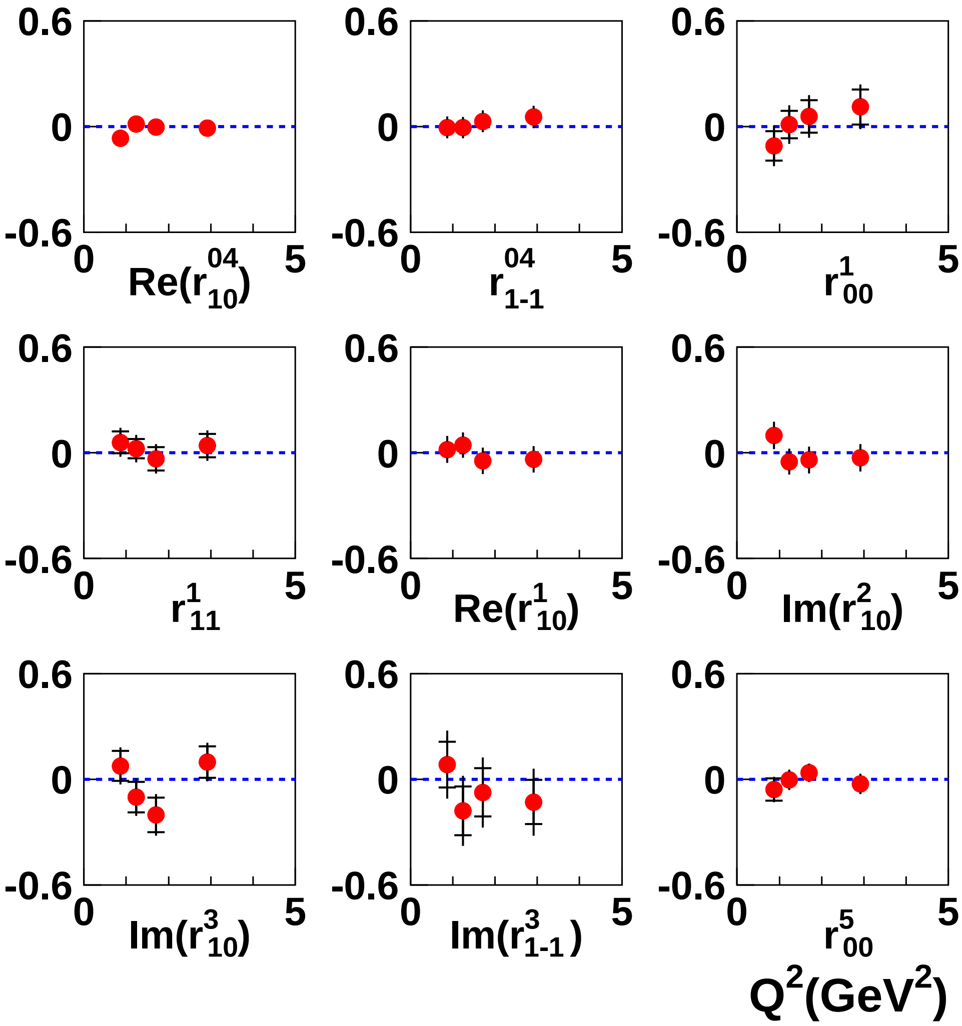

Figure C.1. First set of spin-density matrix elements plotted as a function of Q^2. The dashed lines indicate the value expected in the case of SCHC. The inner error bars on the points represent the statistical uncertainty, while the outer error bars indicate the statistical and systematic uncertainties added in quadrature. The systematic uncertainty for each kinematic bin is taken to be the average systematic uncertainty from Table 4.29.

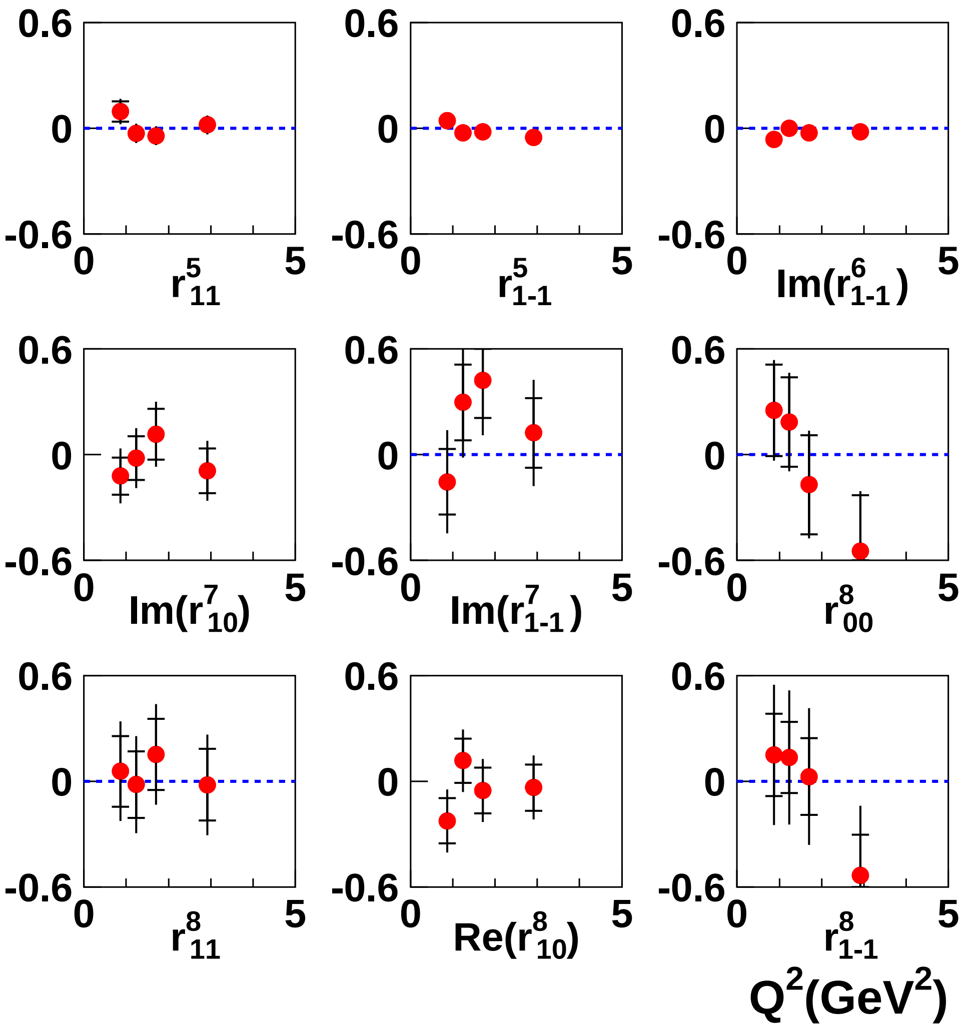

Figure C.2. Second set of spin-density matrix elements plotted as a function of Q^2. The dashed lines indicate the value expected in the case of SCHC. The inner error bars on the points represent the statistical uncertainty, while the outer error bars indicate the statistical and systematic uncertainties added in quadrature. The systematic uncertainty for each kinematic bin is taken to be the average systematic uncertainty from Table 4.29.

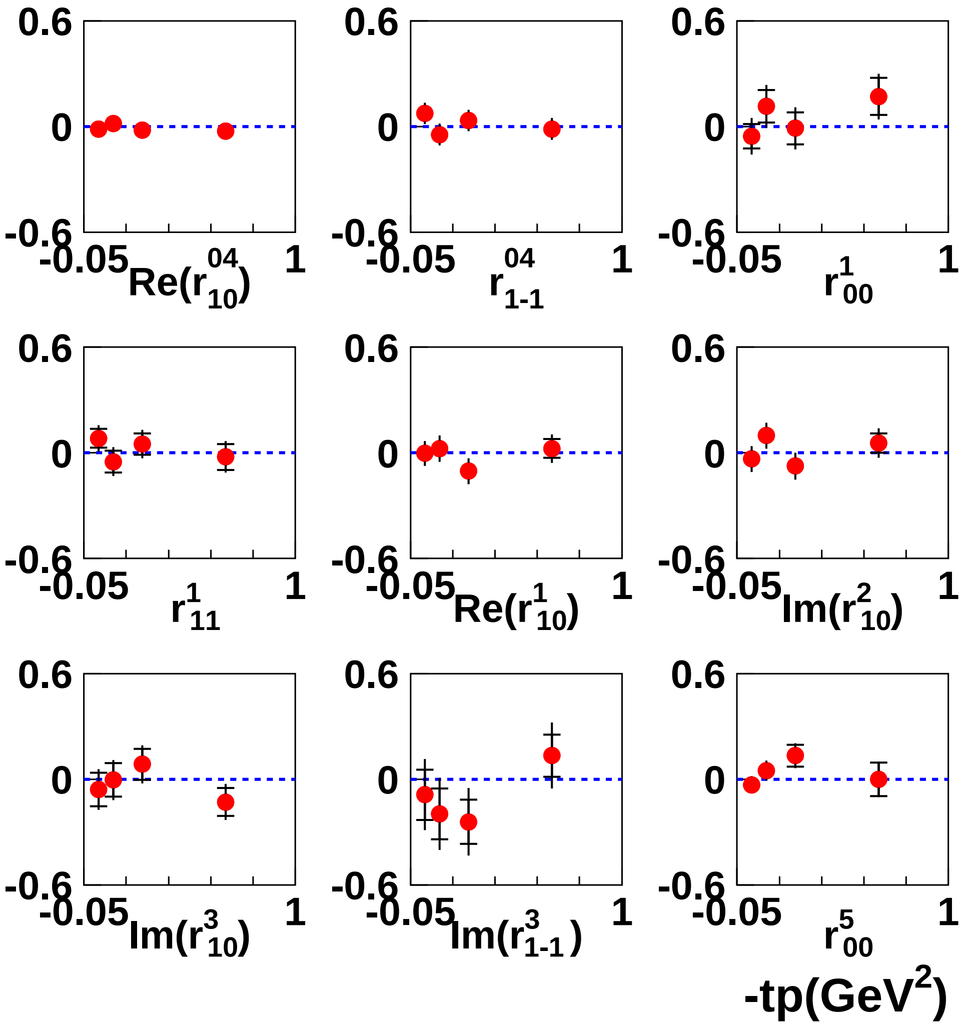

Figure C.3. First set of spin-density matrix elements plotted as a function of $-t'$. The dashed lines indicate the value expected in the case of SCHC. The inner error bars on the points represent the statistical uncertainty, while the outer error bars indicate the statistical and systematic uncertainties added in quadrature. The systematic uncertainty for each kinematic bin is taken to be the average systematic uncertainty from Table 4.29.

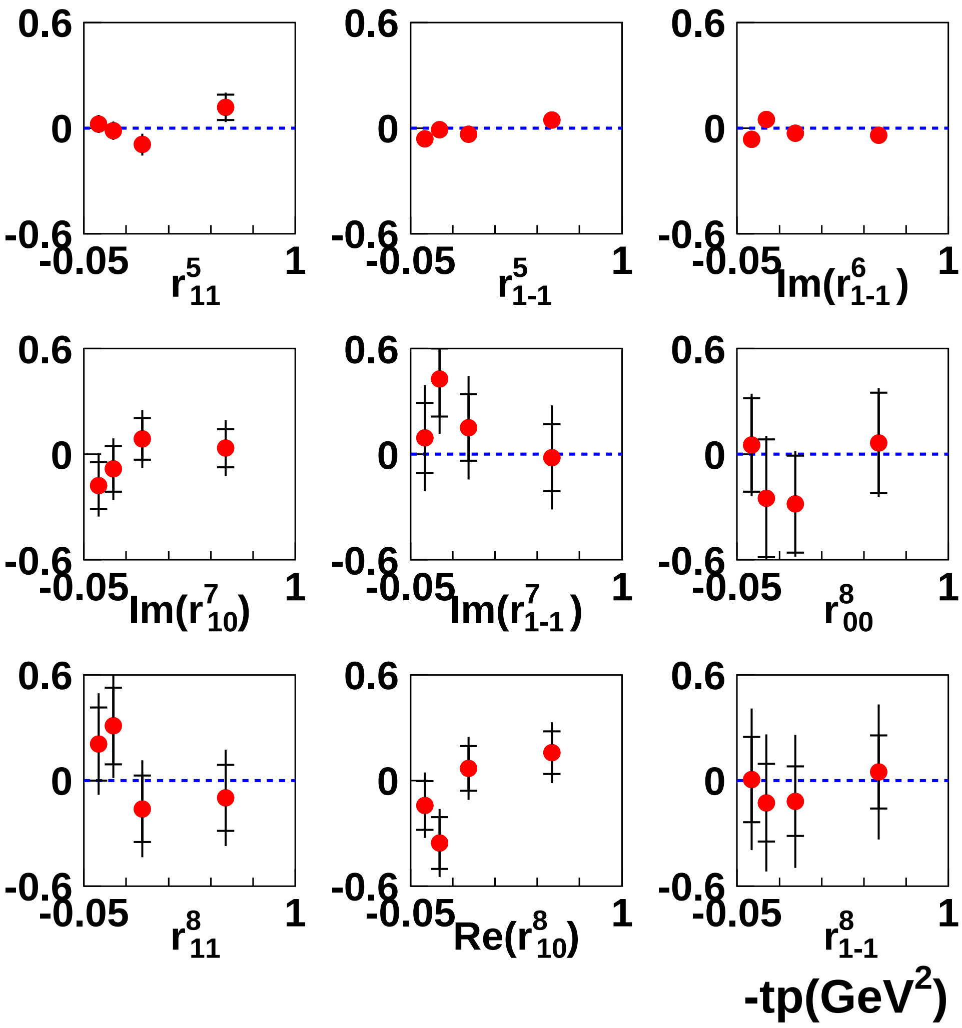

Figure C.4. Second set of spin-density matrix elements plotted as a function of $-t'$. The dashed lines indicate the value expected in the case of SCHC. The inner error bars on the points represent the statistical uncertainty, while the outer error bars indicate the statistical and systematic uncertainties added in quadrature. The systematic uncertainty for each kinematic bin is taken to be the average systematic uncertainty from Table 4.29.

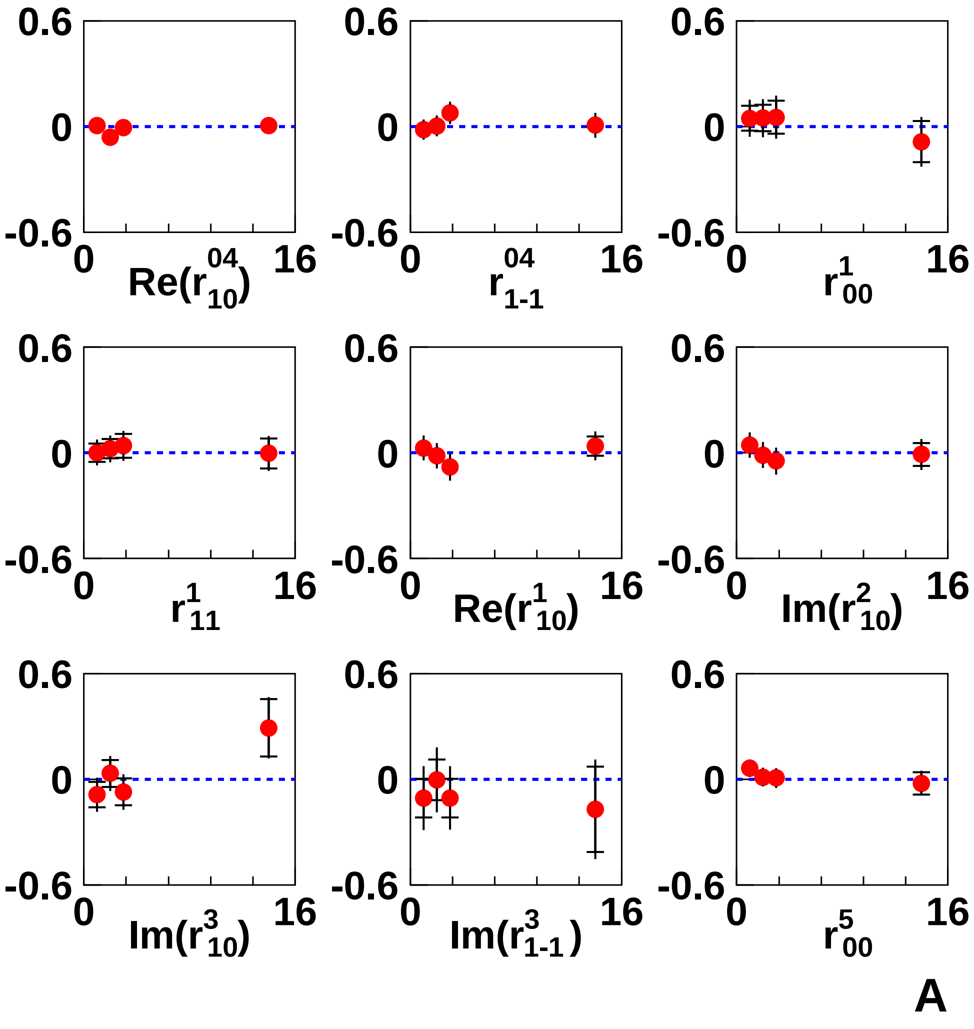

Figure C.5. First set of spin-density matrix elements plotted as a function of A. The dashed lines indicate the value expected in the case of SCHC. The inner error bars on the points represent the statistical uncertainty, while the outer error bars indicate the statistical and systematic uncertainties added in quadrature. The systematic uncertainty for each target type is taken to be the average systematic uncertainty from Table 4.29.

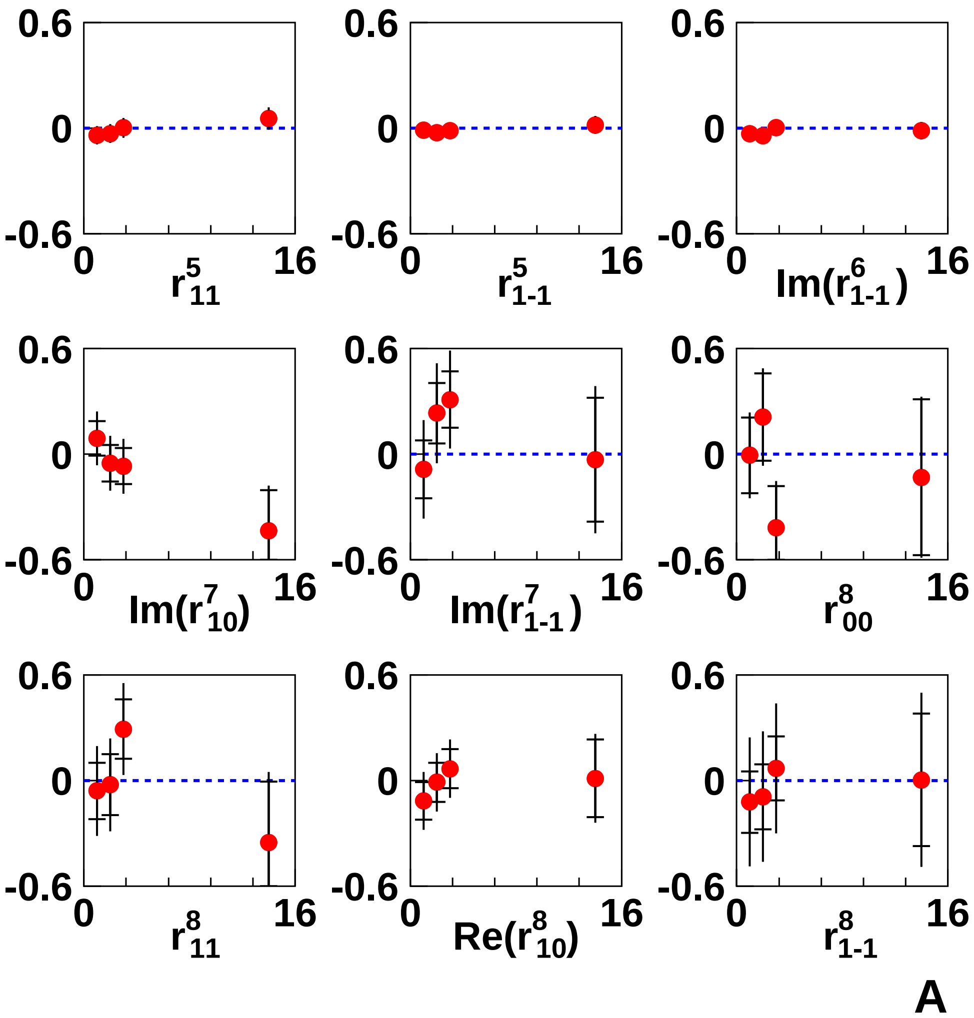

Figure C.6. Second set of spin-density matrix elements plotted as a function of A. The dashed lines indicate the value expected in the case of SCHC. The inner error bars on the points represent the statistical uncertainty, while the outer error bars indicate the statistical and systematic uncertainties added in quadrature. The systematic uncertainty for each target type is taken to be the average systematic uncertainty from Table 4.29.

Table C.1. Spin-density matrix elements in four intervals of Q^2. The uncertainties are statistical. The average Q^2 values in the table labels have units of GeV^2, and the ranges of Q^2 in the four intervals are $0.5 < Q^2 < 1.05\,\mathrm{GeV}^2$, $1.05 < Q^2 < 1.45\,\mathrm{GeV}^2$, $1.45 < Q^2 < 2.05\,\mathrm{GeV}^2$, and $2.05 < Q^2 < 5.0\,\mathrm{GeV}^2$, respectively.

r^{α}_{ij}	$\langle Q^2\rangle = 0.87$	$\langle Q^2\rangle = 1.24$	$\langle Q^2\rangle = 1.71$	$\langle Q^2\rangle = 2.91$
r^{04}_{00}	0.235 ± 0.035	0.289 ± 0.037	0.311 ± 0.037	0.392 ± 0.044
$\mathrm{Re}(r^{04}_{10})$	-0.067 ± 0.029	0.013 ± 0.025	-0.005 ± 0.023	-0.010 ± 0.025
r^{04}_{1-1}	-0.005 ± 0.034	-0.006 ± 0.032	0.029 ± 0.037	0.053 ± 0.037
r^{1}_{11}	-0.111 ± 0.084	0.010 ± 0.078	0.057 ± 0.093	0.111 ± 0.099
r^{1}_{00}	0.059 ± 0.063	0.024 ± 0.055	-0.033 ± 0.065	0.041 ± 0.067
$\mathrm{Re}(r^{1}_{10})$	0.019 ± 0.045	0.044 ± 0.040	-0.045 ± 0.045	-0.036 ± 0.044
r^{1}_{1-1}	0.443 ± 0.059	0.341 ± 0.054	0.277 ± 0.062	0.159 ± 0.070
$\mathrm{Im}(r^{2}_{10})$	0.100 ± 0.047	-0.051 ± 0.040	-0.041 ± 0.043	-0.028 ± 0.047
$\mathrm{Im}(r^{2}_{1-1})$	-0.415 ± 0.061	-0.349 ± 0.058	-0.306 ± 0.058	-0.099 ± 0.060
$\mathrm{Im}(r^{3}_{10})$	0.076 ± 0.084	-0.101 ± 0.087	-0.202 ± 0.098	0.098 ± 0.088
$\mathrm{Im}(r^{3}_{1-1})$	0.083 ± 0.130	-0.179 ± 0.138	-0.075 ± 0.137	-0.130 ± 0.126
r^{5}_{11}	-0.059 ± 0.063	-0.003 ± 0.046	0.038 ± 0.040	-0.027 ± 0.047
r^{5}_{00}	0.095 ± 0.058	-0.029 ± 0.033	-0.043 ± 0.031	0.019 ± 0.032
$\mathrm{Re}(r^{5}_{10})$	0.116 ± 0.033	0.142 ± 0.023	0.131 ± 0.019	0.161 ± 0.024
r^{5}_{1-1}	0.042 ± 0.027	-0.027 ± 0.029	-0.022 ± 0.031	-0.053 ± 0.030
$\mathrm{Im}(r^{6}_{10})$	-0.130 ± 0.024	-0.178 ± 0.019	-0.196 ± 0.021	-0.184 ± 0.021
$\mathrm{Im}(r^{6}_{1-1})$	-0.063 ± 0.031	-0.002 ± 0.028	-0.026 ± 0.030	-0.021 ± 0.031
$\mathrm{Im}(r^{7}_{10})$	-0.121 ± 0.105	-0.020 ± 0.124	0.117 ± 0.145	-0.092 ± 0.126
$\mathrm{Im}(r^{7}_{1-1})$	-0.154 ± 0.185	0.297 ± 0.216	0.423 ± 0.213	0.124 ± 0.198
r^{8}_{11}	0.252 ± 0.260	0.186 ± 0.254	-0.171 ± 0.282	-0.546 ± 0.318
r^{8}_{00}	0.057 ± 0.201	-0.019 ± 0.188	0.152 ± 0.203	-0.020 ± 0.204
$\mathrm{Re}(r^{8}_{10})$	-0.225 ± 0.129	0.118 ± 0.126	-0.052 ± 0.130	-0.036 ± 0.131
r^{8}_{1-1}	0.151 ± 0.234	0.135 ± 0.201	0.027 ± 0.217	-0.535 ± 0.231

Table C.2. Spin-density matrix elements in four intervals of $-t'$. The uncertainties are statistical. The average $-t'$ values in the table labels have units of GeV^2, and the ranges of $-t'$ in the four intervals are $0.0 < -t' < 0.05\,\mathrm{GeV}^2$, $0.05 < -t' < 0.15\,\mathrm{GeV}^2$, $0.15 < -t' < 0.35\,\mathrm{GeV}^2$, and $0.35 < -t' < 2.0\,\mathrm{GeV}^2$, respectively.

r_{ij}^{α}	$\langle -t' \rangle = 0.02$	$\langle -t' \rangle = 0.10$	$\langle -t' \rangle = 0.24$	$\langle -t' \rangle = 0.65$
r_{00}^{04}	0.282 ± 0.034	0.354 ± 0.040	0.344 ± 0.038	0.271 ± 0.043
$\mathrm{Re}(r_{10}^{04})$	-0.015 ± 0.022	0.018 ± 0.025	-0.020 ± 0.024	-0.028 ± 0.029
r_{1-1}^{04}	0.074 ± 0.034	-0.047 ± 0.035	0.034 ± 0.033	-0.014 ± 0.036
r_{11}^{1}	-0.055 ± 0.069	0.114 ± 0.093	-0.011 ± 0.090	0.170 ± 0.105
r_{00}^{1}	0.083 ± 0.053	-0.050 ± 0.063	0.050 ± 0.061	-0.023 ± 0.073
$\mathrm{Re}(r_{10}^{1})$	-0.003 ± 0.036	0.024 ± 0.043	-0.104 ± 0.043	0.024 ± 0.053
r_{1-1}^{1}	0.288 ± 0.057	0.300 ± 0.059	0.318 ± 0.056	0.357 ± 0.072
$\mathrm{Im}(r_{10}^{2})$	-0.035 ± 0.039	0.098 ± 0.041	-0.075 ± 0.046	0.055 ± 0.055
$\mathrm{Im}(r_{1-1}^{2})$	-0.172 ± 0.053	-0.353 ± 0.060	-0.292 ± 0.056	-0.368 ± 0.066
$\mathrm{Im}(r_{10}^{3})$	-0.057 ± 0.095	-0.004 ± 0.095	0.085 ± 0.087	-0.130 ± 0.080
$\mathrm{Im}(r_{1-1}^{3})$	-0.088 ± 0.143	-0.197 ± 0.145	-0.242 ± 0.126	0.135 ± 0.120
r_{11}^{5}	-0.031 ± 0.034	0.050 ± 0.045	0.134 ± 0.062	0.000 ± 0.094
r_{00}^{5}	0.023 ± 0.026	-0.015 ± 0.031	-0.094 ± 0.044	0.118 ± 0.073
$\mathrm{Re}(r_{10}^{5})$	0.114 ± 0.018	0.189 ± 0.021	0.027 ± 0.051	0.182 ± 0.027
r_{1-1}^{5}	-0.062 ± 0.026	-0.009 ± 0.030	-0.036 ± 0.025	0.047 ± 0.031
$\mathrm{Im}(r_{10}^{6})$	-0.151 ± 0.019	-0.122 ± 0.020	-0.170 ± 0.026	-0.240 ± 0.025
$\mathrm{Im}(r_{1-1}^{6})$	-0.065 ± 0.029	0.048 ± 0.031	-0.031 ± 0.029	-0.042 ± 0.035
$\mathrm{Im}(r_{10}^{7})$	-0.178 ± 0.132	-0.083 ± 0.130	0.087 ± 0.118	0.035 ± 0.109
$\mathrm{Im}(r_{1-1}^{7})$	0.093 ± 0.198	0.429 ± 0.214	0.152 ± 0.188	-0.019 ± 0.191
r_{11}^{8}	0.052 ± 0.267	-0.251 ± 0.335	-0.282 ± 0.276	0.065 ± 0.286
r_{00}^{8}	0.209 ± 0.208	0.311 ± 0.218	-0.160 ± 0.190	-0.099 ± 0.189
$\mathrm{Re}(r_{10}^{8})$	-0.141 ± 0.139	-0.355 ± 0.147	0.068 ± 0.127	0.158 ± 0.121
r_{1-1}^{8}	0.006 ± 0.242	-0.126 ± 0.220	-0.118 ± 0.197	0.049 ± 0.207

Table C.3. Spin-density matrix elements extracted using the targets ^{1}H, ^{2}H, ^{3}He, and ^{14}N. The uncertainties are statistical. The mass values, A, in the table labels are in atomic units.

r_{ij}^{α}	$A=1$	$A=2$	$A=3$	$A=14$
r_{00}^{04}	0.282 ± 0.031	0.305 ± 0.035	0.317 ± 0.041	0.343 ± 0.054
$\mathrm{Re}(r_{10}^{04})$	0.004 ± 0.021	-0.062 ± 0.022	-0.006 ± 0.026	0.005 ± 0.034
r_{1-1}^{04}	-0.018 ± 0.029	0.003 ± 0.031	0.077 ± 0.038	0.007 ± 0.048
r_{11}^{1}	0.046 ± 0.070	0.048 ± 0.076	0.052 ± 0.093	-0.087 ± 0.118
r_{00}^{1}	0.001 ± 0.051	0.023 ± 0.055	0.040 ± 0.067	-0.003 ± 0.084
$\mathrm{Re}(r_{10}^{1})$	0.027 ± 0.036	-0.016 ± 0.038	-0.081 ± 0.046	0.039 ± 0.055
r_{1-1}^{1}	0.315 ± 0.049	0.307 ± 0.055	0.350 ± 0.067	0.219 ± 0.083
$\mathrm{Im}(r_{10}^{2})$	0.044 ± 0.036	-0.013 ± 0.039	-0.046 ± 0.046	-0.009 ± 0.064
$\mathrm{Im}(r_{1-1}^{2})$	-0.280 ± 0.050	-0.287 ± 0.054	-0.304 ± 0.060	-0.225 ± 0.073
$\mathrm{Im}(r_{10}^{3})$	-0.087 ± 0.073	0.033 ± 0.076	-0.072 ± 0.077	0.292 ± 0.163
$\mathrm{Im}(r_{1-1}^{3})$	-0.107 ± 0.110	-0.003 ± 0.116	-0.106 ± 0.110	-0.170 ± 0.242
r_{11}^{5}	0.064 ± 0.037	0.012 ± 0.041	0.007 ± 0.045	-0.023 ± 0.063
r_{00}^{5}	-0.042 ± 0.028	-0.032 ± 0.032	0.001 ± 0.036	0.053 ± 0.047
$\mathrm{Re}(r_{10}^{5})$	0.136 ± 0.018	0.154 ± 0.019	0.144 ± 0.022	0.137 ± 0.032
r_{1-1}^{5}	-0.011 ± 0.023	-0.028 ± 0.026	-0.015 ± 0.030	0.017 ± 0.039
$\mathrm{Im}(r_{10}^{6})$	-0.173 ± 0.018	-0.164 ± 0.018	-0.178 ± 0.024	-0.152 ± 0.029
$\mathrm{Im}(r_{1-1}^{6})$	-0.032 ± 0.025	-0.045 ± 0.027	0.002 ± 0.031	-0.015 ± 0.039
$\mathrm{Im}(r_{10}^{7})$	0.090 ± 0.098	-0.051 ± 0.105	-0.068 ± 0.103	-0.435 ± 0.230
$\mathrm{Im}(r_{1-1}^{7})$	-0.086 ± 0.165	0.234 ± 0.172	0.311 ± 0.161	-0.031 ± 0.352
r_{11}^{8}	-0.006 ± 0.214	0.211 ± 0.249	-0.417 ± 0.237	-0.131 ± 0.442
r_{00}^{8}	-0.059 ± 0.160	-0.024 ± 0.173	0.292 ± 0.169	-0.354 ± 0.348
$\mathrm{Re}(r_{10}^{8})$	-0.115 ± 0.107	-0.010 ± 0.111	0.067 ± 0.110	0.013 ± 0.221
r_{1-1}^{8}	-0.122 ± 0.175	-0.092 ± 0.184	0.070 ± 0.182	0.003 ± 0.376

[1] F. Halzen and A. D. Martin, "Quarks and Leptons: An Introductory Course in Modern Particle Physics", John Wiley & Sons, New York (1984).

[2] M. E. Peskin and D. V. Schroeder, "An Introduction to Quantum Field Theory", Addison-Wesley, Menlo Park, California (1995).

[3] J. J. van Hunen, "Deep-Inelastic Scattering off ^{14}N", Ph. D. thesis, Universiteit Utrecht (2000) unpublished.

[4] B. E. Tipton, "Measurement of Polarized Parton Distributions with Spin-Dependent Deep-Inelastic Scattering", Ph. D. thesis, Massachusetts Institute of Technology (1999) unpublished.

[5] J. W. Martin, "Measurement of the Spin Asymmetry $A_{\|}$ in the Photoproduction of High-p_T Hadron Pairs", Ph. D. thesis, Massachusetts Institute of Technology (2000) unpublished.

[6] J. Blouw, "Spin-Dependent Deep-Inelastic Positron Scattering from Polarized ^{3}He", Ph. D. thesis, Vrije Universiteit te Amsterdam (1998) unpublished.

[7] B. Povh and J. Hüfner, Phys. Rev. Lett. **58**(1987)1612.

[8] H. Beier, "Diffractive Production of ρ^0 Mesons in Deep Inelastic Scattering at HERA", Ph. D. thesis, Universität Hamburg (1997) unpublished.

[9] T. H. Bauer, *et al.*, Rev. Mod. Phys. **50**(1978)261.

[10] A. D. Martin, M. G. Ryskin, and T. Teubner, Phys. Rev. D **55**(1997)4329.

[11] A. D. Martin, M. G. Ryskin, and T. Teubner, hep-ph/9912551 (1999).

[12] F. Meißner, "Measurement of the J/Ψ-Cross Section and Double-Spin Asymmetries in Vector Meson Production in Polarised Lepton-Nucleon Scattering at HERMES", Ph. D. thesis, Humboldt-Universität zu Berlin (2000) unpublished.

[13] M. A. Pichowsky and T.-S. H. Lee, Phys. Rev. D **56**(1997)1644.

[14] A. Donnachie and P. V. Landshoff, Phys. Lett. B **348**(1995)213.

[15] A. Donnachie and P. V. Landshoff, Nucl. Phys. B **311**(1988)509.

[16] G. A. Schuler and T. Sjöstrand, Nucl. Phys. **B407**(1993)539.

[17] B. Kopeliovich, private communication.

[18] J. A. Crittenden, "Exclusive Production of Neutral Vector Mesons at the Electron-Proton Collider HERA", Springer Tracts in Modern Physics, Volume 140, Springer, Berlin and Heidelberg (1997). Or see hep-ex/9704009.

[19] D. Yu. Ivanov and R. Kirschner, Phys. Rev. D **58**(1998)114026. Or see hep-ph/9807324.

[20] I. Royen and J.-R. Cudell, Nucl. Phys. **B545**(1999)505. Or see hep-ph/9807294

[21] G. Cvetič, *et al.*, Eur. Phys. J. C **13**(2000)301. Or see hep-ph/9908473.

[22] H. G. Dosch, *et al.*, Phys. Rev. D **55**(1997)2602.

[23] M. G. Ryskin, Z. Phys. C **57**(1993)89.

[24] E. V. Kuraev, *et al.*, JETP Lett. **68**(1998)696.

[25] P. G. O. Freund, Nuovo Cimento, **48A**(1967)541.

[26] R. Dixon, *et al.*, Phys. Rev. Lett. **39**(1977)516.

[27] NM Collab., M. Arneodo, *et al.*, Nucl. Phys. **B429**(1994)503.

[28] ZEUS Collab., M. Derrick, *et al.*, Phys. Lett. B **380**(1996)220.

[29] H1 Collab., C. Adloff, *et al.*, hep-ex/0005010.

[30] M. Arneodo, private communication. ZEUS Collab., "Angular distributions in exclusive electroproduction of ρ^0 and ϕ mesons at HERA", Abstracts 792/793 Addendum to the XXIX International Conference on High Energy Physics (1998). Or see http://www-zeus.desy.de/conferences98/ichep98papers/diff/add-792-793/add.ps.gz.

[31] P. Joos, *et al.*, Nucl. Phys. **B113**(1976)53.

[32] E665 Collab., M. R. Adams, *et al.*, Z. Phys. C **74**(1997)237.

[33] EM Collab., J. J. Aubert, *et al.*, Phys. Lett. B**161**(1985)203.

[34] HERMES Collab., K. Ackerstaff, *et al.*, to be published in Eur. Phys. J. C. Or see hep-ex/0002016.

[35] H1 Collab., C. Adloff, *et al.*, Eur. Phys. J. C **13**(2000)371. Or see hep-ex/9902019.

[36] B. Clerbaux, "Electroproduction Elastique de Mésons ρ à HERA", Ph. D. thesis, Université Libre de Bruxelles (1998) unpublished.

[37] ZEUS Collab., J. Breitweg, *et al.*, Eur. Phys. J. C **12**(2000)393.

[38] K. Schilling and G. Wolf, Nucl. Phys. **B61**(1973)381.

[39] H. Fraas and D. Schildknecht, Nucl. Phys. **B14**(1969)543.

[40] J. D. Jackson, "Classical Electrodynamics", 2nd ed., John Wiley & Sons, New York (1975).

[41] M. Gourdin, Nuovo Cimento **21**(1961)1094.

[42] C. W. Akerlof, *et al.*, Phys. Rev. **163**(1967)1482.

[43] L. N. Hand, Phys. Rev. **129**(1963)1834.

[44] J. Ballam, *et al.*, Phys. Rev. D **5**(1972)545.

[45] M. Jacob and G. C. Wick, Ann. Phys. **7**(1959)404.

[46] HERMES Collab., K. Ackerstaff, *et al.*, Phys. Rev. Lett. **82**(1999)3025.

[47] J. J. Sakurai, Phys. Rev. Lett. **22**(1969)981.

[48] D. Schildknecht, G. A. Schuler, and B. Surrow, Phys. Lett. B **449**(1999)328.

[49] M. Gell-Mann and F. Zachariasen, Phys. Rev. **124**(1961)953.

[50] J. Feltesse, *et al.*, Nucl. Phys. **B93**(1975)242.

[51] M. L. Perl, "High Energy Hadron Physics", John Wiley & Sons, New York (1974).

[52] D. G. Cassel, *et al.*, Phys. Rev. D **24**(1981)2787.

[53] J. Hüfner and B. Z. Kopeliovich, Phys. Lett. B **426**(1998)154. Or see hep-ph/9712297 (1997).

[54] P. G. O. Freund, Nuovo Cimento, **44A**(1966)411.

[55] G. Wolf, private communication.

[56] J. C. Collins, L. Frankfurt, and M. Strikman, Phys. Rev. D **56**(1997)2982.

[57] M. G. Ryskin, R. G. Roberts, A. D. Martin, and E. M. Levin, Z. Phys. C **76**(1997)231.

[58] D. Ivanov and R. Kirschner, private communication.

[59] W. Wander, "Reconstruction of High Energy Scattering Events in the HERMES Experiment", Ph. D. thesis, Universität Erlangen-Nürnberg (1996) unpublished. For English translation see HERMES internal note 97-031.

[60] M. Kolstein, "Exclusive ρ^0-Meson Electroproduction at HERMES", Ph. D. thesis, Vrije Universiteit te Amsterdam (1998) unpublished.

[61] HERMES Collab., K. Ackerstaff, *et al.*, Nucl. Instr. and Meth. **A417**(1998)230.

[62] J. D. Jackson, Rev. Mod. Phys. **48**(1976)417.

[63] A. A. Sokolov and I. M. Ternov, Soviet Physics-Doklady, **8**(1964)1203.

[64] G. Schnell, "Longitudinal Polarization of the Λ in Deep Inelastic Scattering of Polarized Positrons from Nucleons", Ph. D. thesis, New Mexico State University (1999) unpublished.

[65] P. Chumney, private communication.

[66] N. A. Filatova, *et al.*, Nucl. Instr. Meth. **143**(1977)17.

[67] G. Rakness, "Study of Front Drift Chamber Resolution and Efficiency", HERMES Internal Note 98-037.

[68] W. R. Leo, "Techniques for Nuclear and Particle Physics Experiments", Springer-Verlag, New York (1987).

[69] HERMES Collab., A. Airapetian, *et al.*, Phys. Lett. B **442**(1998)484.

[70] T. G. O'Neill, private communication.

[71] `http://hermes.desy.de/~abr/dq.html`

[72] S. Rudnitsky, "ϕ Meson Production and Beam Polarimetry at HERMES, DESY", Ph. D. thesis, University of Pennsylvania (1997) unpublished.

[73] J. D. Jackson, Nuovo Cimento **34**(1964)1645.

[74] A. Borissov, private communication.

[75] P. R. Bevington and D. K. Robinson, "Data Reduction and Error Analysis for the Physical Sciences", 2nd ed., McGraw-Hill, Inc., New York (1992).

[76] J. R. Taylor, "An Introduction to Error Analysis", University Press, Mill Valley, CA (1982).

[77] F. K. Martens, "Elastic Production and Decay of Rho Mesons at HERMES", M. S. thesis, University of Alberta (1998) unpublished.

[78] A. I. Titov, Y. Oh, and S. N. Yang, Phys. Rev. Lett. **79**(1997)1634. Or see nucl-th/9702015.

[79] ZEUS Collab., J. Breitweg, *et al.*, Eur. Phys. J. C **2**(1998)247.

[80] I. Akushevich, Eur. Phys. J. C **8**(1999)457.

[81] I. Akushevich and P. Kuzhir, Phys. Lett. B **474**(2000)411.

[82] S. Baker and R. D. Cousins, Nucl. Instr. and Meth. **221**(1984)437.

[83] H. Böttcher, Y. Gärber, and U. Stösslein, HERMES Internal Note 99-053 (1999).

[84] B. Clerbaux, from the Workshop of Low-x Physics, hep-ph/9908519 (1999).

[85] M. Diehl, *et al.*, Phys. Rev. D **59**(1999)034023.

[86] A. D. Martin, R. G. Roberts, and W. J. Stirling, Phys. Lett. B **387**(1996)419. Or see hep-ex/9606345.

[87] HERMES Collab., A. Airapetian, *et al.*, to be published in Eur. Phys. J. C. Or see hep-ex/0004023.

[88] S. Brodsky, private communication.

[89] J. Ballam, *et al.*, Phys. Rev. D **10**(1974)765.

[90] C. del Papa, *et al.*, Phys. Rev. D **19**(1979)1303.

[91] J. T. Dakin, *et al.*, Phys. Rev. D **8**(1973)687.

[92] W. R. Francis, *et al.*, Phys. Rev. Lett. **38**(1977)633.

[93] ZEUS Collab., M. Derrick, *et al.*, Z. Phys. C **69**(1995)39.

[94] ZEUS Collab., J. Breitweg, *et al.*, Eur. Phys. J. C **6**(1999)603.

[95] H1 Collab., S. Aid, *et al.*, Nucl. Phys. **B468**(1996)3.

[96] W. D. Shambroom, *et al.*, Phys. Rev. D **26**(1982)1.

[97] B. Clerbaux, private communication.

[98] M. Tytgat, private communication.

[99] CEBAF Experiment proposal 93-022. H. Funsten, P. Rubin, and E. S. Smith, Spokespersons.

[100] CEBAF Experiment proposal 99-105. M. Guidal, C. Marchand, and E. Smith, Spokespersons.